Doctoral Thesis

Sea Surface Remote Sensing with GNSS and Sunlight Reflections

François Soulat

Director: Giulio Ruffini[1]

October 2003

Advisor: Antoni Broquetas[2]

[1]Starlab
Edifici de l'Observatori Fabra
C. de l'Observatori s.n., Muntanya del Tibidabo
08035 Barcelona, Spain
http://starlab.es

[2]Universitat Politècnica de Catalunya
Depart. of Signal Theory and Comm.
Jordi Girona, 31
08034 Barcelona, Spain
http://www-tsc.upc.es

Acknowledgements

I would like to express my deep and sincere gratitude to many people who made this thesis possible. Special thanks are due to the two persons who have directed me during this thesis: Giulio Ruffini, head of Starlab, Spain, and Bertrand Chapron, head of the Oceanographic Space Research Department at Ifremer, France. I owe my most sincere gratitude to the former especially for his wide knowledge, encouragement and personal guidance. Many thanks to the latter—king grasshopper—for his exhaustive advice.

I wish to express my warm and sincere thanks to the Starlab team for the support they provided. I warmly thank Olivier Germain, Marco Caparrini, Leo Ruffini and Ernest Mendoza who provided me, among others, discipline in my work and useful comments. Ana Maiques and Araceli Pi have been exceptional with their unforgettable maternal attention.

My sincere thanks are also due to the GNSS-R community, with a particular acknowledgement to Manuel Martìn-Neira and Pierluigi Silvestrin from the European Space Research and Technology Centre, The Netherlands, and ESA/ESTEC, who supported together with Starlab most of this research. I am also grateful to Antonio Rius (IEEC), Estel Cardellach (JPL/NASA), Tony Elfouhaily (CNRS/IRPHE/IOA), Donald Thompson (Johns Hopkins University/APL), and Jordi Vilà from the Barcelona Port Authority.

I also would like to thank the young French team of Ifremer/DRO/OS composed by Jérôme Gourrion, Nicolas Reul and Olivier Archer, as well as Fabrice Collard from Boost Technologies.

My sincere thanks are due to my tutor at the Universitat Politècnica de Catalunya, Antoni Broquetas, who advised me during my thesis project, and to Adriano Camps (UPC/TSC) for his kindness and support.

Personal thanks to those who cheered me on during these three years:
Laurence, Françoise, Jean-Louis, Bénédicte, Christine, Paul, Eloise, Alice, André, Marie-Alice, Yvonne, Simon, Emile, Michèle, Marc, Guy, Fanchon, François, Edith, Isabelle, Guillaume, Ambroise, Aurélien, Fructu, Silvia, Marie, Antoine, Jézabel, Line, the Stéphanes, Stéphanie, Bruno, Ignasi, Olivier, Chloé, Martin, Anne, Anne-Laure, Marianne, Astrild, Pauline, Ariane, Julien, Félicien, Nicola, Catherine, Christian, Jason, Jordi (there are a lot!), Miguel-Angel, Ana, Carles, Ensaladilla Sound System, Tiboum, the Bass.

Abstract

This thesis investigates the remote-sensing capabilities of GNSS reflections (GNSS-R) for oceanographic applications, through theoretical studies and experimental data analysis. We first provide an overview of the models related to involved physical processes, such as spectral and statistical characteristics of random sea surface, electromagnetic scattering and signal processing. From a theoretical and numerical point of views, we particularly focus on the validation at L-band of the Geometric Optics approximation of the Kirchhoff scattering theory over the ocean. A new model for the scatterometric bi-dimensional waveform, namely the Delay-Doppler Map (DDM), is then proposed. A GNSS-R simulation toolkit is developed, which enables the synthesis of the electromagnetic reflected field over ocean surface. This simulator is used for assessing the retrieval of sea-state from a coastal platform. Furthermore, we focus on GNSS-R sensitivity to sea-surface dynamics, roughness and salinity through experimental data analysis. Particular interest is put on the investigation of scatterometric applications analyzing data from an experimental flight under quite strong wind conditions. A complete DDM inversion is carried out to infer directional sea-surface mean square slope (DMSS), which defines the size, the direction and the isotropy of a Gaussian slope PDF. This technique is validated and appears to be a very efficient tool for GNSS-R scatterometry. Simultaneously gathered, solar bistatic reflection measurements (SORES) enhance the understanding of quasi-specular scattering through the bi-dimensional Tilt-Azimuth Mapping of the sea surface. Considered as a repetition of the famous Cox and Munk experiment, SORES inversion provides DMSS which are consistent with L-band derived DMSS, and reveals a significant non-Gaussianity of the slope PDF. Based on a spectral analysis, we investigate the important impact of swell in addition to wind stress over DMSS. Both optical and L-band total MSS are 20% higher than what predicts a wind-driven model for the observed wind speeds. We conclude that DMSS should be considered as a self-standing product and not be systematically linked to the near-surface wind vector. Additional ground experiments are reported in order to draw preliminary conclusions on the possible retrieval of sea-surface salinity and emissivity with GNSS-R. The impact of salinity is observed through analysis of the interference between direct signal along with reflected signal, which shows a strong noise compared to the expected estimated magnitude. Concerning the radiometric capability of GNSS-R, it is shown that the ratio of the direct and reflected signals allows the estimation of emissivity, although an a priori knowledge of sea-state is required.

Contents

Acknowledgements **3**

Abstract **5**

Introduction **11**

I Bistatic Sea Surface Remote Sensing with GNSS Signals **17**

1 GNSS Signal Characteristics **19**
1.1 Global Positioning System: GPS . . . 19
1.1.1 Signal structure . . . 19
1.1.2 Signal detection . . . 21
1.1.3 The modernization of GPS . . . 22
1.1.4 GPS reflections coverage . . . 25
1.2 GLONASS . . . 26
1.3 Galileo . . . 26

2 Sea Surface Model **29**
2.1 Sea-surface spectral model . . . 29
2.1.1 The involved geophysical parameters . . . 29
2.1.2 Elfouhaily et al. spectrum . . . 30
2.1.3 Sea surface generation . . . 31
2.1.4 Discussion on the use spectral models for scatterometric purposes . . . 31
2.1.5 Summary . . . 32
2.2 Gaussian sea-surface statistics . . . 33
2.2.1 Statistical characterization of random surfaces . . . 33
2.2.2 Slope distribution . . . 34
2.2.3 Impact of current on sea-surface slope variance . . . 35

3 Scattering Model **37**
3.1 Bistatic electromagnetic models . . . 37
3.1.1 Kirchhoff approximation or Physical Optics . . . 39
3.1.2 The Geometric Optics or Stationary Phase Approximation . . . 40
3.1.3 Small Perturbation Method . . . 43
3.1.4 The Two-Scale (Composite or Hybrid) Model . . . 44
3.2 GO validation at L-band . . . 45
3.2.1 Radius of curvature and scatterer size . . . 45
3.2.2 Parabolic surface . . . 46
3.2.3 Gaussian surface . . . 48

3.2.4 Conclusions on GO assumption for GNSS-R . . . 51
3.3 Waveform model: DDM . . . 52
3.3.1 Integral expression of the power waveform . . . 52
3.3.2 Expression as a 2-D integral on sea-surface . . . 58
3.3.3 Comparison with Zavorotny's and Picardi's models . . . 58

4 GNSS-R Signal Processing 61
4.1 From raw data to Level 0: Delay-Doppler PRN code despreading . . . 61
4.1.1 Initialization . . . 63
4.1.2 Tracking the 1-D waveforms . . . 67
4.1.3 2-D waveforms generation (DDM) . . . 67
4.2 From Level 0 to Level 0b data: incoherent averaging . . . 68
4.3 From Level 0b to Level 1 data: retracking . . . 68

II GNSS-R Signal Simulations 71

5 GNSS-R Simulation Toolkit 73
5.1 Model 1: GRADAS . . . 74
5.1.1 How to simulate the field for large ocean surfaces? . . . 74
5.1.2 GNSS direct and reflected signals . . . 76
5.1.3 GRADAS algorithm . . . 77
5.1.4 Validation . . . 79
5.2 Model 2: Intermittent Screamers . . . 82
5.2.1 Specular point specifications . . . 83
5.2.2 Code implementation . . . 85
5.2.3 Simulated data and analysis . . . 86
5.3 Conclusions . . . 87

6 An Application for Sea State Monitoring 89
6.1 Simulation specifications . . . 89
6.2 Results . . . 90
6.2.1 Phase analysis . . . 90
6.2.2 Amplitude analysis . . . 90
6.2.3 Field derivative analysis . . . 92
6.3 Conclusions . . . 93

III GNSS-R Airborne Scatterometric Performance Analysis 95

7 The Eddy Experiment Flight 97
7.1 Experimental campaign . . . 97
7.1.1 Instrumental set-up . . . 99
7.1.2 Satellite configuration . . . 100
7.2 Ground truth . . . 100

8 Scatterometry with Sunlight 105
8.1 The data set . . . 105
8.2 Inversion procedure . . . 107
8.2.1 The directional mean square slope . . . 107
8.2.2 Forward model . . . 109

8.2.3 Parameter search . . . 113
8.2.4 Results . . . 113
8.3 Wind and waves characterization . . . 117
8.3.1 Spectral analysis . . . 117
8.3.2 Simulations . . . 120
8.4 Comparison with Cox and Munk's measurements . . . 125
8.5 Conclusions . . . 128

9 Scatterometry with GNSS-R 131
9.1 The data set . . . 131
9.2 Retracking and inversion . . . 132
9.2.1 The forward model . . . 132
9.2.2 Inversion scheme . . . 133
9.2.3 Empirical adjustments . . . 138
9.3 Analysis of the results . . . 138
9.3.1 Estimated DMSS . . . 138
9.3.2 Convergence and residual . . . 140
9.4 Comparison of optical and L-band derived DMSS . . . 140
9.4.1 Link to wind speed . . . 143
9.5 Conclusions . . . 143

IV Other GNSS-R Applications 147

10 Sensitivity to Salinity 149
10.1 Experimental campaign . . . 149
10.1.1 Description . . . 149
10.1.2 Instrumentation . . . 150
10.1.3 Satellites in view . . . 150
10.2 Theoretical analysis . . . 150
10.2.1 Received power versus elevation angle . . . 152
10.2.2 Dielectric constant model . . . 153
10.2.3 How do the polarization coefficients depend on salinity? . . . 157
10.2.4 Power model . . . 159
10.3 Data analysis . . . 159
10.4 Discussion on salinity estimation . . . 162
10.5 Conclusions on salinity retrieval with GNSS-R . . . 162

11 Emissivity Retrieval 165
11.1 Experimental campaign . . . 165
11.2 Power model . . . 166
11.2.1 Reflected to direct signal ratio analysis . . . 168
11.2.2 Summary . . . 169
11.3 Simulations . . . 169
11.3.1 Reflected to direct signal ratio analysis . . . 171
11.4 Data analysis . . . 171
11.5 Conclusions on radiometry with GNSS-R . . . 174

Conclusions and Perspectives 175

V Appendix **179**

A Relevant Symbols **181**

B Acronyms **183**

List of Figures **185**

List of Tables **191**

Bibliography **193**

Introduction

The sea surface represents the interface between the ocean and the atmosphere, the two most crucial systems governing the dynamics of climate and global change of the planet. Improved understanding of the coupled interactions of the physical processes taking place at the ocean-atmosphere interface is thus essential.

It has long been recognized that the retrieval of oceanographic data is a key component in modern meteorological analysis and forecasting, as well as an essential resource for climate research. Oceanographic studies suffered during a long period from lack of measurements. Indeed first observations began with in-situ measurements such as buoys, radars on-board planes or boats. During the last twenty years, ocean observation has increased in efficiency with the use of remote-sensing instruments such as scatterometers, synthetic aperture radars and radar-altimeters on-board satellites. The interaction between emitted waves and the sea surface can provide a geophysical signature.

The sea responds to atmospheric forcing on many scales in both time and space. Remote-sensing of near-surface wind speed over the ocean by microwave techniques relies on the modification of short surface waves by the surface layer winds. This inter-relationship is typically sampled, formulated, and utilized on spatial scales of 10-50 km: the mesoscale.

In the last past few years, an original remote-sensing concept has focused on the *passive bistatic* retrieval of geophysical data. The term *passive* indicates that the developed systems do not emit any signal, they just "listen". The term *bistatic* means that emitter and receiver are located at two different places in space. The underlying principle is the use of reflected signals originating from sources of opportunity to infer properties of the reflecting surface, such as significant wave height (SWH), mean sea level (MSL) and directional mean square slope (DMSS). It can potentially provide more information compared to monostatic approaches, where emitter and receiver are put on the same platform, due to the potential availability of multiple sources.

Here, we consider Global Navigation Satellite Systems (GNSS) as sources of opportunity emitting at L-band ($\sim$20 cm). GNSS reflections (GNSS-R) is an offspring of bistatic radar in which only the receivers need to be deployed on a specific platform (coastal, airborne or spaceborne); the emitters are already in place for other purposes. We emphasize that GNSS systems are premium candidates for remote-sensing applications, given their coverage, potential resolution, long-term availability and signal characteristics.

Objectives

The main objective of the thesis is to analyze the GNSS-R capabilities in ocean surface remote-sensing. For this purpose, we aim at developing models with specific data products, carrying out dedicated experimental campaigns. The use of GNSS signals reflected off the sea surface as a remote-sensing tool has generated considerable attention since the pioneering

study of [Martìn-Neira1993]. Two classes of applications have rapidly emerged in the community: sea-surface altimetry, which aims at retrieving the mean sea level like classical radar altimeters and sea-surface scatterometry for the determination of sea-roughness. The former consists in an estimation of the relative delay between the direct and reflected signals, whereas the latter—addressed in this dissertation—focuses on the modification of the scattered signal to infer sea-surface characteristics. In addition, particular interest has been put on another parameter usually provided by radiometers, the emissivity, which has not been yet investigated with GNSS-R. We will also consider a component of the emissivity, salinity, although the retrieval is much more challenging.

We will present for this purpose the models related to involved physical processes, such as spectral and statistical characteristics of the random sea surface, electromagnetic scattering and signal processing. We aim at determining the reflected signal characteristics through the modeled return 2-D waveform, namely the Delay-Doppler Map (DDM). Several experiments will be presented in order to investigate retrievals of specific geophysical sea-surface parameters. The received signal can be treated with several processing strategies depending on the desired product.

We emphasize in this study the investigation on the directional sea-surface roughness, which is one key missing integrated element, essential to understand and quantify the ocean-atmosphere flux of energy and momentum. DMSS can help to better control the width of the directional distribution of wave energy. It is a simple parameter—often related to the sea-surface wind vector—required to characterize the sea-state degree of development. This parameter shall constrain the source terms in wave energy evolution equation. It can be readily assimilated and help routine forecast of waves.

In order to enhance the understanding of GNSS-R response to sea-surface roughness, sunlight can also be used as a source of opportunity. The approach is simply based on the observation and analysis of the visible glitter pattern over the sea surface.

The three key concepts to bear in mind in this dissertation are:

- **Bistatic scattering**: bistatic remote-sensing differs from the monostatic one by the fact that transmitter and receiver have different locations.
- **Specular reflections**: they dominate radar forward scattering in the microwave domain and at shorter wavelengths. Scatterometry may be thus re-named *speculometry*.
- **Sea-surface roughness**: it is mainly described by the mean square slope (MSS)—or the directional MSS (DMSS)—which is by definition the second order moment of the sea-surface slope probability density function (PDF). The MSS does not provide any information on the directivity of the sea-surface slope PDF, whereas the DMSS is a parameter of the 2-D PDF.

Context

The investigation includes theoretical analysis and experimental campaigns, both of which have been carried out at Starlab within the scope of projects for the European Space Agency (ESA), the Institut Français de Recherche et d'Exploitation de la MER (IFREMER), and Starlab. Table 1 summarizes the geophysical products observed and modeled during the thesis for different platforms (coastal, airborne and spaceborne).

A particular motivation of this study was to gather simultaneously optical and L-band data sets from the same airborne platform during the PARIS-γ Experiment, as fully described

in Chapter 7. This experimental campaign was conducted by Starlab in September 2002 along the Catalan Coast for the demonstration of GNSS-R altimetry. An aircraft flying at 1000 m collected roughly 1.5 hours of GNSS-R data along a track of 150 km total length. We investigate the full exploitation of the bi-dimensional DDM product to infer the three parameters fully describing the sea-surface PDF.

In addition to GNSS-R, high resolution optical photographs of Sun glitter were taken, providing the so-called SORES data (SOlar REflectance Speculometer). Since the famous study of [Cox and Munk1954], it is well known that sea-roughness can be inferred from such data and its availability thus provides an extra source of co-located information. Since there is a strong similarity between products (DDM for GNSS-R and Tilt-Azimuth Map (TAM) for SORES) and models, the same inversion methodology was applied to both datasets.

Platform	**Wavelength**	**Experiment**	**Contract**	**Products**
Coastal	L-band	OceanPal (simulations) L-band Radiometry Salpex	Starlab Ifremer Ifremer	Sea-state Radiometry Salinity
Airborne	L-band	OPPSCAT II PARIS-γ	ESA ESA	Speculometry Altimetry
Airborne	Optical	PARIS-γ	ESA	Speculometry
Spaceborne	L-band	PARIS-β (artificial data)	ESA	Speculometry Altimetry

Table 1: Related experiments carried out during the thesis.

State of the art

Many GNSS-R applications have emerged recently. A complete overview of GNSS scattering over the sea surface can be found in [Ruffini *et al.*1999] and [Ruffini *et al.*2001a]. In addition to the well-known altimetric and scatterometric measurements, attempts have taken place to retrieve new products, such as ground reflectivity properties ([Kavak *et al.*1996]), ice detection ([Komjathy *et al.*2000a]) and soil moisture determination ([Masters *et al.*2002, Masters *et al.*2003]).

As far as speculometry is concerned, the inversion of GNSS-R data requires (i) a parametric description of the sea surface, (ii) an electromagnetic model for sea-surface scattering at L-band and (iii) the choice of a GNSS-R data product to be inverted. A review of these models can be found in the OPPSCAT projects supported by ESA. In the literature, it is often assumed that bistatic scattering at L-band can be reasonably described by the Geometric Optics approximation of the Kirchhoff theory. This assumption is studied and validated in this dissertation. This important conclusion allows us to state that the most important feature of sea surface is the statistics of small facet slopes: the bi-dimensional slope PDF. Under a Gaussian assumption, three parameters, encapsulated by DMSS, suffice to fully define the ellipsoidal shape of the slope PDF: the size (total MSS), the direction (Slope PDF azimuth) and the isotropy (Slope PDF isotropy).

The bistatic radar equation proposed by [Zavorotny and Voronovich2000] is to date the reference model for the community. Even though the sea surface is directly parametrized by DMSS, it is rarely presented as the geophysical parameter of interest. Rather, most authors prefer to link it to the near surface wind vector which is thought to be more explicit for

oceanographic and meteorological users. Nevertheless, this link requires the assumption that sea-roughness be wind-driven and no swell be present. Under such assumptions, one can use a given sea-elevation spectrum (like [Elfouhaily *et al.*1997]) to infer wind speed from the measurement of total MSS. We will argue that this assumption is restrictive.

Generally, the product inverted in GNSS-R speculometry is a waveform, that is a 1-D delay mapping of the reflected signal amplitude. Using one waveform, the wind speed can be inferred assuming an isotropic slope PDF (i.e., the PDF's shape is a circle) [Garrison2002, Cardellach *et al.*2003, Komjathy *et al.*2000b]. Attempts have also been made to measure the wind direction by fixing the PDF isotropy to some theoretical value (around 0.7) and using at least two satellites with different azimuths [Zuffada and Elfouhaily2000, Garrison2003]. [Ruffini *et al.*2000] and [Elfouhaily *et al.*2002] proposed to work on a product of higher information content: the Delay-Doppler Map (DDM), that is a 2-D delay-Doppler mapping of the reflected signal amplitude. The provision of this extra dimension opens the possibility to a full estimation of the DMSS. In particular, [Elfouhaily *et al.*2002] developed a rapid but sub-optimal method based on the moments of the DDM to estimate the full DMSS. However, this approach neglects the impact of the bistatic Woodward Ambiguity Function modulation of the Delay-Doppler return.

Plan of the dissertation

This dissertation is divided into four parts. The first part is, from a theoretical point of view, dedicated to bistatic sea surface remote-sensing using GNSS frequencies. We present then in a second part a simulator for GNSS-R based on the knowledge of the previous chapters. As a third part, we investigate the GNSS-R airborne scatterometric performance during the Eddy Experiment Flight carried out in the frame of the ESA project PARIS-γ. An optical device was also used to enhance the understanding of the L-band scattering in specular regime. Finally, a fourth part reports additional experimental and theoretical studies on the capability to retrieve sea-surface dielectric constant and emissivity with GNSS-R measurements. The Chapter structure is as follows:

- **PART I**: Bistatic Sea Surface Remote-Sensing with GNSS Signals.
  This part describes the mechanisms involved in bistatic sea-surface scattering at GNSS frequencies. It starts in Chapter 1 with a brief description of the available and future GNSS signals. A statistical description of the sea surface is then presented in Chapter 2, as well as the sea spectrum model used for this study. The bistatic electromagnetic models are presented in Chapter 3. Then, the signal processing of GNSS reflections and speculometric data products are presented in Chapter 4. The structure of this part is illustrated in figure 1.

- **PART II**: GNSS-R Signal Simulations.
  We present a spaceborne simulator for GNSS-R in Chapter 5. An example of application of such simulator is then reported in Chapter 6 with the derivation of empirical inversion laws for sea-state monitoring at low altitude.

- **PART III**: GNSS-R Airborne Scatterometric Performance Analysis.
  We provide in Chapter 7 the flight plan, instrumentation and set-up of the Eddy Experiment Flight. We report then in Chapter 8 a re-do of the Cox and Munk experiment which aimed at DMSS retrieval through inversion of Tilt-Azimuth Map of Sun glitter optical photographs. Furthermore, Chapter 9 is dedicated to the first inversion of GNSS-R full Delay-Doppler Map for the retrieval of the sea-surface directional mean square slope. In addition, a comparison of the SORES and GNSS-R data inversions is undertaken.

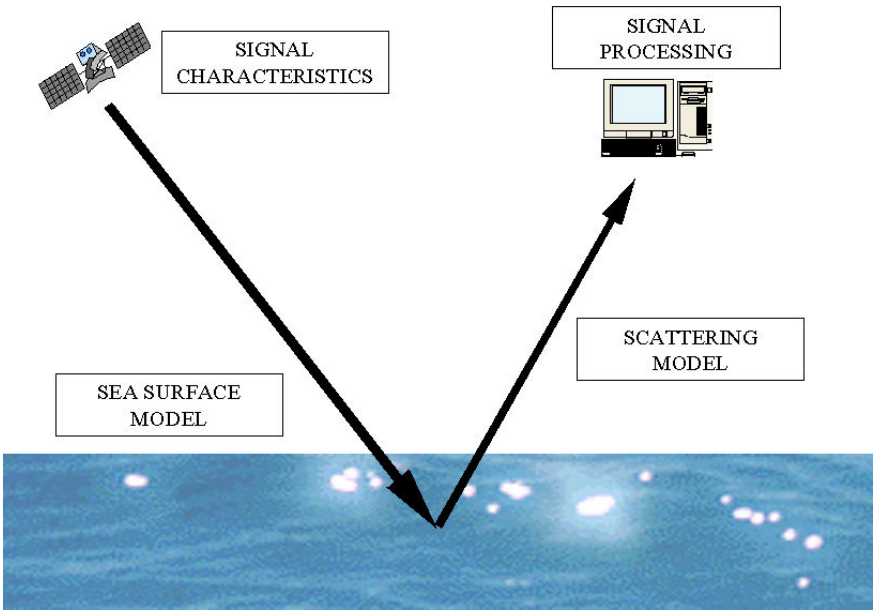

Figure 1: Structure of Part I.

- **PART IV**: Other GNSS-R Applications.
  Two coastal radiometric experiments are presented as an attempt to retrieve sea-surface salinity and emissivity through GNSS-R power characterization. Chapter 10 describes the Salpex experimental campaign and the related model to infer dielectric properties of the sea surface. The L-band Radiometry Experiment is then addressed in Chapter 11.

The conclusions of the dissertation and perspectives for future work are presented in page 175. The reader can find the list of relevant symbols and units used in this dissertation in Appendix A, and acronyms in Appendix B.

Part I

Bistatic Sea Surface Remote Sensing with GNSS Signals

Chapter 1

GNSS Signal Characteristics

This Chapter provides an overview of Global Navigation Satellite Systems (GNSS) with a focus on the issues relevant to this study. It includes the present Global Positioning System (GPS) along with its future improvements, the Russian system GLONASS and the future European navigation satellite system, Galileo. We focus especially on the former, since it is the basis of all the experiments carried out during this study. The goal of this Chapter is to describe the structure of the signal to better understand the scattering models presented in Chapter 3.

1.1 Global Positioning System: GPS

The GPS operational constellation, GPS-24[1], was designed to provide, from any fixed point on the Earth surface and at any instant of time, three-dimensional navigation capabilities. It consists of a constellation of 24 satellites orbiting in 6 different planes (inclined at 55^o) at an altitude of about 20200 km over the Earth's surface. There are four satellites in each plane. The satellites have a period of 12 h sideral time.

We depict in the following section the GPS structure of the two presently available L_1 and L_2 signals. Section (1.1.2) introduces briefly the main components of a GPS receiver in order to detect the incoming signal. An overview of the updates and future improvements of the whole system is then presented in section (1.1.3). Finally, GPS reflections coverage from space is presented to highlight the great number of observations compared to a monostatic system.

1.1.1 Signal structure

The structure of the GPS signal is based on spread spectrum signal techniques. It consists in spreading the bandwidth of the data signal (modulation at 50 Hz for the navigation data) by multiplying it by a pseudo-random ± 1 signal sequence of rectangular unit pulses (Pseudo-Random Noise PRN) at a much higher rate than the data stream, but synchronous to it. The goal of such spreading of the signal is to drop down the power spectral density for a given total radiated power, to increase the tolerance to multi-path and jamming, in addition to provide the system with multiple access capability (by means of different pseudo-random sequences for different transmitters).

Two main spreading signals are used: the Coarse/Acquisition (C/A) and the Precise (P) code. The C/A code is the civil GPS signal. It is a $\pm$ 1 pseudo-random sequence with a clock rate of 1.023 Mbps, and a short period of 1 ms allowing a rapid acquisition. The rate defines

[1] 27 satellites are operational as of 11-2000 (see http://www.navcen.uscg.gov/gps/).

a chip length of approximately 9.775×10^{-7} second, i.e., a length of around $\tau_{C/A}$=300 meters. Note that no information is carried by the unit pulse of the code. For this reason, we call them *chip* instead of *bit*, which is reserved for the navigation information unit pulse.

The P code is a $\pm$ 1 pseudo-random sequence with a clock rate of 10.23 Mbps, and a longer period of exactly 1 week. The transmitter-receiver range measurement through this code offers a better precision than C/A observables, since its chip length τ_P is ten times shorter than $\tau_{C/A}$.

The whole signal structure lays in L-band, as shown in figure 1.1. This avoids in particular rain effects (observed at higher frequencies). There are two emitted frequencies: L_1 and L_2 synthesizing respectively 19 cm and 24 cm long waves.

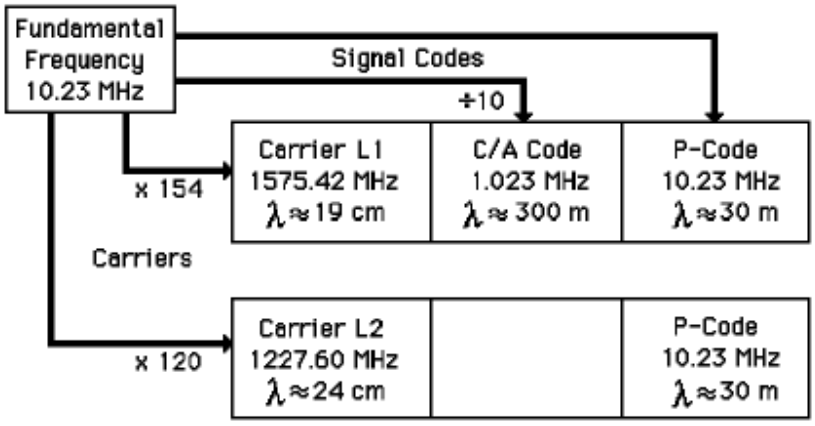

Figure 1.1: Present GPS signals.

The L_1 signal

The GPS L_1 signal (1575.42 MHz) for satellite i is given by [Parkinson and Spilker1996]:

$$S^i_{L_1}(t) = \sqrt{2P_c} \cdot XG^i(t) \cdot D^i(t) \cdot \cos(\Omega_1 t + \phi) + \sqrt{2P_p} \cdot XP^i(t) \cdot D^i(t) \cdot \sin(\Omega_1 t + \phi),$$

where Ω_1 is the L_1 angular frequency, ϕ represents phase noise and oscillator drift and P_c and P_p are the C/A and P signals powers, respectively. The term $XG^i(t)$ stands for the C/A code and $XP^i(t)$ for the P code. The binary data $D^i(t)$ is the navigation bit stream and also has an amplitude of $\pm$ 1 at 50 bps. It provides the user with ephemeris, almanacs, corrections and some other information required to obtain a satisfactory navigation and time transfer solution. The navigation data is formated into 30-bit word and has a 6 s sub-frame and a 30 s frame period. Figure 1.2 presents the structure of the L_1 signal.

Each satellite i transmits unique C/A and P codes. The C/A code is nominally 3 dB stronger than the P code on L_1. To avoid spoofing, the P code (which is of public knowledge) is replaced by an encrypted code (the Y code) when the "anti-spoof" mode of operation (AS) is on. Selective availability (SA), on the other hand, is a purposeful degradation of the GPS clocks and orbits. It has been turned off on May 1st 2000. The resulting accuracy improvement has lead to 22 meters horizontal, 33 meters vertical and 200 nanoseconds (60 light-meters) relative to UTC, all 95 percent of time.

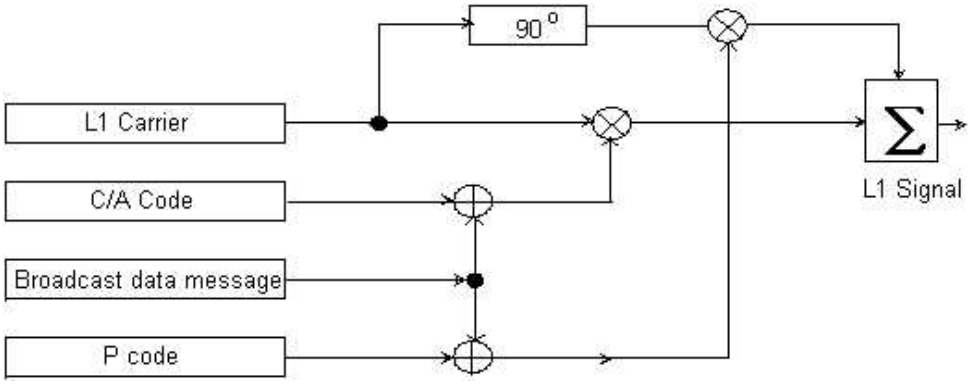

Figure 1.2: L_1 signal structure.

The L_2 signal

The L_2 signal (1227.6 MHz) is bi-phase modulated by the C/A or the P code, as selected by ground command. In the normal P operation, it is given by:

$$S^i_{L_2}(t) = \sqrt{2P_2} \cdot XP^i(t) \cdot D^i(t) \cdot \cos(\Omega_2 t + \phi),$$

where $\sqrt{2P_2}$ represents the L_2 signal amplitude, and $XP^i(t)$ is the P code for the ith satellite, which is clocked in synchronism with the L_1 codes. It is possible to recover the L_2 carrier without knowing the code, by squaring the signal or cross-correlating L_1 with L_2 with a delay offset that matches the L_1 to L_2 ionospheric delay difference.

Signal strength and pattern

The minimum specified received signal strength at output from a user receiver Right Hand Circular Polarized 0dBic antenna for satellites above 5^o of elevation is -160 dBw for the C/A component and -163 for the P code at L_1. For L_2, both figures become -166 dBw. Maximum figures (with a 0.6 dB atmospheric loss) are never over -153 dBw ([Parkinson and Spilker1996],vol I, p. 82). The total flux density in a 4-kHz band is below the permitted -154 dBw/m^2, thanks to the spread spectrum of GPS signals.

The transmitted signal is Right-Hand Circularly Polarized (RHCP), with an ellipticity better than 1.2 dB for L_1, and better than 3.2 dB for L_2 within the angular range $\pm 14.3^o$ from the antenna bore-sight (ellipticity here defined as the semi-axis ratio).

In terms of power Signal to Noise Ratio (SNR), the direct received signal has carrier power-to-noise density ratio with typical values ranging between 39 and 52 dB-Hz, depending on the geometry, real transmitted power and instrumental/propagation losses.

1.1.2 Signal detection

A positioning solution can be derived from the GPS signals without any a priori knowledge of neither the receiver location nor the constellation status. First, the receiver operates with a cold start sequence corresponding to a search with a clean replica of a PRN C/A code into several Doppler frequencies and delays to find a correlation peak. Once the peak is found, the receiver is able to track the C/A signal and thus to decode the navigation data message. The location of other visible satellites is then feasible along with their delay and frequency offsets to appropriately adjust the PRN C/A replicas. The whole set of C/A signals gathered by the receiver antenna can be demodulated and the carriers locked: the primary GPS observables

are tracked. They include the pseudo-range and the phase of the GPS signal, as shown in figure 1.3.

The pseudo-range is a rough estimation of the geometric distance (i.e., range) between the emitter and the receiver. This distance is called pseudo-range since it is not corrected for the multiple possible corrupting effects, which are mainly the clock errors and atmospheric delays (see below). Given an a priori delay, the Delay Lock Loop (DLL) follows the variation of the time delay between transmitter and receiver, directly related with the pseudo-range through the speed of the light. Provided that the a priori delay is accurate enough and the rate of change in the delay is low, the DLL acts as a maximum likelihood estimator. It uses the derivative of the code as a discrimination function, so that the product with the incoming signal yields the error in the delay of the discrimination function, permitting its iterative correction. The uncertainty in the pseudo-range observable depends on the computation of the discriminating function. High uncertainty is obtained for wide interval of derivation (δT in the early-late difference). The error in delay estimation is (see [Parkinson and Spilker1996]):

$$\sigma_{code} = c\tau_c \sqrt{\frac{B_{DLL}\delta T}{2SNR_0}}, \tag{1.1}$$

where δT has chip units, c is the speed of the light, τ_c the chip time length, B_{DLL} the noise bandwidth of the DLL and SNR_0 the carrier power-to-noise density ratio (receiver dependent). Fine early-late spacing yields good precision, but on the contrary, the reduction of this spacing length also corrupts the tracking of the dynamics of the signal. This error ranges between 0.3 m and 1 m for the C/A code and is below 0.2 m for the P code. The code measurements are not precise but accurate.

The phase observable represents the history of the frequency adjustments performed by the Numerically Controlled Oscillator (NCO) to maintain the lock of the signal. This is equivalent to the integrated Doppler frequency, due to the relative motion between emitter and receiver. Therefore, this data does not provide the range itself, but a variation in the carrier cycle, which can be expressed as a range variation by the relation: $\lambda\delta\phi/2\pi$. It is thus called the Accumulated Delta Range (ADR). The tracking of this observable is done through a Phase Lock Loop (PLL) and the precision is given by:

$$\sigma_{phase} = \frac{\lambda}{2\pi} \sqrt{\frac{B_{PLL}\delta T}{2SNR_0}}, \tag{1.2}$$

where B_{PLL} is the bandwidth of the PLL. Typically, the error magnitudes are very small (below 1 mm). It is a precise measurement but very inaccurate, since it provides the integrated rate of change of the range up to an unknown bias offset.

1.1.3 The modernization of GPS

In 1998, US Vice President Gore announced that a second civil signal will be broadcast on the L_2 carrier, and that beginning in 2005 a third civil signal specifically designed for safety-of-life services will also be broadcast. The role of the civil L_2 signal is to provide needed ionospheric corrections. For non-differential real-time GPS users, the addition of these new signals provides redundancy, improved accuracy, availability and integrity, continuity of service and resistance to RF interference. For differential applications, they also assist in high precision applications. The next paragraphs are devoted to two papers recently published in GPS World ([Shaw2000],[Dierendonck2000]). Figure 1.4 shows the current and future civil GPS frequencies. For military applications, new codes are being developed, the M-codes, which will modulate the L_1 and L_2 carriers.

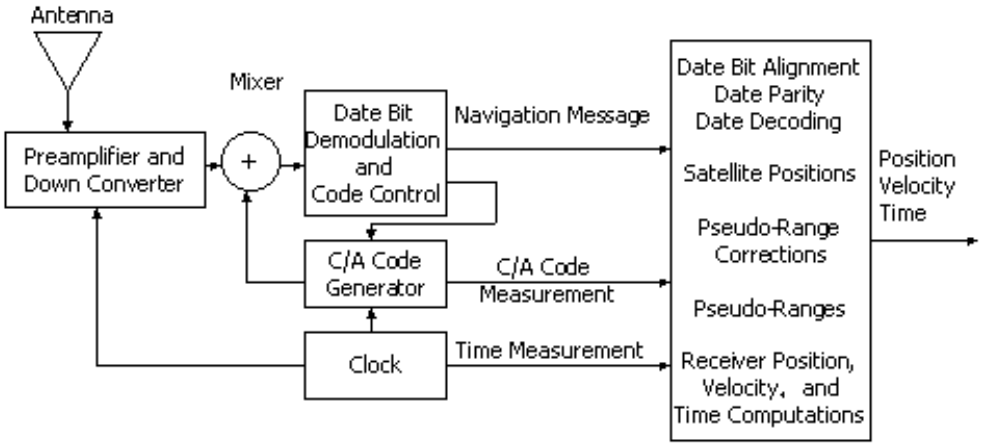

Figure 1.3: Structure of a GPS receiver.

In [MacDonald2002] a review of the development, status and current capabilities of GPS can be found. The author investigates also the implications of the GPS modernization and enhancement activities and their relationship to the analogous European Galileo program activities presented below in section (1.3).

Civil signal on L_2

The L_2 signal is shared between civil and military codes. The new L_2 civil signal (L2C) will be transmitted by modernized IIR (IIR-M) scheduled to be launched in 2003. L2C is limited to a single bi-phase component in phase quadrature with the P/Y code. It is also limited to a 1.023 MHz clock rate in order to maintain spectral separation from the new military M code. The L2C signal contains two codes of different lengths. The moderate length code (CM) has 10230 chips, repeats every 20 ms, and is modulated with message data. The long code (CL) has 767250 chips, repeats every 1.5 s, and has no data modulation. The composite signal is clocked at 1.023 MHz and alternates between chips of each code (chip-by-chip time multiplexed). A detailed description of the signal can be found in [Fontana *et al.*2001].

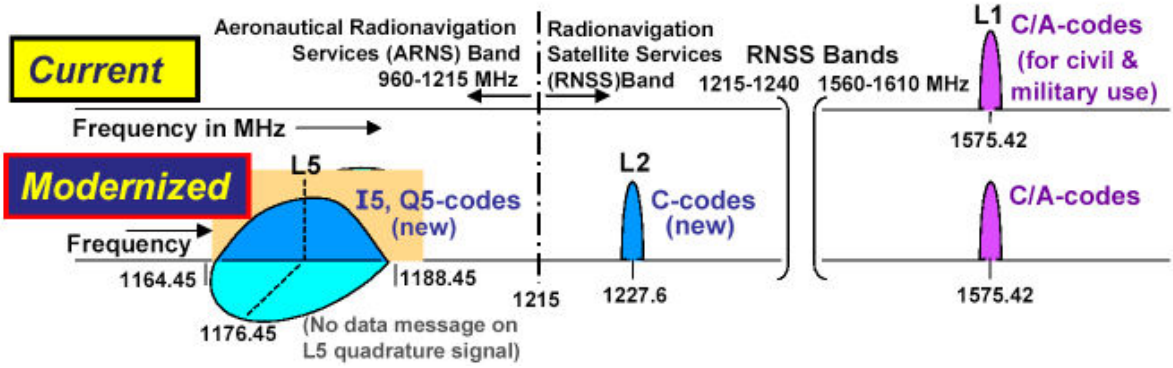

Figure 1.4: Present and future civil GPS frequencies (from [MacDonald2002]'s paper).

The new civil L_5 signal

The third civilian signal, L_5, will be added to the first Boeing Block IIF satellite along with C/A-code on L_2, and M-code on L_1 and L_2. L_5 is allocated at 1176.45 MHz with a 24 MHz bandwidth. A higher chipping rate and a longer code than the C/A to reduce self-interference are improved features of this signal. L_5 power will be increased by 6 dB compared to the current L_1, equally split in a phase data channel (I) and a quadrature data-free channel (Q) to improve resistance to interference, especially from other pulse emitting systems in the same band as L_5. The latter includes Distance Measuring Equipment (DME) systems already used for en route and terminal area air navigation and the military Joint Tactical Information System (JTIDS) used for critical military command and control commands. The data-free component of the new signal also provides more robust carrier phase tracking. This signal is located in the Aeronautical Radio Navigation Service (ARNS) band specially designed for the mentioned aviation applications. A complete description of this signal can be found in [ICD-GPS-7052002].

The current GPS modernization efforts will end in 2010, with a total deployment of up to 12 GPS Block IIF satellites. For the period 2010–2030, a new generation of satellites, Block III is planned.

Satellite Schedule Launch

The modernization of the GPS signals will be carried out through different launches:

- **Block IIR modernization**: presently, twelve IIR satellites are modernized (the IIR-M) to speed up the avaibility of the military M code on L_1 and L_2 and the civil code on L_2. The first launch of a Block IIR-M satellite is foreseen in 2003 and it will carry the new signal, as will all subsequent GPS satellites. Initial Operational Capability (IOC=18 properly placed satellites) is anticipated in 2008 and Full Operational Capability (FOC=24 satellites) for 2010.

- **Block IIF modernization**: these satellites will be the fourth generation of satellites and will continue with the L2C signal on L_2 and the M code on the L_1 and L_2 frequencies, but will add a new civil code at the L_5 frequency. The first launch of the Block IIF is foreseen for 2005. IOC is anticipated for 2012 and FOC for 2015.

- **GPS-III**: the goal of the GPS-III program is to deliver best-value acquisition and architectural solutions that will satisfy the currently defined, yet evolving, military and civilian needs for a space-based positioning, navigation and timing system through 2030. This system will have two other channels that provide navigation signals for civilian use in local, regional and national applications. One of the new civil signals is expected to transmit higher power than the other two signals for improved reception worldwide. The first of the new satellites is to be launched in 2010. IOC is expected for 2016 and FOC for 2018, with the entire constellation expected to remain operational through at least 2030.

Impact on GNSS-R measurements

As far as GNSS-R is concerned, the main consequence of the future GPS modernization shall come from the signal redundancy and real-time double frequency applications. In particular, it shall impact the ionospheric and clock errors, and enhance the interferometric capacities of the system:

- **Ionospheric error**: after SA, the next largest contributor to the GPS positioning error budget is the atmosphere—mainly the ionosphere. Ionospheric effects can be accurately estimated through the use of dual frequency measurements. The use of C/A code on the L_2 frequency in conjunction with L_1 will reduce the typical ionospheric error of 7 meters to 1 cm. This will result in a stand-alone accuracy as low as 8.5 meters (95 percent of the time). To implement the C/A code on L_2, the GPS Block II Replenishment satellite contract will be revised to direct Lockheed Martin to modify the last 12 Block IIR satellites.

- **Clock error**: after atmospheric errors, the next source in the GPS error budget are ephemeris and clock errors. In the current constellation, the clock and ephemeris errors contribute approximately to 1.8 and 1.4 meters, for a combined 2.3 meters User Equivalent Range Error (UERE). A new technique, called the Accuracy Improvement Initiative (AII), is expected to reduce the GPS clock and ephemeris contribution to UERE to approximately 1.25 meters. As a result, we will obtain a 6 meter or better horizontal accuracy 95 percent of the time.

- **Interferometry**: the combination of two different signals (chosen between L_1, L_2 and L_5) permits to synthesize larger wavelengths. Studies have been undertaken to investigate the improvement in altimetric measurements ([Ruffini and Soulat2000b]).

To summarize, initial operational capability for dual frequency navigation will occur in 2008, with launches beginning in 2003, a status based on a constellation of 18 properly placed satellites broadcasting L_2 C/A in phase-quadrature to the military P signal. The L_5 signal will be available on 18 GPS satellites by 2012, requiring the launch of 6 to 12 GPS-III satellites. Stand-alone horizontal accuracy will improve from 100 to 6 meters or better. For non-dynamic or non-real time applications, centimeter level accuracies will be achieved more quickly and cost effectively than today, through the existence of 3 wide lanes to resolve integer ambiguities.

1.1.4 GPS reflections coverage

Bistatic radar offers several advantages over monostatic systems. One of them is the superior coverage and lower cost than monostatic systems. The geometry of bistatic GNSS scattering, shown in figure 1.5, highlights the high across track sampling possible due to the large number of GNSS satellites producing specular reflections.

Studies on GPS reflections coverage from space have been carried out by [Cardellach2002] and [Aparicio *et al.*2000], and more recently by Astrium and Starlab in the PARIS-γ project (see [PARIS Gamma2003]).

1.2 GLONASS

GLONASS is the Russian GNSS system[2], and is very similar to GPS. A 24 satellite constellation was available in 1996, distributed in three orbital planes at an inclination angle of 64.8 degrees—only 16 satellites are operating as of today. The orbits are nearly circular, with an altitude of 19100 km and a period of 11.25 h. The major difference with GPS is that broadcast frequencies are satellite-specific. The individual carrier frequencies, $f^i_{L_1}$ and $f^i_{L_2}$ are:

$$f^i_{L_1} = 1602.0000 + i \cdot 0.5625 \text{ MHz}$$
$$f^i_{L_2} = 1246.0000 + i \cdot 0.4375 \text{ MHz},$$

[2] see http://www.glonass-center.ru/ .

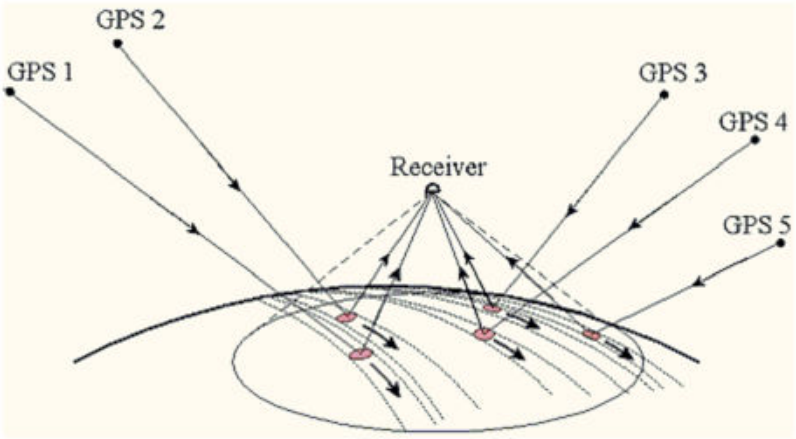

Figure 1.5: Geometry of multistatic GNSS radar system (from V. U. Zavorotny, Bistatic GPS Signal Scattering from an Ocean Surface: Theoretical Modeling and Wind Speed Retrieval from Aircraft Measurements, 1999).

where i=0,...,24 is the channel number specific to each satellite [Hofmann-Wellenhof *et al.*1997]. Some satellites have the same frequencies but are placed in antipodal slots of orbit planes and they never appear at the same time in user's view. The two codes modulated onto the carriers are the same for all satellites. The public C/A code has a period of 1 ms, a chip rate of 0.511 MHz and is modulated on L_1 only. The P-code has a period of 1 s, a chip rate of 5.113 MHz and is modulated on both L_1 and L_2, although its use is not open to the public. There is no analog of Selective Availability in GLONASS, however.

1.3 Galileo

The future European navigation satellite system, Galileo, will complement the existing satellite navigation system, which presently relies mainly on GPS, the American Global Positioning System. Developed by the European Space Agencies and the European Union on the basis of equal co-funding, Galileo is designed to provide a complete civil system and scheduled to be operational by 2008.

The Galileo system will be built of around 30 satellites (27 operational and 3 reserve craft) occupying three circular earth orbits, inclined at 56^o to the Equator, at an altitude of 23616 km. This configuration will provide excellent coverage of the planet. Two Galileo control centers will be established in Europe to control satellite operations and manage the navigation system. The contracts for the first Galileo satellites were signed on Friday 11 July 2003 at ESTEC, the European Space Agency's research and technology center.

The European Satellite Navigation System is currently under design development. The last update on the system, dated September 2002, on the Galileo frequencies and signal design can be found in [Hein *et al.*2002]. Galileo will provide 10 navigation signals in RHCP in the frequency ranges 1164-1215 MHz (E5a and E5b), 1215-1300 MHz (E6) and 1559-1592 MHz (E2-L1-E1), which are part of the Radio Navigation Satellite Service (RNSS) allocation. An overview is shown in figure 1.6. The carrier frequencies, as well as the frequency bands that are common to GPS and GLONASS are also highlighted.

All the Galileo satellites will share the same nominal frequency, making use of Code Division Multiple Access compatible with the GPS approach.

Six signals, including three data-less channels, so-called pilot tones (ranging codes not modulated by data), will be accessible to all Galileo users on the E5a, E5b and L1 carrier

frequencies for Open Service (OS) and Safety-of-life Service (SoL). Two signals on E6 with encrypted ranging codes, including one data-less channel will be accessible only to some dedicated users that gain access through a given Commercial Service (CS) provider. Finally, two signals (one in E6 band and one in E2-L1-E1 band) with encrypted ranging codes and data will be accessible to authorized users of the Public Regulated Service (PRS).

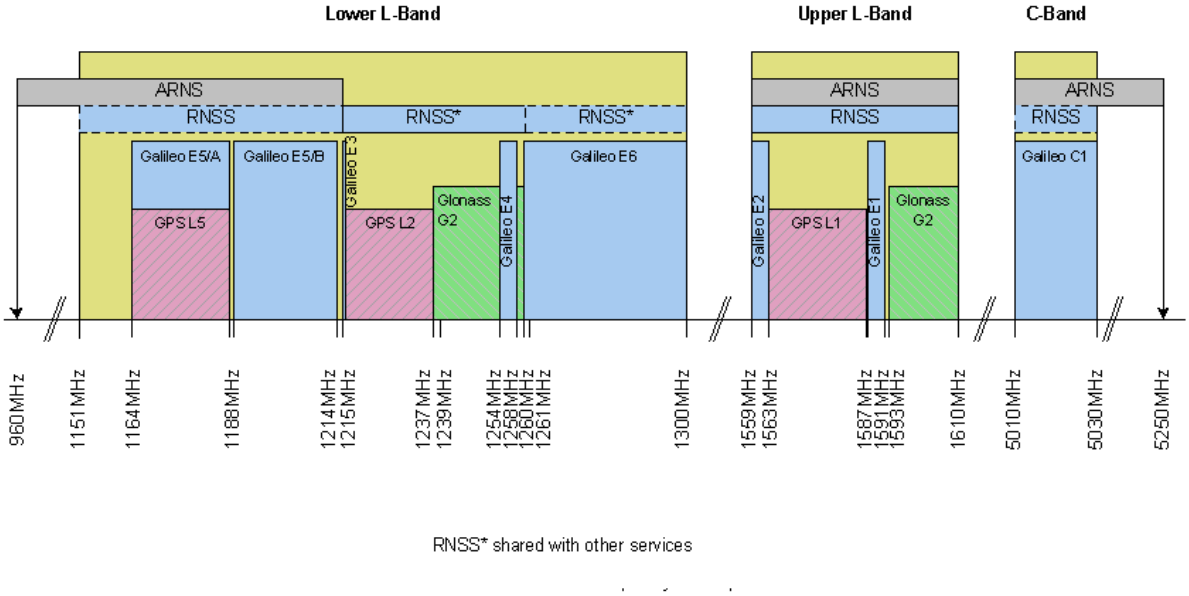

Figure 1.6: Galileo frequency plan (as of 2003) together with GPS and GLONASS systems. ARNS is the acronym for Aeronautical Ratio Navigation Service. This band is dedicated to safety-of-life services (i.e., civil aviation). RNSS is the acronym for Radio Navigation Satellite Service.

Chapter 2

Sea Surface Model

The purpose of this Chapter is to investigate sea-surface characteristics to get a good understanding of the scattering process. Indeed, the scattered field can be determined from ensemble averages of sea-surface heights. Following a Gaussian model, these ensemble averages can be analytically derived and exclusively related to the two first moments of the distribution. These moments can be computed from the sea-surface spectrum.

We first present in section (2.1) an overview of the sea spectra, with special attention to the spectrum developed by [Elfouhaily *et al.*1997]. A short discussion on the use of spectral models to infer the sea-surface slope variance is proposed. The sea-surface statistics are then reviewed in section (2.2) under the Gaussian assumption.

2.1 Sea-surface spectral model

This section addresses the status on sea-surface spectrum models. An overview of the main components of such spectra is done, with a particular interest on the [Elfouhaily *et al.*1997]'s spectrum. The simulation of sea surfaces is then easily done from the spectrum (section (2.1.3)). A short discussion on the use of spectral representation of ocean to infer roughness (scatterometry) is finally proposed (section (2.1.4)).

2.1.1 The involved geophysical parameters

There are three important aspects in wave generation:

- the *wind speed* at ten meters over the surface U_{10} in m/s,
- the *duration* of wind blowing action,
- the *fetch*: the distance to nearest shore. This is a measure of the effective area in which wind is blowing on the water. The *fetch* on a small lake, for instance, is very limited.

The general features one expects to see in a wave spectral model are:

- A spectral peak at radial frequency ω_m that depends on wind speed U_{10} and *fetch*.
- A high frequency tail falling off as ω^{-5}.

A formula summarizing recent work and englobing these two points is (see [Apel1995], page 199):

$$S(\omega) = \frac{\alpha(U_{10}, x_f) g^2}{(2\pi)^4} e^{-\frac{5}{4}\left(\frac{\omega}{\omega_m}\right)^{-4}} \frac{F(\omega, U_{10})}{\omega^5}, \tag{2.1}$$

where g is the gravitational acceleration constant and x_f the *fetch*. Its features are:

1. Waves having frequencies below ω_m are traveling faster than the wind and have no net forcing to grow.

2. Waves at higher frequencies are dominated by breaking and cusp-like crests, whose frequency spectra may be shown to behave as ω^{-5}.

3. Wind speeds and limited *fetch*, accounted for in $\alpha(U_{10}, x_f)$, modify the overall energy level of $S(\omega)$ and hence of wave height without affecting its shape.

4. The function $F(\omega, U_{10})$ increases the peakedness of the spectral maximum and parametrizes the weak nonlinear wave/wave scattering interactions that cause the spectrum to be more narrow and cohesive than it would be the case of linear, independent Fourier components. The older [Pierson and Moskowitz1964] spectral shape does not include these features.

For instance, in order to generate a *fully developed sea*—a saturated spectrum—a wind of 10 m/s needs to blow with a duration of 18 hours over about 320 km of ocean. Under these conditions, SWH is about 2 meters and wave period will be about 7.5 seconds.

Unlike electromagnetic waves in air, ocean waves are dispersive. The dispersion relation for surface waves is given by:

$$\omega(\vec{k}) = \pm\sqrt{(gk + k^3\tau_s/\rho)\tanh kH}, \tag{2.2}$$

where τ_s is the surface tension, ρ is the density, and H is the depth. At long wavelengths the capillary terms (i.e., waves of the order of the cm) are negligible and the dispersion relation for *deep water* becomes:

$$\omega(\vec{k}) = \pm\sqrt{gk\tanh kH}. \tag{2.3}$$

It is often emphasized that the use of radar data in the derivation of sea models should be avoided. Indeed, the use of radar data implies the choice of an electromagnetic model, and to date, no satisfactory model exists (see [Anderson1999, Elfouhaily *et al.*1997]). Moreover, using a model would bias future model evaluation using such spectra.

2.1.2 Elfouhaily et al. spectrum

Let us discuss the spectrum of [Elfouhaily *et al.*1997], since it is the most popular one in the community. They emphasize that the models available do not meet fundamental criteria: they should properly account for different *fetch* conditions, and agree with the *in situ* observations of [Cox and Munk1954] (of wind-dependent mean square slopes), [Jähne and Riemer1990] and [Hara *et al.*1994] (gravity-capillary wave curvature laboratory measurements) in the high wavenumber regime.

They further criticize that these models suffer undesirable features such as discontinuities across wavenumber limits, non-physical tuning parameters, and non-centrosymmetric directional spreading functions. They propose to remedy this situation with a new model: a two-dimensional wavenumber spectrum valid over all wave-numbers and analytically amenable for use in electromagnetic models. Radar data is excluded from the model development. The spectrum is derived for the case of wind-generated seas, with wind and waves aligned. The authors begin by reviewing the several available *full wavenumber* models:

1. The [Bjerkaas and Riedel1979] spectrum. This widely used spectrum is defined in four separate wavenumber ranges, and the connection across ranges is provided through arbitrary constants to match the curves. This spectrum applies to fully developed sea

conditions only. The first range, near the peak for gravity (long) waves corresponds to the [Pierson and Moskowitz1964] spectrum. Note that [Fung and Lee1982] use a simplified, two-regime, version of this spectrum.

2. The [Donelan and Pierson1987] spectrum. This is a two-regime spectrum. In the low wavenumber regime the long-wave spectrum resulting from the Joint North Sea Wave Project (JONSWAP [Hasselmann1973]) is used. It is well-accepted that this spectrum gives a reasonable description of fetch-limited wind wave development. Shorter waves are theoretically derived by requiring an energetic balance between wind input and dissipation due to viscous damping and wave breaking.

3. The [Apel1994] spectrum. He called his spectrum the "Donelan-Banner-Jähne" spectrum. [Elfouhaily *et al.*1997] follow Apel's objective of building an analytically amenable model to satisfy the primary need of electromagnetic models: the autocorrelation function or elevation energy spectrum. [Elfouhaily *et al.*1997] criticize that this model is not consistent with [Cox and Munk1954]'s observations of the mean square slope statistics, however.

The [Elfouhaily *et al.*1997] energy spectrum can be summarized by the expression:

$$\Psi(k,\phi) = \frac{1}{2\pi} k^{-1}[S_l(k) + S_h(k)][1 + \Delta(k)\cos(2\phi)]. \tag{2.4}$$

The term $[1+\Delta(k)\cos(2\phi)]$ is the centrosymmetric spreading function. The term $k^{-1}[S_l(k)+S_h(k)]$ is the omni-directional part of the spectrum, divided into low and high frequencies. A detailed expression of each term is presented in the paper. The model contains two parameters: U_{10} and k_m (associated to the phase velocity c_m), the wave number of the dominant wave or the spectral peak. These quantities are related to the *inverse wave age* Ω through $\Omega = U_{10}/c_m \equiv U_{10}\sqrt{k_m/g}$. The friction velocity u_*, which is linked to U_{10} through a drag coefficient [Duncan *et al.*1974]), is also considered.

2.1.3 Sea surface generation

The generation of sea surfaces is done in the following way. We define ϕ_r a matrix of random phases uniformly distributed between 0 and 2π; the sea height at $\vec{r} = (x, y)$ is then:

$$\zeta(\vec{r}, t) = FFT^{-1}[\sqrt{\Psi(k_x, k_y)}e^{i(\phi_r - \omega t)}]. \tag{2.5}$$

We use here the mentioned unified spectrum Ψ from [Elfouhaily *et al.*1997]. We recall that this spectrum is made without radar data and is derived for the case of wind-generated seas, with wind and waves aligned. The time dependence implements the wave propagation.

For specific scenarios (namely airborne and spaceborne) the receiver is moving above the observation scene. Instead of moving the receiver, a trick consists in "moving" the ocean below it. For this purpose, we add another phase term in the integral. This phase contains the receiver speed vector. For a receiver speed $\vec{v_r}$, the ocean heights are now defined as:

$$\zeta(\vec{r} + \vec{v_r}t, t) = \int [\sqrt{\Psi(k_x, k_y)}e^{i(\phi_r + (\vec{k}\cdot\vec{v_r} - \omega)t)}]e^{i\vec{k}\cdot\vec{r}}d\vec{k}. \tag{2.6}$$

2.1.4 Discussion on the use spectral models for scatterometric purposes

The sea-surface MSS is historically used to derive wind speed estimates. However, it consists in the high-pass filtered integration of the all sea elevation spectrum, which is not solely dependent on local wind conditions.

In the open ocean, the cutoff wavenumber for the equilibrium range at the lower frequency part of the spectrum is very close to the spectral peak k_m, which is generally assumed wind-dependent, through the relation:

$$k_m = \frac{g}{U_{10}^2}. \tag{2.7}$$

At the high wavenumber end, it is controlled by capillarity waves. It is assumed that the major contribution to surface slopes comes from higher wavenumbers. Using a simplified saturation spectrum ($1/k^4$), we can give a good sea-surface MSS estimation [Phillips1966]:

$$\sigma_s^2 = \int_k k^2 \Psi(\vec{k}) d\vec{k} = B \ \mathrm{Log}\frac{k_c}{k_m} = B \ \mathrm{Log}\left(\frac{k_c U_{10}^2}{g}\right), \tag{2.8}$$

where k_c is the cutoff frequency and B a non-dimensional constant (equal to 0.00405).

Therefore, this model states that sea-surface roughness is purely a function of wind speed. However, this result is based on wave motion alone. If the wave motion encounters a current for instance, the characteristics of the waves will be different as a consequence of the kinematic and dynamic interaction. The impact of surface current on sea-surface roughness has been discussed by [Huang *et al.*1973] (see section (2.2.3)).

During the Mid-Term review of the ESA Contract No. 12934/98/NL/GD on the "Study of the impact of sea-state on nadir looking and side looking microwave backscatter", an important point was made. Co-located Topex/Buoy data sets (using 41 buoys) show that the correlation between radar cross section σ^o—which is inversely proportional to sea-surface MSS—and U_{10} is higher for underdeveloped seas, and also higher for shorter radar wavelengths (Ku-band). The sea-state was defined a "fully developed sea" using the Pierson-Moskowitz condition, $\sigma_\zeta > 0.02352 * U_{10}^2$, with the buoy data.
Other interesting conclusion were that algorithms using both σ^o and σ_ζ reduce significantly the error in wind speed retrieval (from 1.5 m/s down to 1.23 m/s) and that the dual-frequency algorithms [Elfouhaily *et al.*1999a] do not seem to improve wind speed retrievals. The sea-state impact on the scattering cross section has been deeply investigated in [Gourrion *et al.*2002a].

As a conclusion of this short discussion, we emphasize that the sea-surface slope variance is not a simple function of wind. Other parameters such as sea-state (SWH) and surface currents may strongly impact the roughness as well. The roughness estimations undertaken during experimental campaigns (see Chapter 7) illustrate this point.

2.1.5 Summary

For a good, up-to-date review of the state-of-the-art in spectrum modeling, see [Anderson1999]. Here we summarize the important conclusions:

- There is no accepted description of the wave spectrum.
- A recent attempt can be found in [Elfouhaily *et al.*1997], valid from 6 mm to 600 m wavelengths. This spectrum depends on U_{10}, Ω, and friction velocity u_*. No attempt is made to include swell. This is a problem common to other models. No radar data have been used in this model.

- For short wave (0.01 to 10 cm) spectra, where tension is important, the model developed by [Elfouhaily *et al.*1997] seems the best available, although shortcomings are pointed out. This is a strongly non-linear regime, and unexplored theoretical ground abounds.
- Wave breaking is included on models based on experimental data (optical data is used in [Elfouhaily *et al.*1997]). Very poorly understood.
- Wave breaking, currents, slicks and rain all affect the short wave spectrum, and experiments continue to provide more unexplained phenomena.

2.2 Gaussian sea-surface statistics

2.2.1 Statistical characterization of random surfaces

We give here an overview of the important statistical parameters used to describe the sea surface under the Gaussian assumption. We address the standard deviation of the surface height variation (or RMS height) σ_ζ, the *surface correlation length* l, the mean square slope MSS=σ_s^2 and the mean radius of curvature r_c. However, higher order statistical parameters, such as the skewness, would also be needed to properly depict sea-surface height statistics. Note that specification of higher order statistics are necessary for non-Gaussian surfaces.

Significant Wave Height

Let $\bar{\zeta} \equiv \langle \zeta(\vec{\rho}) \rangle$ be the average height of a surface $\zeta = \zeta(\vec{\rho})$, where $\vec{\rho}$ is the horizontal displacement vector. Then, the RMS height is defined by:

$$\sigma_\zeta \equiv \sqrt{\langle (\zeta - \bar{\zeta})^2 \rangle}. \tag{2.9}$$

We recall that from a spectral point of view, it is given by the integral of the sea-surface spectrum. We usually address the Significant Wave Height (SWH) related to σ_ζ by:

$$\text{SWH} = 4\ \sigma_\zeta. \tag{2.10}$$

Correlation length

The surface correlation length l in some direction is given in terms of the autocorrelation function of the surface. This is a measure of the spatial scale associated to the statistical relationship between points in the surface.

To have an idea of the behavior of the ocean model relative to wind speed, the autocorrelation function of sea heights that defines the autocorrelation length l is shown in figure 2.1. It appears clearly that l increases with wind speed, in agreement with reality: for high wind speed the waves become more developed and roughness increases also.

Surface slope variance

One can show that if the height distribution is Gaussian, then the distribution of slopes is also Gaussian. Let $A(x)$ be the autocorrelation function of the surface (let us restrict ourselves to the 1-D case for now, the generalization is simple). One can show that the slope variance of the surface ("average slope"—a misnomer) is given by ([Ulaby *et al.*1986], Appendix 12 F, page 1012, and [Fung1994], Appendix 2B, page 117):

$$\sigma_s^2 = -\sigma_\zeta^2 A''(0). \tag{2.11}$$

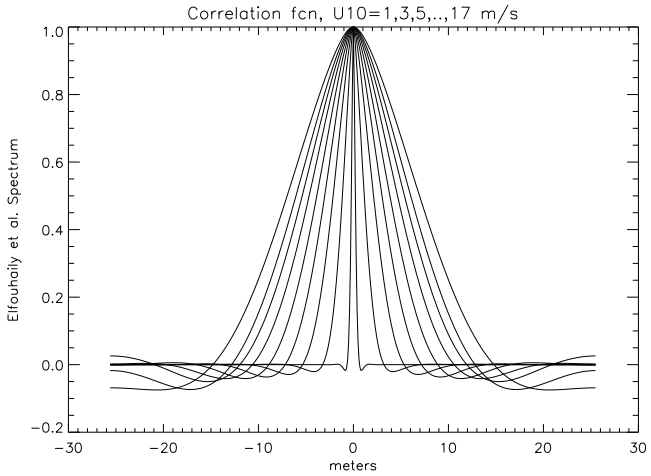

Figure 2.1: Correlation function for different wind speeds (U_{10}=1, 3, 5, ..., 17 m/s), with Gaussian spectrum from [Elfouhaily *et al.*1997].

For the more specific case of a Gaussian autocorrelation function with autocorrelation length l, $A(x) = e^{-x^2/l^2}$, this yields

$$\sigma_s = \sqrt{2}\sigma_\zeta / l. \tag{2.12}$$

Sometimes the slope $\tan\beta_0$ is also used as a measure of the average slope variance of the surface, where $\tan\beta_0 = 2\sigma_\zeta/l$ (see [Beckmann and Spizzichino1963], page 89 and Appendix D, page 193).

From a spectral point of view, the sea-surface slope variance is given by the integral of the spectrum multiplied by the wave-vector squared.

Radius of curvature

Another quantity which will be considered in scattering model requirements—see section (3.2.1) of Chapter 3—is the mean radius of curvature, which will also have a Gaussian distribution if the height distribution is Gaussian. One can show that if the autocorrelation function is Gaussian, the mean radius of curvature writes (see [Ulaby *et al.*1986] volume II, Appendix 12F):

$$r_c = \frac{l^2}{\sigma_\zeta}\sqrt{\pi/24} = \frac{l}{\sigma_s}\sqrt{\pi/12}. \tag{2.13}$$

In [Apel1994], some typical values for the correlation length, average radius of curvature and ocean wavelength (this is in fact the wavelength of ocean waves travelling at the wind speed) are given as function of wind speed (these values belong to the ocean model discussed there). For a wind speed of 6 m/s, they are respectively l=2.4 m, r_c=0.8 m, and D=23 m, for instance.

2.2.2 Slope distribution

We here use an anisotropic Gaussian assumption to describe the 2-D slope probability density function:

$$\mathcal{P}_s(s_x, s_y) = \frac{1}{2\pi\sqrt{\det(M)}} \exp\left[-\frac{1}{2}\begin{pmatrix} s_x \\ s_y \end{pmatrix}^\dagger M^{-1} \begin{pmatrix} s_x \\ s_y \end{pmatrix}\right], \tag{2.14}$$

where $s_x = \partial\zeta/\partial x$ and $s_y = \partial\zeta/\partial y$ stand for the directional slopes in some frame xy and M is the matrix of slope second order moments: the directional mean-square slopes (DMSS). The xy frame mapped on sea-surface is defined as follows: it is centred on the specular point and has its x axis aligned with the Transmitter-Receiver line. Mean-square slopes along major and minor principal axes are often referred to as (respectively) MSS up-wind (σ_u^2) and MSS cross-wind (σ_c^2). The M matrix is then obtained via a simple rotation:

$$M = \begin{bmatrix} \cos\psi & -\sin\psi \\ \sin\psi & \cos\psi \end{bmatrix} \cdot \begin{bmatrix} \sigma_u^2 & 0 \\ 0 & \sigma_c^2 \end{bmatrix} \cdot \begin{bmatrix} \cos\psi & \sin\psi \\ -\sin\psi & \cos\psi \end{bmatrix}, \tag{2.15}$$

where ψ is the angle between x axis and the slope principal axis.

The three geophysical parameters of interest are σ_u^2, σ_c^2 and ψ. They can be understood as the three parameters of an ellipse (see figure 2.2) representing the slope PDF mapped on sea-surface. In this dissertation, we will actually consider the equivalent set of parameters:

- Total MSS, defined as: MSS $= \sigma_s^2 = 2\sqrt{\sigma_u^2.\sigma_c^2}$. This magnitude is actually proportional to ellipse area and can be interpreted in terms of wind speed, considering a particular wind-driven sea-surface spectrum, like the Elfouhaily's spectrum [Elfouhaily *et al.*1997].
- Slope PDF isotropy (SPI), defined as SPI $= \sigma_c^2/\sigma_u^2$. When SPI=1, the slope PDF is fully isotropic and the glistening zone is circular. Low values of SPI indicate a highly directive PDF. Typically, SPI is expected to be around 0.65 for well developed sea-surface.
- Slope PDF azimuth (SPA), defined as the direction of semi-major axis with respect to North. As shown by figure 2.2, this angle (modulo 2π) is SPA $= \pi + \Phi - \psi$, if Φ is the satellite azimuth w.r.t. North.

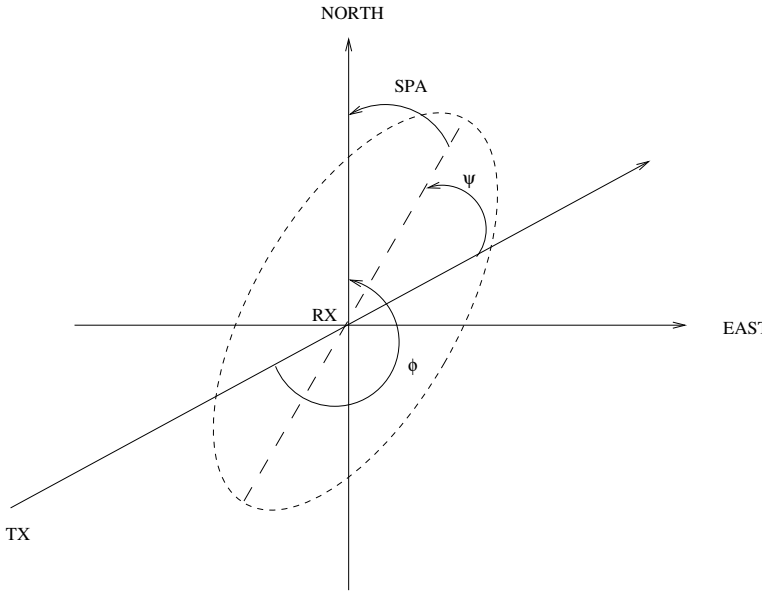

Figure 2.2: Sketch of sea-surface slope PDF and related frames.

2.2.3 Impact of current on sea-surface slope variance

This section aims at introducing the dependence of MSS with current conditions. By taking into account the surface current velocity U_c and considering equation 2.8, the MSS writes

[Huang *et al.*1973]:

$$\sigma_s^2 = \int_{k_m}^{k_c} \frac{B}{\left(1+\frac{U_c}{c}\right)^7}\frac{dk}{k}. \tag{2.16}$$

Introducing the phase velocities c_m and c_c corresponding respectively to the spectral peak and cutoff wavenumbers, we get (up to the second order):

$$\sigma_s^2 = 2B\left\{\mathrm{Log}\left|\frac{U_c+c_m}{U_c+c_c}\right| + 6\left(\frac{U_c}{U_c+c_m}-\frac{U_c}{U_c+c_c}\right) - \frac{15}{2}\left[\left(\frac{U_c}{U_c+c_m}\right)^2 - \left(\frac{U_c}{U_c+c_c}\right)^2\right] + ...\right\}. \tag{2.17}$$

Note that when U_c=0, equation 2.17 reduces to equation 2.8.

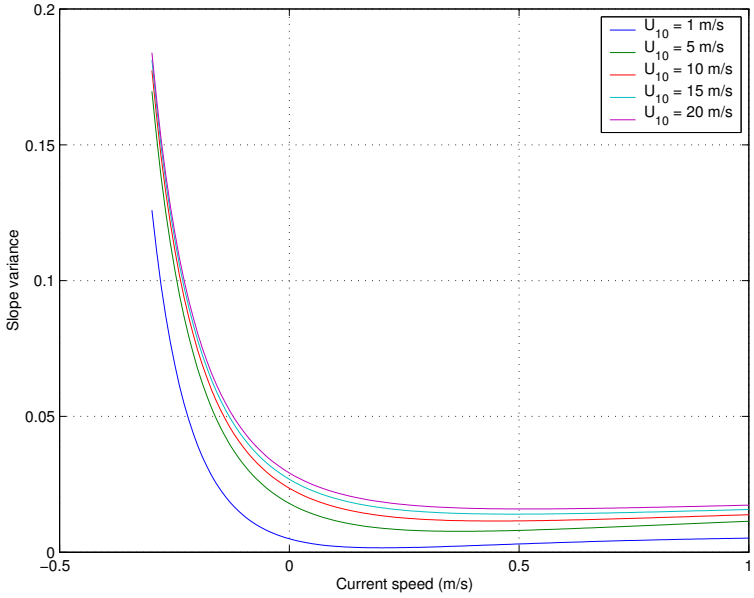

Figure 2.3: Variation of sea-surface slope variance at L-band with current speed, with wind speed as a parameter (see equation 2.17).

Due to the presence of current velocity in the above equation, the dependence of σ_s^2 on wind speed becomes less obvious. Figure 2.3 shows the variations of sea-surface slope variance at L-band with current speed, with wind speed as a parameter. The sharp slope of the curves immediately reveals the sensitive dependence between σ_s^2 and current speed especially for moderate currents, probably the prevailing state over most of the ocean.

Chapter 3

Scattering Model

The purpose of this Chapter is to provide the basics of the common electromagnetic models involved in scattering over sea surfaces. Starting from the Kirchhoff model and its conditions, we focus then on the Geometric Optics theory, which is validated at L-band through Monte-Carlo simulations in section (3.2). Furthermore, a waveform model for GNSS-R is proposed in section (3.3), following [Zavorotny and Voronovich2000]'s work.

The signatures of oceanic features which can be detected by active or passive microwave sensors like scatterometers, imaging radars and GNSS-R are associated with surface effects: they result from an interaction between the electromagnetic waves and water waves. The ability of the ocean surface to scatter electromagnetic power back towards the receiver is characterized by its normalized radar backscattering cross section (NRCS), which depends on the frequency used, polarization and incidence and scattering angles.

It is necessary to have a clear picture of the physical process involved in the *electromagnetic ocean-surface interaction* in order to extract the ocean variables such as near-surface wind speed, wave height, wave slope, ocean wave spectrum, etc. When calculating the cross section, two sets of approximations are currently used. The first set of approximations concerns the scattering theory, presented hereafter, and the second set enters in the statistical description used to ensemble average the resulting cross section—presented above in Chapter 2.

Note that to predict electromagnetic scatter one should also consider the hydro-dynamics of ocean waves. The statistical distribution of sea-surface displacement is Gaussian in the linear approximation of a superposition of non-interactive sinusoidal water waves. But the non-linear coupling of the ocean waves produces a continuous redistribution of energy and momentum of the waves causing the statistics to be non-Gaussian. Besides the energy balance of the ocean waves is controlled by several competing processes: the input from the wind, the energy transfer by non-linear wave-wave interactions and the energy lost by viscosity and wave breaking. It is well known that waves riding on an non-homogeneous spatially varying field will have their growth, dissipation, speed, wavelength and height modified. These modifications will thus directly enter in the amplitude strength and Doppler signature of the radar cross section. This is not however the purpose of the present study.

3.1 Bistatic electromagnetic models

All available closed-form models for electromagnetic reflected field from random surfaces are asymptotic solutions of the Maxwell equations. Two limits are generally considered: 1) the Kirchhoff approximation ([Beckmann and Spizzichino1963]) and 2) the small perturbation method (SPM) ([Rice1951]). The former is obtained under the condition of small slopes and

long waves while the latter is derived for small slopes and short waves. The Kirchhoff approximation described below in section (3.1.1)—together with its high frequency limit approximation (Geometric Optics)—accurately models the quasi-specular scattering but does not consider the sensitivity to polarization. On the contrary, SPM, presented in section (3.1.3), carries the polarization factors but fails to reproduce the near-specular regime, since it does not properly account for the longer scale features.

A "two-scale" or composite-surface model has been tested. This approach, presented in section (3.1.4), combines two "classical" methods of wave-propagation theory: the method of small perturbations or tangent plane and the semi-classical approximation. However, in addition to lacking the necessary accuracy for quantitative predictions, this method uses a somewhat arbitrary scale-dividing parameter that makes the solution ambiguous. Many important characteristics of scattering, such as polarization, angle, and dependence of cross sections on wind speed, cannot be accounted for over realistic ranges of parameter values. A more accurate theory is required that is free of fitting parameters.

For a long time, no solutions to this problem were known. [Holliday1987] proposed an approach that includes the polarization under both situations: specular and moderate-incident scattering. He showed in the combination of the two limits that for the case of backscatter in the SPM limit, the deficiency in the Kirchhoff field can be corrected through the inclusion of the next iterative correction to the surface current.

Other authors have also investigated this issue, such as [Rodriguez and Kim1992], [Tatarskii1993], [Voronovich1994] and [Fung1994]. More recently, [Elfouhaily *et al.*1999b] generalized Holliday's results to develop a bistatic Kirchhoff model that is polarization sensitive.

The main assumption for these models is to consider the surface as a perfect conductor. Starting from the Stratton-Chu equations and assuming that the incoming incident field is a plane wave $\vec{B_i} = \vec{B_0} exp(-ik_i \cdot r)$, the total magnetic field is:

$$\vec{B}(r_0) = \vec{B}_i(r_0) - \oint_S \vec{J}(r_1) \times \nabla G(r_0, r_1)\, dA_1, \tag{3.1}$$

where S is the surface described by $z{=}\zeta(x)$ and x is the horizontal component of the three-dimensional vector r. The integrand in equation (3.1) is the cross product between the total surface current $\vec{J(r)} = \hat{n}(r) \times \vec{B}(r)$ and the gradient of the Green's function:

$$G(r_0, r_1) = -\frac{1}{4\pi} \frac{exp(ik|r_0 - r_1|)}{|r_0 - r_1|}, \tag{3.2}$$

where k is the electromagnetic wave number. The complexity of the above equation is that the total surface current is a function of the total magnetic field $\vec{B}(r)$. At the scattering surface it follows the integral equation:

$$\vec{J}(r_1) = \vec{J}_i(r_1) - 2\hat{n}(r_1) \times \oint_S \vec{J}(r_2) \times \nabla G(r_1, r_2)\, dA_2, \tag{3.3}$$

where $\hat{n}$ is the unit vector normal to the scattering surface. It is directly determined according to the local slopes of the sea surface:

$$\hat{n} = \frac{\hat{e}_z - \nabla\zeta}{\sqrt{1 + (\nabla\zeta)^2}} = n_z(\hat{e}_z - \nabla\zeta). \tag{3.4}$$

3.1.1 Kirchhoff approximation or Physical Optics

An integral equation such as equation (3.3) is defined by a kernel K, and symbolically, it may be described in generality by:

$$f = f_0 + \Lambda K f, \tag{3.5}$$

where f_0 is the inhomogeneous (given) term, Kf stands for the convolution of the kernel with the unknown function f, and Λ is a constant. An iterative solution to this problem is given by a Newmann series (see [Courant and Hilbert1989]):

$$f = f_0 + \Lambda K f = f_0 + \Lambda K(f_0 + \Lambda K f) = ..., \tag{3.6}$$

and so on. For instance, to first order in Λ, the solution is $f_1 = f_0 + \Lambda K f_0$.

We consider in the Kirchhoff approximation the first term in the iterative series solution of the surface-current integral equation. In this first iteration, the total current $\vec{J}_1$ is forced to match the input current $\vec{J}_i$:

$$\vec{J}_1(x_1) \equiv \vec{J}_i(x_1) = 2\hat{n}(x_1) \times \vec{B}_i(x_1). \tag{3.7}$$

The needed assumption for this approximation is that the incident and scattered fields at the surface be related (linearly) through the Fresnel reflection coefficient $\mathcal{R}$, which is a function of the local incidence angle and polarization. In this way, the integral equations are reduced to integration of the incident field over the surface.

The final form of the Kirchhoff field is given by [Elfouhaily *et al.*1999b] as follows:

$$\vec{B}^s(r_0) = \vec{B}(r_0) - \vec{B}_i(r_0) = -\frac{i}{2\pi}\frac{e^i k r_0}{r_0} B_0 k \vec{P}^s_{(1)} \int exp(-iq_z\zeta(x_1)) exp(-iq_\perp \cdot x_1) dx_1, \tag{3.8}$$

where $\vec{P}^s_{(1)}$ is an outgoing vector that depends on the incident polarization, the incident and scattering directions, the normal to the surface and the Fresnel coefficient. The subscript (1) is referred to the first iteration of the surface-current integral equations. The vector $\vec{q} = (\vec{q_\perp}, q_z)$ is the scattering vector, defined as the difference between the scattered wave number $\vec{k_s}$ and the incident wave number $\vec{k_i}$—as shown in figure 3.1. It is the vector normal to the plane that would specularly reflect the rays in the direction of observation. This vector coincides with the normal $\hat{n}$ for a specular facet defined in the Geometric Optics theory in section (3.1.2).

This formulation is compact and shows clearly that the reflected field depends on the scattering vector, the polarization vector and the surface shape, of course.

Limitation of the Kirchhoff approximation

Physically, in this approximation we assume that the surface is smooth enough to be locally represented by planes. The validity of Kirchhoff theory relies on a main aspect: the radius of curvature r_c. Generally the requirement is:

$$2kr_c \cos\theta >> 1, \tag{3.9}$$

where θ is the incident angle.

It follows, from this requirement, that at sufficiently large distances from the point of tangency—compared to the incident wavelength λ—the tangent plane shall not be appreciably distant from the surface. The radius of curvature should be greater than the incident

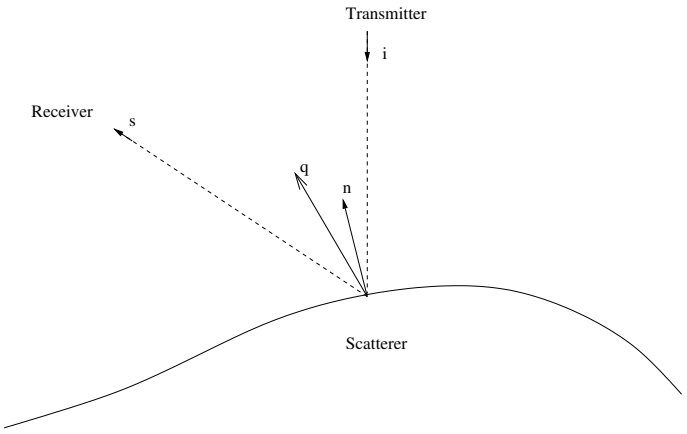

Figure 3.1: Definition of the scattering vector $\vec{q} = k(\vec{s} - \vec{i})$.

wavelength. For the particular sea-surface case, this radius of curvature is dominated by small scales, i.e., the capilarity-gravity waves.

Toward grazing incidence more complex mechanisms that cannot be accounted for by the Kirchhoff approximation begin to play a role: shadowing, diffraction, multiple scattering, and trapping by atmospheric ducts and waves. In fact, all of the models fail in this regime to some degree.

Since a large r_c (compared to effective wavelength) can be an operating constraint in the Kirchhoff approximation, it is useful to rewrite in the case of Gaussian statistics of the sea surface. As seen in equation 2.13 (section (2.2) of Chapter 2):

$$r_c \sim l/\sigma_s, \tag{3.10}$$

with l the surface correlation length and σ_s the sea-surface slope RMS. We can also write:

$$r_c \sim l^2/\sigma_\zeta, \tag{3.11}$$

with σ_ζ the sea height RMS.
This means that the large r_c condition can be met if:
i) l is large compared to effective wavelength ($\lambda/\cos\theta$), or if
ii) σ_s is small. This condition can be met again if l is large (back to i) or if σ_ζ is small compared to effective wavelength.

3.1.2 The Geometric Optics or Stationary Phase Approximation

The goal of the present section is to review the mechanisms involved in the Geometric Optics (GO) theory, with an emphasis on the *Stationary Phase Approximation* (SPA).

The Geometric Optics approximation to the Kirchhoff theory for electromagnetic scattering represents a high frequency limit. The physical picture can be understood in terms of a specular point (SP) model. The field at the receiver is the superposition of the fields generated by a number of "mirrors" (not flat mirrors, though) on the scattering surface which are oriented in the correct manner. The radiation from each specular point is as coherent as the incoming radiation, but there is no coherence in the phase relationship between the radiation out-coming from the different mirrors. The result is that there is power at the receiver, but that the phase of the received signal is randomly distributed. The behavior of the resulting

phase will depend on the geometry, on the number and distribution of mirrors, and also on the temporal variation of these quantities.

Generally, the reflected field is determined by a rapidly oscillating integral over the rough surface (see equation (3.8)). We will see that specular points are identified with the critical points of the integrand's phase. We will treat here the radiation coming from each mirror separately, as was mentioned above. We will use the Fraunhofer approximation (plane waves all the way through) to estimate the out-coming field. To fulfill the Fraunhofer requirements, the size of each mirror must be of the order of the first Fresnel zone, defined as the set of points near the specular with ranges to the receiver equal or less than the specular range plus a wavelength. In other way, the radius of this zone is $\sqrt{2\lambda H}$, where H is the height of the receiver and λ the incident wavelength.

Let the incoming field be described by[1]:

$$U_o(p) = \frac{e^{ikr}}{r}. \tag{3.12}$$

The quasi-specular scattered field under Kirchhoff approximation, the Fresnel integral, writes (see [Born and Wolf1993]):

$$U(p) = \frac{-i}{4\pi} \int \mathcal{R} \cdot \frac{e^{ik(r+s)}}{rs} (\vec{q} \cdot \hat{n})\, dS, \tag{3.13}$$

where r is the range between receiver and the surface and s the range between emitter and the surface. The scattering geometry from figure 3.2 leads to:

$$k_i r = k_i r' + \vec{k_i} \cdot \vec{r}. \tag{3.14}$$

The sign before the scalar product changes as we consider the out-coming vector $\vec{k}_s$. We can consequently rewrite the phase of the integrand:

$$k(r+s) \approx k(r'+s') - \vec{q} \cdot \vec{r}. \tag{3.15}$$

In the far field both emitter and receiver are very far compared to the size of the scatterer and since our integral is near a specular point with $\hat{n} \approx \hat{q}$, we find:

$$U(p) = \frac{-i}{4\pi} \frac{e^{ik(r'+s')}}{r's'} \int \mathcal{R} \cdot e^{-i\vec{q}\cdot\vec{r}} (\vec{q} \cdot \hat{n})\, dS. \tag{3.16}$$

Now, let us focus on a single specular point: imagine that there is only one specular point on the surface. This means $\vec{q} \cdot \hat{n} = q$. To perform the integral let us use a coordinate system in which the z axis is parallel to $\vec{q}$. In this coordinate system the tangent plane at the specular plane is therefore parallel to the x-y plane. Hence, $dS = \frac{d^2\vec{\rho}}{\hat{n}\cdot\hat{e}_z} = d^2\vec{\rho}$. We need to compute:

$$I = q \int \mathcal{R} \cdot e^{-iq\,\zeta(x,y)}\, d^2\vec{x}. \tag{3.17}$$

Now we use the *Stationary Phase Approximation* that states that the main contribution comes from the specular point. The basic idea of this approximation is to expand the argument of the exponential into a series about the specular point $\vec{\rho}_{spec}(x,y)$:

$$\zeta(\vec{\rho}_{spec} + \vec{\epsilon}) = \zeta(\vec{\rho}_{spec}) + \nabla\zeta\big|_{spec} \vec{\epsilon} + \frac{1}{2!} \nabla^2_{ij}\zeta\Big|_{spec} \epsilon_i \epsilon_j + ... \tag{3.18}$$

[1] Here we do a scalar treatment, think of U as a component of the field.

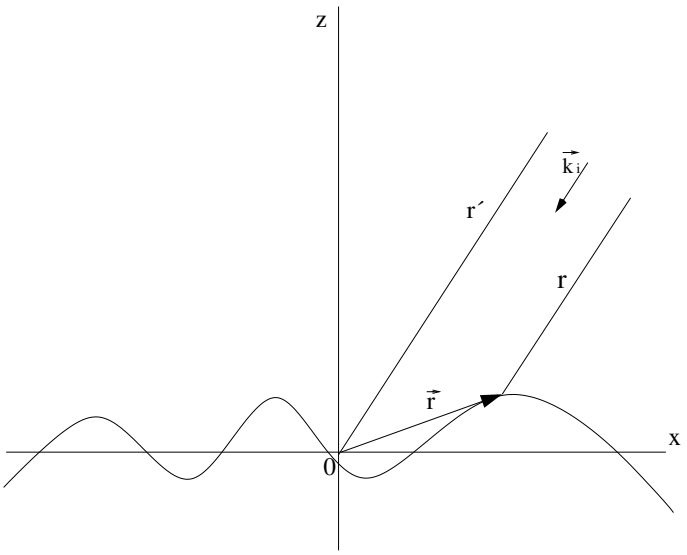

Figure 3.2: Vector geometry for scattering.

At this point the linear terms of the series vanish, since specular facets are characterized by a zero-slope. In other words, as q gets larger the integral gets contributions only very near the specular point—the contributions farther out cancel out. Indeed in the one dimension case, the integral can be expressed as follows:

$$I = q \int_{-\epsilon}^{\epsilon} \mathcal{R} \cdot e^{-iq\,\zeta(x)}\, d^2\vec{x} + q \int_{x \neq [-\epsilon,\epsilon]} \mathcal{R} \cdot e^{-iq\,\zeta(x)}\, d^2\vec{x}. \tag{3.19}$$

The phase of the second integral oscillates rapidly for large q so that the integral tends to cancel. On the contrary, the phase around the specular point doesn't vary so fast.

Back to the two-dimensional case, we obtain with a development at the order two:

$$\begin{aligned} I &\approx q\,\mathcal{R}_{spec} e^{-iq\,\zeta_{spec}} \int e^{-i\frac{q}{2}\,\nabla^2_{ij}\zeta\big|_{spec}\,x_i x_j}\, d^2\vec{x} && (3.20)\\ &= q\,\mathcal{R}_{spec} e^{-i\vec{q}\cdot\vec{r}_{spec}} \frac{2\pi}{(-i)q\,\det^{1/2}\left(\nabla^2_{ij}\zeta\Big|_{spec}\right)} && (3.21)\\ &= i\,\mathcal{R}_{spec} e^{-i\vec{q}\cdot\vec{r}_{spec}} \frac{2\pi}{\det^{1/2}\left(\nabla^2_{ij}\zeta\Big|_{spec}\right)}. && (3.22) \end{aligned}$$

Now, it is not hard to show that $\det^{1/2}\left(\nabla^2_{ij}\zeta\Big|_{spec}\right) = 1/\sqrt{r_x r_y}$—the determinant just yields the products of the radii of curvature at the specular point (r_x and r_y are the radii of curvature in x and y respectively, here at the specular point).

We obtain:

$$I = i\,\mathcal{R}_{spec} e^{-i\vec{q}\cdot\vec{r}_{spec}} 2\pi\sqrt{r_x r_y}. \tag{3.23}$$

Finally, we get the *Specular field*, defined as the reflected electromagnetic field under GO assumption (here for one specular point):

$$\begin{aligned} U(p) &= \frac{-i}{4\pi}\frac{e^{ik(r'+s')}}{r's'} \cdot i\,\mathcal{R}_{spec} e^{i\vec{q}\cdot\vec{r}} 2\pi\sqrt{r_x r_y} && (3.24)\\ &= \frac{\mathcal{R}_{spec}}{2}\frac{e^{ik(r_{spec}+s_{spec})}}{r_{spec}s_{spec}}\sqrt{r_x r_y}. \end{aligned}$$

The coefficient $\mathcal{R}_{spec}$ depends on the Fresnel coefficients and on the local geometry. The scattering cross section is defined as the ratio of the scattered power per unit area and the incident power density. At the specular point it becomes:

$$\begin{aligned} \sigma^o_{spec} &= \frac{|U|^2/A_o}{|U_o|^2/4\pi r_o^2} \\ &= \frac{|U|^2\ 4\pi r_{spec} s_{spec}}{|U_o|^2\ l_x l_y} \\ &= |\mathcal{R}_{spec}|^2 \pi \frac{r_x r_y}{l_x l_y} \\ &\equiv \frac{|\mathcal{R}_{spec}|^2}{\sigma_s^2}. \end{aligned} \tag{3.25}$$

The scattering cross section of the surface is the sum of each specular point contribution. The reader must keep in mind that we keep in the development of the integrand's phase the terms to the second order only. As we will see later through simulations in section (3.2.2), the GO method can be perfectly applied for surfaces that have for highest orders the quadratic terms (parabolic case).

In the general case of a Gaussian sea surface, the scattering cross section writes:

$$\sigma^o = \pi |\mathcal{R}|^2 \frac{q^4}{q_z^4}\ \mathcal{P}_s\left(\frac{-q_x}{q_z}, \frac{-q_y}{q_z}\right), \tag{3.26}$$

where $\mathcal{P}_s$ is the Gaussian sea-surface slope PDF, presented in section (2.2.2) of Chapter 2.

3.1.3 Small Perturbation Method

The Small Perturbation Method (SPM) belongs to a large family of perturbation expansion solutions to the wave equation. It is a partial differential equation boundary value problem approach. The basic idea is to find a solution in terms of plane waves that match the surface boundary conditions, which state that the tangential component of the field must be continuous across the boundary. The surface fields are expanded in a perturbation series,

$$\vec{E} = \vec{E}^{(0)} + \vec{E}^{(1)} + \vec{E}^{(2)} + \cdots \tag{3.27}$$

where $\vec{E}^{(n)}$ depends on the n-th power of the surface elevation ζ and its gradient, which is related to the mean squared slope σ_s^2. In the expansion, for instance, $\vec{E}^{(0)}$ would be the surface field if the surface was flat. The philosophy behind this approach is that small effective surface currents on a mean surface replace the role of the small-scale roughness. So this method applies to surfaces with small surface height variation and small surface slopes , i.e., when both σ_ζ and σ_s are small, independently of the radius of curvature. Therefore, the surface no longer needs to be approximated by planes, as the Kirchhoff approximation.

The small scale roughness is expanded in a Fourier series and the contributions to the field are therefore analyzed in terms of the different wavelength components. A consequence of this analysis is that frequencies in the surface spectrum that match the Bragg condition, thus contributing coherently to the field, play a predominant role. Since Bragg scattering is fundamental to the operation of modern scatterometers, let us briefly detour to discuss this aspect in more detail.

Microwave frequencies used in modern scatterometers are resonant to components of the ocean surface spectrum that are either very short gravity waves or surface tension waves which

ride on top of larger ocean waves. The resonance effect is so strong for incident radiation from about 20^o to 65^o that capillary waves of the order of one millimeter of height play a dominant role in the return signal, even if the underlying waves are several meters high. Even in this case, however, non-Bragg scattering from longer ocean waves cannot be neglected.

In order to assess the impact of the Bragg scattering component, the spectrum of the scattering surface must be considered. Resonance occurs with the components of this spectrum that are multiples of $\lambda/2\sin\theta$. In the case of standard scatterometers, the wavelengths involved are resonant with capillary waves, which are the first link in the wind-sea coupling chain of events. Bragg scattering at GNSS frequencies competes with the dominant diffuse scattering at low elevation incidence angles [Zavorotny et al., 1998b]. In [Zuffada el al., 1998], moreover, it is noted that Bragg scattering at GNSS frequencies does not originate from capillary waves (which are sub-centimetric).

When Bragg scattering is the dominant mechanism, it provides a rich tool to study the surface. Indeed, fixing a Bragg frequency fixes a surface spectral frequency and this can be related—through the dispersion relation for ocean waves—to Doppler effects in the scattered signal.

To summarize, SPM is a good model for small slope statistics, with both standard deviation of the sea-surface height and correlation length below the electromagnetic wavelength. It is the most appropriate for Bragg scattering issues and polarimetric performances.

3.1.4 The Two-Scale (Composite or Hybrid) Model

When there are two relevant scales in the surface roughness (one large and one small), the results from the rough scale model can be used by incoherently averaging the effective incidence and scattering angles with the large scale slopes. This is done in four steps:

1. The surface height fluctuation ζ is divided into a large scale and a small scale fluctuation, $\zeta = \zeta_l + \zeta_s$, each with its own spectrum, W_l and W_s, and it is assumed that the total spectrum (which is the sum of the two spectra) is effectively one or the other depending on whether the ocean wavelength is larger or smaller than a given wavelength.

2. The small scale spectrum is used to compute the SPM scattering coefficient $\sigma^o_{rt}(\theta, \theta_s, \phi_s)$, the subscript s standing for the scattered angles.

3. Using the large scale statistics tilting angle (Ω) statistics, through the probability distribution function $P(\Omega)$, the SPM scattering coefficient is averaged,

$$\sigma'^0_{rt}(\theta, \theta_s, \phi_s) \equiv \int d\Omega\, P(\Omega)\, \sigma^o_{rt}(R^\Omega[\theta, \theta_s], \phi_s). \tag{3.28}$$

   In this expression, $R^\Omega[\theta, \theta_s]$ stands for the local incident and scattering angles after rotation to the locally tilted reference frame. The original expressions for the tilting angles given in [Valenzuela1978] are corrected in recent work by [Elfouhaily *et al.*1999b].

4. Finally, using the large scale portion of the spectrum the Kirchhoff approximation cross section is added to σ'^0_{rt}, $\sigma^o_T = \sigma'^0_{rt} + \sigma^o_K$ to account for the specular part missing in the SPM. Adding this last step (not crucial for backscattering but important for forward scattering) makes the model a *composite model*. See [Marchand and Brown1998] for a slight modification of this recipe—it is argued that the Kirchhoff portion needs to be down-weighted due to the loss of scattering area caused by the small-scale structure.

One of the problems with this approach is that the real surface is not correctly described by two scales, and some recipe must be used to divide the spectrum. In [Durden and Vesecky1990], an ensemble of 1-D small Gaussian surfaces (24λ) is generated, and the cross section is calculated using the Moment Method—a computationally intensive method impractical for large 2-D surfaces like the ocean. The optimal wavelength for the spectrum split is found to be roughly at $k/2$, but is found to depend on incidence angle. The authors state that the result is in rough agreement with theoretical results found by [Chen and Fung1988].

In section (3.1), we have reviewed different electromagnetic models. The Kirchhoff approximation requires a large mean radius of curvature compared to the incident wavelength. The Geometric Optics model is a high frequency limit approximation of the Kirchhoff field. The Small Perturbation approach requires small mean slopes and heights compared to wavelength, with no restrictions on the radius of curvature. The Two-Scale model uses these two approaches to take into account basically the small scales and the big scales of the ocean spectrum. It seems to be the most successful in terms of experimental data.

However we keep the GO method during the present study since it is parameter-free. The work done in the following section shows that its validation holds at GNSS frequencies.

3.2 GO validation at L-band

We first define in section (3.2.1) the requirements needed to apply the GO method, based on the radius of curvature and size of the scatterer. We present then simulations carried out in order to understand the validation of GO scattering over a parabolic surface in section (3.2.2) and over a Gaussian surface in section (3.2.3). This work refers to [Ruffini and Soulat2000b] and [Ruffini and Soulat2000a].

3.2.1 Radius of curvature and scatterer size

For the use of the GO method at L-band we have to consider in addition of the joint probability of slopes and heights the probability of radii of curvature. At the specular point the radius of curvature must be large enough and the height difference between the associated parabola—i.e., parabola with same radius of curvature—and the surface must be less than one wavelength. This defines a tolerance related to the radius of curvature in order to apply the GO method as shown in figure 3.3. We can compare this approach to the flatness tolerance defined by Schooley for the optical case, see [Schooley1962].

If we assume that the z-axis is normal to the specular tangent plane, so that the slope is zero at the specular point, the condition in the one dimensional case is:

$$\left|\zeta(x) - \left[\zeta(x_{spec}) + \frac{1}{2!}\nabla^2\zeta(x_{spec})(x - x_{spec})^2\right]\right| < \lambda, \tag{3.29}$$

where $x < 10 \cdot \sqrt{(\lambda r_x)/(4\pi)}$ and λ is the incident wavelength.

In the 1-D case, if we consider one of the radii of curvature, r_x or r_y, the integral to be computed from equation (3.20) is essentially of the form:

$$I = \int_{-l_x}^{l_x} dx\, e^{iqx^2/r_x}. \tag{3.30}$$

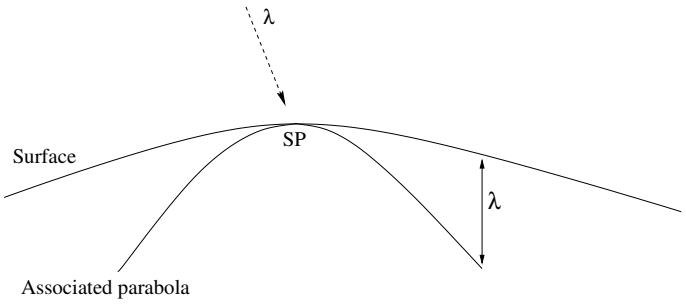

Figure 3.3: Associated parabola for specular point determination.

With the simple change of variable $u = x\sqrt{q/r_x}$, we obtain:

$$I = \sqrt{r_x/q} \int_{-l_x\sqrt{q/r_x}}^{l_x\sqrt{q/r_x}} e^{iu^2} du. \tag{3.31}$$

In this high frequency approximation the scattering vector $\vec{q}$ has to be large. The important question is how large q has to be compared to the surface characteristics (scatterer size, radius of curvature). For the integral to be reasonably close to $\sqrt{\pi}$, we need $l_x\sqrt{q/r_x}$ to be greater than 10, say. The inferior limit for l_x is thus $10\sqrt{\lambda r_x/4\pi}$.

Finally, in the bidimensional case, the requirements become for the characteristic radius L of the scatterer:

$$10 \cdot \sqrt{\frac{\lambda\sqrt{r_x r_y}}{4\pi}} < L. \tag{3.32}$$

3.2.2 Parabolic surface

First we consider a parabolic surface in order to understand how its resolution and curvature were involved in the computations of the reflected field. The surface is bell shaped and the radii of curvature in x and y are equal (r_x=r_y). The receiver is at nadir incidence—one specular point is thus considered—with a height defined by:

$$H = H_o + \zeta(x, y), \tag{3.33}$$

where $\zeta(x, y) = -(x^2 + y^2)/(2\sqrt{r_x r_y})$, and H_o is a constant altitude. We compute the scattered *Fresnel and Specular fields* neglecting the phase and under the far-emitter approximation:

$$U_{Fresnel}(p) = \frac{-i}{4\pi} \int \frac{e^{i2kH_0}}{r'} exp\left[i2k\frac{(x^2+y^2)}{2\sqrt{r_x r_y}}\right] 2kdS, \tag{3.34}$$

$$U_{Specular}(p) = \frac{e^{i2kH_0}\sqrt{r_x r_y}}{2H_0}. \tag{3.35}$$

The *Fresnel field* should not depend on the wavelength and the resolution. Nevertheless, the oscillations of the exponential in the integrand of equation (3.34) increase with frequency. We need consequently a small resolution in the numerical simulation as defined by following equality:

$$\frac{d\zeta}{dx} \cdot resolution << \lambda. \tag{3.36}$$

The impact of simulation resolution in the *Fresnel field* computation is shown in figure 3.4 for the bi-dimensional case. The straight line stands for the *Specular field* magnitude: $\sqrt{r_x r_y}/(2H_0)$,

the exact solution in this case. We took a 10×10 m^2 parabolic surface with a radius of curvature at the nadir point (in x and y) of (a) 5 meters and (b) 10 meters; the receiver is at H=500 meters over the surface and the transmission is in L-band (λ=19 cm). A resolution of 10 cm seems to be the limit for a tabulation size of 10 meters. This limit decreases for smaller wavelengths and increases for greater values of radius of curvature as shown in figure 3.4(b). Indeed the above inequality is much respected because the derivative of ζ reaches smaller values.

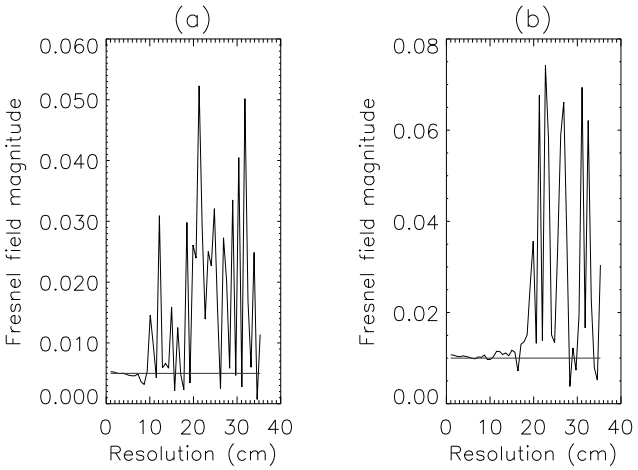

Figure 3.4: Fresnel field magnitude relative to surface resolution for two different radii of curvature: (a) r_x=r_y=5 m, (b) r_x=r_y=10 m. The receiver is at 500 meters over a 10×10 m^2 parabolic surface.

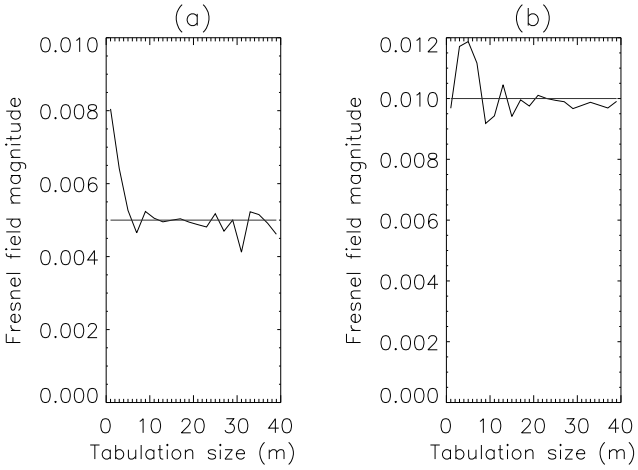

Figure 3.5: Fresnel field magnitude relative to the tabulation size of the surface for two different radii of curvature: (a) r_x=r_y=5 m and (b) r_x=r_y=10 m. The resolution is 3 cm and the receiver is at 500 meters transmitting in L-band.

The size of the surface (the size of the scatterer) is also a very important physical parameter, as we discussed. Figure 3.5 shows the *Fresnel field* magnitude relative to the size of the scattering surface for two different radii of curvature: (a) r_x=r_y=5 m and (b) r_x=r_y=10 m.

Similarly, the straight line stands for the *Specular field* magnitude: $\sqrt{r_x r_y}/(2H_0)$. From figure 3.5(a), we can check the requirement of (3.32) for the size of the scatterer. The "specular" scatterer needs to be big enough. For the same parabolic surface and if the inequality (3.32) is verified, the receiver "sees" one specular point only and the *Specular field* magnitude should also be $\sqrt{r_x r_y}/(2H_0)$ as expected in equation (3.24). Geometric Optics is therefore expected to be a good approximation for high enough frequencies.

In addition, a simple simulation has been carried out to check if the Geometric Optics is still available if we add very small ripples on the parabolic surface. The ripples are generated by a sinusoidal signal characterized by its amplitude and wavelength. The effect of ripples on the reflected field is shown in figure 3.6 for a 10×10 m^2 parabolic surface (r_x=r_y=5 m). Under the curve, there is a difference of $\pm10\%$ between Fresnel magnitude and the magnitude computed on a perfect parabolic surface in L-band.

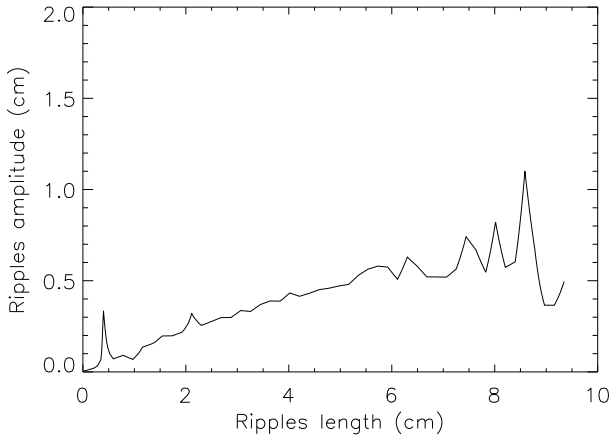

Figure 3.6: Effect of small ripples added on a very smooth parabolic wave. Under the curve, there is a difference of $\pm10\%$ between Fresnel magnitude and the magnitude computed on a perfect parabolic surface in L-band.

Physically we assume in the Kirchhoff theory that the surface is flat enough to be locally represented by planes. The case of two scale model is interesting because the GO approximation is not valid any more. Indeed the diffraction caused by short scale waves has a great part in the return signal. Their contribution appears in the higher terms of the phase development. We emphasize that the GO method works for a perfect parabolic surface but is destroyed when small scale features are added.

3.2.3 Gaussian surface

The GO validity is undertaken by comparing the *Fresnel* and *Specular fields*. The latter is computed 1) applying equation 3.24 to all specular points detected on the sea surface and 2) summing incoherently their complex fields. We first focus on the specular point detection and then compare the two fields.

Specular point determination

We consider the incident radiation as a plane wave normal to a Gaussian surface and a receiver centered above the scattering surface. Using Geometric Optics, the point $(x, y, \zeta(x, y))$ of the

surface is considered to be specular if the slopes (in x and y) follow geometrical conditions, see [D.E.Freund 1997]:

$$\frac{d\zeta}{dx} = \frac{\frac{x-x_r}{u_r} + \frac{x-x_s}{u_s}}{\frac{z_r-\zeta}{u_r} + \frac{z_s-\zeta}{u_s}} = \frac{x - x_r}{z_r - \zeta} \tag{3.37}$$

$$\frac{d\zeta}{dy} = \frac{\frac{y-y_r}{u_r} + \frac{y-y_s}{u_s}}{\frac{z_r-\zeta}{u_r} + \frac{z_s-\zeta}{u_s}} = \frac{y - y_r}{z_r - \zeta}, \tag{3.38}$$

where u_r (resp. u_s) is the distance between the point of the surface of coordinates (x, y, ζ) and the receiver of coordinates (x_r, y_r, z_r) (resp. the source, considered here very high). Our approach consists in the detection of slope variations around the expected specular slopes defined above. We compute at each point P of the surface, and for both directions x and y, the expected specular slope S—i.e., the slope needed to reflect the incident wave to the receiver—and the slopes of the facets located just before (slope S_{before}) and after (slope S_{after}) the point P. The condition for P to be a speckle is that $(S_{before} - S)$ and $(S - S_{after})$ must be of the same sign. This determination is attractive because we do not need to define any tolerance on the specular slopes. Therefore it doesn't take in account the *saddle points* defined as inflection points.

Barrick derived the average number of specular points per unit of area n in terms of the surface statistics, see [Barrick1968]:

$$n \sim \frac{1}{l^2} \exp\left(-\frac{\tan^2\beta}{s^2}\right), \tag{3.39}$$

where s^2 is the mean square value of the total slope at a point of the two-dimensionally rough surface, defined as $s^2 = \left\langle \zeta_x^2 + \zeta_y^2 \right\rangle$, and β is defined as the angle between the mean normal to the surface and the local surface normal at the specular point. For backscattering—i.e., when the incident angle θ is zero—it is easy to see that the term in the exponential vanishes. Thus the specular points density is inversely proportional to the autocorrelation length of the surface. Figure 3.7 shows the specular point number relative to wind speed for the backscattering case. The underlying idea is that as the wind speed increases the waves are more developed and consequently the autocorrelation length increases.

As an example, figure 3.8 shows the specular points position—represented by a cross—on a Gaussian surface for a wind at 45^o of the x-axis with two different speeds. The surface is a 30 meter side square with 10 cm resolution so that the surface is a matrix of 300×300 pixels. Black areas stand for troughs and white areas for crest zones. For (a) U_{10}=5 m/s, the receiver (500 meters high, at nadir incidence) "sees" 1038 specular points while 881 in case (b) U_{10}=15 m/s.

Fields comparison

Based on simulated Gaussian ocean surfaces, we have observed that there is no strong correlation between the *Fresnel* and *Specular fields*, neither in magnitude nor in phase. However, a very important result is that the power from the *Fresnel field* correlates well with the number of specular points. Figure 3.9 illustrates how involved is the number of specular points in the reflected power computed by the Fresnel integrals. The computation has been done for a moving Gaussian surface based on [Elfouhaily *et al.*1997]'s spectrum (5×5 m^2 with 5 cm resolution) during 2 seconds, under a 15 m/s wind and a fetch of 10 km; the receiver is at 50 meters over the surface.

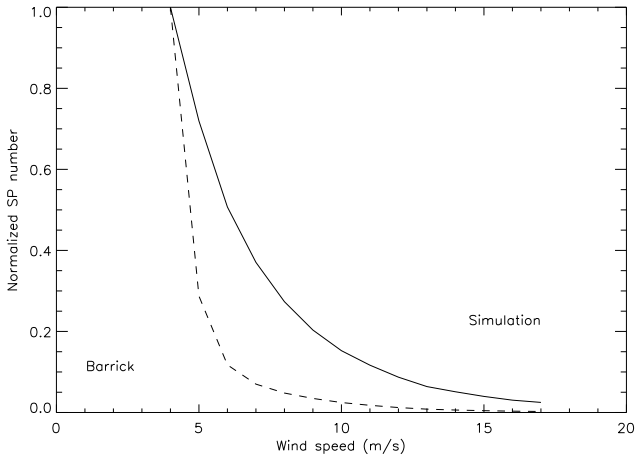

Figure 3.7: Specular points number relative to wind speed for backscattering (25x25 meter surface with 5 cm resolution).

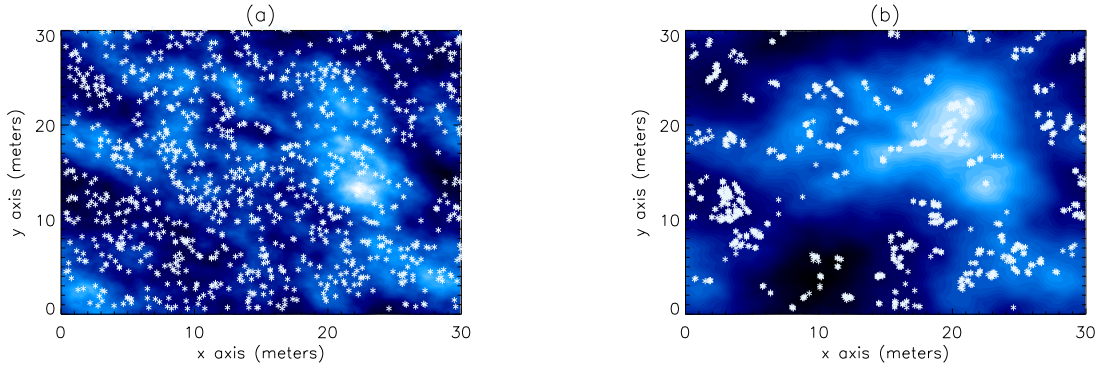

(a) U_{10}=5 m/s

(b) U_{10}=10 m/s

Figure 3.8: Specular points position for (a) U_{10}=5 m/s and (b) U_{10}=15 m/s.

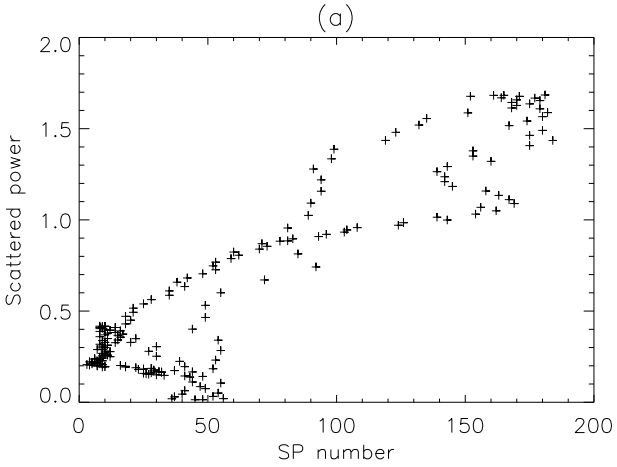

Figure 3.9: Correlation between the reflected power and specular point number on a Gaussian ocean model in L-band (L_1=19 cm) within 2 seconds: 5×5 m^2, 5 cm resolution, U_{10}=15 m/s, receiver at nadir incidence at 50 meters.

It is rather clear that there is a correlation between specular point number and the return signal power. The surface is quite well developed—U_{10}=15 m/s—and consequently smooth enough to apply the GO method.

But is this correlation big enough to state that counting specular points can itself be useful to describe the reflected field? We have compared the above correlation in L-band to that with an incident wavelength of 1 cm, which is much better in terms of the *high frequency limit* requirements. In figure 3.10, we see that the correlation is much better for a 1 cm incident wavelength than for the L-band case, as expected.

We also see that as the mean radius of curvature increases with high wind speeds, i.e., the requirements of the Kirchhoff theory are better respected, the correlation increases. Similarly, the diffraction terms effects decrease with increasing ocean scale, so that their contribution in the integrand's phase decreases with increasing wind speed. These diffraction terms are those neglected by the usual stationary phase method which evaluates the reflected field with terms of order two only in the integrand's phase.

3.2.4 Conclusions on GO assumption for GNSS-R

The computation of the reflected field corresponds to a rapidly oscillating integral over the rough surface. The specular points are identified with the critical points of the integrand's phase, as stated by the Stationary Phase Approximation. Thus, in the high frequency limit, almost all the scattered field intensity comes from the specular points. It is exact in the parabolic case, provided that Kirchhoff assumption applies and the size of the scatterer is large enough. We saw that small perturbations added on the parabolic surface destroy the Stationary Phase Approximation integrity.

In the realistic case of a large but finite incident wavenumber, the scattering from the specular point often carries the major contribution to the reflected signal. Therefore, in many circumstances, the area that contains the major contribution to the reflected field—the bright area—can be identified as the part of the sea surface where the probability for specular reflection is significant.

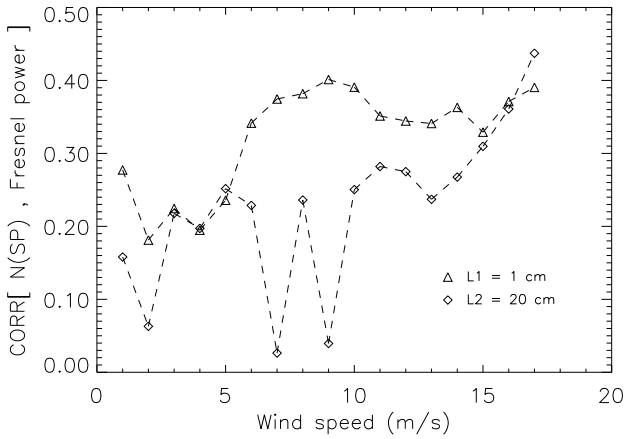

Figure 3.10: Correlation between the specular points number and the reflected power computed with the Fresnel integral, for an incident wavelength L_1=1 cm or L_2=20 cm.

Recall one more time that the GO method is: *a*) the Stationary Phase approach, *b*) an approximation to the field up to second order and *c*) incoherent averaging.

We have not seen a good correlation between the *Fresnel field* and the *Specular field* computed directly from the specular points. There exists, however, a correlation between the specular point number and the reflected power (points *a*) and *c*)). In general the higher the electromagnetic frequency and wind speed—i.e., higher roughness and larger scales in the ocean—the better this correlation is, as expected from our theoretical understanding of the approximation.

Several conclusions can be extracted from this study:

- Most of the radiation comes from specular points, hence the good correlation between specular point number and field power. This means that the surface slope PDF will play an important role in bistatic scattering modeling at L-band.
- The stationary phase approximation can be used but higher order terms must play a role at L-band. These corrections are usually called diffraction corrections. This explains the poor correlation between the *Specular* and *Fresnel fields*.
- GO's success in GNSS-R work stems more from the use of specular point number statistics than from the use of precise field calculations based on the stationary phase approximation. That is, the successful use of the PDF in GNSS scattering is not a validation of GO. In retrospect, this is all evident: the lesson from GO for L-band is limited to understanding the importance of the slope PDF to approximate the field. The slope PDF is the tool to count specular points. Necessary but not sufficient, of course.

With this caveat, the GO model is thus further used in all L-band scattering processes presented in this dissertation, such as the waveform model developed in the following section.

3.3 Waveform model: DDM

We present in the following section the integral expression of the power GNSS waveform. A comparison is then done with the models developed by [Zavorotny and Voronovich2000] and

[Picardi *et al.*1998].

3.3.1 Integral expression of the power waveform

Bistatic scattering of a monochromatic wave

If the ocean surface is illuminated with a monochromatic spherical wave, the complete quasi-specular scattered field writes under Kirchhoff approximation:

$$u(\Omega,t) = \frac{i}{4\pi} \int \mathcal{R}\ \vec{q}.\hat{n}\ \frac{G_t G_r}{R_t R_r}\ \ e^{-i\Omega(t-l(\vec{r},t)/c)}\ \ d\vec{r}, \tag{3.40}$$

with:

- $\mathcal{R}$: Fresnel coefficient,
- $\vec{q}$: scattering vector,
- $\hat{n}$: normal to the surface,
- G_t, G_r : transmitter and receiver amplitude antenna patterns,
- R_t, R_r : transmitter-ocean and ocean-receiver distances,
- Ω : carrier pulsation,
- $l(\vec{r},t) = R_t + R_r$: length of the path Transmitter to generic point (R_t) to Receiver (R_r).

At high altitudes, many of the above magnitudes do not vary significantly over the integration area. First G_t, R_t and $\mathcal{R}$ can reasonably be considered constant. Then, for smooth ocean surface and in quasi-specular regime, we have $\hat{n} \simeq \hat{e}_z$ and $\vec{q} \simeq q\hat{e}_z$. Therefore, $\vec{q}.\hat{n} \simeq \frac{2\sin\gamma}{c}\Omega$ (where γ is the elevation of the satellite). Finally, for high enough altitudes, G_r and R_r are also uniform functions. As a result, the Kirchhoff integral simplifies to:

$$u(\Omega,t) = \frac{i\sin\gamma}{2\pi c}\ \mathcal{R}\ \frac{G_t G_r}{R_{t0} R_{r0}}\ \Omega \int e^{-i\Omega(t-l(\vec{r},t)/c)}\ \ d\vec{r}. \tag{3.41}$$

Receiver and transmitter motions make the travel path time-dependent in fast-varying functions. To first order, this effect can be written:

$$l(\vec{r},t) \simeq d(\vec{r}) + \frac{\lambda}{2\pi}\omega_D(\vec{r})t, \quad \text{for } \ 0 < t < T_i, \tag{3.42}$$

where $\omega_D/2\pi$ is the Doppler contribution of point $\vec{r}$ and T_i is the coherent integration time defined below. Finally, we can state that the scattered field for a monochromatic incident wave at Ω is:

$$u(\Omega,t) = \frac{i\sin\gamma}{2\pi c}\ \mathcal{R}\ \frac{G_t G_r}{R_{t0} R_{r0}}\ \Omega \int e^{-i(\Omega-\omega_D(\vec{r}))t}\ \ e^{i\Omega d(\vec{r})/c}\ \ d\vec{r}. \tag{3.43}$$

PRN modulation as a wave packet

In GNSS-R, the incident wave is not a pure monochromatic wave. The PRN code—let's name it here $a(t)$ for both C/A and P codes—actually modulates the carrier, broadening the incident spectrum. Note that the carrier is Ω=1.5 GHz and the bandpass is either 1 MHz (C/A code) or 10 MHz (P code). Since the Kirchhoff scattering mechanism is linear, the outgoing field

can be seen as the superposition of a series of monochromatic components scattered by the ocean surface:

$$u(t) = \int_{-\infty}^{+\infty} \tilde{a}(\nu) \cdot u(\Omega + \nu, t)\ d\nu, \tag{3.44}$$

where $\tilde{a}(\nu)$ is the Fourier baseband spectrum of the PRN code and $u(\Omega + \nu, t)$ is given by equation (3.43). Note that in the equation above, ν appears as the frequency broadening from the carrier Ω.

Code despreading

As introduced in section (1.1.2), the GNSS receiver performs signal detection through code despreading, that is by correlating over a period T_i the incoming signal with a clean modulated replica of the PRN code:

$$y(\tau, \omega) = \frac{1}{T_i} \int_{T_i} u(t) \cdot a(t - \tau) e^{i(\Omega - \omega)t}\ dt. \tag{3.45}$$

The result of this processing is nothing but the complex delay-Doppler map at time-frequency shift (τ, ω).

Combining equations (3.43), (3.44) and (3.45) leads to:

$$y(\tau, \omega) = \frac{i \sin\gamma}{2\pi c T_i}\ \mathcal{R}\ \frac{G_t G_r}{R_{t0} R_{r0}} \iiint (\Omega + \nu)\ a(t - \tau)\ \tilde{a}(\nu) e^{i[(\omega_D - \omega - \nu)t + (\Omega + \nu)d/c]}\ d\nu\ dt\ d\vec{r}. \tag{3.46}$$

Let us first perform the integration on ν:

$$\int (\Omega + \nu)\ \tilde{a}(\nu) e^{-i\nu(t - d/c)}\ d\nu \simeq \Omega\ a(t - d/c), \tag{3.47}$$

where we have assumed that the factor $(\Omega + \nu)$ is basically identical to Ω over the GNSS bandpass.
The integration over t writes:

$$\int_{T_i} a(t - d/c)\ a(t - \tau)\ e^{i(\omega_D - \omega)t}\ dt = T_i\ \chi(\delta\tau, \delta\omega), \tag{3.48}$$

where we have introduced:

$$\begin{cases} \delta\tau &= \tau - d(\vec{r})/c \\ \delta\omega &= \omega - \omega_D(\vec{r}). \end{cases} \tag{3.49}$$

The function χ is known in radar pulse-compression techniques as the Woodward Ambiguity Function (WAF) of pseudo-random sequences, defining here the spatial resolution of the system. It is here assumed separable:

$$\chi(\delta\tau, \delta\omega) = \Lambda(\delta\tau) \cdot S(\delta\omega) \tag{3.50}$$

$$= \Lambda(\delta\tau) \cdot \mathrm{sinc}(\delta\omega\ T_i). \tag{3.51}$$

The function Λ is the triangle function of width twice a chip length and $\mathrm{sinc}(x)$ is $\sin(\pi x)/\pi x$.

Finally, the despread signal writes:

$$y(\tau, \omega) = \frac{i \sin\gamma}{\lambda}\ \mathcal{R}\ \frac{G_t G_r}{R_{t0} R_{r0}} \int \Lambda(\delta\tau) \cdot S(\delta\omega)\ e^{i\Omega d/c}\ d\vec{r}. \tag{3.52}$$

Delay-Doppler map

Let us make explicit the expression of the delay and Doppler mapping on sea-surface (namely $d(\vec{r})/c$ and $\omega_D(\vec{r})$). Note that we will assume w_D deterministic (Doppler mapping is computed on a flat surface) whereas d has a random contribution through sea-elevation $z{=}\zeta(x,y)$.

The distances to any point (x,y,z) on the ocean surface write:

$$\left\{\begin{array}{rcl} R_t^2 &=& R_{t0}^2\left(1+2\frac{x\cos\gamma}{R_{t0}}-2\frac{z\sin\gamma}{R_{t0}}+\frac{x^2+y^2+z^2}{R_{t0}^2}\right)\\ R_r^2 &=& R_{r0}^2\left(1-2\frac{x\cos\gamma}{R_{r0}}-2\frac{z\sin\gamma}{R_{r0}}+\frac{x^2+y^2+z^2}{R_{r0}^2}\right),\end{array}\right. \tag{3.53}$$

where R_{t0} and R_{r0} are the distances of transmitter and receiver to the specular point. Retaining only significant terms, we have:

$$\frac{d(\vec{r})}{c}\simeq\frac{d_0}{c}-\frac{2\sin\gamma}{c}z+\frac{\sin^2\gamma}{2cR_{r0}}x^2+\frac{1}{2cR_{r0}}y^2, \tag{3.54}$$

where d_0 stands for the bistatic path to specular point $(R_{t0}+R_{r0})$, that is the parameter of interest for an altimetric application.

If we neglect the Doppler spread due to transmitter motion and only retain the contribution of the receiver with velocity $\vec{v}$, we have:

$$\begin{array}{rcl}\omega_D &=& \frac{2\pi}{\lambda}\,\vec{v}.\frac{\vec{R}_r}{R_r}\\ &=& \frac{2\pi v\cos\Phi}{\lambda}\,\frac{x+y\tan\Phi-R_{r0}\cos\gamma}{\sqrt{R_{r0}-2x\cos\gamma+x^2+y^2}},\end{array} \tag{3.55}$$

where Φ is the angle between the Transmitter-Receiver line (x axis) and $\vec{v}$. To first order:

$$\omega_D=\omega_{D0}+\frac{2\pi v\cos\Phi}{\lambda}\left(\sin^2\gamma\frac{x}{R_{r0}}+\tan\Phi\frac{y}{R_{r0}}\right), \tag{3.56}$$

where $\omega_{D0}=-\frac{2\pi v\cos\Phi\cos\gamma}{\lambda}$ is the Doppler of the specular point.

Averaging in power

At this point, it is time to point out which are the contributions of the ocean surface and by this mean, identify the random parameters in the above integral. There are actually three sources of randomness:

- The most crucial one is obviously d in the exponential term. Note that only this random contribution was considered in [Zavorotny and Voronovich2000]. This approach yields a statistical sea surface model only featuring MSS.
- The argument of Λ is also random through d. If it is taken into account, the statistical description of sea surface will also feature SWH, as in [Picardi *et al.*1998].
- In principle, the argument of S is also random because w_D slightly depends on the sea-surface topography through receiver radial speed. However, this effect is really tiny and will not be considered here.

In the following, we will therefore assume that $\delta\omega$ is deterministic (w_D is computed on a flat surface) and that d is the only random variable:

$$y(\tau,\omega)=\frac{i\sin\gamma}{\lambda}\,\mathcal{R}\,\frac{G_tG_r}{R_{t0}R_{r0}}\int S(\delta\omega)\;\Lambda(\tau-d/c)\;e^{i\Omega d/c}\;\;d\vec{r}. \tag{3.57}$$

It is then convenient to introduce the Fourier transform of $\Lambda(\tau)$, that is the delay-spectrum of the despread code:

$$\Lambda(\tau) = \int \tilde{\Lambda}(\nu)\ e^{i\nu\tau}\ d\nu, \tag{3.58}$$

so that we can write:

$$y(\tau,\omega) = \frac{i\sin\gamma}{\lambda}\ \mathcal{R}\ \frac{G_t G_r}{R_{t0}R_{r0}}\ \int \tilde{\Lambda}(\nu)\ e^{i\nu\tau} \int S(\delta\omega)\ e^{i(\Omega-\nu)d/c}\ \ d\vec{r}\ d\nu, \tag{3.59}$$

and hence isolate the random contribution in the exponential term. The average power signal is then defined as:

$$Y(\tau,\omega) = \langle\ |y(\tau,\omega)|^2\ \rangle. \tag{3.60}$$

That is:

$$\begin{aligned} Y(\tau,\omega) &= \frac{\sin^2\gamma}{\lambda^2}\ |\mathcal{R}|^2\ \frac{G_t^2 G_r^2}{R_{t0}^2 R_{r0}^2} \\ &\cdot \int d\nu_1 \int d\nu_2\ \ \tilde{\Lambda}(\nu_1)\ \tilde{\Lambda}^*(\nu_2)\ e^{i\tau(\nu_1-\nu_2)} \\ &\cdot \int d\vec{r}_1 \int d\vec{r}_2\ \ S(\delta\omega_1)\ S^*(\delta\omega_2)\ \langle\ e^{i\left(\frac{\Omega-\nu_1}{c}d_1 - \frac{\Omega-\nu_2}{c}d_2\right)}\ \rangle. \end{aligned} \tag{3.61}$$

Plugging the delay mapping in $Y(\tau,\omega)$ yields:

$$\begin{aligned} Y(\tau,\omega) &= \frac{\sin^2\gamma}{\lambda^2}\ |\mathcal{R}|^2\ \frac{G_t^2 G_r^2}{R_{t0}^2 R_{r0}^2} \\ &\cdot \int d\nu_1 \int d\nu_2\ \ \tilde{\Lambda}(\nu_1)\ \tilde{\Lambda}^*(\nu_2)\ e^{i(\tau-d_0/c)(\nu_1-\nu_2)} \\ &\cdot \int d\vec{r}_1 \int d\vec{r}_2\ \ S(\delta\omega_1)\ S^*(\delta\omega_2)\ e^{\frac{i}{2cR_{r0}}\left[(\Omega-\nu_1)(\sin^2\gamma x_1^2+y_1^2)-(\Omega-\nu_2)(\sin^2\gamma x_2^2+y_2^2)\right]} \\ &\cdot \langle\ e^{-i\frac{2\sin\gamma}{c}[(\Omega-\nu_1)z_1-(\Omega-\nu_2)z_2]}\ \rangle. \end{aligned} \tag{3.62}$$

Approximations

So far, the integration is performed over the six variables x_1, x_2, y_1, y_2, ν_1 and ν_2. For each couple of variables, we introduce the mean and the difference. For instance:

$$(x_1,x_2) \longrightarrow \left\{ \begin{array}{lcl} \delta x &=& x_1 - x_2 \\ \bar{x} &=& \frac{x_1+x_2}{2}. \end{array} \right. \tag{3.63}$$

Note that the Jacobian of this transformation is unitary. In the following, we will focus on the expression of $Y(\tau,\omega_{D0})$, i.e., the waveform obtained after exact compensation of the specular point Doppler [2]. We have:

$$\begin{aligned} Y(\tau,\omega_{D0}) &= \frac{\sin^2\gamma}{\lambda^2}\ |\mathcal{R}|^2\ \frac{G_t^2 G_r^2}{R_{t0}^2 R_{r0}^2} \cdot \int d\bar{\nu} \int d(\delta\nu) \int d\bar{x} \int d(\delta x) \int d\bar{y} \int d(\delta y) \\ &\cdot \tilde{\Lambda}(\bar{\nu}+\frac{\delta\nu}{2})\ \tilde{\Lambda}(\bar{\nu}-\frac{\delta\nu}{2}) \\ &\cdot e^{i(\tau-\frac{d_0}{c})\delta\nu} \\ &\cdot S(\bar{x}+\frac{\delta x}{2},\bar{y}+\frac{\delta y}{2})\ S(\bar{x}-\frac{\delta x}{2},\bar{y}-\frac{\delta y}{2}) \\ &\cdot e^{\frac{-i}{2cR_{r0}}\delta\nu\left[\sin^2\gamma\ \ (\bar{x}^2+\frac{\delta x^2}{2})+\bar{y}^2+\frac{\delta y^2}{2}\right]} \\ &\cdot e^{\frac{i}{2cR_{r0}}2(\Omega-\bar{\nu})(\sin^2\gamma\ \ \delta x\cdot\bar{x}+\delta y\cdot\bar{y})} \\ &\cdot \langle\ e^{-i\frac{2\sin\gamma}{c}[(\Omega-\bar{\nu})\delta z-\bar{z}\delta\nu]}\ \rangle. \end{aligned} \tag{3.64}$$

[2] Note that $S(\omega_{D0}-\omega_D)$ is then a function of (x,y) only.

We therefore end-up with a tough integral featuring six distinct terms where the variables are coupled. Some approximations can reasonably be made. We remind that $\bar{\nu}$ is bound by the compressed pulse bandwidth (1 MHz for C/A code) , and that δx and δy are bound by the ocean correlation length (some tenth of meters).

Approximation 1.1

In the sixth and fifth term of (3.64), we assume:

$$\Omega - \bar{\nu} \simeq \Omega. \tag{3.65}$$

As a matter of fact, the maximum phase contributions induced by $\bar{\nu}$ is negligible in both cases.

Approximation 1.2

In the fourth term of (3.64), we assume:

$$\sin^2\gamma\ (\bar{x}^2 + \frac{\delta x^2}{2}) + \bar{y}^2 + \frac{\delta y^2}{2} \simeq \sin^2\gamma\ \bar{x}^2 + \bar{y}^2. \tag{3.66}$$

As a matter of fact, the maximum phase contributions induced by δx and δy are negligible.

Approximation 1.3

In the third term of (3.64), we assume:

$$S(\bar{x} + \frac{\delta x}{2}, \bar{y} + \frac{\delta y}{2})\ S(\bar{x} - \frac{\delta x}{2}, \bar{y} - \frac{\delta y}{2}) \simeq S^2(\bar{x}, \bar{y}), \tag{3.67}$$

because the correlation length of sea surface is short and S is a slow-varying function.

Simplified expression

According to the above approximations, the expression (3.64) rewrites:

$$\begin{aligned} Y(\tau, \omega_{D0}) \simeq\ & \frac{\sin^2\gamma}{\lambda^2}\ |\mathcal{R}|^2\ \frac{G_t^2 G_r^2}{R_{t0}^2 R_{r0}^2} \cdot \int d\bar{\nu} \int d(\delta\nu) \int d\bar{x} \int d(\delta x) \int d\bar{y} \int d(\delta y) \\ & \cdot\ \tilde{\Lambda}(\bar{\nu} + \frac{\delta\nu}{2})\ \tilde{\Lambda}(\bar{\nu} - \frac{\delta\nu}{2}) \\ & \cdot\ e^{i(\tau - \frac{d_0}{c})\delta\nu} \\ & \cdot\ S^2(\bar{x}, \bar{y}) \\ & \cdot\ e^{\frac{-i}{2cR_{r0}}\delta\nu\left[\sin^2\gamma\ \bar{x}^2 + \bar{y}^2\right]} \\ & \cdot\ e^{\frac{i\Omega}{cR_{r0}}(\sin^2\gamma\ \delta x\cdot\bar{x} + \delta y\cdot\bar{y})} \\ & \cdot\ \langle\ e^{-i\frac{2\sin\gamma}{c}(\Omega\delta z - \bar{z}\delta\nu)}\ \rangle. \end{aligned} \tag{3.68}$$

Geometric Optics

In order to calculate the ensemble average in the latter expression, we follow the standard procedure of the Geometric Optics limit. As described in section (3.1.2), the essence of this approach is to consider the sea-surface as a set of plane facets so that δz can be expressed to first order as a function of the local directional slope:

$$\delta z \simeq \partial_{\vec{r}} z \cdot \delta\vec{r}. \tag{3.69}$$

We are here dealing with two random processes of interest: the sea-surface elevations z and the sea-surface directional slopes $\partial_{\vec{r}} z$. If these are considered independent:

$$\langle\ e^{-i\frac{2\sin\gamma}{c}(\Omega\delta z-\bar{z}\delta\nu)}\ \rangle = \langle\ e^{-i\frac{2\Omega\sin\gamma}{c}\partial_{\vec{r}}z\cdot\delta\vec{r}}\ \rangle \cdot \langle\ e^{i\frac{2\sin\gamma}{c}\bar{z}.\delta\nu}\ \rangle. \tag{3.70}$$

The above ensemble averages are then identified as characteristic functions of the random processes. Introducing the sea-elevation PDF $\mathcal{P}_\zeta$ and the sea-slope PDF $\mathcal{P}_s$, we end-up with:

$$\langle\ e^{-i\frac{2\sin\gamma}{c}(\Omega\delta z-\bar{z}\delta\nu)}\ \rangle = \tilde{\mathcal{P}}_s\left(\frac{2\Omega\sin\gamma}{c}\delta\vec{r}\right)\cdot\tilde{\mathcal{P}}_\zeta\left(\frac{2\sin\gamma}{c}\delta\nu\right), \tag{3.71}$$

where $\tilde{.}$ denotes the Fourier Transform. The expression of $Y(\tau,\omega)$ becomes:

$$\begin{aligned} Y(\tau,\omega_{D0}) &\simeq \frac{\sin^2\gamma}{\lambda^2}\,|\mathcal{R}|^2\,\frac{G_t^2G_r^2}{R_{t0}^2R_{r0}^2}\cdot \int d\bar{\nu}\int d(\delta\nu)\int d\bar{x}\int d(\delta x)\int d\bar{y}\int d(\delta y)\\ &\cdot\ \tilde{\Lambda}(\bar{\nu}+\frac{\delta\nu}{2})\ \tilde{\Lambda}(\bar{\nu}-\frac{\delta\nu}{2})\ \ \tilde{\mathcal{P}}_\zeta\left(\frac{2\sin\gamma}{c}\delta\nu\right)\ \ e^{i\Delta\tau\delta\nu}\\ &\cdot\ S^2(\bar{x},\bar{y})\ \ \tilde{\mathcal{P}}_s\left(\frac{2\Omega\sin\gamma}{c}\delta\vec{r}\right)\ \ e^{\frac{i\Omega}{cR_{r0}}(\sin^2\gamma\ \delta x\cdot\bar{x}+\delta y\cdot\bar{y})}, \end{aligned} \tag{3.72}$$

with:

$$\Delta\tau = \tau - \frac{d_0}{c} - \frac{\sin^2\gamma\ \bar{x}^2+\bar{y}^2}{2cR_{r0}}. \tag{3.73}$$

3.3.2 Expression as a 2-D integral on sea-surface

Integration

The six-variable integral reduces to:

$$\int d\bar{x}\int d\bar{y}\ \ S^2(\bar{x},\bar{y})\cdot J(\bar{x},\bar{y})\cdot K(\bar{x},\bar{y}), \tag{3.74}$$

with:

$$J(\bar{x},\bar{y}) = \int d\bar{\nu}\int d(\delta\nu)\ \ \tilde{\Lambda}(\bar{\nu}+\frac{\delta\nu}{2})\ \tilde{\Lambda}(\bar{\nu}-\frac{\delta\nu}{2})\ \tilde{\mathcal{P}}_\zeta\left(\frac{2\sin\gamma}{c}\delta\nu\right)\ e^{i\Delta\tau\delta\nu}, \tag{3.75}$$

$$K(\bar{x},\bar{y}) = \int d(\delta x)\int d(\delta y)\ \ \tilde{\mathcal{P}}_s\left(\frac{2\Omega\sin\gamma}{c}\delta\vec{r}\right)\ e^{\frac{i\Omega}{cR_{r0}}(\sin^2\gamma\ \delta x\cdot\bar{x}+\delta y\cdot\bar{y})}. \tag{3.76}$$

Integration of J

Integrating first on $d\bar{\nu}$, we recognize the autocorrelation of $\tilde{\Lambda}$ and the second integral appears as the Fourier transform of the product of two functions:

$$\begin{aligned} J(\bar{x},\bar{y}) &= \int d(\delta\nu)\left[\tilde{\Lambda}\star\tilde{\Lambda}\right](\delta\nu)\ \ \tilde{\mathcal{P}}_\zeta\left(\frac{2\sin\gamma}{c}\delta\nu\right)\ \ e^{i\Delta\tau\delta\nu}\\ &\propto \left[\Lambda^2(\tau)\star\mathcal{P}_\zeta\left(\frac{c\tau}{2\sin\gamma}\right)\right](\Delta\tau)\\ &\equiv \Lambda_e^2(\Delta\tau). \end{aligned} \tag{3.77}$$

This result shows that the main impact of sea-state is to introduce an effective compressed pulse Λ_e^2 defined as the convolution between Λ^2 and the sea-elevation PDF. As a result, the nominal compressed pulse width τ_c is broaden by an additive factor proportional to significant wave height.

Integration of K

We recognize here a Fourier transform:

$$K(\bar{x},\bar{y}) \propto \mathcal{P}_s\left(\sin\gamma\frac{\bar{x}}{2R_{r0}}, \frac{1}{\sin\gamma}\frac{\bar{y}}{2R_{r0}}\right). \tag{3.78}$$

2-D integral expression

The waveform now writes as a 2-D integral over sea-surface:

$$\begin{aligned} Y(\tau,\omega_{D0}) \quad \propto \quad & \int d\bar{x}\int d\bar{y} \\ & . \quad S^2(\bar{x},\bar{y})\cdot\Lambda_e^2\left(\tau-\frac{d_0}{c}-\frac{\sin^2\gamma\ \bar{x}^2+\bar{y}^2}{2cR_{r0}}\right) \\ & . \quad \mathcal{P}_s\left(\sin\gamma\frac{\bar{x}}{2R_{r0}}, \frac{1}{\sin\gamma}\frac{\bar{y}}{2R_{r0}}\right). \end{aligned} \tag{3.79}$$

3.3.3 Comparison with Zavorotny's and Picardi's models

Comparison with Zavorotny's model

Expression (3.79) can be compared to the model of [Zavorotny and Voronovich2000], equation 31. We have a 2D surface integral with three terms respectively accounting for the WAF in Doppler, the WAF in delay and σ^o. The two fundamental differences are:

- Sea-state has been included in this formulation through the effective compressed pulse Λ_e. Note however that the sea-elevation PDF is very narrow compared to the pulse and sea-state impact is therefore quite tiny.
- We have not retained the explicit expressions of delay-Doppler mapping but performed second and first order expansions instead. We feel one could obtain the same expression with the full delay-Doppler expressions (not expanded).

Comparison with Picardi's model

Expression (3.79) can be compared to the model of [Picardi *et al.*1998]. The improvements of the proposed approach are:

- correction of a mistake. Compare equation (3.54) to their equation (4). They forgot a $\sin\gamma$ term, thus addressing the monostatic case (iso-range are circles) instead of the bistatic (iso-ranges are ellipses).
- inclusion of the Doppler spreading effect.
- inclusion of the *directional* MSS.

On the other hand, their model includes height distribution skewness.

As a conclusion, we have presented a new model (which we will refer to as the GNSS-R Starlab model) for quasi-specular sea-surface scattering of L-band PRN-encoded signals, in a fully bistatic geometry. As in Zavorotny's model, sea-surface roughness is described by the DMSS. Following Picardi, wave-height impact was also included as a slight modification of Zavorotny's model: an additional input parameter for sea-surface description is SWH. However, due to its 300 m chip length, the C/A code signal is not sensitive to SWH. Consequently,

Zavorotny's model is sufficient in the present study. Nevertheless, the new model could become useful in the future when dealing with P-code: the chip length of 30 m is, in this case, much closer to typical SWH and the latter will become significant.

Chapter 4

GNSS-R Signal Processing

We describe in this Chapter the processing of the GNSS-R data. A step-by-step description is presented from the raw data to the final product to be inverted: the Delay-Doppler Map. The correlation of the raw GNSS signal with a clean PRN replica is the basis of the processing. Due to the transmitter's motion and the possible receiver's motion, the correlation peak is found when the correct Doppler frequency (Doppler center) is inserted into the clean PRN replica.

We provide hereafter the different data product levels, as presented in figure 4.1.

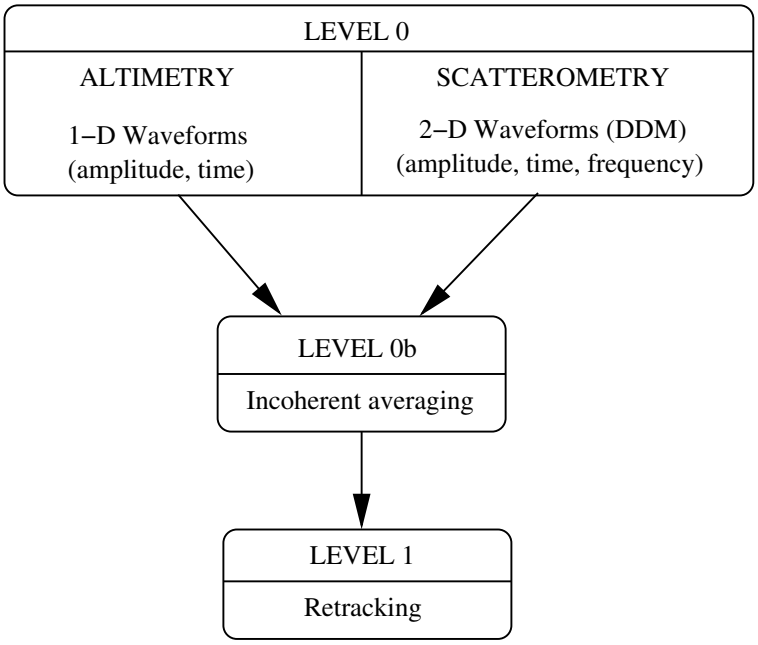

Figure 4.1: Data product levels in GNSS-R processing.

4.1 From raw data to Level 0: Delay-Doppler PRN code despreading

In order to specify our definition of Level 0 data, we take into account that any future GNSS-R payload will be more than a simple antenna front-end: the delay-Doppler PRN code despreading that is presently performed on ground will be actually carried out on board.

Based on this, our Level 0 data will be time series of Delay-Doppler Maps (DDMs) for both direct and reflected GPS signals. This definition is actually CEOS-compliant:

> Unprocessed payload data in chronological order at full space/time resolution with all supplementary information to be used in subsequent processing (e.g., orbital data, health, time conversion, etc.) appended, after removal of all communication artifacts (e.g., synchronization frames, communications headers, duplicate data).

We use the Starlab in-house software (Starlight), implemented in Matlab, to produce DDMs time-series (one per PRN). The general strategy of the processing is to track the delay-Doppler of direct signal and then compute DDMs for both direct and reflected signals. Those DDMs actually represent complex amplitude of incoming signals when processed with a delay-Doppler value slightly different from the estimated delay-Doppler center.

The very high level flowcharts of the processor is presented in figure 4.2. The three basics blocks are:

- the **initialization**: it corresponds to the estimation of the Doppler center and all parameters corrupting the signal extraction (navigation bit, direct-reflected signals synchronization, ...),
- the **tracking**: the correlation process itself,
- the **DDM generator**: the generation of the delay waveforms at different Doppler frequencies around the Doppler center.

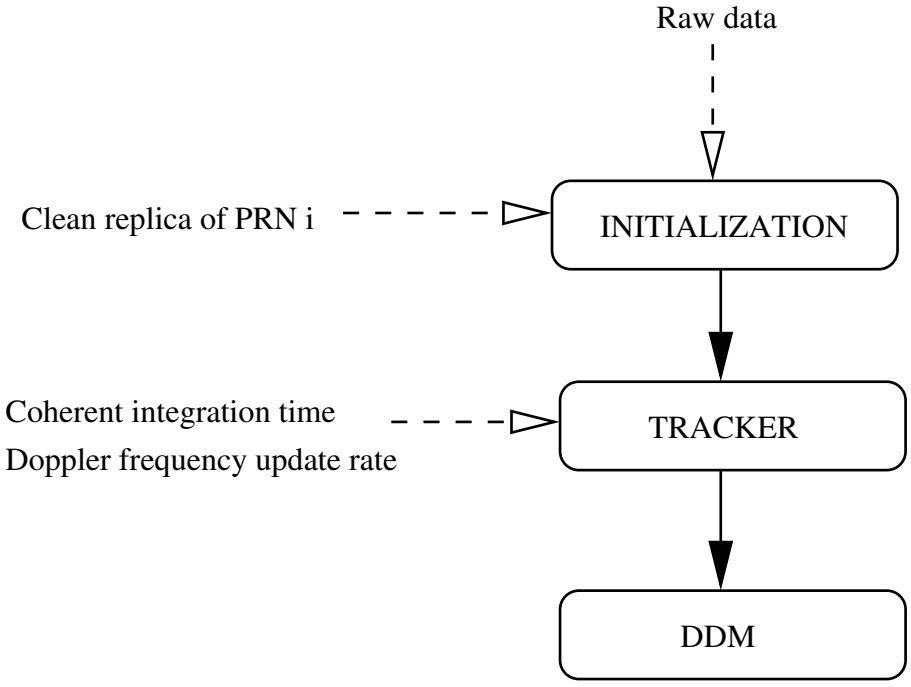

Figure 4.2: The top high level flowchart of the GNSS-R processor for PRN i.

The processor assumes as input data the available GPS signal (I or Q component), at a certain Intermediate Frequency (IF), sampled at a certain rate f_s, and with a two level quantization. Each signal is then represented by a bit stream, in natural-time sequence. As an example, in the case of data coming from the TurboRogue receiver (like those in the ESA GPS-R hardware), the IF is 308 kHz and the sampling frequency is 20.456 MHz.

4.1.1 Initialization

The first module, the *initializer*, pre-processes the data in order to generate an ASCII file containing all the information needed to track both direct and reflected signals (i.e., the second block). The input of this block are the data files, the PRN number and an additional file containing all the parameters that will be used during the processing. It is assumed that the GPS satellites provided to the first block is a visible satellite.

This block is subdivided into four modules applied on the direct signal:

- First Doppler estimation: this module is in charge of finding a first estimation of the Doppler frequency of the PRN under investigation.
- Navigation bit synchronization: taking benefit of the previous outputs, this module finds the position of the navigation bit inside the data stream of the direct signal.
- Fine Doppler estimation: once the position of the navigation bit is known, a series of correlations, uncorrupted by the navigation bit transition, are performed. The output is a new and more precise value of the Doppler frequency of the PRN under examination.

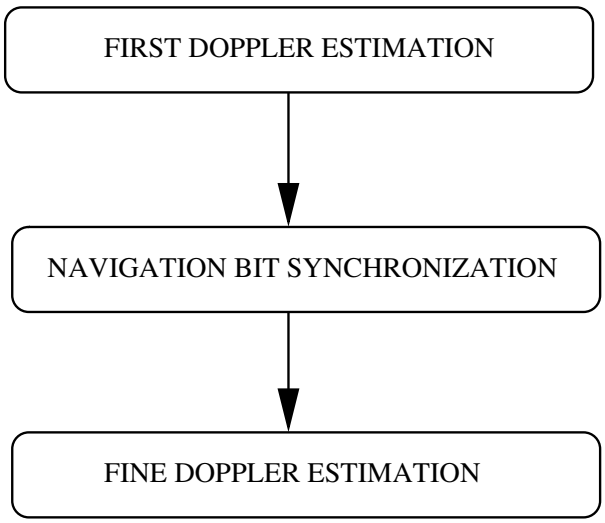

Figure 4.3: Initialization module of the GNSS-R processor.

Let's describe the three parts of this module.

First Doppler estimation

The goal of this module is to find a first estimation of the Doppler frequency for a given PRN and direct signal data file. The algorithm is based on the consideration that correlating the direct signal with a clear replica of the PRN code under investigation, the correlation peak will be higher if the Doppler frequency used to down-convert the signal is closer to the real one. Thus, performing many correlations using different Doppler frequencies—chosen as to span the whole range of possible Doppler for the given situation—the one generating the highest peak or, better said, the best signal-to-noise ratio during the correlations, is assumed to be the actual Doppler.

The number of C/A code periods used for the coherent integration is set to 3. If no satisfying Doppler frequency estimation is found, a second trial is done, using an incoherent averaging of three successive correlations. This procedure allows fast estimation of the Doppler

frequency when dealing with high SNR signals. Of course, the execution time increases, as the number of incoherently averaged waveforms increases. This procedure is robust also with respect to the possibility of finding a navigation bit change in the piece of data analyzed by this module.

This procedure provides a Doppler estimation which is in general within ±40 Hz from the real one. An example of the correlating process output is shown in figure 4.4.

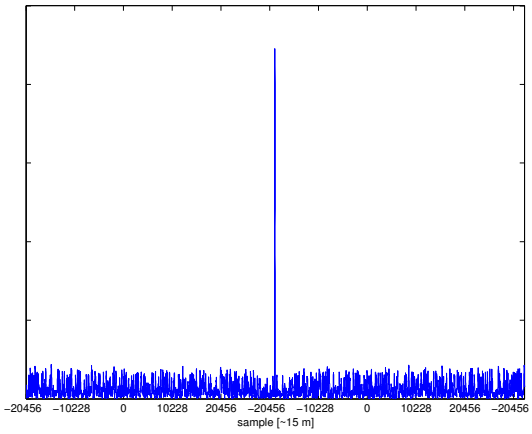

Figure 4.4: An example of correlation peak in arbitrary units, for 5 ms of coherent integration time, using the PRN code number 9.

Navigation Bit Synchronization

The goal of this module is to find the position of the navigation bit inside the direct signal data stream.

We recall that the GPS navigation code represents the actual data provided by each GPS satellite to the users. It consists in a 50 hertz data stream containing all the information necessary to the GPS receiver, such as the ranging signal time of transmission, the satellite's orbital elements, the ranging corrections, status flags, etc... To successfully correlate a received GPS signal with a local replica, the navigation code should be removed.

To understand this method, consider figure 4.5. The top drawing represents the multiplication of two replicas of a PRN code, that is the value of its autocorrelation at lag zero. As we know this value is one. The central drawing represents the multiplication between a PRN code and its replica multiplied by -1. In this case the value of such operation is -1. The last drawing represents the multiplication between a PRN code and its replica after that the second half of this code has been multiplied by -1. The result is now zero.
This third scenario illustrates what happens when the navigation bit transition appears right in the middle of the portion of signal that we are coherently integrating, i.e., correlating with its clear replica. If the transition of the navigation bit occurs somewhere along the code and not in the middle, the maximum absolute value of the correlation will be less than one.

We take advantage of this behavior in order to detect the navigation bit position within the received signal. Let's imagine that we use a 20 ms long replica of a certain C/A code (equal to 20 C/A code periods, that is equal to the duration of one navigation bit). Suppose that we are synchronous with the navigation bit and that we start multiplying the signal and the code replica. Since we are synchronous the value of the multiplication will be maximum.

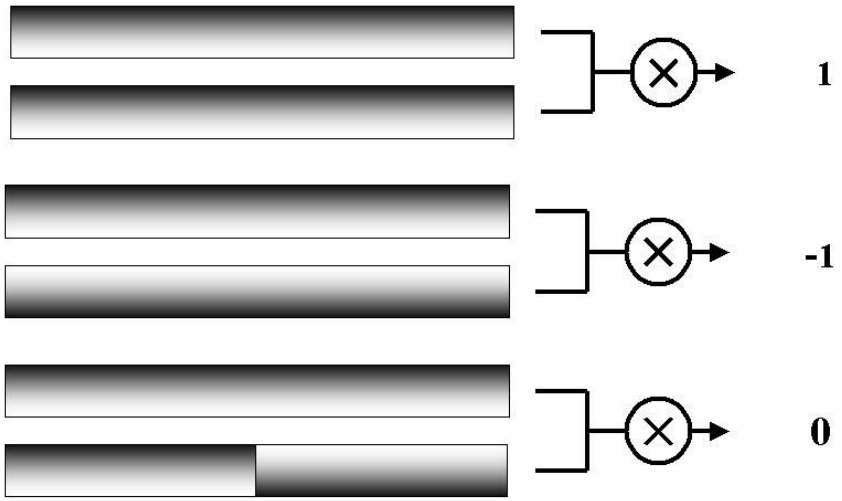

Figure 4.5: Effect of the navigation bit transition on the correlation process.

Now we shift the replica by one period, i.e. 1 ms, and we perform again the multiplication. This time, the replica will have its last C/A code period inside the new navigation bit and this will degrade the multiplication value (if the navigation bit changes). Iterating the process shifting the clear replica of 1 ms each time, when the navigation bit transition reaches the middle of the code, the result of the multiplication between the two signals will reach its minimum value. After that, it will increase again. This process can be repeated so that many estimations of the minimum values of the multiplication of the signal with the replica can be incoherently summed to provide a more reliable estimate. This procedure is shown in figure 4.6.

Once this synchronization with the navigation bit is completed, the coherent integration time can be set to 20 ms without the fear for SNR losses. Of course this process has to be iterated for every PRN code present in the signal. Moreover, since the direct data stream and the reflected one are not synchronized, this procedure has to be done separately for the direct and the reflected signal.

The output of this module is the number of samples to remove from the direct signal bit stream to be synchronized with the navigation bit (and thus with the C/A code) for the PRN under investigation.

Fine Doppler

This module is in charge of providing a better estimation of the Doppler frequency of the signal relative to the PRN code under investigation.

The algorithm is based on the fact that the change in the phase of the correlation peak between two successive correlations (normally very small, say in the order of one tenth of a cycle) should be, on the average, zero. If the Doppler frequency used to down-convert the signal is wrong, the average of the delta phase will be different from zero. The value of this

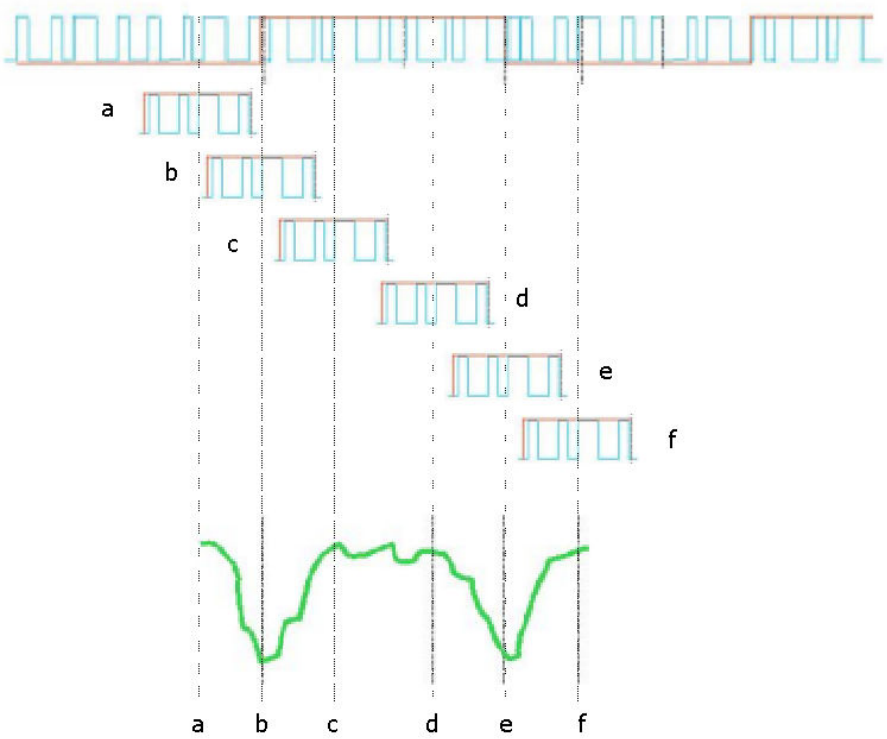

Figure 4.6: Example of the search for the navigation bit synchronism. As the 20 ms long code replica slides on the signal (a, b, c, d, e, f), the value of its product (green curve at the bottom) with the signal (first row) depends on the position of the navigation bit (red) transition within the code replica.

average is directly related to the error in the Doppler by the following equation:

$$\Delta f_{Doppler} = \frac{< \delta phase >}{T_i}, \tag{4.1}$$

with intuitive notation. The precision of this estimation is of the order of one Hertz.

4.1.2 Tracking the 1-D waveforms

The tracking module simply correlates the direct and reflected signals with the clean PRN replica. The waveform is computed through the correlation coefficients. As shown in figure 4.7, two parameters are required in addition to the outputs of the initialization module:

- the **coherent integration time**: it corresponds to the length in number of periods of the replica. Typical values are 1, 2, 5, 10 or 20 ms.
- the **Doppler update rate**: this parameter indicates how often the Doppler frequency is updated while carrying out the correlations along the data stream. Typical values are 0.25 or 0.5 second.

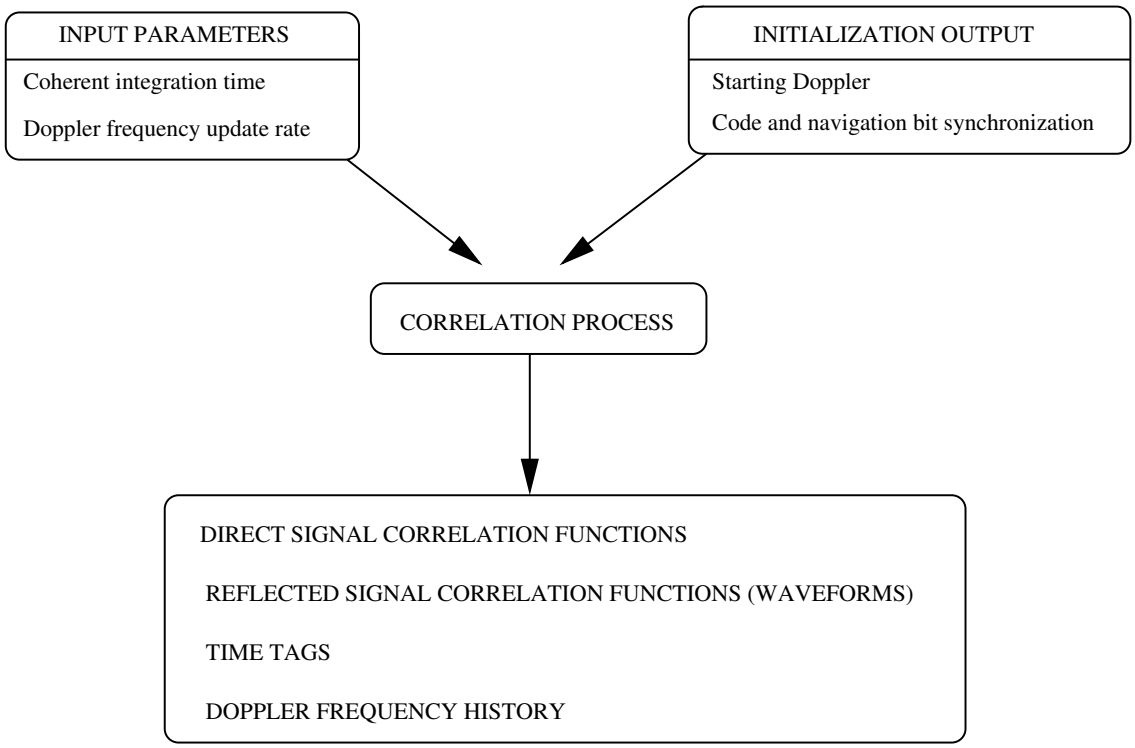

Figure 4.7: Tracking module of the GNSS-R processor.

The correlation process uses Fast Fourier Transforms (FFT). The output of this module are basically the correlation functions of the direct and reflected signal, with a time tag and the Doppler frequency used.

4.1.3 2-D waveforms generation (DDM)

In the case of scatterometric applications, we simply construct the Delay-Doppler Maps through the generation of delay waveforms at different Doppler frequencies around the Doppler

center. Examples of DDMs for both direct and reflected signals are shown in figure 4.8. They correspond to an airborne scenario (see the Eddy Experiment Flight in Chapter 7). The coherent integration time was set to 20 ms to ensure a Doppler resolution of 50 Hz. The delta-delay spans -40 to 40 correlation lags (i.e., +/- 1.95 μs) with a lag step (48.9 ns) and the delta-Doppler spans -200 Hz to 200 Hz with a step of 20 Hz. The DDMs are plotted in amplitude times 10^3.

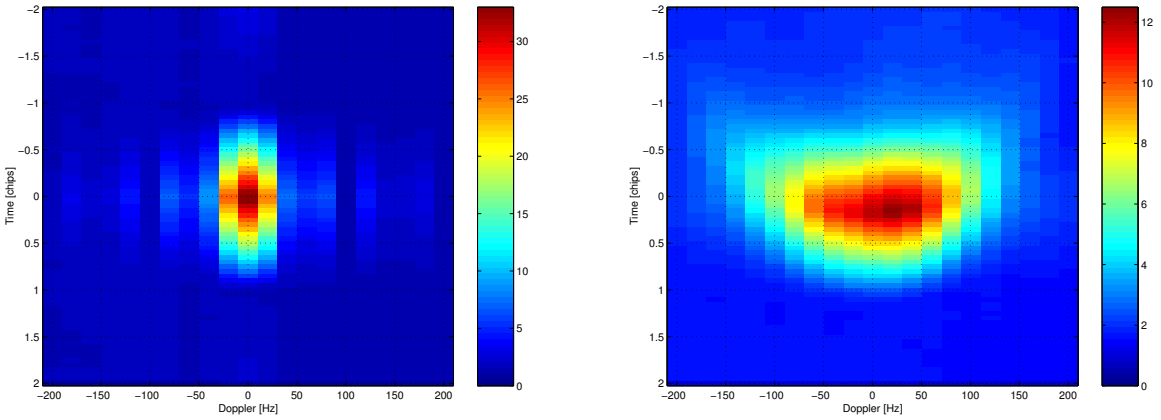

(a) Direct signal DDM

(b) Reflected signal DDM

Figure 4.8: DDM of direct (a) and reflected (b) signals from the Eddy Experiment Flight (PARIS$-\gamma$ ESA Contract). The DDMs are plotted in amplitude times 10^3.

4.2 From Level 0 to Level 0b data: incoherent averaging

The Level 0b data consists in incoherently averaging Level 0 data over a given accumulation time T_a. This process aims at reducing both thermal and speckle noises by a factor of $\sqrt{N}$, N being the number of DDMs. It is however limited by the blurring effect as T_a increases and the required resolution.

4.3 From Level 0b to Level 1 data: retracking

Finally, in order to reach the needed sub-sample accuracy for both altimetric and scatterometric purposes, we rely on the use of the waveform (or correlation function) model developed in section (3.3) of Chapter 3. The natural model for *retracking* of the direct signal waveforms is the mean autocorrelation of the GPS C/A code in presence of additive Gaussian noise, which accounts mainly for the receiver noise. As far as the reflected signal is concerned, the model is not so straightforward. In fact, the reflection process induces modifications on the GNSS signals which depend on sea surface conditions (directional roughness), receiver-emitter-surface kinematics and geometry, and antenna pattern. Among all these quantities, the least known ones are those related to the sea surface conditions. In principle, these quantities should be considered as free parameters in the model for the reflected signal waveform and estimated during the *retracking* process of the waveform.

The crucial step of *retracking* is also known in altimetry by the Radar Altimeter (RA) community. Once a correlation waveform is obtained for both the direct and reflected signals,

the lapses can be estimated. We emphasize that this is not as trivial as considering the maximum sample of each waveform or the waveform centroid, for instance, as the bistatic reflection process deforms severely the signals and, in general, such distortions will displace the waveform maximum or centroid location. Moreover, the sampling rate of 20.456 MHz, while much higher than the Nyquist rate for the C/A code, is equivalent to an inter-sample spacing of 49 ns—about 15 light-meters. This coarseness in the lapse estimation is not sufficient to reach the final altimetric precision target. The main challenge for GNSS-R using the GPS Coarse Acquisition (C/A) code is to provide sub-decimetric altimetry using a 300 m equivalent pulse length, something that can only be achieved by intense averaging with due care of systematic effects. For reference, pulse lengths in monostatic altimeters such as Jason are almost three orders of magnitude shorter.

For these reasons, the temporal position of each waveform (the *delay* parameter) is estimated via a Least Mean Squares model fitting procedure (see [Ruffini *et al.*2003]). The implementation of accurate waveform models (for direct and reflected signals) is fundamental to *retracking*. Conceptually, a *retracking* waveform model allows for the transformation of the reflected waveform to an equivalent direct one (or vice-versa), and a coherent and meaningful comparison of direct and reflected waveforms for the lapse estimation.

The *retracking* is actually necessary for scatterometric purposes, in order to invert correctly the DMSS, as shown in section (9.2) of Chapter 9.

Part II

GNSS-R Signal Simulations

Chapter 5

GNSS-R Simulation Toolkit

In this Chapter, we present a software simulation tool—called GRADAS (GNSS Reflections Artificial Data Synthesiser)—able to produce GNSS-R Artificial Data (AD) [Soulat *et al.*2002a]. We show here simulations of spaceborne data received from a Low Earth Orbit platform (LEO). We consider one GNSS satellite emitting at nadir the C/A code in L_1 and L_2, in prevision of the implementation of C/A code in L_2 in 2003—see section (1.1.3) of Chapter 1.

The inputs of this software are the position and velocity of the receiver (amplitude and direction), and sea-state model parameters (such as significant wave height, wind speed and direction). By Artificial Data, we mean synthetic data in the same format as the data generated by the ESA Sony recorders used in all ESA campaigns, with the extrapolation to the space scenario. A complete description of the ESA material can be found in section (7.1.1) of Chapter 7. Thus, the output is a set of recorded data simulating the 20.456 Mbit/s data streams produced by the Sony recorder as if it was in orbit. The goal of this work is indeed to simulate data which can then be read and processed by the Starlab in-house software, with the goal of assessing retrieval feasibility from space—by extraction of the pseudo ranges and phases.

In order to construct the simulator, many aspects of the problem—most presented in previous Chapters—have to be taken into account:

- Geometry,
- Incoming signal structure (L_1, L_2, PRN codes, navigation message),
- Specular point location,
- Atmospheric effects,
- Ocean model,
- Electromagnetic interaction model,
- Instrumental aspects (down conversion, sampling, recording).

Given the complexity of the task, we will focus not on absolute flexibility or details (all geometries, navigation message, etc). Rather, the goal of this work is to get samples of data for a given scenario with flexibility on ocean modeling: we used a Gaussian ocean surface. We present hereafter two different approaches. The first model developed in the next section is based on the Kirchhoff approximation as the electromagnetic interaction model, where the reflected field is given by the Fresnel integral, as described in section (3.1.1) of Chapter 3. The second one of section (5.2) considers a direct application of the GO approximation to the Kirchhoff theory (see section (3.1.2) of Chapter 3). The two models have been validated through the carrier phase retrieval from our in-house GPS pre-processor.

5.1 Model 1: GRADAS

We first concentrate on ocean simulations for huge areas. A special attention will be paid on the difficulty to simulate ocean surfaces within the First Chip Zone (FCZ) with required resolution (20 cm). Indeed, its radius can reach 17 km for a receiver's altitude of 500 km, which implies tremendous memory and CPU requirements. We propose a democratic sampling of the FCZ.

Section (5.1.2) gives an overview of the structure of the GNSS signal. An expression of the reflected signal is proposed, which determines the basics of the developed algorithm presented in section (5.1.3). This latter section first describes the inputs of the algorithm and the assumptions made and then presents a block diagram which details the different tasks performed by the simulator.

Section (5.1.4) presents two kinds of validations of the proposed algorithm. First, the validity of the ocean surface sampling presented in section (5.1.1) is verified. Then, the quality of the GNSS-R AD is confirmed.

5.1.1 How to simulate the field for large ocean surfaces?

This section concentrates on the generation of sea surface. Before focusing on the synthesis of Artificial Data—meaning basically that we take into account the C/A code—we present in this section our approach to generate ocean surfaces, when the reflected field has to be computed for a large area. This requires for the LEO scenario, a sampling of the area, that we validate with the notion of *minimum representative patch*.

Sea-surface elevations are generated as shown in section (2.1.3) of Chapter 2, and determined by a Gaussian sea spectrum as proposed in [Elfouhaily *et al.*1997]—see section (2.1.2). We recall that the inputs of the spectrum are the wind speed at 10 m above the surface U_{10} (amplitude and direction) and the fetch. The spacecraft is moving over the surface at 7 km/s, say.

The inputs of the implemented code are the size of the sea patch with the required resolution—a resolution of 20 cm has been considered for this study, accordingly to Paris-α analysis (see [Ruffini *et al.*2001b]) on the resolution—and the time increment.

As mentioned above, it is not possible to simulate ocean surfaces over the total first chip zone in a LEO scenario. It represents the points on the surface whose delay with respect to the specular point is less or equal to one chip length τ_{chip}. For a nadir-looking receiver at 500 km and considering the C/A code, this represents a disk of radius 17 km and hence a 85000×85000 matrix. To overcome this problem, it has been suggested in Paris-α, that the scattered field can be computed only from a sample of "small" patches randomly distributed over the FCZ.

Let us now focus on the size of these "small" patches and introduce the notion of *minimum representative patch*. Considering statistical homogeneity of the sea-surface roughness over a relatively large area, we seek for a surface size over which the statistical features of the reflected field are congruent to the average one coming from the whole zone defined by the Woodward Ambiguity Function (WAF). This would enable us to synthesize a big patch with only several sub-patches taken randomly, and thus compute the reflected field with a drastically reduced time.

For this purpose, we focus now on the temporal spectrum of the reflected field that contains most of the information we need. Let F_S be the field reflected by the whole surface S and F_A the field reflected by a sub-surface A of S. Their respective temporal Fourier transforms $\hat{F}_S$

and $\hat{F}_A$ can be described in the discrete domain as:

$$\hat{F}_S = \frac{1}{T}\sum_{j=0}^{T-1} \mathrm{e}^{\left(-ikj\frac{2\pi}{T}\right)} \left(\sum_{p=0}^{N_S-1} I(p,j)\right), \tag{5.1}$$

$$\hat{F}_A = \frac{1}{T}\sum_{j=0}^{T-1} \mathrm{e}^{\left(-ikj\frac{2\pi}{T}\right)} \left(\sum_{p=0}^{N_A-1} I(p,j)\right), \tag{5.2}$$

where $I(p,j)$ is the usual integrand presented below in equation 5.6. The index p indicates the summation over the surface and j the summation over time. N_S (respectively N_A) is the number of discrete elementary scatterers that compose the surface S (respectively A). Under stationary and homogeneous statistical assumptions, the spectrum estimation gives:

$$|\hat{F}_S| = \sqrt{\frac{S}{A}}|\hat{F}_A|. \tag{5.3}$$

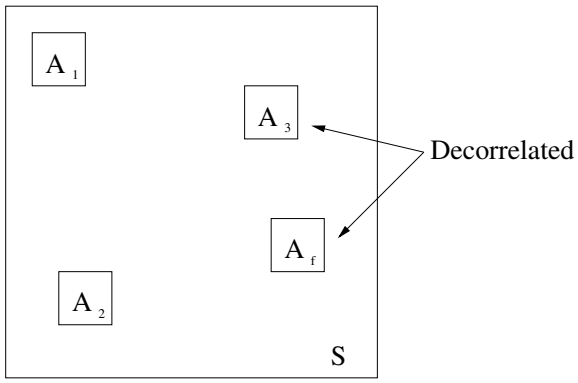

Figure 5.1: Schematic drawing of the *minimum representative patch*.

If we consider now different sub-surfaces A_f of S (see figure 5.1) and making the assumption that the heights distribution is decorrelated from a sub-surface to another, the temporal spectrum of the field reflected by the surface S can be estimated by the incoherent sum of the Fourier transforms of the fields reflected by the sub-patches A_f.

Simulations have been carried out to validate the spectrum estimation presented in equation 5.3. We computed the spectrum of the reflected field for a 2.5 second period (with 2.5 ms of time increment) over a 200×200 m^2 patch (with 20 cm of spatial resolution). The receiver is very high (100 km) at nadir. Figure 5.2 shows the spectrum estimation computed from two sub-patches only, with their centers at 50 meters of the big patch, symmetrically located relative to it. We studied the normalized spectrum—see equation 5.3—for three different sizes of the sub-patches: 12.8 m, 25.6 m and 51.2 m side long. The wind speed is 4 m/s, so that the length of the sub-patches is much longer than the correlation length of the sea (the wind sea peak is corresponding to a 7 m wavelength). We see that the estimation is quite good for the 25.6 m and 51.2 m cases, and a bit worse for the 12.8 m case. From this analysis, we can conclude that the sea surface reflected field is sufficiently homogeneous over the whole area to consider the existence of a *minimum representative patch* that describes the total average reflected field quite well. As anticipated, we also tested the spectrum estimation considering 4 sub-patches (each 25.6 m side) with very good success.

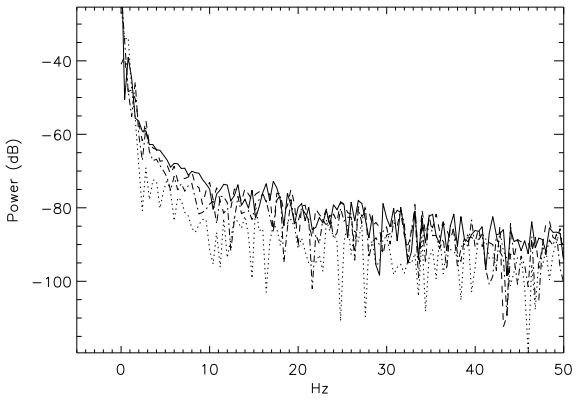

Figure 5.2: Spectrum estimation of the true temporal spectrum of the reflected field over a 200×200 m^2 surface (thick line) with 2 sub-patches only: 12.8 m side (dotted line), 25.6 m side (dashed line), 51.2 m side (dashed dot dot line).

A democratic sample of the first chip zone seems to be a good way to compute the reflected field.

5.1.2 GNSS direct and reflected signals

Direct signal

As described in Chapter 1, the direct GNSS signal is a spherical wave, modulated in phase by a PRN code, that propagates with a carrier frequency f_c. It can be considered as quasi-monochromatic, because the code bandwidth is much less than the carrier frequency.

The direct signal after down-conversion at the receiver, located at $\vec{R_r}$, can be written as:

$$U_d(\vec{R_r}, t) = Code(t)\frac{e^{ikR_d}}{R_d}e^{-i2\pi f_{IF}t}, \tag{5.4}$$

where k is the L_1/L_2 wavenumber, R_d is the distance between the transmitter and the receiver, and f_{IF}=308 kHz is the carrier frequency in base-band (after down-conversion). We consider here $Code(t)$ as the C/A code.

Reflected signal

The GNSS reflected signal is modified by the interaction with the ocean surface. Note that such process has been analyzed and simulated in the scope of [PIPAER2000] and PARIS-α/β ESA projects. We now complete the modeling by introducing the code itself and a large space integration to compute the reflected field.

Let us first introduce some comments about signal Doppler frequency content. We can consider the surface frozen during 1 ms according to the dynamics of the sea elevations for normal conditions. However, a sea-surface sampling of 10 kHz has been chosen to capture the Doppler effect introduced by the receiver's velocity (7 km/s). Let us remind that in the case of the reflected signal, another Doppler frequency is added. An elementary scatterer in $\vec{r}$ at time t, induces a Doppler frequency:

$$f_D(\vec{r}, t) = [\vec{v_t} \cdot \vec{i}(\vec{r}, t) - \vec{v_r} \cdot \vec{s}(\vec{r}, t)]/\lambda + [\vec{q}(\vec{r}, t) \cdot \vec{v}(\vec{r}, t)]/2\pi, \tag{5.5}$$

where $\vec{i}$ is the unit vector of the incident wave, $\vec{s}$ is the unit vector of the scattered wave, $\vec{v_t}$ and $\vec{v_r}$ are the velocities of the transmitter and the receiver respectively, $\vec{r}$ is the position of the scatterer, $\vec{q} = k(\vec{s} - \vec{i})$ is the *scattering vector* (see figure 3.1 in section (3.1.1) of Chapter 3 for vector definitions) and $\vec{v}$ the sea-surface velocity.

If we consider the first chip zone at nadir, the Doppler bandwidth introduced by a satellite moving at 7 km/s at 500 km altitude is 1.2 kHz (without considering transmitter's Doppler). Considering that the maximal orbital velocity for a wave is 10 m/s, this implies a sea-surface induced Doppler of 100 Hz, which is much less than the one introduced by the satellite motion.

Let us now consider $I(\vec{r}, t)$ the Fresnel integrand:

$$I(\vec{r}, t) = \frac{e^{ik(r+s)}}{rs} (\vec{q} \cdot \vec{n}), \tag{5.6}$$

where r and s are the distances transmitter-scatterer and scatterer-receiver respectively. When integrating over the space and considering the carrier already as the baseband pulsation ω_{IF}, we obtain:

$$U_r(\vec{R_r}, t) = \int Code[t - \tau_r(\vec{r}, t)] I(\vec{r}, t) e^{i\omega_{IF} t} dS, \tag{5.7}$$

with $\tau_r(\vec{r}, t)$ the time delay between the receiver and a scatterer at $\vec{r}$ at time t.

It is necessary to sample the code at high rate. If sampled at the chip rate for instance, the code will have a fixed value for any scatterer of the first chip zone, because the range $c\tau_r(\vec{r})$ will be equal or less than the length of one chip $c\tau_{chip}$ (293 m for C/A code), by definition of the FCZ! It is important to notice at this point that at a code sampling rate of 20.456 MHz, the sea elevations do not impact much the location of a code transition within the first chip zone. Indeed, the waves will introduce variations of τ_r of the order of meters, whereas the range resolution is about 15 m at 20.456 MHz. Therefore the delay τ_r will be computed ignoring the sea elevations, that is for a flat surface. As a result, the delay τ_r becomes time independent.

Finally, we have:

$$U_r(\vec{R_r}, t) = e^{i\omega_{IF} t} \times \int Code[t - \tau_r(\vec{r})] I(\vec{r}, t) dS. \tag{5.8}$$

5.1.3 GRADAS algorithm

The GRADAS algorithm implements equation 5.8 with IDL routines, taking into account the patch sampling of the first chip zone and the high sampled C/A code.

Inputs/outputs

The main assumptions are summarized in figure 5.3. There are two kinds of inputs:

- the ocean surface features,
- and the receiver's position and velocity.

The geometry of this scenario is presented in figure 5.4. The receiver is looking at nadir and moving at the speed $\vec{v_r}$ at a fixed altitude. The transmitter is fixed and emitting a spherical wave. Since its altitude is very large, we consider the incoming wave as plane.

The output of this simulator is simply a bit data stream. We generate 0.5 s of data at 20.456 MHz. This data set can be read by the Starlab in-house Starlight processor. Results of the processing of the data are presented in the following section.

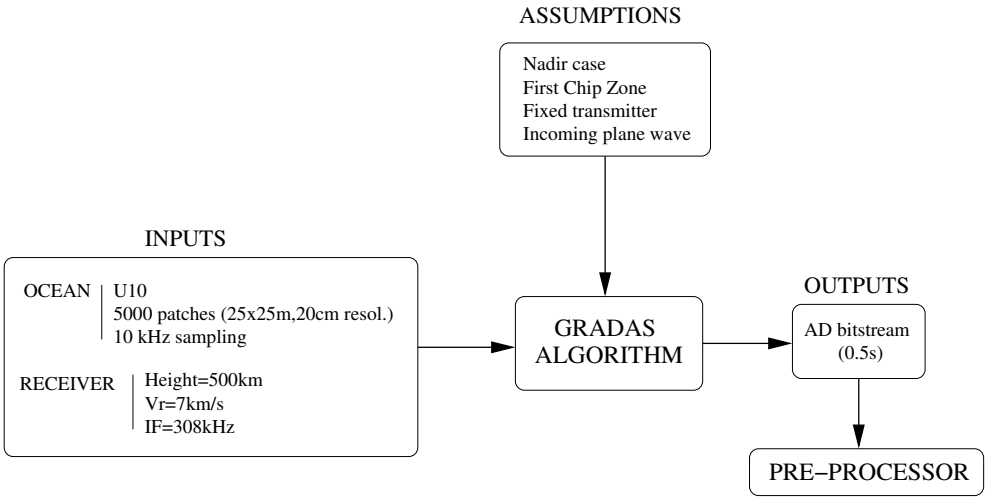

Figure 5.3: Inputs and outputs of the GRADAS simulator.

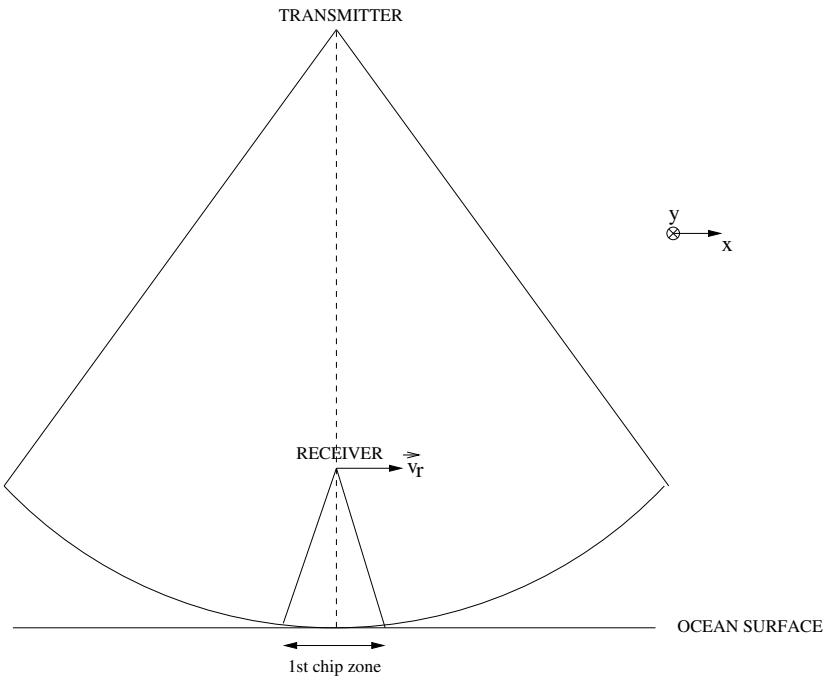

Figure 5.4: LEO geometry for the GRADAS simulator.

From the Fresnel field to Artificial Data

The GRADAS algorithm is described in the block diagram of figure 5.5. After generating a democratic sampling of N patches of the FCZ, the routine is based on two main loops. The first one considers one patch after the other. The second one is over time. The sea elevations are generated with different random phases from one patch to the other.

Let us consider one patch randomly located in the FCZ. As already mentioned, the sampling rate of the reflected field is 10 kHz to capture the Doppler frequency introduced by the receiver speed. Note that the fields are computed at both L_1 and L_2 frequencies. The C/A code sampled at 20.456 MHz is then *inserted* onto the time series of the Fresnel field for that patch. It is important to stress out at this point, that this *insertion* depends on the position of the patch. As we consider for now the first chip zone, it is easy to see that, at a given time, the code can have a maximum of two values within the corresponding area. The 20.456 MHz sampling rate of the C/A code corresponds approximatively to 20 samples per chip (293 m)—i.e., 15 m spatial resolution. That means that the first chip zone can be divided into 20 zones, as shown in figure 5.6. Let us imagine now that a code transition in the GNSS signal is hitting the surface: the zone 1 in figure 5.6 is reached first, because its distance to the transmitter is the smallest one. Then the transition is displaced along the FCZ. For instance, a patch in the zone 2 will *receive* a transition in the code before a patch located in the zone 3 and farther. This is a key point to *insert* the code into the reflected field.

GRADAS is the sum over all the patches of the modulated electromagnetic fields. The base-band frequency is then added to it. The amount of noise to add is determined by the mission scenario, i.e., by the receiver antenna gain which drives the expected SNR of the signal. According to [Lowe1999], a space-borne scenario with a $25dB$ gain antenna would produce a single-sample voltage SNR of 0.0651. Finally, the data stream is the in-phase component of this field, sampled at one bit.

It is important to stress out at this stage the introduction of the *induced* weighting function on the backscattered field due to the GPS receiver processing—the WAF function described in [Zavorotny and Voronovich2000]. This function selects and weights the field in a given area of the FCZ and weights the contribution of each scatterer. The part of the ocean involved in the reflection process is determined by the integration time used for correlations. Therefore, the democratic sampling can be reduced to this area, which clearly saves some computation time.

The computational time is of the order of 4 minutes to compute 0.5 second of the reflected field from one patch. We used 6 computers working in parallel to compute the time series of the fields. Then a routine is dedicated to gather all these data and sum them, as shown in the bottom of the block diagram of figure 5.5.

5.1.4 Validation

The process of validation for the output of this study, as clearly comes out from the previous sections, can be thought as a two step process. The problem of generating an electromagnetic field, backscattered by huge surfaces, was solved with the concept of democratic patching. A first step of validation is therefore needed at this level, in order to verify the validity of such approach. Further, the reflected field is modified so that it simulates the GNSS backscattered signal. Essentially, the presence of a code that modulates the carrier field must be accounted for. The way this modification is carried out must also undergo a validation process. These two kinds of validations are described in the next sections.

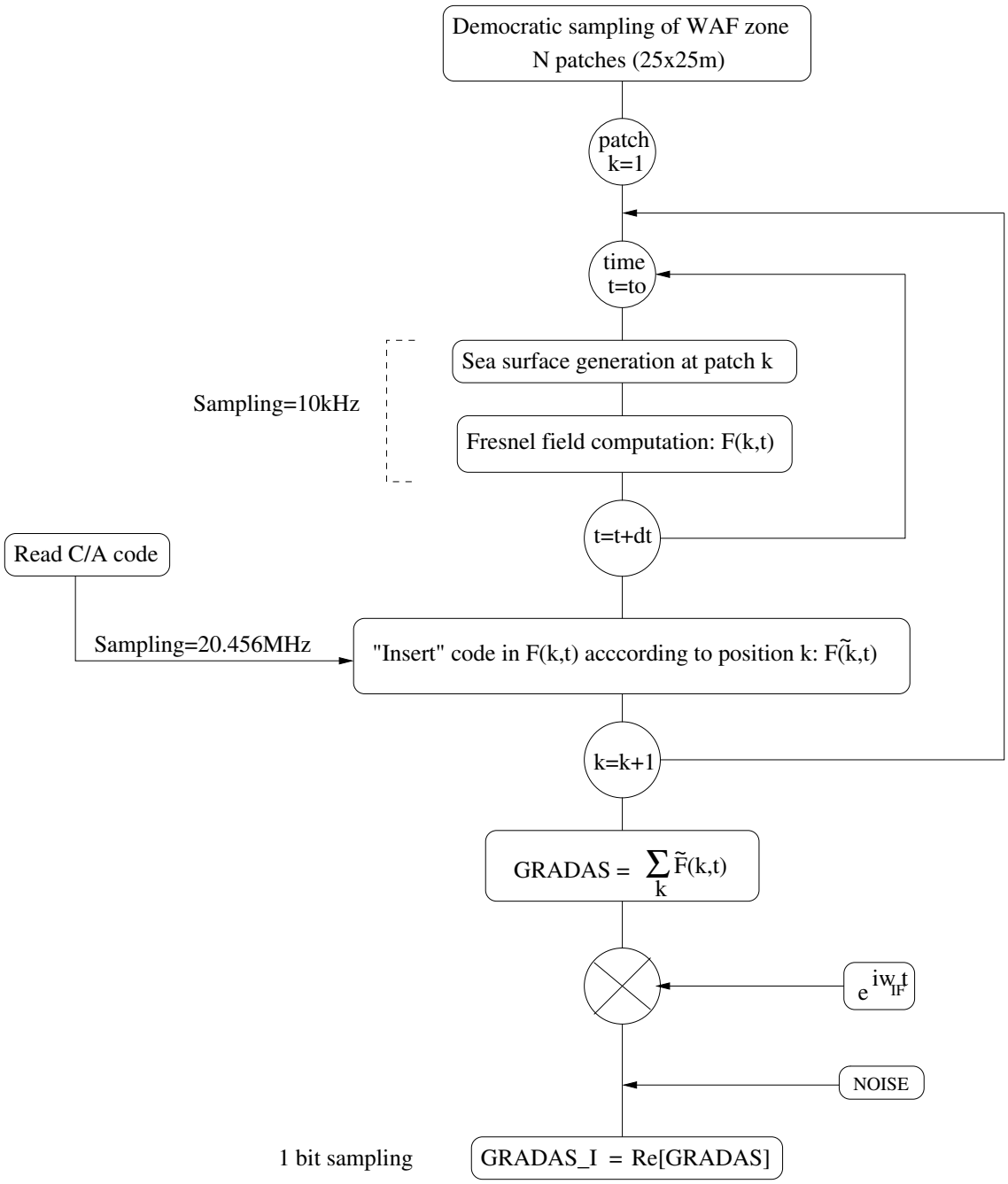

Figure 5.5: GRADAS algorithm.

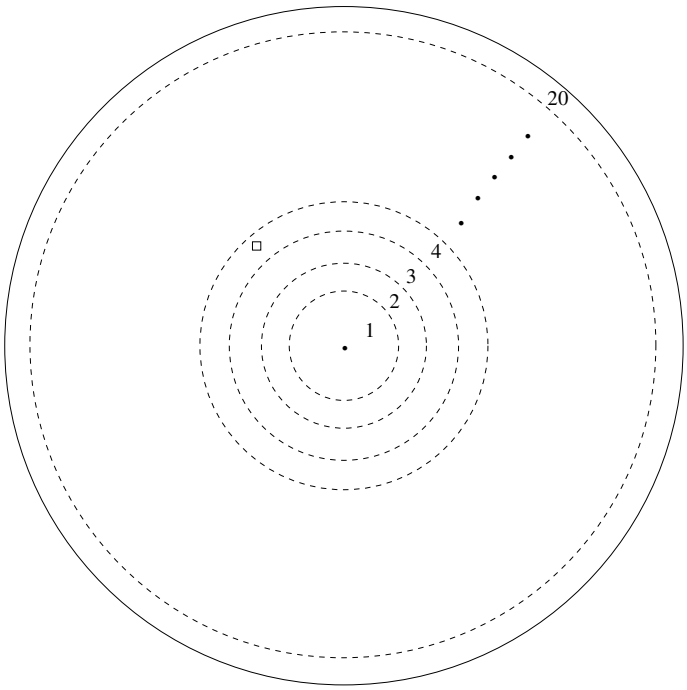

Figure 5.6: First chip zone: the 20.456 MHz sampling rate of the C/A code corresponds approximatively to 20 samples each chip. The first chip zone is divided into 20 rings. We can see an example of a patch (25×25 m^2) located in zone 4.

Reflected field validation

First, this section aims at giving a clear picture of the reflected field without any C/A code modulation. This field is the one compared to the field retrieved by the pre-processor as described below. We would like to understand if the field generated by sampling the FCZ has a physical meaning. What should be the spectrum of the reflected field?

We present in figure 5.7 the phase, the amplitude and the power spectrum of the reflected field from 240 patches (6×400 m^2) democratically located in the 200 Hz Doppler zone of the FCZ. We see clearly, in this 0.5 second evolution, the large Doppler bandwidth, which is theoretically equal to 400 Hz for this Doppler zone. Therefore, the phase behavior for this 10 m/s simulation behaves accordingly to our expectations.

As observed, the spectrum is not continuous and peaks spaced by a fixed frequency of 273.4 Hz are sub-sampling the Fourier transform. These peaks come from the fact that the signal is highly periodic. Let's remind that the receiver motion is simulated by adding a phase term when generating the sea elevations. This trick has the peculiarity to "shift" the surface in such way that after a certain time—function of the receiver speed—the surface comes back to its initial position. This repetition time is 3.6 ms for a receiver speed of 7 km/s, corresponding to the 273.4 Hz spacing frequency. That means that it takes approximately 3.6 ms for a scatterer to enter a 25×25 m^2 patch and to leave it. During that time, the sea waves haven't propagated very much, which gives the periodicity in the field.

To face this issue, we generated rectangular patches, so that the waves propagate in a longer range in order to increase the repetition time. Typically, we used 6×400 m^2 side patches, giving a 17 Hz frequency spacing in the Fourier domain.

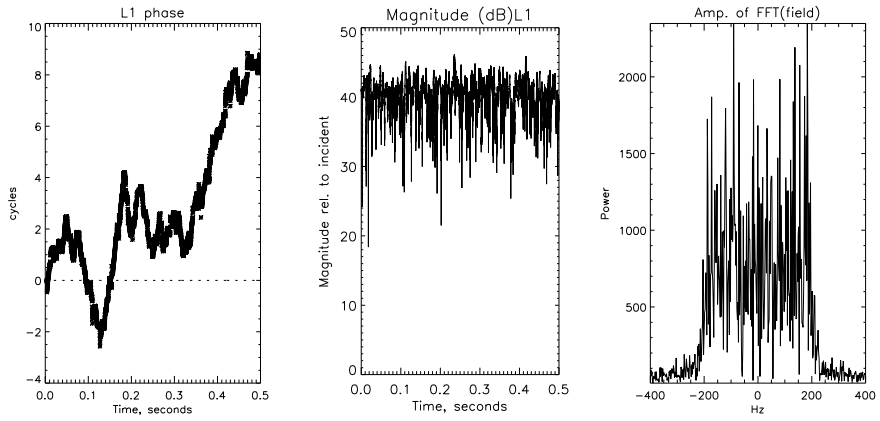

Figure 5.7: From left to right are plotted the phase, the amplitude and the power spectrum of the reflected field from 240 patches (6×400 m^2) democratically located in the 200Hz Doppler zone of the first chip zone. The receiver moves at 7 km/s along the x-axis, its altitude is 500 km. The sampling rate is 10 kHz, 0.5 second evolution, U_{10}=10 m/s.

Pre-processing of GRADAS

The best way to validate the simulated AD is to process them with an *open loop* GPS receiver. This open loop receiver behaves like a normal GPS receiver, using the correlation between the received (simulated, in our case) signal and a replica of the C/A code under investigation. The integration time used to compute the correlations is 20 milliseconds. The C/A code used in these simulations is the PRN number 9.

Figure 5.8 represents a situation with a wind speed U_{10}=10 m/s. On the left-hand side, the red curve represents the phase of the field before *adding* the C/A code and after 20 ms of coherent integration. The black curve represents the phase of the field as tracked by the open loop GPS receiver, with the same integration process to be consistent when comparing the two phases. The tracked phase is obviously very similar to the original one. Clearly in this example, the phase is lost at some points of the curve, due to some fading as shown in the right-hand side. The crosses represent the phase difference between the red and black curves. As observed, it is mainly constant except at the points where the amplitude is low (fadings occurring in the green curve).

5.2 Model 2: Intermittent Screamers

The foundation of this model is a physical understanding of the dominant mechanism in the near specular forward scattering, namely, quasi-specular scattering. Is has been called Intermittent Screamers (IS), since each specular point is considered as source of a time-limited independent tone. This is the result of the observation that GO-like scattering approximation holds for near specular L-band bistatic measurements, as confirmed in the study of section (3.2) of Chapter 3. As expected, the power return in this regime, as demonstrated by previous work during the OPPSCAT project, is dominated by the sea-surface slope statistics. While we assume here that a GO model is appropriate, we take into account the finite size of the specular lobe (in GO this lobe has zero width). The goal here is to produce a signal resembling closely the signals to be received from space within the first chip zone, but without the computational effort required for GRADAS.

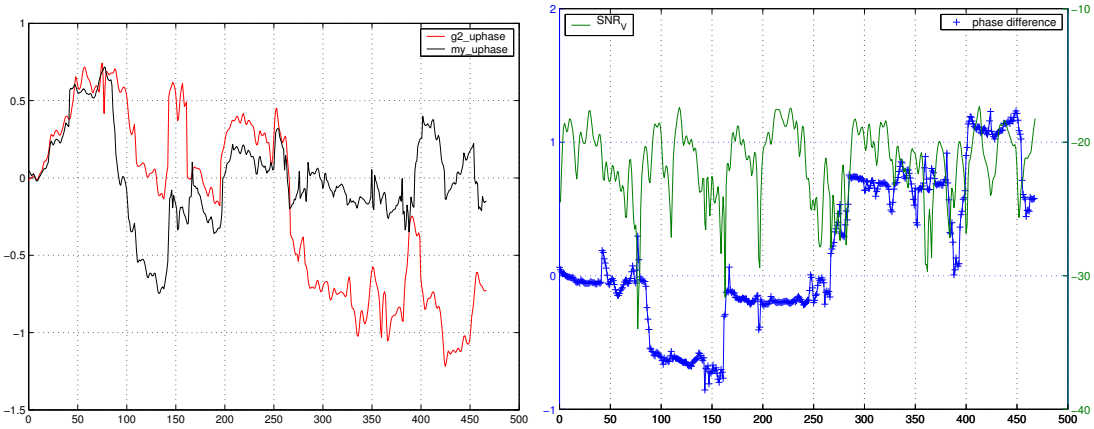

Figure 5.8: The lower line in the left-hand figure, represents the phase of the electromagnetic field generated with the democratic patching of the ocean surface, before C/A code modulation. In this example, 240 patches located in the 200Hz Doppler zone are considered, the receiver is moving at 7 km/s, the wind speed is U_{10}=10 m/s. The red curve is the phase retrieved with the GPS open loop processor. On the right-hand side, the retrieved amplitude is shown with the difference in phase (crosses) between the unwrapped phase. The relation between fadings and the lose of the phase is clearly observed.

The following are our assumptions:

1. The power is dominated by specular reflections.

2. The power from each scattered is characterized by the scatterer *lifetime*, *radius of curvature*, *delay*, *Doppler* and a *random phase*.

3. Under a Gaussian assumption, all necessary parameters can be deduced from an ocean surface elevation spectrum.

We recall that under GO assumption the complex reflected field from one scatterer writes:

$$U_0(p) = \frac{\mathcal{R}_{spec}}{2} \frac{e^{-ik(r_{spec}+s_{spec})}}{r_{spec}s_{spec}} \sqrt{r_x r_y}. \tag{5.9}$$

At this stage we see all the relevant features of the specular field: a random phase related to the Significant Wave Height, and a magnitude related to the effective radius of curvature. In order to produce a sensible simulation we have to be able to generate random draws of these quantities based on an ocean model.

5.2.1 Specular point specifications

We emphasize here the derivation of specular point statistics under the Gaussian assumption, as introduced in section (2.2) of Chapter 2. Our attention is focused on the first chip from space, therefore the mean square slope will only enter in our simulation through the specular point density.

We remind that in [Barrick1968] a previous result by Kodis ([Kodis1966]) is extended to the bistatic case with finite conductivity. It is shown that taking ensemble averages of the surface statistics before or after computation of the Kirchhoff integral in the stationary phase

approximation integral is equivalent. Starting from equation 3.26 of Chapter 3, the radar cross section is expressed in the following—very intuitive—manner:

$$\begin{aligned} \sigma^o &= \pi n \cdot \langle |r_x r_y| \rangle \cdot |\mathcal{R}(\theta_l)|^2 \\ &= \pi \sec^4 \beta \cdot \mathcal{P}_s(s_{xspec}, s_{yspec}) \cdot |\mathcal{R}(\theta_l)|^2. \end{aligned} \tag{5.10}$$

We recall that n is the average number of specular points per unit area, $\langle |r_x r_y| \rangle$ is the average absolute value of the product of the principal radii of curvature at specular point (i.e., the effective area of each scatterer), and θ_l is the local angle of incidence at specular points[1]. The following conditions for validity are stated: i) the radius of curvature everywhere on the surface is much greater than the wavelength so that the tangent plane approximation can be applied, ii) multiple scattering is neglected and iii) $k^2 \sigma_\zeta^2 \cos\theta^2 >> 1$, so that the surface can be considered rough and power can be summed incoherently.

If Gaussian statistics are assumed the result is[2]:

$$\sigma^o = \frac{\sec^4 \beta}{\tan^2 \beta_0} e^{-\frac{\tan^2 \beta}{\tan^2 \beta_0}} |\mathcal{R}(\theta - \beta)|^2. \tag{5.11}$$

We can translate this here to mean that at the specular (β=0):

$$n \cdot \langle |r_x r_y| \rangle = \frac{1}{\tan^2 \beta_0} = \frac{1}{2\sigma_s^2}. \tag{5.12}$$

Recalling Barrick, at β=0, assuming a Gaussian correlation function with correlation length l, we have for an isotropic surface:

$$n = \frac{7.255}{\pi^2 l^2}, \tag{5.13}$$

and

$$\langle |r_x r_y| \rangle = 0.1378\pi \frac{l^2}{\pi^2 \sigma_s^2}. \tag{5.14}$$

For a directional sea, we follow recent developments by [Gardashov2000] helping to simplify a seminal analysis from [Longuet-Higgins1958]. Under Gaussian statistics, the necessary statistical characteristics associated with the joint statistical distribution of the mean and differential curvature of the surface can be simply derived from the 2nd and 4th order sea-surface elevation spectral moments, defined as:

$$m_{pq} = \int \int k_x^p k_y^q S(k_x, k_y) dk_x dk_y. \tag{5.15}$$

For our application, the average number of facets entering a tangent plan approximation will be evaluated by considering a filtered ocean surface. To a good approximation for our purpose, this implies the above expectation to be taken up to a given cutoff wavenumber. Numerically, taking the cutoff to correspond to 60 cm wavelength (3 times the L-band wavelength), the average number of facets and mean radius of curvature can be numerically evaluated.

Under low wind conditions 5 m/s, we find $n \simeq 1.6$ m^{-2} and $\langle |r_x r_y| \rangle \simeq 16$ m^2. Under higher wind conditions 10 m/s, the average curvature remains almost the same and the average number of facets slightly decreases to give $n \simeq 1$ m^{-2}. For comparison, expectations taken up to a cutoff wavenumber corresponding to 5 cm wavelength give $n \simeq 106$ m^{-2} and $\langle |r_x r_y| \rangle \simeq 0.08$ m^2 for the 10 m/s case.

[1] We have: $\cos 2\theta_l = \hat{n}_i \cdot \hat{n}_s$; also $\theta_l = \theta_i - \beta$, where β is the local facet inclination angle—the specular angle.

[2] We recall that $\tan\beta_0 = 2\sigma_\zeta / l$ and that the mean square slope is also related to this quantity, $\sigma_s = \sqrt{2}\sigma_\zeta / l$.

5.2.2 Code implementation

An IDL code has been developed in order to use the above presented GNSS signal ocean reflection model. This relatively simple code is structured as described in figure 5.9. The

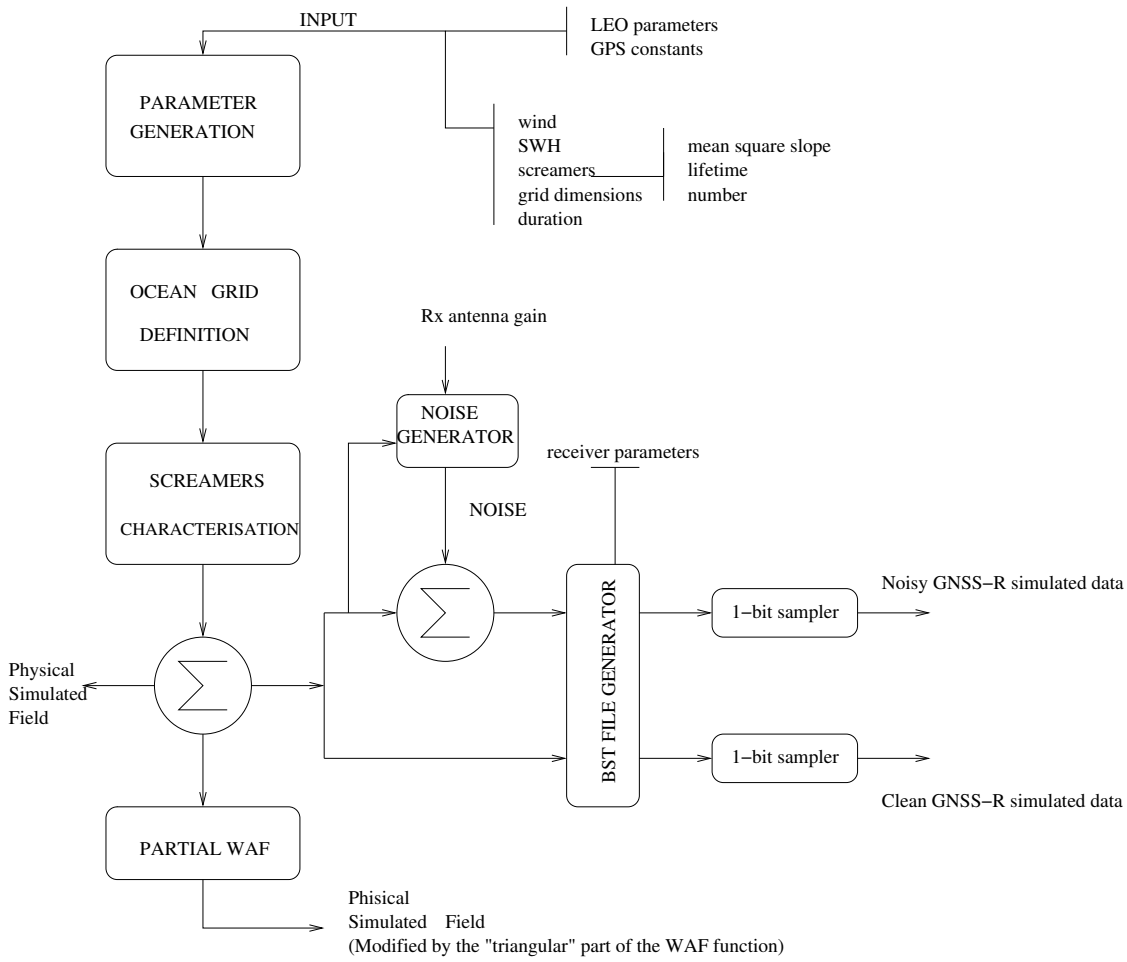

Figure 5.9: Flowchart of the code implementing the IS-model.

input parameters can be divided basically into two different categories:

Signal related inputs	Sea-surface related inputs
GPS signal frequencies	grid dimensions
GPS C/A code	grid resolution
LEO receiver satellite height	wind speed
receiver antenna gain	SWH
simulated signal time duration	number of *screamers*
	screamers lifetime
	surface mean square slope

Essentially, the code generates the grid on the sea surface and throw randomly on this grid the predetermined number of *screamers*, according to the characteristics specified. At each time instant (the sampling frequency is 20.456 MHz), the contribution of all the *screamers* are summed together. The time series of such values is the time series of the simulated electromagnetic field backscattered from the sea surface. This field undergoes two different processes.

One process consists in *adding* to this field the effect of the GPS C/A code and the noise. The amount of noise to add is determined by the mission scenario, i.e., by the receiver antenna gain which drives the expected SNR of the signal. Similarly to the GRADAS simulator, we consider a single-sample voltage SNR of 0.0651. This is the value taken into consideration in our simulations. Scaling properly this value it is easily possible to simulate different scenarios.

Moreover, the simulated electromagnetic field is also spatially weighted by a triangular function (in the domain of time-delay), which emulate the effect of the GPS receiver correlation process, i.e., the delay-depending factor of the WAF. This is done in order to have a field whose phase is comparable to the one retrieved with the GPS processor.

The IS simulator has been implemented also in C++ language to improve its speed. The current version is able to generate one millisecond of GNSS-R data in $15.2 * N$ milliseconds, where N is the number of independent *screamers* considered on the sea surface.

5.2.3 Simulated data and analysis

The GNSS-R synthetic data are fed into an open-loop GPS receiver to track the carrier phase. An example of correlation peak is shown in figure 5.10. The red peak is the (scaled) autocorrelation of the C/A code considered. The blue one is the correlation of the clear C/A code with the simulated reflected signal, i.e., the *waveform*. The result of this open loop processing is the series of the carrier phase values, which is then compared to the phase extracted from the *partial WAF-modified* field (i.e., the simulated physical field after spatial filtering with the *triangular function*).

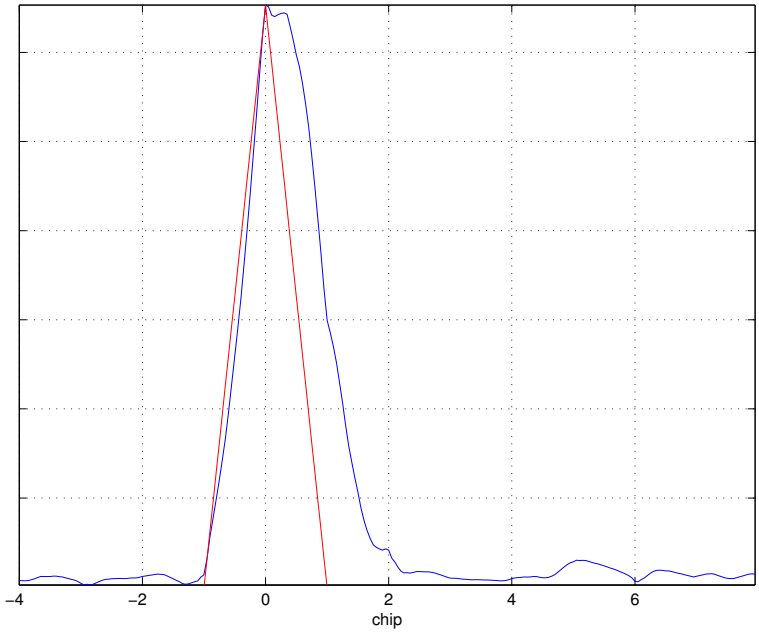

Figure 5.10: The waveform (blue curve) resulting from the correlation between the simulated ocean-reflected GPS data and a clear replica of the corresponding C/A code. In red, for purpose of comparison, the autocorrelation of the same code. The asymmetry of the waveform reflect the extension, in chips units, of the sea surface taken into consideration in the signal generation process. The number of chips is the time-delay unit on the x-axis. On the y-axis, arbitrary units.

Let us now consider a complete simulation process, applied to a well defined scenario. We will consider the PETREL (PARIS Explorer for Tracking and REflectometry in L-band)

scenario. This mission has been proposed to the European Space Agency (ESA) in 2002 by a consortium of European companies, led by Starlab.

The key parameters of this mission to be considered in this case are:

receiving LEO satellite altitude	500 km
receiving antenna gain	25

The other inputs to the simulation are:

grid dimensions	200×200
grid resolution	20 m
wind speed	4 m/s
SWH	31 cm
number of *screamers*	3000
screamers mean lifetime	10 ms
surface mean square slope	0.01
simulated signal time duration	200 ms

The simulated GNSS-R data have been processed using 1 ms of coherence integration time with a subsequent of incoherent integration of 10 ms. The result of the processing of this simulated data are shown in figures number 5.11 and 5.12. It is clear that the phase tracking

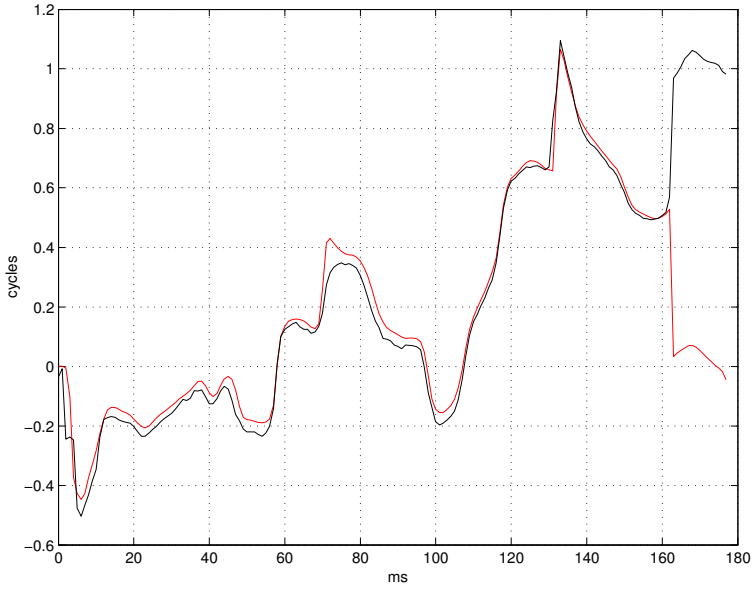

Figure 5.11: The phases as retrieved by the open-loop GPS processor (in black) and the one from the simulated physical field (in red), after the spatial filtering with the *triangular function*. A cycle slip in the tracker can be observed.

in this condition has been successful.

5.3 Conclusions

GRADAS and IS are two related approaches for simulation of reflected data, and we are now able to generate realistic artificial data of GNSS reflected signal at 20.456 MHz as will be gathered from a space-borne receiver. We have used the data to begin optimization of a GNSS-R processor, with the aim of demonstrating, in-silico, code and phase tracking. After

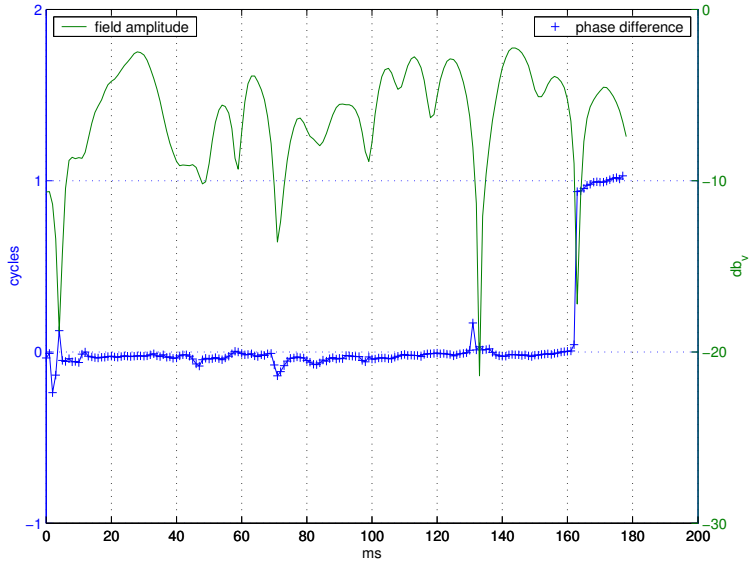

Figure 5.12: The blue curve represents the difference between the retrieved phase and the one of the electromagnetic field. The green curve represents the field amplitude, in dB_v. Clearly, when a fading occurs, the tracking of the phase can fail. In normal conditions the phase is well reconstructed.

processing of GRADAS data, the phase of the reflected signal has been correctly tracked. That is, the virtual experimental loop is closed: generation of a physical field, simulation of reception, sampling, and post-processing to return to the original input. This, at the very least, guarantees consistency of the approach.

An important aspect of this work has been a thorough understanding of the GNSS signal structure and of the mechanism of reflection from the sea surface. This knowledge allows modeling of the involved phenomena to a degree of reality that is enough for producing realistic artificial data but, at the same time, not too detailed to result in an unbearable computational burden.

Of course, the final proof of the concept will come from a real space-borne experiment.

Chapter 6

An Application for Sea State Monitoring

This Chapter provides an application of the GNSS-R simulator developed in Chapter 5. Monte-Carlo simulations have been undertaken in order to infer an empirical inversion law relating sea-surface parameters with statistics of the complex reflected electromagnetic field. These simulations consider GNSS reflections gathered from a coastal platform.

As observed in these simulations, it appears that the reflected field is quite sensitive to sea-surface dynamics, which are modeled by a wind-driven ocean. We see that the dynamics of the variations in phase and amplitude correlate linearly with the sea-state. It is then shown that looking at the statistics of the derivative of the entire field improves the inversion law.

6.1 Simulation specifications

We present simulations of GNSS-R from a coastal platform using the GRADAS simulator—see section (5.1). The incoming signal is assumed to be a plane wave bouncing off a wind-driven sea surface, which is modeled by a 50×50 m^2 patch of Gaussian sea elevations. The surface resolution is set to 20 cm. The receiver is located at 30 meters over one edge of the patch, with the wind blowing in the direction of sight, away from it.

One minute simulations have been undertaken with a time increment of Δt=2.5 ms for different wind speeds, ranging between 1 and 15 m/s. We have considered here the corresponding sea height RMS σ_ζ, or SWH (ranging from 0 to 90 cm). We have focused on the future L_5 GNSS frequency, which synthesizes a 25.5 cm wavelength. The reflected field, computed with the Fresnel integral, can be described as a complex phasor whose amplitude and phase are function of time:

$$F(t) = r(t)e^{i\theta(t)}. \tag{6.1}$$

As seen from a static platform, the field scattering from a frozen ocean could be represented as a static complex phasor. The motion of the ocean surface thus translates into motion of the phasor in the complex plane. We can see such a phasor representation of the reflected electromagnetic field in figure 6.1. The underlying idea is that the analysis of the dynamics of the reflected phasor provides the key to estimating sea-surface parameters from such static platforms.

Let us consider for instance the field at time t_1: $r(t_1)e^{i\theta(t_1)}$ and at $t_2 = t_1 + \Delta t$: $r(t_2)e^{i\theta(t_2)}$. The goal of this study is to understand how high can be the variations in phase from $\theta(t_1)$ to $\theta(t_2)$ and the variations in amplitude from $r(t_1)$ to $r(t_2)$ as a function of the sea-surface

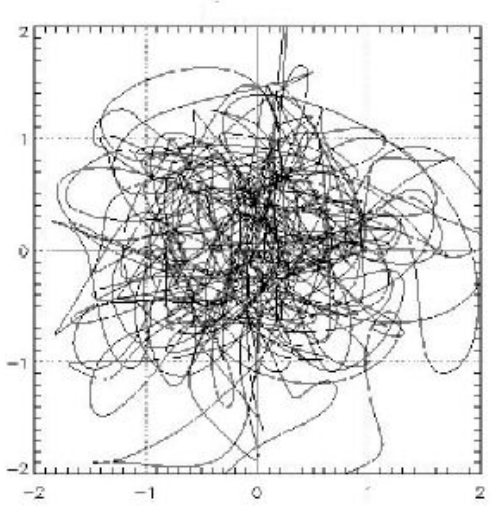

Figure 6.1: The dynamic L-band electromagnetic field in a complex phasor representation produced by a wind-driven ocean model.

elevation RMS. Intuitively, these variations are quite small for a calm sea and increase as waves become big.

Therefore, a focus on the derivatives of both phase and amplitude has been undertaken, respectively $\delta\theta$ and δr with variances $\sigma^2_{\delta\theta}$ and $\sigma^2_{\delta r}$. Then, the derivative of the field is considered.

6.2 Results

6.2.1 Phase analysis

Figure 6.2 presents the standard deviation $\sigma_{\delta\theta}$ of the derivative of the phase in Hz (cycles/Δt) as a function of sea elevation RMS σ_ζ. The jitter in phase is obviously increasing quite linearly with SWH. It spans between 2 Hz and 5.5 Hz when SWH ranges from 0 to 90 cm. However, it appears that the phase variations are not the best way to infer sea-surface features. Indeed high variations in phase occurring when the field magnitude is small has not the same meaning as big excursions in phase occuring on a field of high magnitude. In other words, the phase has less physical content when the magnitude of the field becomes low. Besides, as observed in our simulated time series, the tail of the distribution of $\delta\theta$ is quite high: big cycle slips may appear from time to time. The uncertainty in the estimation of $\sigma_{\delta\theta}$ is thus quite high.

6.2.2 Amplitude analysis

A first analysis has been made on the standard deviation σ_r of the amplitude r as a function of SWH. As observed on figure 6.3, the variance increases quite rapidly with σ_ζ and then saturates. This saturation is reached when σ_ζ is around 6.4 cm (dot dashed line in the figure) which corresponds to a Significant Wave Height of 25.6 cm. This value is similar to the incident wavelength L_5. This would mean that the amplitude of the field stabilizes when the height of the waves becomes greater than the incident wavelength.

A second analysis focused on the standard deviation $\sigma_{\delta r}$ of the time derivative of the amplitude of the reflected field, as shown on figure 6.4. The derivative of the amplitude has

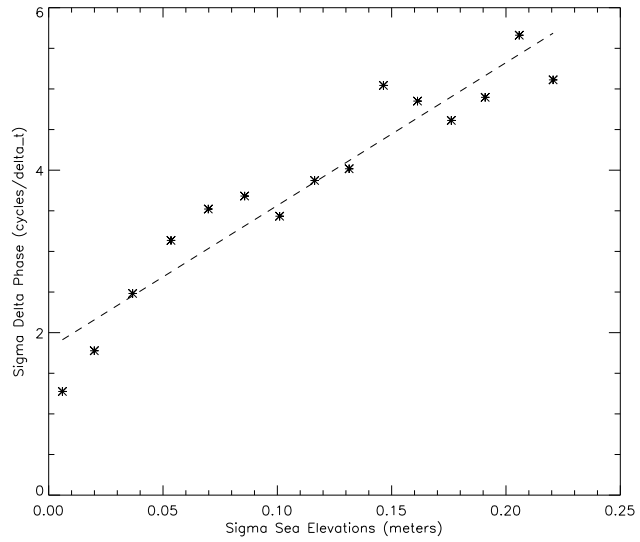

Figure 6.2: Standard deviation of the derivative of the reflected phase ($\sigma_{\delta\theta}$) as a function of sea elevation RMS σ_ζ. L_5, 1 minute simulation.

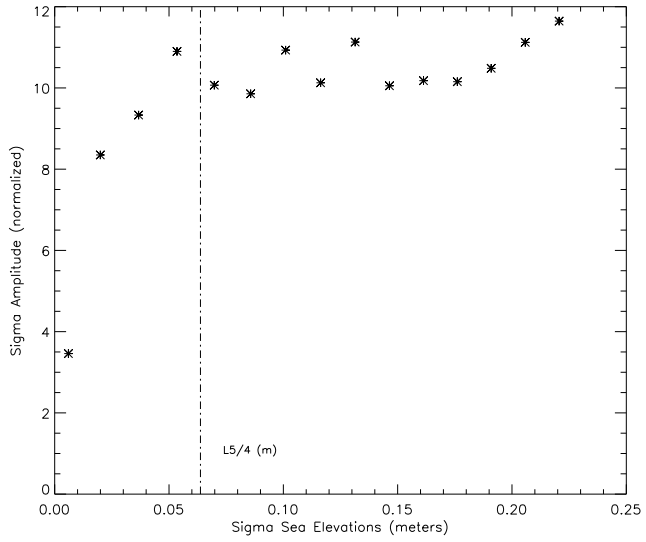

Figure 6.3: Standard deviation of the reflected amplitude (σ_r) as a function of sea elevation RMS σ_ζ. L_5, 1 minute simulation.

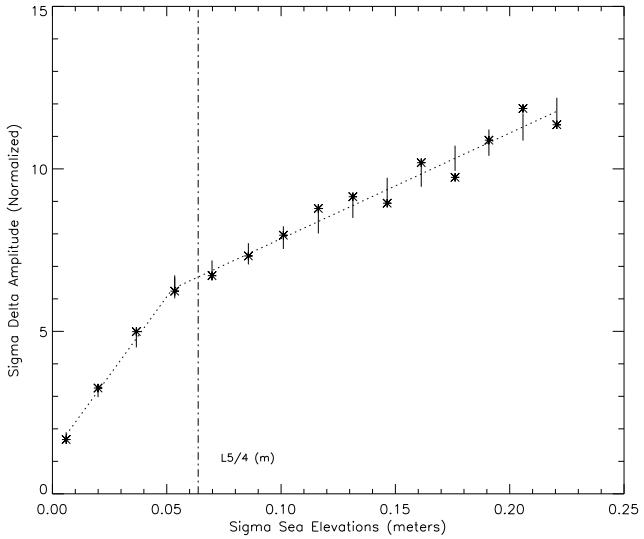

Figure 6.4: Standard deviation of the derivative of the amplitude of the reflected field ($\sigma_{\delta r}$) as a function of sea elevation RMS σ_ζ. L_5, 1 minute simulation, with 4σ error bars.

been normalized as follow:

$$\delta r = H\frac{\delta}{\delta t}(|F - \overline{F}|), \tag{6.2}$$

where $\overline{F}$ is the mean of the reflected field, and H the receiver height.

As observed, two linear regimes can also be distinguished around the critical value SWH=25.6 cm. First, the parameter $\sigma_{\delta r}$ increases rapidly with σ_ζ, whereas the increase becomes a bit slowly in the second regime. On the contrary to the $\sigma_{\delta\theta}$ parameter, $\sigma_{\delta r}$ does not saturate with SWH.

Assuming that the derivative of the amplitude follows a Gaussian distribution, the standard deviation of the estimation $\hat{\sigma}_{\delta r}$ is $\sigma_{\delta r}/\sqrt{2N}$, with N the number of independent measurements. The 1 minute errors bars are plotted on the graph (4σ is represented). As observed, the regression line of the second regime has a slope of 32.51. Then, knowing that one minute simulation gives a maximum incertainty of 0.83 in the estimation of $\sigma_{\delta r}$, we conclude a maximum incertainty in the SWH retrieval of $4 \times 0.83/32.51$=10.2 cm. Naturally, this figure will decrease considerably for longer simulations. For instance, this maximum uncertainty would decrease to 3.2 cm after 10 minutes of simulation.

6.2.3 Field derivative analysis

Let us consider now the derivative of the reflected field, or *speed vector*:

$$\delta F = (\delta r + ir\delta\theta)e^{i\theta}. \tag{6.3}$$

Taking the absolute value of this complex field, we obtain:

$$|\delta F| = \sqrt{\delta r^2 + r^2\delta\theta^2}. \tag{6.4}$$

Intuitively, this parameter depends on the orbital velocities of the sea elevations. It contains both phase and amplitude variations and does not present such rare intense magnitudes, as observed in the phase or amplitude alone. Therefore the uncertainty in SWH retrieval is

improved. Figure 6.5 presents $\sigma_{|\delta F|}$ as a function of σ_ζ. On the left hand side, 1 minute estimations are plotted, together with the linear regression line. On the right hand side, 10 second estimations are added (5 points for each value of σ_ζ). As observed, the parameter $\sigma_{|\delta F|}$ does not saturate with sea-state and follows a linear trend.

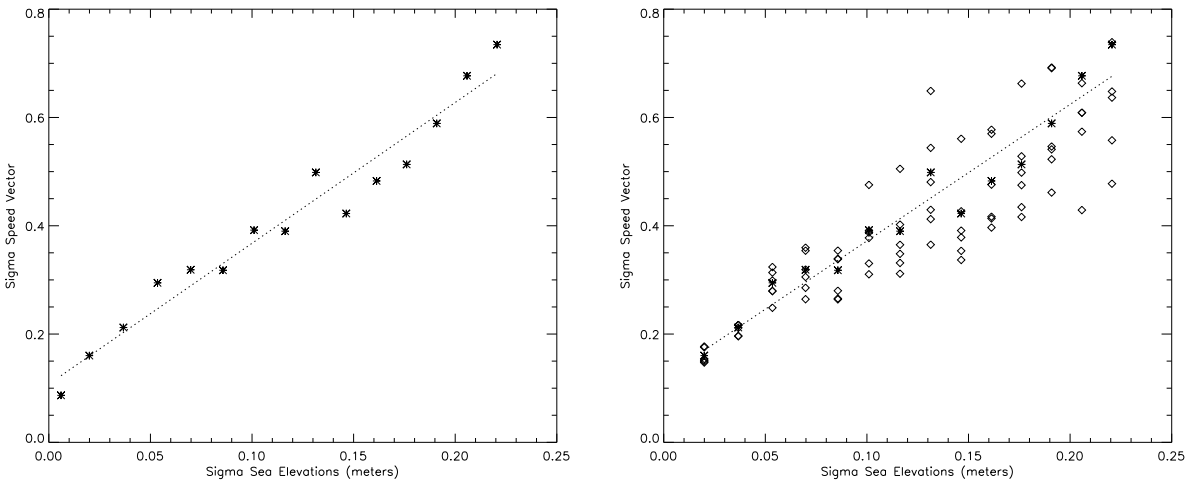

Figure 6.5: *Left*: Standard deviation $\sigma_{|\delta F|}$ of the amplitude of derivative of the reflected field as a function of sea elevation RMS σ_ζ. L_5, 1 minute simulation. *Right*: Same plot with 10 s $\sigma_{|\delta F|}$ estimation (squares).

6.3 Conclusions

We reported coastal simulations as an attempt to derive empirical laws for sea-state estimation. The GRADAS simulator has been used under a coastal scenario. We have analyzed phase, amplitude and derivative of the reflected field as a function of σ_ζ in order to derive inversion curves.

Under the assumption of a wind-driven ocean, several conclusions on SWH/wind speed inversion using the reflected electromagnetic field can be made:

- The analysis of the derivative of the phase provides an inversion law through the sea-elevation RMS parameter.
- The variance of the amplitude saturates rapidly with SWH. However, an analysis of its derivative showed that the $\sigma_{\delta r}$ parameter does not saturate with sea-state and presents two regimes whose separation is determined by the incoming wavelength magnitude. In both regimes, a linear inversion curve is empirically obtained. Under the assumption that this parameter has a Gaussian distribution, we found a maximum incertainty in SWH of 10.2 cm after one minute simulation. However, some rare events of high magnitude may affect considerabely the quality of the estimations and longer times series would allow a better precision.
- The derivative of the field, or the so-called *speed vector*, is a more appropriate parameter to derive SWH. The fluctuations $\sigma_{|\delta F|}$ versus SWH follow a linear trend for the whole range of sea-states expected in a coastal area.

Part III

GNSS-R Airborne Scatterometric Performance Analysis

Chapter 7

The Eddy Experiment Flight

As part of ESA project PARIS-γ (TRP ETP 137.A—Phase 1), an experimental flight was conducted by Starlab on September 27th 2002 along the Catalan coast in order to gather sea-reflected GPS signals. This experiment was carried out in order to demonstrate the possibility of GNSS-R mesoscale mapping of the ocean surface from an airborne platform. The scientific/technological goal was first to demonstrate the capability of mapping a mesoscale phenomenon such as eddies, with decimetric altimetric signatures. We intentionally do not emphasize here the altimetric processing. Rather, the goal of this Chapter is to provide all information required to validate the scatterometric inversions.

We present hereafter the experimental campaign including flight plan, instrumentation and set-up. We report then in section (7.2) the available ground truth as a basis of the validation of DMSS estimations presented in Chapters number 8 (optical) and 9 (L-band).

7.1 Experimental campaign

The experiment consisted in gathering GNSS-R data along a 140 km long track over the sea surface. The aircraft was a Partenavia P-68 Observer, provided by the Catalan Cartographic Institute (ICC). The flight altitude was 1000 m and the nominal airspeed and heading were 50 m/s (180 km/h or 100 knots) and 30^o from North, respectively. The tilt of the plane was required to be less than 15^o in order to maintain the maximum number of collected PRNs without discontinuities (which would endanger Kinematic solution) and avoid phase pattern disturbances.

Figure 7.1 shows the map of the flight trajectory. The track of the plane has been chosen to follow the ascending cycle track 187 of Radar Altimeter (RA) Jason. It is almost parallel to the Catalan coast, but only close enough in the latitude range from 41.5^o to 42.5^o North. During its way, the track crosses the Palamos Canyon, a strong bathymetric feature that affects the surface topography.

Three main ground stations were deployed at Llafranc, Creus and at the Barcelona airport (see figure 7.1). These three temporal GPS ground stations provided additional navigation information to recover the trajectory of the flight in the most accurate way. P1 and P2 are two points along the Jason's track. The P1-P2 distance is roughly 140 km. The total flight duration was 3h 43 mn and the time of acquisition was 2h 54 mn.

A GPS two-buoy system, gathering double frequency 1 Hz observables was also deployed on the Jason's ground-track, under the airplane trajectory. Unfortunately, time series of the sea level could not be obtained from the GPS buoy observables during the whole experiment, since the sea conditions were too strong for buoy deployment (see figure 7.2). However, the

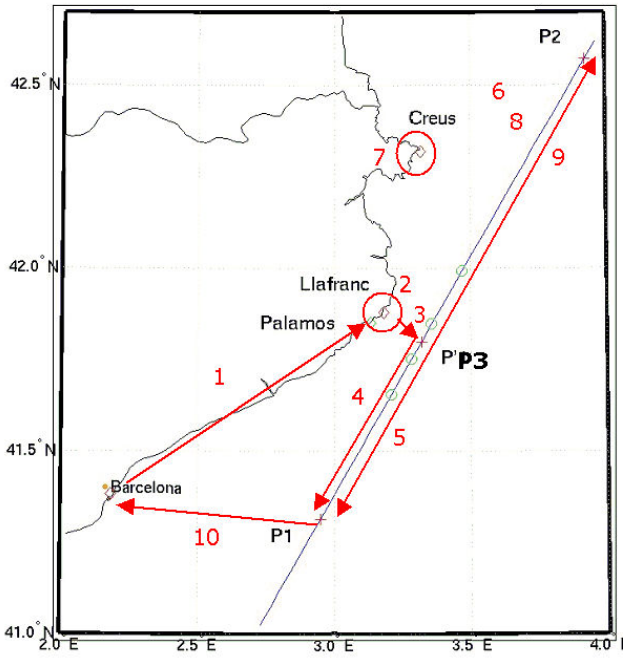

Figure 7.1: Map of the flight trajectory. The blue line shows the Jason's track. The points P1 and P2 mark the experiment boundaries, while the green points indicate the positions of scheduled GPS buoy measurements.

Figure 7.2: Views of the sea surface during the experiment from the air and sea.

first 30 minutes of measurement allowed to find a significant wave height in the middle of the track of around 1.7 m.

7.1.1 Instrumental set-up

The instrument configuration is presented in figure 7.3. Both direct and reflected L_1 signals are collected at high sampling rate. The receivers shared the internal receiver clock.

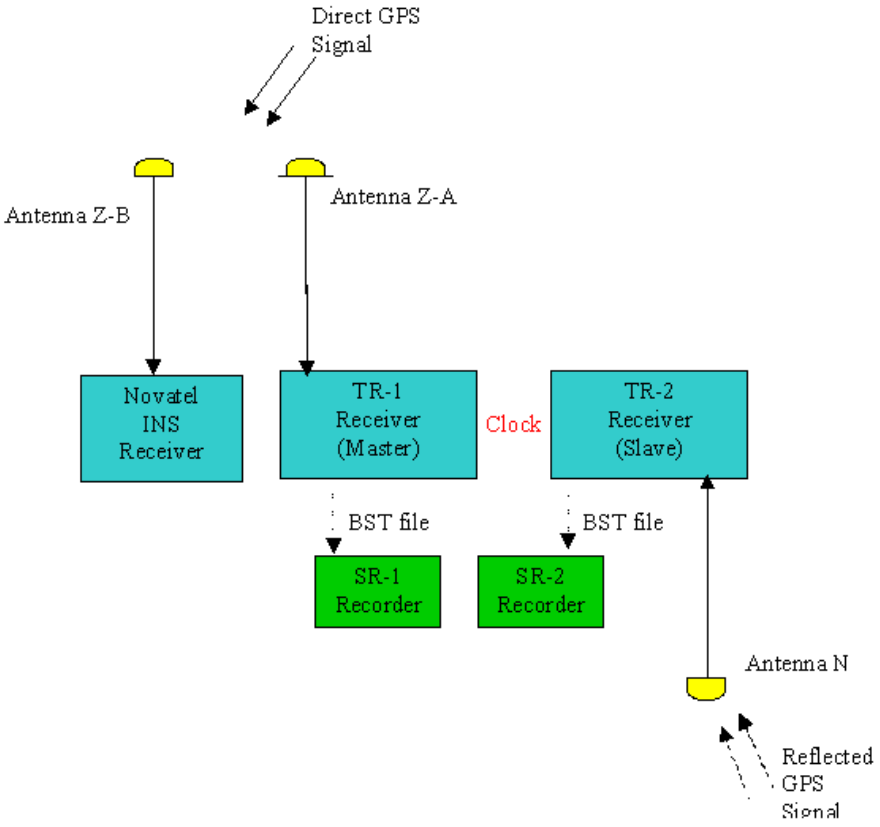

Figure 7.3: Aircraft set-up configuration.

The equipment used during this ESA experiment was lent by the European Space Research and Technology Centre (ESTEC). It is presented in figure 7.4 and includes:

- A LHCP antenna, Allan Osborne Associates (ESTEC/ESA). The antenna is located at the bottom of the plane. It is nadir looking for GNSS-R signal reception.
- A RHCP antenna, Allan Osborne Associates (ESTEC/ESA). The antenna is located at the top of the plane. It is zenith looking for GNSS direct signal reception.
- Two Turbo Rogue receivers (ESTEC/ESA). These commercial receivers have been modified to extract the data from their IF at 20.4 Mbps. They still act as commercial receivers obtaining the GNSS observables. Each of these two receivers were connected to a GNSS antenna (RHCP, LHCP).
- Two SONY recorders (ESTEC/ESA): These recorders can work at 20.456 Mbps using a single channel. Each of them collected data from one Front End of the Turbo Rogue receiver. Before coming into the recorder, the signal passes through a Digital Level Converter (SONY SBS-LC1) in TTL input mode.

We also used the Inertial Navigation System (INS) data provided by ICC. This provides the rate of change of the angular speed of the aircraft in its three components (heading, pitch and roll). This data is needed to precisely position the nadir looking antenna from the zenith looking antenna trajectory.

The PCScan software was used to download the data from tapes to hard disk, where they were automatically saved and named with the extension ".BST" (bit stream). Then, word-by-word byte swapping (used in BST file format) was removed, and the data files were named with the extension ".bit". At this stage, the files contain the received bits, ordered according to their actual time of reception. Those BST files are referred to as raw data. The volume of these files, considering that the signal sampling frequency is 20.456 MHz, is of around 3 GB for 1 minute of data (direct and reflected).

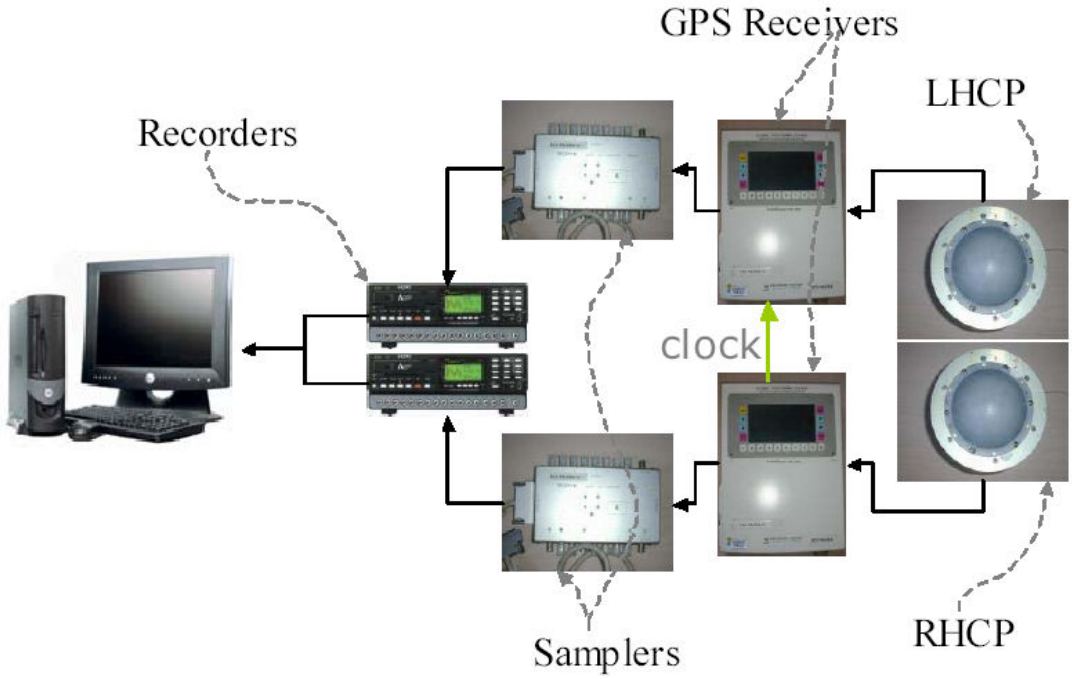

Figure 7.4: ESA equipment used during the Eddy Experiment Flight.

7.1.2 Satellite configuration

The analysis of the data has been carried out on three PRNs, namely PRN number 08, 24 and 27. They are the three highest satellites in view during the flight. Their elevations and azimuths are given in figure 7.5. The plots of figure 7.6 show the delay-Doppler mapping at the beginning and end of the track.

7.2 Ground truth

The ground truth is provided by a numerical model developed by the Spanish National Meteorology Institute (INM), and by Jason's GDR data.

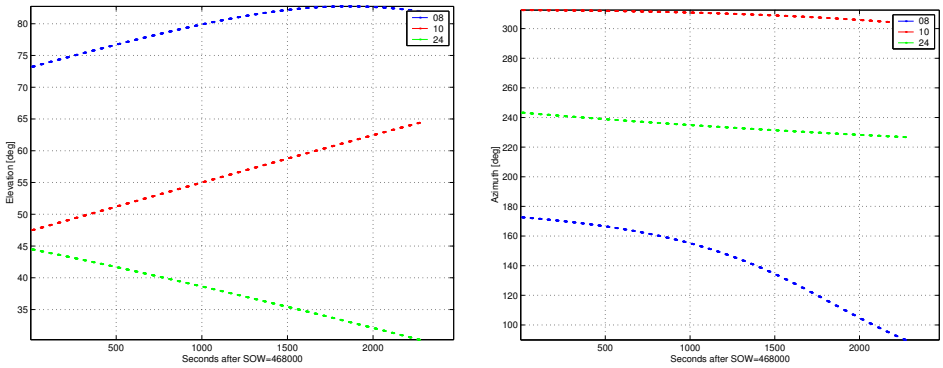

Figure 7.5: Elevation and azimuth of three GPS satellites in view during the experiment.

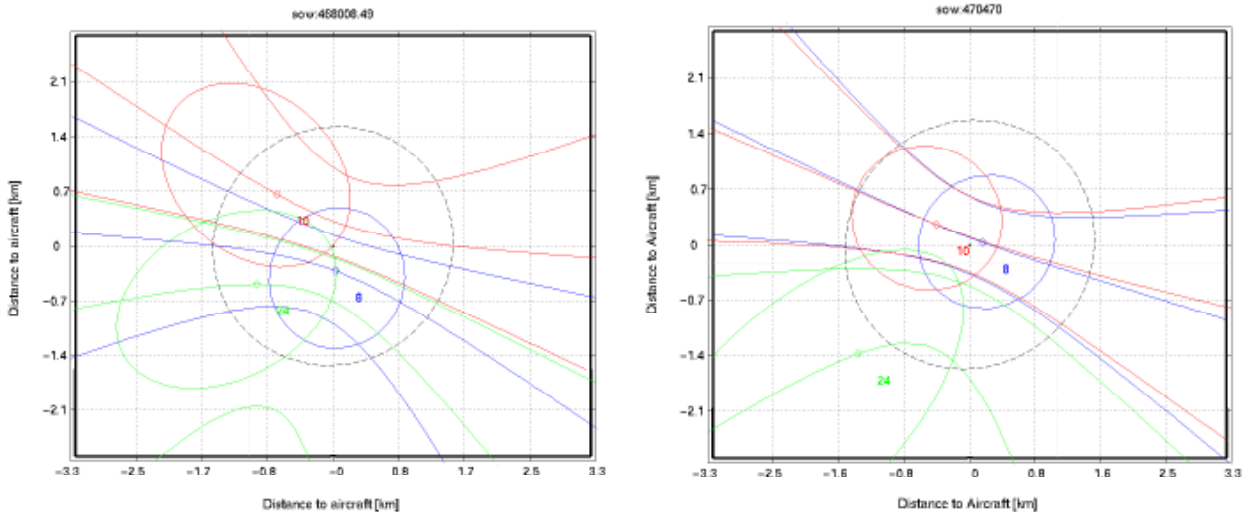

Figure 7.6: Map of the one-chip iso-delays and iso-Dopplers (-100 Hz, 0 and +100 Hz) for PRNs 08 (blue), 10 (red) and 24 (green) at the beginning (*left*) and end (*right*) of the track. The -3dB antenna pattern is also represented in black.

Wind/wave model

Wind vector (speed and direction) provided by INM is shown in figure 7.7(a) and SWH in figure 7.7(b) at 12 UTC of the day of PARIS-γ Experiment. The experiment started at around 10 UTC. Therefore, these graphs give an overall picture of the sea-state during the experiment. The black straight line corresponds to the observation track: it starts at latitude 41.32^o North and ends at latitude 42.58^o North, which fits the top of the graph.

The sea-surface roughness was quite strong during the experiment, which was principally due to a strong wind coming from the Golfe du Lion. As observed along the track, the wind direction represented by the green arrows varies quite significantly from 30^o North to -30^o North approximately. The wind speed varies between 9 and 13 m/s approximately along the considered track. It increases regularly from latitude 41.32^o North to latitude 42.2^o North, and then starts decreasing slowly.

The SWH increases from around 1.5 to 2 meters along the observation track. The green arrows indicate the presence and direction of wind generated waves, meaning that a young sea was observed that day along the track. Developed swell is observed principally South to

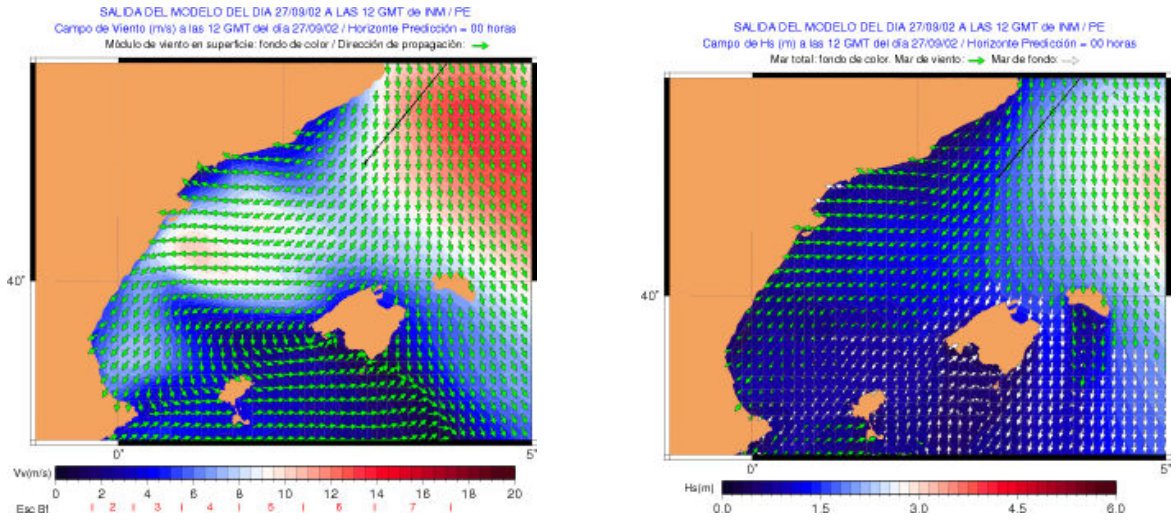

(a) Wind Field

(b) SWH

Figure 7.7: Wind field and SWH at 12 UTC in the observation area (data from INM).

Baleares islands.

Jason's GDR data

The Jason radar altimeter essentially provides the sea-surface height from the elapsed time of the radar pulse, from the satellite to the surface and back. In addition to giving estimate of sea-surface height, it also gives significant wave height from the slope of the leading edge of the return waveform and wind speed over the ocean from the strength of the returned backscattered power. Jason's data are sampled at 1 Hz with an accuracy of 20 km. Figure 7.8 shows the MSS in Ku- and C-bands and wind speed as obtained by Jason the day of the experiment. The SWH is shown in figure 7.9.

The sea-surface slope variance is computed with the backscatter coefficient σ^o, through the relationship:

$$MSS_{Jason} = \frac{\kappa}{\sigma^o}, \tag{7.1}$$

where κ is a proportionality constant; here it includes the Fresnel reflection coefficient, slope statistical description and possible radar calibration offset. In absence of the last two pieces of information κ is set here to 0.64 for both wavelengths, the nominal Fresnel coefficient value.

The wind speed obtained from Jason's GDR data is shown on figure 7.8(b). It is calculated through a relationship with σ^o in Ku-band and the significant wave height using the algorithm developed by [Gourrion *et al.*2002b]. The wind speed model function is evaluated at 10 meters above the sea surface, and is considered to be accurate to 2 m/s. The wind direction is given by an interpolation of the ECMWF model with an accuracy of about 20^o.

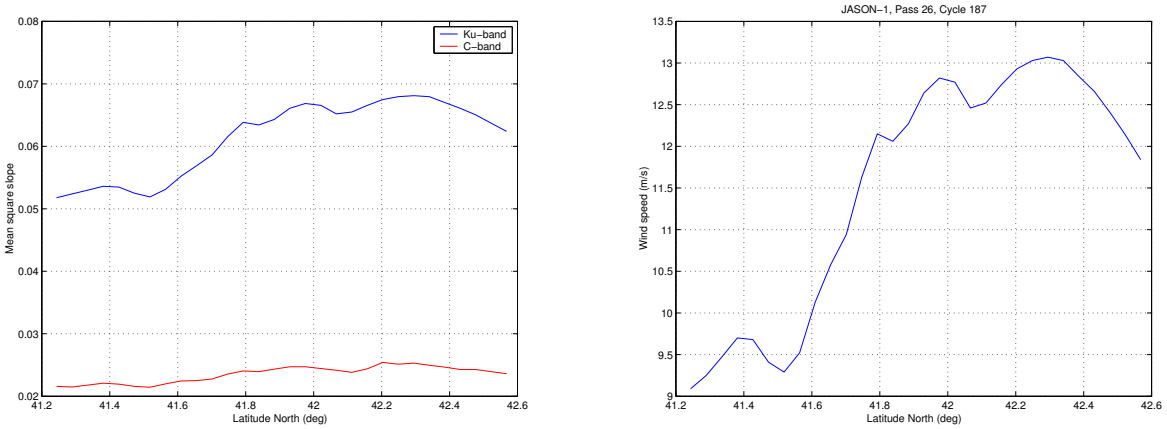

(a) MSS from RA Jason

(b) Wind speed from RA Jason

Figure 7.8: (a) Mean square slope from Jason along the track in both Ku-band (blue curve) and C-band (red curve). (b) Wind speed from Jason along the track.

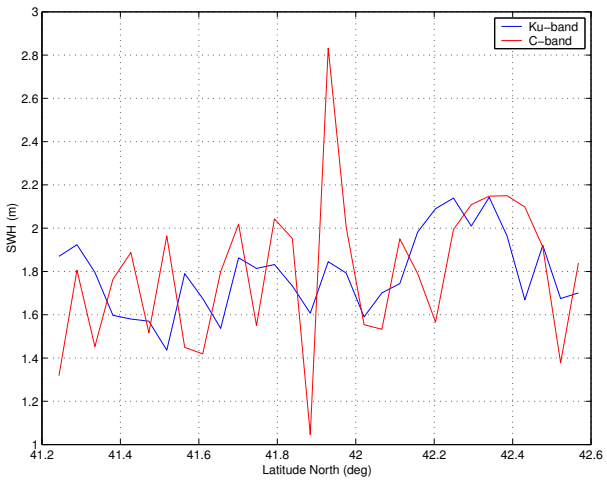

Figure 7.9: The SWH from RA Jason in Ku-band (blue curve) and C-band (red curve).

Chapter 8

Scatterometry with Sunlight

As a complementary remote-sensing instrument, high resolution optical photographs of Sun glitter were taken during the flight, providing the SORES data (SOlar REflectance Speculometer, a Starlab acronym). The goal of this Chapter is to perform Least-Square inversion of these data to obtain optical estimates of directional sea-surface mean square slope. The forward model and inversion technique have been developed within the OPPSCAT II project (see [Soulat *et al.*2002b] and [Soulat *et al.*2003]).

The Chapter begins with the presentation of the data set in section (8.1). The inversion procedure is then reported in section (8.2) including forward model, parameter search and results. A spectral analysis of the images is then undertaken in section (8.3) to enhance the sea surface characterization. We depict in particular the wind induced long waves wavelength, direction and mean square slope. Furthermore, simulations highlight the impact of wave height and wind/wave misalignment on the three parameters of the DMSS. Finally in section (8.4), the results are compared to Cox and Munk's measurements.

8.1 The data set

The photographs were taken from time to time along the track when the roll, pitch and yaw of the plane were low enough. The first photograph was taken at 10:00 UTC. The Jason pass on the area of interest was observed at 9:33 UTC. Therefore, the SORES data were very well co-located in space and time with Jason. The Sun elevation was approximately 45^o during the whole experiment. The plane over-flew the altimeter track both upward and downward.

The camera was a Leica dedicated to aerial photography lent by ICC. Figure 8.1 shows the camera together with the GPS LHCP antenna, both located at the bottom of the plane. An inertial system provides the position and time of each snapshot. Figure 8.2 presents the localization of the snapshots numbered from 35 to 60. The film was a panchromatic Aviphot Pan 80. The focal length is 15.2 cm, and the photographic plate has an area of 23×23 cm^2. The aperture angle is consequently 74.2^o. Given the altitude of the plane, the observed scene is a square with area 1.124×1.124 km^2. The exposure time is fixed at 1/380 and aperture at f/4.

The argentic photographs have been scanned by ICC. The original images are composed of 16128×16128 squared pixels which size is around 260 Mb. Then, the images have been bi-linearly resampled to 400×400 squared pixels, in order to be easily processed. An example of SORES raw data is shown in top of figure 8.3.

Note that the roughness of the sea surface being quite strong during the experiment, breaking events and foam occur on many pictures (see bottom of figure 8.3). They have not

Figure 8.1: High resolution camera and GPS LHCP antenna located at the bottom of the plane.

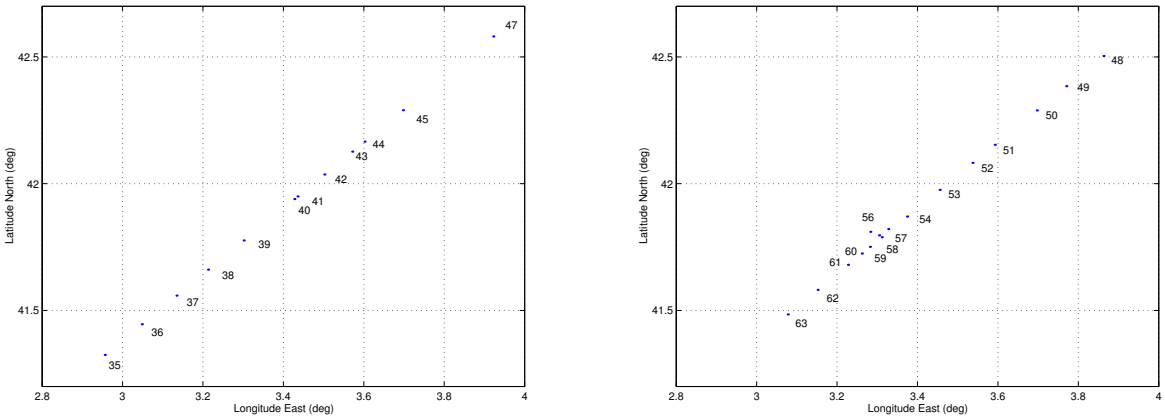

(a) Ascending track

(b) Descending track

Figure 8.2: Localization of the snapshots along the track of the plane. Each photograph is labeled by a number ranging from 35 to 63.

been corrected for the sea-surface slope variance estimation presented in this study.

8.2 Inversion procedure

8.2.1 The directional mean square slope

To date, and as systematically referenced when modeling the sea-surface slope statistics, results derived from the glitter-pattern of reflected sunlight as photographed by Cox and Munk in 1951 [Cox and Munk1954] remain the most reliable direct measurements of wind-dependent slope statistics. We do not propose here the slope distribution as in section (2.2.2) of Chapter 2, but consider higher order terms. Based on Cox and Munk analysis, we fit the logarithm of sea-surface slope probability density function $\mathcal{P}_s$:

$$\begin{aligned} \log(\mathcal{P}_s) &= a_o - a'_o s^2 + a''_o s^4 + s(a_1 - a'_1 s^2)\cos\alpha' \\ &\quad + s^2(a_2 + a'_2 s^2)\cos 2\alpha' + a_3 s^3 \cos 3\alpha' + a_4 s^4 \cos 4\alpha'. \end{aligned} \tag{8.1}$$

The slope $s = \tan\beta$ is defined as the tangent of the tilt of steepest ascent of each sea-surface facet, $\alpha' = \alpha - \alpha_o$ is the azimuthal angle of the facet according to the principal axis α_o, which is the direction of highest MSS encountered in the 2-D probability density function. See figure 8.4 for the definition of these two angles. The fit coefficients a_n^m have then been related to the expansion coefficients pertaining the cumulants of the slope distribution under a Gram-Charlier approximation. Note that a_o in equation 8.1 is an arbitrary offset due to the inability to fully resolve the steepest angles.

The model is simplified in this analysis by removing the first and third order moments and the directionality in the fourth moment. Only part of the glitter pattern could be actually observed given the quite low Sun elevation. The skewness parameter would thus not be observable. Equation 8.1 simplifies to:

$$\log(\mathcal{P}_s) = a_o + [-a'_o + a_2\cos(2(\alpha - \alpha_o))]s^2 + a''_o s^4. \tag{8.2}$$

The slope vector is defined in the frame (X,Y,Z) shown in figure 8.4 with the components:

$$\begin{cases} s_x &= \sin\alpha\tan\beta \\ s_y &= \cos\alpha\tan\beta \end{cases} \tag{8.3}$$

In the (s_x,s_y) frame, the sea-surface slope PDF writes:

$$\begin{aligned} \mathcal{P}_s(s_x, s_y) &= \exp[a_o - (a'_o + a_2\cos 2\alpha_o)s_x^2 \\ &\quad -(a'_o - a_2\cos 2\alpha_o)s_y^2 \\ &\quad +(2a_2\sin 2\alpha_o)s_x s_y \\ &\quad +a''_o(2s_x^2 s_y^2 + s_x^4 + s_y^4)]. \end{aligned} \tag{8.4}$$

There are four parameters of interest and one scaling factor:

- a_o is the normalization parameter,
- a'_o is the inverse overall MSS,
- a_2 addresses the anisotropy of the slope PDF,
- a''_o is for the fourth order moment,

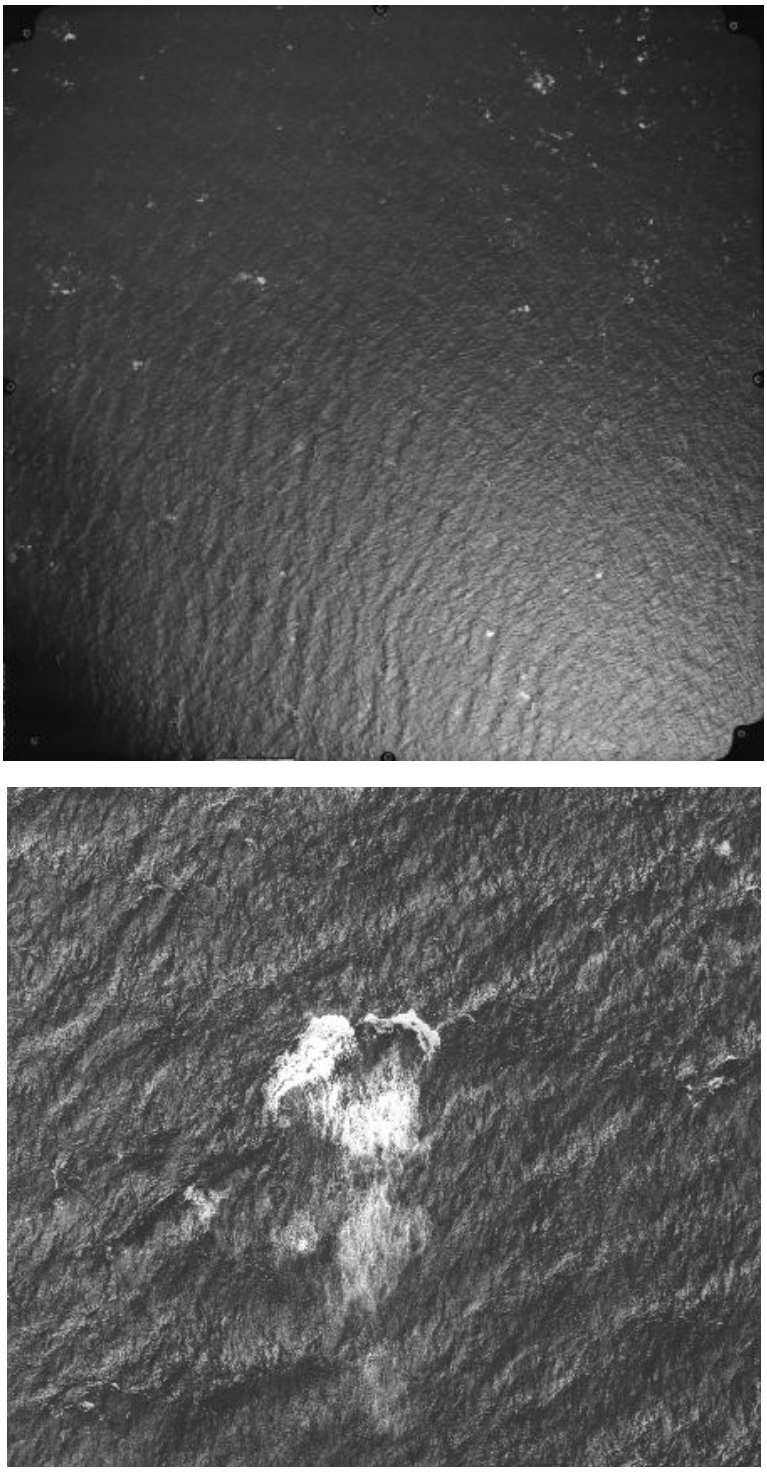

Figure 8.3: **Top**: Example of SORES raw data (photograph 47). **Bottom**: Example of breaking event observed during the experiment.

- α_o provides the direction of steepest encountered MSS relative to the Sun azimuth. This direction is then corrected and given with respect to the North.

Given the three mentioned parameters a'_o, a_2 and α_o, we investigate in this section:

- the **up-wind MSS**: $\sigma_u^2 = \frac{1}{2(a'_o - a_2)}$, which is the higher MSS encountered in the 2-D PDF,
- the **Slope PDF Isotropy**: SPI $= \frac{\sigma_c^2}{\sigma_u^2} = \frac{a'_o - a_2}{a'_o + a_2}$,
- the **Slope PDF Azimuth** (SPA): defined as the direction of the up-wind MSS, simply given by α_o minus the Sun azimuth (the azimuth angles of the TAM are referenced with respect to the Sun azimuth, as presented below). There is however an ambiguity of 180^o in this direction. The direction of the up-wind MSS is expected to be pretty close to the wind direction.

Note that the Total MSS is related to the up-wind and cross-wind MSS by:

$$\text{Total MSS} = 2\sqrt{\sigma_c^2 \cdot \sigma_u^2}. \tag{8.5}$$

The term a''_o gives information on the departure from the Gaussianity of the PDF. We will analyze this fourth order moment through the parameter b''_o (used to remain consistent with Cox and Munk's nomenclature):

$$b''_o = \frac{a''_o}{a'^2_o}. \tag{8.6}$$

According to their results, this parameter is not negligible and almost wind independent. For clean sea surface measurements, the suggested constant value is 0.04.

8.2.2 Forward model

A short overview of the mechanisms involved in the relation between the sea-surface slope PDF and the photograph intensity are summarized in this section. We first present how the sea-surface slope distribution and sea-surface radiance are related. Then, from the instrument point of view, we relate the sea-surface radiance to the pixel intensity. The geometry of the experiment is given in figure 8.4. This development is based on the gridding of the sea surface with cells of required tilts β and azimuths α: the Tilt-Azimuth Map (TAM).

Geometry of the experiment

Hereafter is presented the geometry of the sea surface reflection in figure 8.4, as considered by Cox and Munk. The incident ray is in the plane (Y, Z), makes an angle ϕ with (X, Y), and forms an image on the vertical photographic plate. The angle between the incident ray and the reflected one is 2ω. The points $ABCD$ define a horizontal plane through A and $AB'C'D'$ the plane tangent to the sea surface. The tilt β is measured in the direction AC of steepest descent, and this direction makes an angle α clockwise from the Sun. OO' is parallel to the Z-axis and the plane of the photographic plate is parallel to (X, Z). The unit vectors $\hat{n}$, $\hat{i}$ and $\hat{r}$, respectively normal to the surface, along the incident ray and along the reflected ray, can be expressed as:

$$\begin{aligned} \hat{n} &= (-\sin\alpha\sin\beta, -\cos\alpha\sin\beta, \cos\beta) \\ \hat{i} &= (0, -\cos\phi, -\sin\phi) \\ \hat{r} &= (-\sin\nu\sin\mu, -cos\nu\sin\mu, \cos\mu). \end{aligned} \tag{8.7}$$

According to the law of reflection, these vectors follow:

$$\hat{r} - \hat{i} = (2\cos\omega)\hat{n}. \tag{8.8}$$

We can deduce:

$$\cos\mu = 2\cos\beta\cos\omega - \sin\phi, \tag{8.9}$$

and

$$\tan\nu^{-1} = \frac{1}{\tan\alpha} - \frac{\cos\phi}{2\sin\alpha\sin\beta\cos\omega}, \tag{8.10}$$

with:

$$\cos\omega = \hat{n}.\hat{r} = -\hat{n}.\hat{i} = \cos\beta\sin\phi - \cos\alpha\sin\beta\cos\phi. \tag{8.11}$$

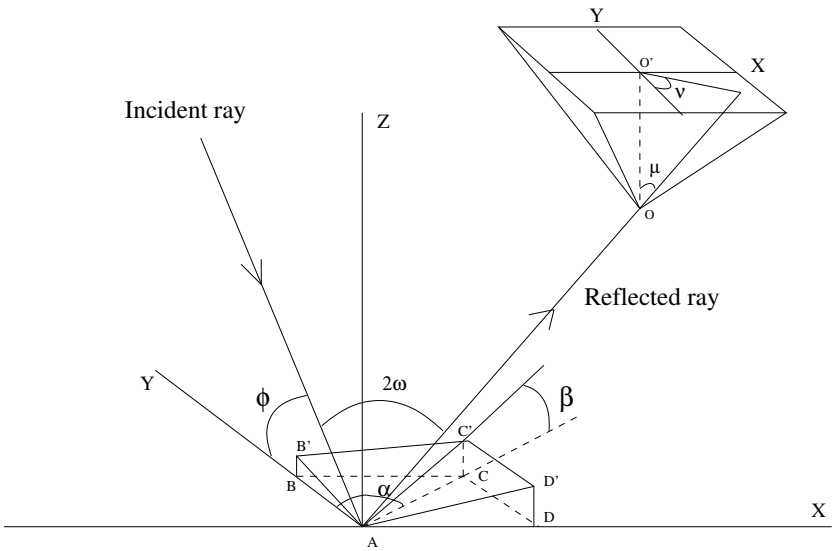

Figure 8.4: Geometry of SORES sensing during the Eddy Experiment Flight.

The Tilt-Azimuth Map (TAM)

The way to read these equations is the following. We can first consider the incident ray bouncing everywhere off the surface with the same angle ϕ, since the Sun is at very high distance. This angle can be known at the moment an observer takes a picture. From equation 8.11, ω becomes a function of α and β, and equations number 8.9 and 8.10 define a simple system of two equations with two unknown variables. Thus, a relation between the detected points on the photographic plate and the wave slopes can be established.

Then, iso-tilts and iso-azimuths on the photograph are plotted on each processed photograph. We call it the Tilt-Azimuth Map (TAM). An example of TAM is shown below in figure 8.5(a). Note that this mapping makes a strong analogy with the Delay Doppler Map presented in the scatterometric GNSS-R data. The original intensity of the photograph is thus re-organized from the metric space (X,Y) to the slope angle space (α,β).

From sea-surface slope distribution $\mathcal{P}_s$ to sea-surface radiance N

As explained by Cox and Munk in their well-documented report [Cox and Munk1956], we have to take into account the tolerance of slopes for the occurrence of a highlight at a fixed point on the surface, as related to the finite size of the Sun. The area of the slope tolerance ellipse at the point (x_0,y_0) with slope characterized by the tilt β_0 and azimuth α_0 is:

$$\Delta_t = \frac{1}{4}\frac{\pi\varphi^2}{\cos^3\beta_0\cos\omega_0}, \tag{8.12}$$

where φ is the angular radius of the Sun and ω_0 the half angle between the incident and reflected rays. The reflected radiant intensity from one specular point is:

$$J = \rho(\omega_0)\frac{H}{\pi\varphi^2}\Delta_h\frac{\cos\omega_0}{\cos\beta_0}, \tag{8.13}$$

where Δ_h designates the area of a single specular point projected onto a horizontal plane, H the Sun irradiance and ρ the reflection coefficient.

Let P(α,β) be the likelihood for a specular point to occur in a certain area (α,β) of slope. By definition, it corresponds to the integration of the slope probability $\mathcal{P}_s$ over the tolerance ellipse: $P = \mathcal{P}_s(\alpha,\beta)\Delta_t(\alpha,\beta)$. The reflected radiant intensity from the entire sea surface with radiance N is then:

$$N\cos\mu = PJ = \mathcal{P}_s\Delta_t J. \tag{8.14}$$

The sea-surface slope probability expression derived by Cox and Munk is:

$$\mathcal{P}_s = \frac{4}{\rho}\cos^4\beta\frac{N}{H}\cos\mu. \tag{8.15}$$

According to [Stegelmann and Garvey1973], this expression must be divided by the correction term

$$\frac{\sin\phi\cos\beta}{\cos\omega}. \tag{8.16}$$

This correction comes from the assumption that specular points are curved rather than flat, as assumed by Cox and Munk. However, it has not a significant impact in the present configuration. Strong discrepancies appear at lower Sun elevations.

From sea-surface radiance N to pixel intensity I

The solid angle subtended by the camera aperture of diameter d is:

$$\frac{\pi d^2\cos\mu}{4r^2}, \tag{8.17}$$

where r is the distance between the focused area and the camera. The flux received into the photosensitive camera system

$$\frac{N\pi d^2\tau(\mu)\cos^2\mu}{4r^2}, \tag{8.18}$$

introduces the transmission $\tau(\mu)$, which allows for the instrument's behavior with the angle of the incoming optical ray. Considering the reflections of the incoming rays with the outer and inner face of the camera length, $\tau(\mu)$ is proportional to $(1-\rho)^3$. Note that the vignetting effect has not been taken into account in $\tau(\mu)$.

It can be shown that the sea-surface radiance and the intensity on the photograph are related by:

$$N \sim \frac{I}{\tau(\mu)\cos^4\mu}, \tag{8.19}$$

where I is the pixel intensity ranging between 0 (black) and 1 (white).

Finally we have:

$$\mathcal{P}_s \sim \frac{I\cos^3\beta\cos\omega}{\rho(1-\rho)^3\sin\phi\cos^3\mu}. \tag{8.20}$$

This probability is not absolute, since we have no absolute relation between N and I in equation 8.19. The intensity on the photograph is thus proportional to the sea-surface slope probability times a function of the geometry (Sun elevation ϕ) and the Tilt-Azimuth Mapping:

$$I(\alpha,\beta) \sim \mathcal{P}_s(\alpha,\beta)\cdot f(\alpha,\beta,\phi), \tag{8.21}$$

with

$$f(\alpha,\beta,\phi) = \frac{\rho(1-\rho)^3\sin\phi\cos^3\mu}{\cos^3\beta\cos\omega}. \tag{8.22}$$

However, this relationship is not valid for observed intensities far away from the glint blob. Indeed, the very infrequent slopes are masked by the background reflectivity of the sea surface.

Background model

The pixel intensity on the image comes principally from the additive contribution of sunglint and reflected skylight. The sunlight scattered by particles beneath the sea surface is assumed negligible and is not considered here. A model has been developed to remove reflections of sky radiance from the glint.

The approach consists in considering each sea surface facet specular because, for a given location of the receiver, it always exists a "source" in the sky that satisfies the specular reflection condition. Let's consider the cell (α_i,β_i) of the TAM. It corresponds to the slope components required to reflect the solar rays onto the camera. The radiance of the sea surface due to reflected skylight in the cell (α_i,β_i) can thus be simply modeled by the integration of intensity I of equation 8.21 over all the azimuths α and tilts β except the azimuth α_i and the tilt β_i of the corresponding cell:

$$I_b(\alpha_i,\beta_i) = \int_{\alpha\neq\alpha_i}\int_{\beta\neq\beta_i} K\cdot\mathcal{P}_s(\alpha,\beta)\cdot f(\alpha,\beta,\phi)d\alpha d\beta, \tag{8.23}$$

with K a constant related to the sky radiance. The background is thus parametrized with the same parameters of interest of the slope PDF and a multiplicative constant.

Forward intensity model

From equations 8.21 and 8.23, the model intensity I_m writes:

$$I_m(\alpha,\beta) = \mathcal{P}_s(\alpha,\beta)\cdot f(\alpha,\beta,\phi) + I_b(\alpha,\beta). \tag{8.24}$$

It is composed of two nuisance parameters (a_o, K) and four parameters of interest (a_o', a_2, a_o'' and α_o). Figure 8.5 shows an example of a photograph with its associated TAM data I_d.

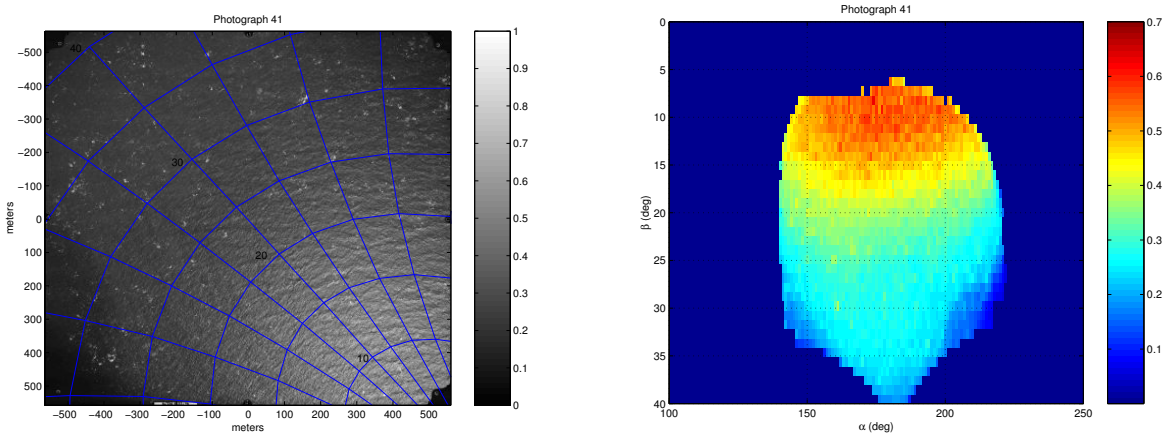

(a) Photograph (b) I_d

Figure 8.5: (a) Photograph 41 with the TAM. (b) Data intensity I_d.

8.2.3 Parameter search

Inversion was based on the least-square approach, i.e., estimation is performed through a minimization of the root mean square error between model and data DDMs. The optimization procedure used to fit a TAM I_d with our model I_m has been carried out through the non-linear fitting Matlab function `nlinfit`. This function has been modified so that a domain of search for each parameter can be specified. The inputs of this function are a first guess of the six parameters and a domain of search for each parameter. The first guesses have been fixed to a_o=3, a_o'=20, a_2=6, a_o''=15, α_o=180^o and K=0. The domains of search are chosen with reference to Cox and Munk's observations:

- $a_o \in [0:5]$,
- $a_o' \in [0:50]$,
- $a_2 \in [0:30]$,
- $a_o'' \in [0:50]$,
- $\alpha_o \in [0^o:180^o]$,
- $K \in [0:\infty]$.

Note that because of the date and time of the experiment, part of the sunglint is visible only. Therefore, the domain of search for α_o is restricted to half the space only.
Figure 8.6 shows an example of data and best-fit model TAMs, together with the residual between model and data. As observed, the residual do not exceed 10% and is below 4% most of the time.

8.2.4 Results

The obtained directional slope variances along the track of the plane are presented in the following figures and summarized in Table 8.1. In this study, DMSS are represented by crosses for the ascending track and by diamonds for the descending track.

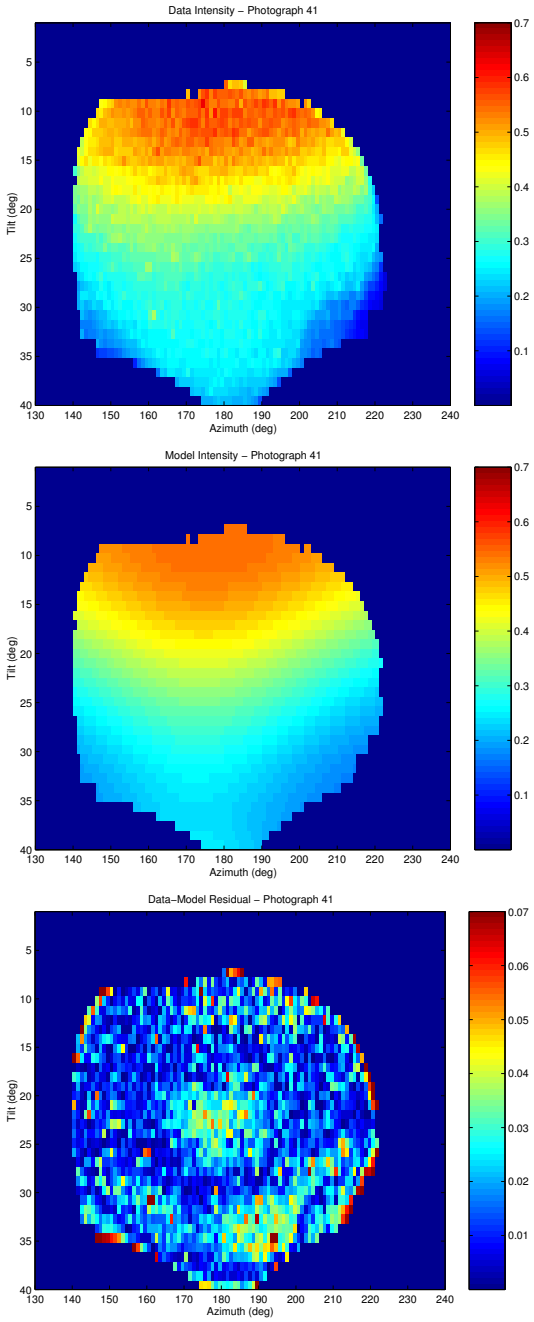

Figure 8.6: Examples of data and best-fit model TAMs. **Top**: Data TAMs. **Middle**: Best-fit model TAMs. **Bottom**: Data-model residual.

In figure 8.7, both estimated up-wind MSS and slope PDF isotropy are plotted as a function of photograph latitude. As observed during the ascending track, the up-wind mean square slope increases regularly from latitude 41.2^o to approximately latitude 42.2^o. A decrease is then observed in the range of latitude [42.2^o-42.6^o]. These variations are in very good agreement with the wind speed provided by INM and with MSS provided by Jason as shown in figures number 7.7(a) and 7.8(a), respectively. At latitudes ranging between 42^o and 42.2^o, the magnitudes of the up-wind MSS obtained during the descending track of the plane are lower than the ones obtained during the ascending track. Two hours have passed between the first photograph (number 35) and the last one (number 60). However, as shown after, this variation in MSS corresponds to wind variations less than 1.5 m/s.

Photograph	Latitude North (deg)	a_o'	a_2	a_o''	SPA from α_o (deg North)
35	41.3245^o	13.8606	1.5815	12.6136	-3.9436^o
37	41.5585^o	14.0545	3.4893	10.4035	-12.6559^o
38	41.6610^o	13.3639	3.3965	9.9729	-11.2093^o
39	41.7760^o	11.1930	2.4997	9.0526	-10.7038^o
40	41.9395^o	10.6231	3.2986	7.4682	-13.4550^o
41	41.9498^o	10.8427	3.0718	7.7430	-14.6193^o
42	42.0362^o	10.9335	3.2780	7.5862	-17.3171^o
43	42.1263^o	11.1635	3.2415	7.7810	-18.3593^o
44	42.1659^o	11.3595	3.6843	7.1311	-18.4752^o
45	42.2897^o	12.6817	4.0638	8.5308	-20.1206^o
47	42.5808^o	13.8954	3.4875	11.5217	-10.7170^o
48	42.5037^o	12.9548	2.8321	11.1340	-26.0437^o
49	42.3845^o	13.5814	3.7823	10.0749	-19.1450^o
50	42.2890^o	13.2319	3.5123	10.5604	-18.4675^o
51	42.1534^o	12.1448	3.2049	9.2280	-9.0746^o
52	42.0819^o	13.7373	4.3761	9.9098	-6.1770^o
53	41.9756^o	12.6535	3.8245	9.1848	-4.1865^o
54	41.8704^o	13.0652	4.0820	9.3435	1.3328^o
55	41.7962^o	15.4996	5.8453	1.4376	-4.2403^o
58	41.7889^o	13.9303	4.7390	9.7291	2.8801^o
59	41.7509^o	12.8656	3.7523	9.6445	7.6377^o
60	41.7245^o	12.9297	3.9557	9.4167	7.7232^o

Table 8.1: Parameter estimation in chronological order.

The isotropy of the PDF decreases quite significantly from 0.8 to reach a minimum value of around 0.5 at latitude 42.2^o, as shown in figure 8.7(b). It is clearly observed, when comparing the behaviors of up-wind MSS and SPI, that the isotropy of the sea-surface slope PDF decreases with sea-surface roughness. However such variations in SPI for the range of wind speeds considered are not expected by Elfouhaily's model, as shown below. We will show a strong correlation between slope PDF isotropy and wind/waves misalignment.

We show in figure 8.8(a) the Slope PDF Azimuth which provides a good a priori of wind direction, although they are not always aligned. SPA is aligned with North at the beginning of the track and rotates progressively to reach -30^o at the end of the track. Discrepancies in

SPA between ascending and descending tracks can be observed, but they do not exceed 15^o. The estimated direction is in pretty good agreement with the ECMWF wind direction for that particular day and with the INM model (see figure 7.7(a)). We can already anticipate that an estimation bias appears when wind direction and wind-generated waves are not exactly aligned.

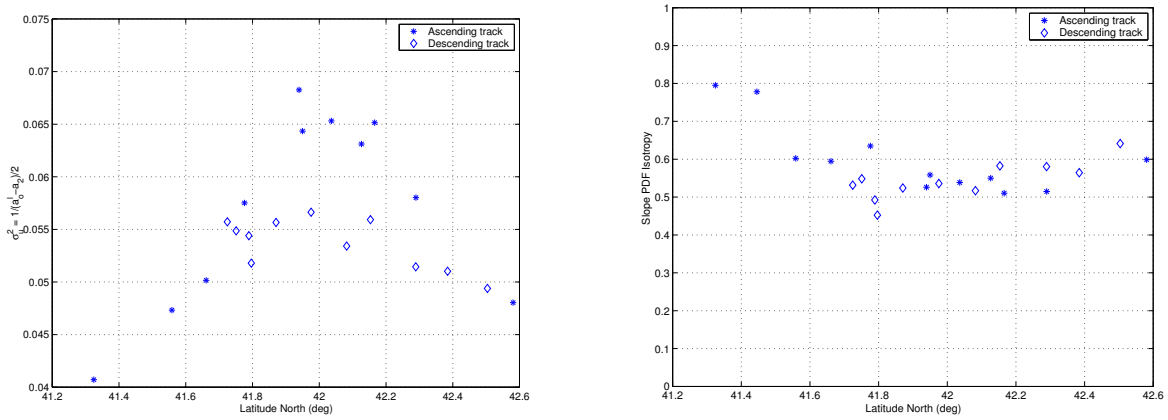

(a) Up-wind MSS

(b) Slope PDF isotropy

Figure 8.7: Up-wind mean square slope and slope PDF isotropy along the track.

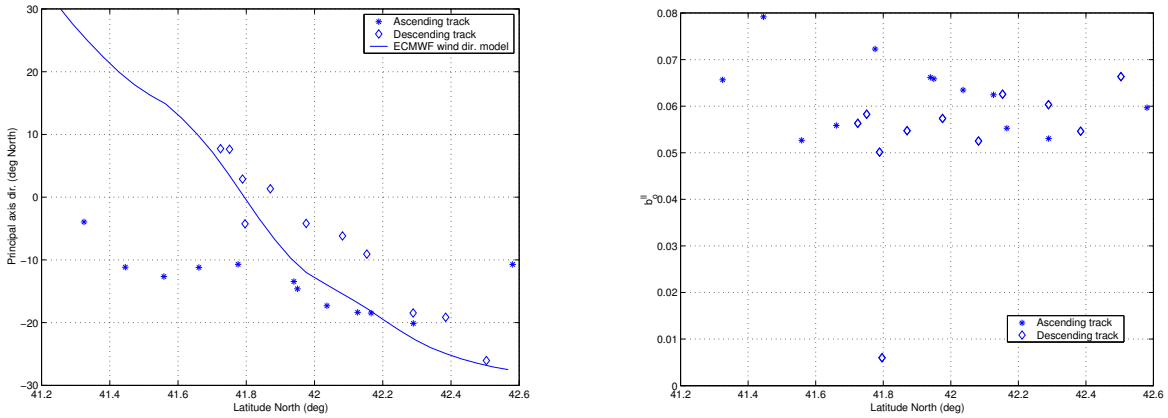

(a) Slope PDF azimuth

(b) b_o''

Figure 8.8: Slope PDF azimuth and b_o'' along the track.

As observed in figure 8.8(b), the parameter b_o'' does not vary significantly along the ascending and descending tracks of the plane. The magnitudes are however higher than the average 0.04 observed by Cox and Munk—see below the discussion in section (8.4).

When compared to ground truth in a more precise way—as shown latter in section (8.4)—the estimation provides high sea-surface slope variances for the considered wind speeds observed that day. The parameters a_o', a_2 and a_o'' present indeed lower values compared to

the ones obtained by Cox and Munk for high wind speeds. This can be explained with two arguments:

- We extended the inversion procedure to the whole image. Given the Sun elevation and camera aperture, we were able to detect slopes up to 40^o, whereas Cox and Munk did not consider slopes greater than 25^o, say. However, they increased their slope variance by a factor of 23% in order to take into account the uncommon steep slopes they intentionally did not measured due to SNR considerations.

- As clearly observed on the photographs, the glitter pattern is modulated by long waves. This modulation corrupted the slope variance estimation and gave the motivation to characterize these long waves.

8.3 Wind and waves characterization

As observed on the photographs, the return intensity is modulated by a wind-generated swell. It is expected that long sea waves do have a non-negligible impact on the DMSS. We depict in this section the contribution of the long waves in the DMSS through a spectral analysis of the images and simulations.

The spectral analysis of the images has been undertaken in section (8.3.1) to estimate the direction and wavelength of the swell along the track of the plane. In addition, we estimated the slope variance of the observed long waves.

The simulations of section (8.3.2) depict the impact of long waves on the estimated sea-surface slope PDF. We focus on the behavior of the up-wind MSS, SPI and SPA with respect to the height and direction of the wind generated waves.

8.3.1 Spectral analysis

We intend in this section to estimate the sea long wave spectrum with a Fourier analysis of the return intensity. This requires usually the centering of the intensity around its mean. The centered intensity I_c at pixel (i,j) is defined in our case by the return intensity at pixel (i,j) divided by the mean value obtained in the corresponding cell (α,β) the pixel is belonging to:

$$I_c(i,j) = \frac{I(i,j)}{\bar{I}(\alpha,\beta)}. \tag{8.25}$$

Figures 8.9(a) and 8.9(b) show the centered intensity I_c in optimal region of photograph 47 and its Fourier transform, respectively.

As shown before, the mean return intensity in cell (α,β) is proportional to the sea-surface slope PDF times a correction factor f which is simplified here to $1/\cos^4\beta$ for further calculation:

$$\bar{I}(\alpha,\beta) \approx \frac{1}{\cos^4\beta} \cdot e^{a_o} e^{[-a'_o + a_2\cos(2(\alpha-\alpha_o))]\tan^2\beta}. \tag{8.26}$$

In specular regime, the amplitude modulation of the backscatter is due to the local tilting of the short waves by underlying longer energy containing swell. So far, in wave spectrum retrieval from SAR images, the Modulation Transfer Function (MTF) under a Gaussian assumption is defined by:

$$MTF(k) = \left[\frac{1}{\bar{I}}\frac{dI}{d\tan\beta} \cdot ik\right]^2. \tag{8.27}$$

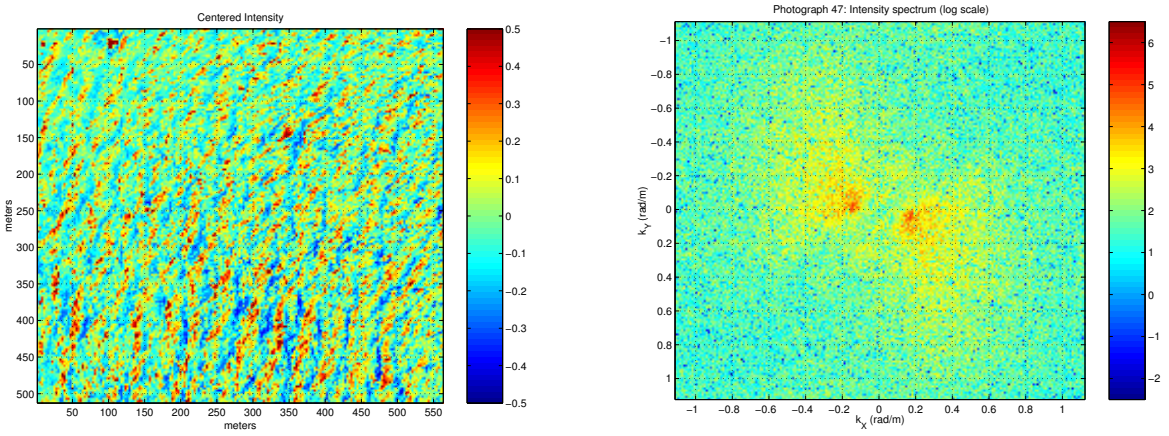

(a) (b)

Figure 8.9: (a) Centered intensity I_c in optimal region of photograph 47. (b) 2-D Fourier transform of I_c.

It comes to:

$$MTF(k) = \left[\left(4\frac{\sin^2\beta}{\tan\beta} - 2\frac{\tan\beta}{mss}\right)\cdot ik\right]^2, \tag{8.28}$$

with here:

$$\frac{1}{mss} = a_o' - a_2\cos[2(\alpha-\alpha_o)]. \tag{8.29}$$

The MTF provides the dynamic of the decay of the return intensity I, i.e., the decreasing occurrence of sea-surface slopes. It allows to describe the fact that the contrast in the image depends on the observation angle.

Then, the relationship between the image power spectrum and the sea wave spectrum writes:

$$S(\vec{k}) = \frac{F^2}{MTF}, \tag{8.30}$$

where F is the Fourier transform of I_c.

The sea wave spectrum estimated from photograph 47 is presented in figure 8.10(a). A passband filter allows a better characterization of the long wave peak (see figure 8.10(b)). The wavelength and direction of the long waves are simply estimated by the position of the peak in the 2-D spectrum.

We also investigate from the estimated long wave spectra the mean square slope mss_l related to the observed long waves. It done through the fitting of the integrated spectrum with the significant wave height (SWH) provided by Jason. This parameter search is motivated by the simple assumption that the Total MSS is the sum of the long wave slope variance mss_l plus a wind-related slope variance mss_w:

$$\text{Total MSS} = mss_w + mss_l. \tag{8.31}$$

A close look to the data has shown that equation 8.28 does not hold. Spectral analyses have been carried out on 128x128 squared pixel images at different observation angles. The

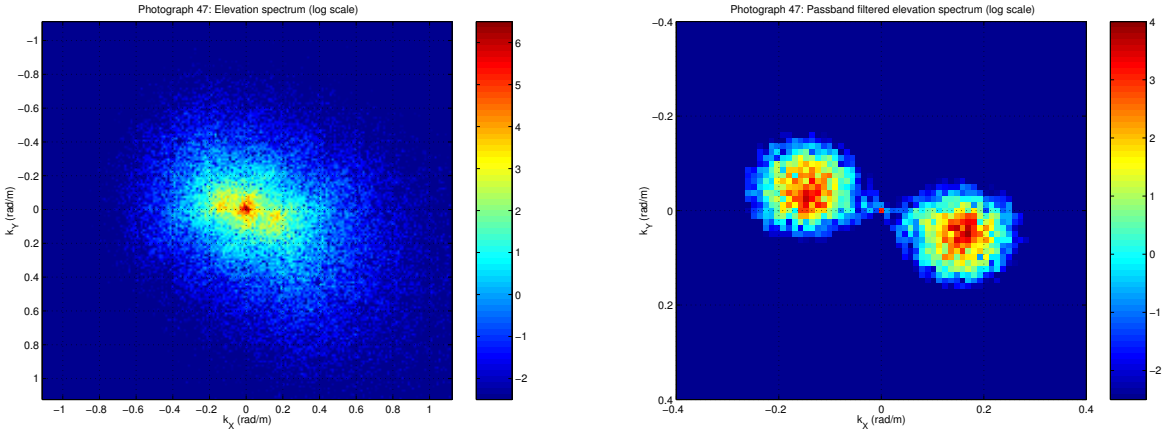

(a) (b)

Figure 8.10: (a) Sea elevation estimated spectrum $S(k)$. (b) Passband filtered $S(k)$.

integrated image spectrum presents three regimes along the tilt axis of the TAM, i.e. the angle of observation, as shown for photograph 37 in figure 8.11. It is first an increasing function of β, then reaches a 4^o large plateau and finally decreases.

When the integrated spectrum does not depend on the observation angle, it implies from equation 8.30 that the MTF does not vary as well. This means that in this range of slopes the derivative of the received intensity (i.e., slope PDF) with respect to the slopes is constant. Consequently, the occurrence of slopes decreases in $exp(-\tan\beta/mss)$ in this range and not in $exp(-\tan^2\beta/mss)$ as in the Gaussian case.

Note that this plateau corresponds to the inflection point of the PDF. As observed on all the set of photographs, it shifts towards large slopes values as the roughness increases.

In this particular range of slopes, the significant wave height can thus be defined by:

$$SWH = 4\sigma_\zeta = 4\sqrt{\int S(\vec{k})d\vec{k}} = 4\sqrt{\int \frac{F^2(\vec{k})}{C^2\vec{k}^2}d\vec{k}}. \tag{8.32}$$

The constant C is an ad hoc parameter replacing the MTF and computed so that SWH fits the values provided by Jason (see figure 7.9). We deduce finally a slope variance of the long waves:

$$mss_l = \frac{1}{C^2}\int F^2(\vec{k})d\vec{k}. \tag{8.33}$$

Results

Finally, we obtained from the spectral analysis the followings results:

- The swell wavelength spans between 40 and 45 meters along the track.
- As shown in figure 8.12, the swell direction α_s rotates quite linearly from about 40^o North at latitude 41.6^o to -60^o North at latitude 42.6^o. At each point of the track where waves have been characterized, the wave orientation does not change in time since there are no significant differences between the directions estimated during the

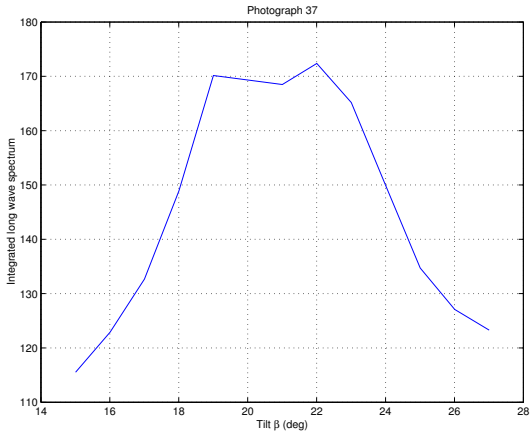

Figure 8.11: Integrated spectrum versus tilt β.

ascending and descending tracks. However, these directions differ from the slope PDF azimuths estimated through the TAM data inversion at low latitudes. As shown below, there is indeed a decoupling between wind and waves as we go South.

- The long waves slope variance mss_l ranges between 0.008 and 0.016 as observed in figure 8.13(a). The Total MSS and mss_w are also plotted. These magnitudes are very consistent with Vandemark's recent measurements [Vandemark *et al.*2003] for coastal observations. Their mss_l includes waves with wavelengths greater than 2 m.

  We quantified in percent of the overall slope variance the mss_l contribution of the long waves in figure 8.13(b). The long wave slope variance represents more than 10% of the overall slope variance along the track and can reach values up to 22%.

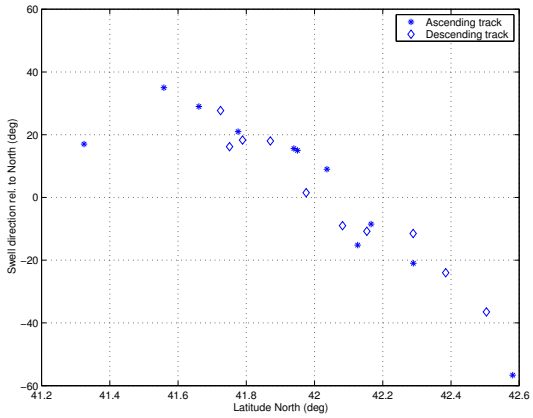

Figure 8.12: Swell direction α_s along the track from a spectral analysis of the images.

8.3.2 Simulations

We investigate in this section the impact of a swell on the Sun glitter through some simulated photographs. The goal is to quantify the long scale slope component of the total sea-surface slope variance.

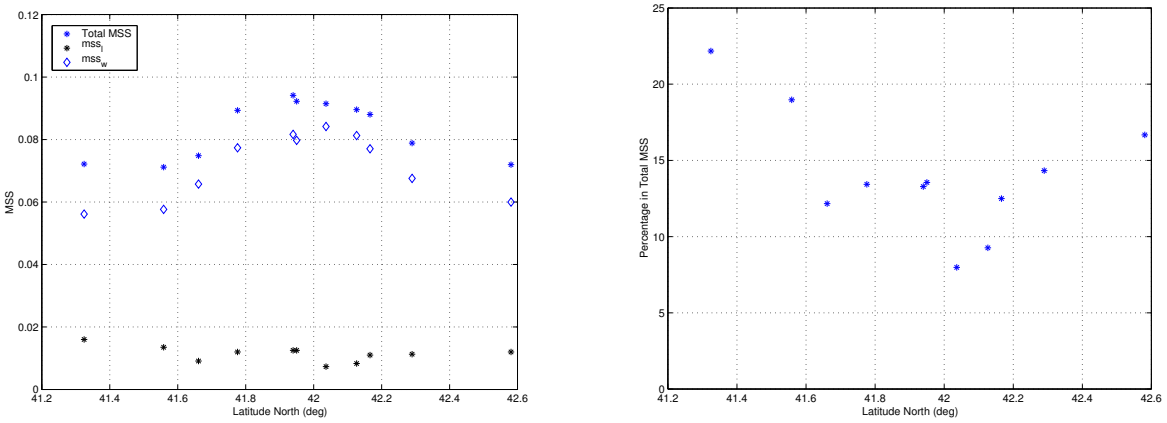

(a) (b)

Figure 8.13: (a) Total MSS, mss_w and mss_l versus latitude. (b) Long wave variance contribution in percent to the overall slope variance.

The swell can be simply modeled by a sine function with three parameters: height H, wavelength L and direction α_s:

$$\eta_s(X,Y) = H\cos\left[\frac{2\pi}{L}(\sin\alpha_s X + \cos\alpha_s Y)\right]. \tag{8.34}$$

As observed from the spectral analysis, the swell wavelength is fixed to L=45 meters. We recall that the induced wind sea-surface slope PDF proposed in section (8.2.1) is:

$$\mathcal{P}_s(\alpha,\beta) = e^{a_o+[-a'_o+a_2\cos(2(\alpha-\alpha_o))]\tan^2\beta}. \tag{8.35}$$

A slope originally specular in the cell (α,β) of the TAM is now tilted along the swell by an angle β_s. The slope (α,β) is to be expressed in the local frame of the swell ($\vec{X}_s$,$\vec{Y}_s$,$\vec{Z}_s$) at that point of the surface, defined as:

$$\begin{cases} \vec{X}_s = \cos\alpha_s\vec{X} - \sin\alpha_s\vec{Y} \\ \vec{Y}_s = \cos\beta_s\sin\alpha_s\vec{X} + \cos\beta_s\cos\alpha_s\vec{Y} - \sin\beta_s\vec{Z} \\ \vec{Z}_s = \sin\beta_s\sin\alpha_s\vec{X} + \sin\beta_s\cos\alpha_s\vec{Y} + \cos\beta_s\vec{Z} \end{cases}$$

Then, the unit vector $\vec{u}$ tangent to the specular facet writes in frames $(\vec{X},\vec{Y},\vec{Z})$ and $(\vec{X}_s,\vec{Y}_s,\vec{Z}_s)$:

$$\vec{u} = \begin{cases} \sin\alpha\cos\beta \\ \cos\alpha\cos\beta \\ -\sin\beta \end{cases}_{(\vec{X},\vec{Y},\vec{Z})} = \begin{cases} \cos\beta\sin(\alpha-\alpha_s) \\ \cos\beta\cos\beta_s\cos(\alpha-\alpha_s) + \sin\beta\sin\beta_s \\ \cos\beta\sin\beta_s\cos(\alpha-\alpha_s) - \sin\beta\cos\beta_s \end{cases}_{(\vec{X}_s,\vec{Y}_s,\vec{Z}_s)}$$

The modified slope PDF comes to:

$$\mathcal{P}_s(\alpha,\beta') = e^{a_o+[-a'_o+a_2\cos(2(\alpha-\alpha_o))]\tan^2\beta'}, \tag{8.36}$$

with:

$$\sin\beta' = \sin\beta\cos\beta_s - \cos\beta\sin\beta_s\cos(\alpha-\alpha_s). \tag{8.37}$$

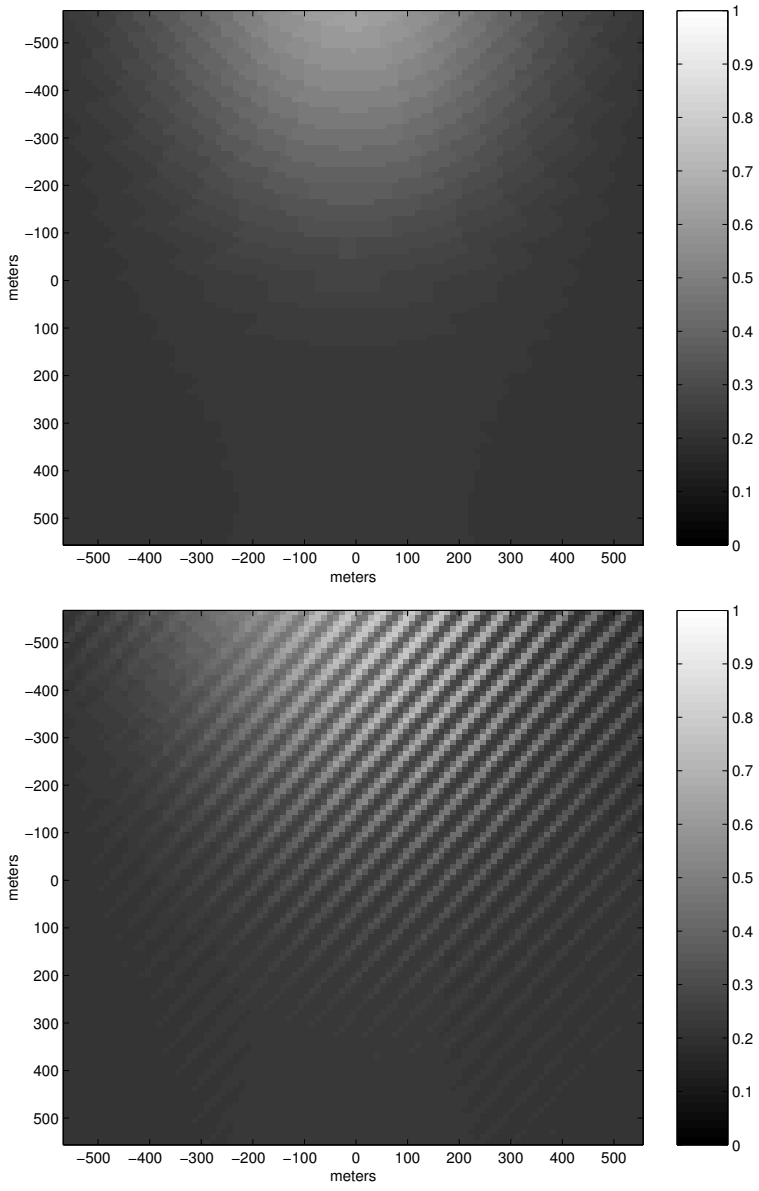

Figure 8.14: Simulated photographs with the Eddy Experiment Flight camera specifications. The up-wind MSS is 0.031. **Top**: without swell. **Bottom**: with swell (H=1 m).

Simulations have been done based on equations 8.36 and 8.37 in order to highlight the impact of H and the relative orientation between wind and waves ($\Delta\alpha = \alpha_s - \alpha_o$) on the up-wind MSS, SPI and SPA. We fixed an initial up-wind MSS to 0.031 (a'_o=20 and a_2=4), which corresponds to an isotropy of 0.67. The bistatic geometry is similar to the one of the photographs, with a Sun elevation of 45^o. However, both Sun azimuth and wind direction are assumed to be aligned with the top of the photograph (α_o=0^o). Figure 8.14 shows an example of simulated glint with and without long waves for that particular DMSS. The swell direction is 50^o away from the wind direction with H=1 m.

The use of the Matlab fitting function is not appropriate in this case, since the domain of search changes significantly from one increment of H or $\Delta\alpha$ to the other. The parameter estimation has been done with a simple least square inversion. The results of the simulations are presented below.

Impact of SWH

We focus on the variations of the mean square slope with the height of wind-generated waves for a fixed orientation, which is chosen to be at $\Delta\alpha = \alpha_s - \alpha_o = 45^o$ from the wind direction. As observed in figure 8.15(a), the up-wind MSS increases with H. For instance, a SWH of 2 m (H=1) will increase the slope variance by a factor 1.24.

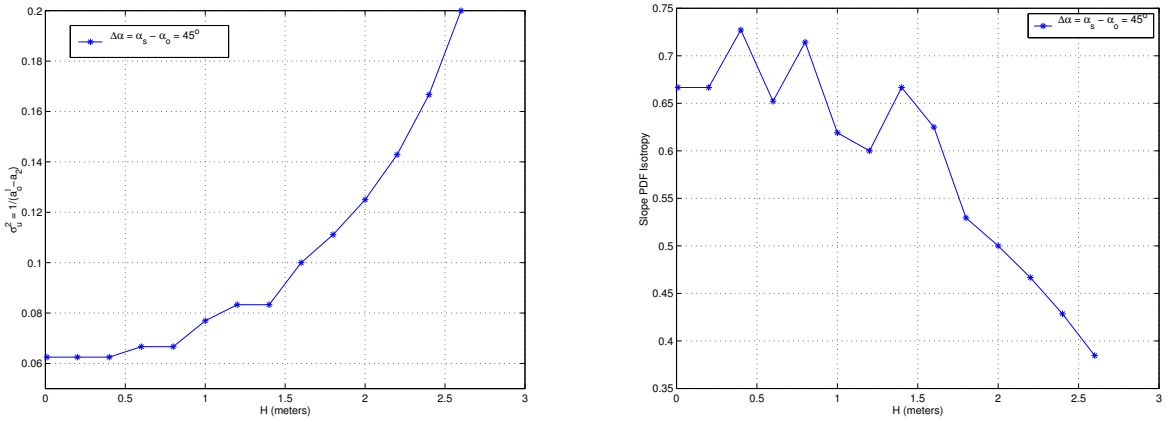

(a) σ_u^2 (b) Slope PDF isotropy

Figure 8.15: Impact of wave height H on σ_u^2 and SPI. $\Delta\alpha = 45^o$.

On the contrary, the isotropy of the PDF decreases with the SWH and is lowered by a factor 1.08 for SWH=2 m (see figure 8.15(b)). We conclude that the SWH increases the anisotropy of the sea-surface slope PDF, but not significantly.

The difference between the slope PDF azimuth and wind direction is plotted as a function of the height of the waves in figure 8.16. The deviation from the true wind direction increases quite significantly with H and can reach 15^o for SWH=2 m.

Impact of a wind/wave misalignment

The parameter H is now fixed to 0.7 (blue curve) and 1 meter (red curve), and $\Delta\alpha$ becomes the varying parameter. Figure 8.17(a) shows that the up-wind MSS increases of about 40%

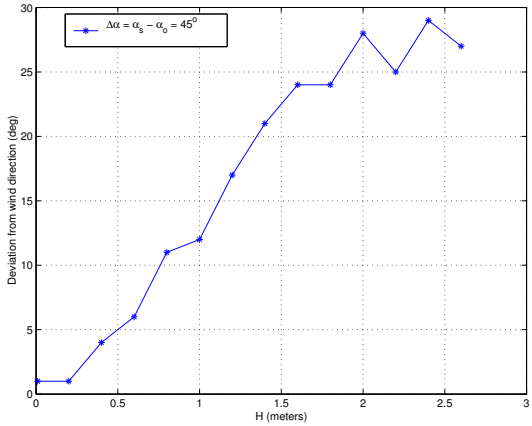

Figure 8.16: Impact of H on wind direction estimation. $\Delta\alpha = 45^o$.

when waves and wind are aligned ($\Delta\alpha$=0) for a SWH of the order of 2 m (H=1 m). It decreases then to the nominal value of 0.031 when the wave direction is perpendicular to the wind direction. Note that shadowing effects are not modeled here, and given the geometry of the scattering (Sun elevation is 45^o) they should have a great impact on the return intensity. A lower increase than the 40% found in the mean square slope is expected.

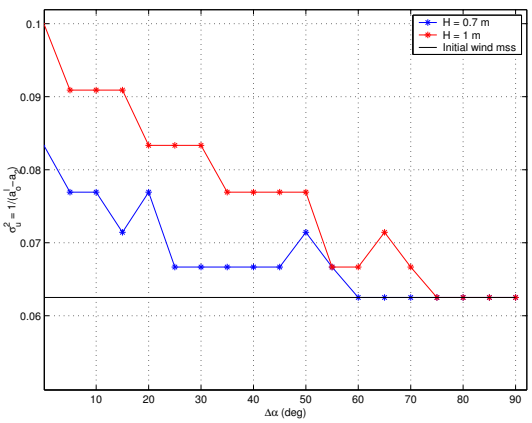

(a) σ_u^2

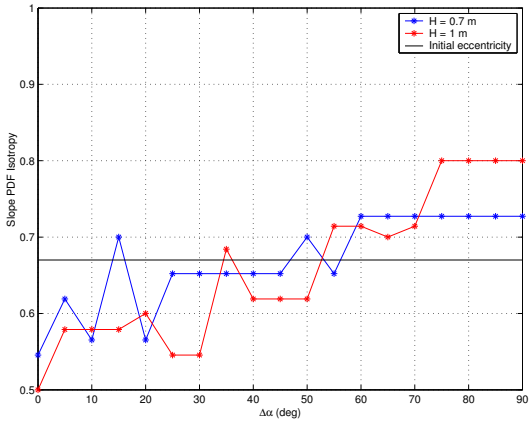

(b) Slope PDF isotropy

Figure 8.17: Impact of $\Delta\alpha$ on σ_u^2 (a) and SPI (b). H is 0.7 (blue curve) and 1 meter (red curve). The black line corresponds to the nominal value of the analyzed parameter.

The slope PDF isotropy equals 0.5 when wind and waves are aligned as shown in figure 8.17(b). As expected in that case, the long wave tilting effect increases the anisotropy of the slope PDF. When the wave orientation differs from the wind direction, the PDF becomes more isotropic and SPI equals 0.8 for $\Delta\alpha = 90^o$. We conclude that the relative orientation of the wind and waves becomes a crucial parameter governing the sea-surface slope shape.

The difference angle between slope PDF azimuth and wind direction is maximum around $\Delta\alpha = 40^o$ to 60^o. The estimation bias is then of the order of 15^o as observed in figure 8.18.

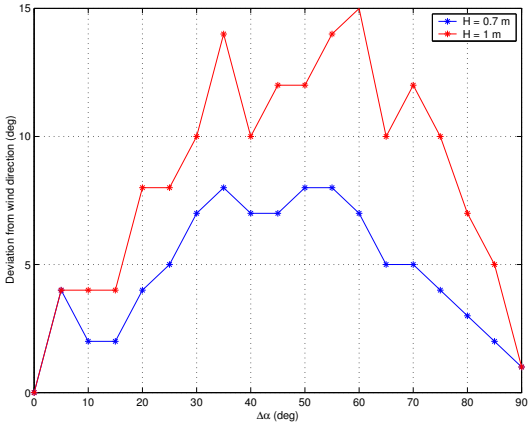

Figure 8.18: Impact of $\Delta\alpha$ on wind direction estimation. H is 0.7 (blue curve) and 1 meter (red curve).

8.4 Comparison with Cox and Munk's measurements

We compare in this section the obtained fitting coefficients with sea-surface roughness and with the ones found by Cox and Munk. The relationship between DMSS and sea-surface characteristics such as SWH and misalignment between wind and waves is discussed. Special attention is then paid to the fourth order moment of the slope PDF.

Sea-surface slope variance

The estimated MSS defined by $1/a'_o$ has been plotted as a function of Jason's wind speed in figure 8.19(a), together with the MSS computed with the Cox and Munk's parameters a'_o (red circle). The latter includes a correction factor (the so-called "blanket" factor) of 23%, which multiplies their inference of an "incomplete" slope variance $1/a'_o$ to account for the infrequent and unmeasured steep slopes (see Cox and Munk, 1956, section 7.3 and section 9). According to the mathematical extrapolation procedure, the mean square slope would then be simply estimated via the deduction:

$$\mathrm{MSS} \simeq \frac{B}{a'_o}, \tag{8.38}$$

where B is the approximated blanket adjustment factor to take into account the very infrequent steep slope components in the total variance.

As understood, this factor thus encompasses the approximation of the ratio a''_o/a'^2_o, and is wind-insensitive. As proposed by Cox and Munk, the value is 1.23 leading to the often-cited deduction for clean surface:

$$\mathrm{MSS}_{clean} = 0.003 + 0.005U_{12} \simeq \left.\frac{1.23}{a'_o}\right|_{clean}, \tag{8.39}$$

where U_{12} is the wind at a 12 meter altitude, g the acceleration gravity. This regression line is also plotted in red. In addition, both Elfouhaily's and Kudryavtsev's models are plotted (see [Kudryavtsev *et al.*1999]).

A linear variation of the optically derived slope variance with the wind speed is observed. The regression line has not been computed since the range of wind speeds during the experiment was too small. The sea-surface slope variances obtained during this experiment are higher than the ones computed by Cox and Munk. We fit perfectly their data by reducing

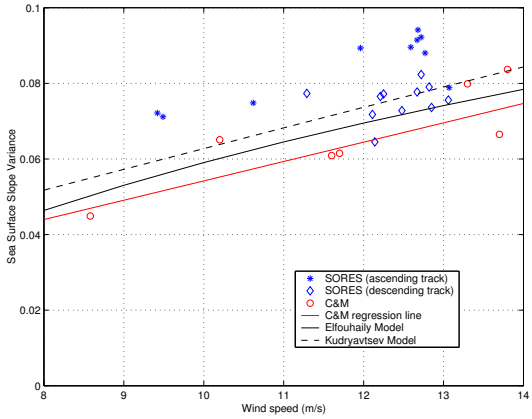

(a) Total MSS

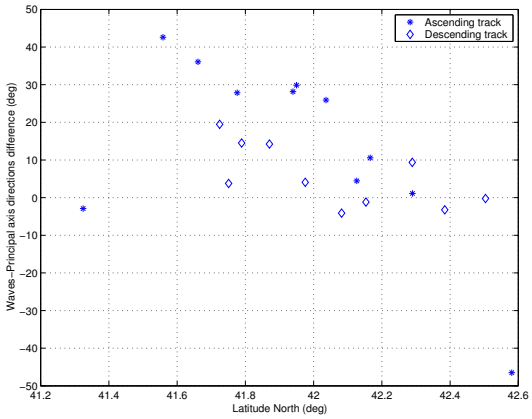

(b) Swell/PDF axis misalignment

Figure 8.19: (a) Total MSS versus wind speed. Cox and Munk slope variances are also plotted (red circles). (b) Angle difference between slope PDF azimuth and swell direction ($\Delta\alpha = \alpha_s - \alpha_o$) versus wind speed.

our estimated variances by 20%. This high slope variances may come particularly from the sea-state. Indeed simulations have highlighted that the non-wind related SWH could increase the MSS by around 20%. We have indeed observed during this experiment a stronger wind-generated swell (SWH≈2 m) than the one observed by Cox and Munk (SWH≈1.2 m) for high wind speeds.

Furthermore, we have seen in section (8.3.1) that the estimated long wave slope variance mss_l contributes to more than 10% of the overall sea-surface slope variance. It confirms the fact that at high wind speed conditions (9 to 13 m/s), high SWHs—i.e., high mss_l—will increase significantly the overall MSS.

Slope PDF azimuth

Cox and Munk have found the slope PDF azimuth to be oriented with the wind in the whole set of data they processed. In our set of data, we detected discrepancies between waves direction and SPA at low latitudes of the track. Figure 8.19(b) presents the differences between the directions of the wind-generated waves and the slope PDF azimuths along the track. Swell and wind are approximately aligned at high latitudes, whereas differences reaching values of the order of 40^o are observed at the beginning of the track. Probably due to strong bathymetric variations in this area, the wind generated waves rotate significantly towards the Catalan coast as we go South, whereas the wind decreases and rotates slowly. Given the results of the simulations, the detection of this difference allows us to think that there is a bias between the estimated SPA and the true wind direction ranging between 0^o and 15^o. This bias could explain the discrepancy of the data with the ECMWF model at the beginning of the track.

Slope PDF isotropy

In their well documented report, Cox and Munk measured isotropies ranging from 0.54 to 1 and noticed that high values of this parameter (i.e., a quasi-omnidirectional slope PDF) were obtained for gusty winds of high variability. Therefore they related isotropy low values with the low variability of the wind. We observe in figure 8.20(a) similar low values of about

0.5 in an area where the wind is strong (12-13 m/s) and particularly aligned with the waves. It is clearly observed that the slope PDF isotropy decreases with wind speed, with higher variations than the ones predicted by the Elfouhaily model (black curve). Indeed, this model does not predict significant variations of the isotropy at this range of wind speeds.

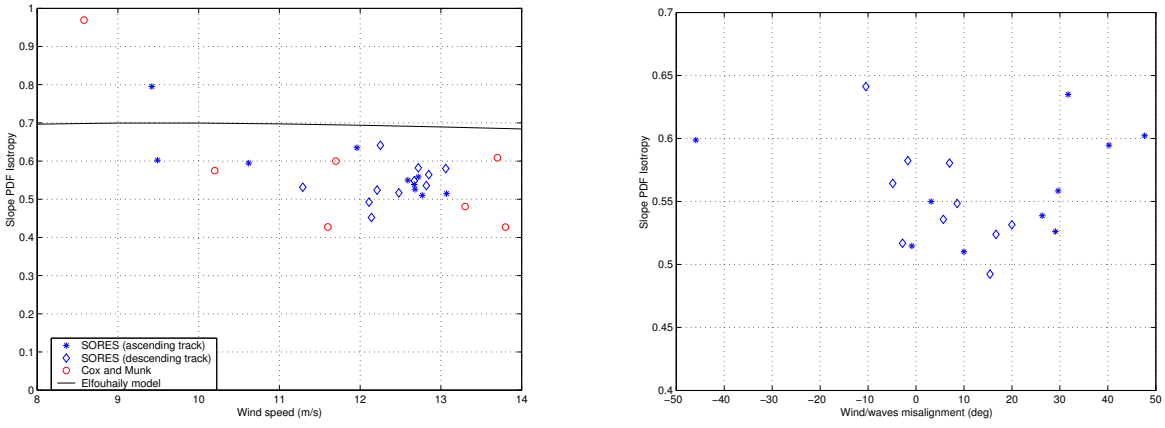

(a) (b)

Figure 8.20: (a) Slope PDF isotropy versus wind speed. (b) Slope PDF isotropy versus $\Delta\alpha$.

We anticipate that high values of SPI are obtained also when there is a misalignment between wind and waves. Cox and Munk's observations do consolidate this dependency since the high isotropy value of 0.97 encountered for a 8.6 m/s wind speed corresponds to a misalignment of 39^o.

The relative orientation of waves and wind and the SWH impact significantly the isotropy of the sea-surface slope PDF, as understood from the simulations. It has been shown however that SPI was much more sensitive to this misalignment than the SWH. Figure 8.20(b) shows indeed the pretty good correlation between SPI and this misalignment. The slope PDF isotropy increases from 0.5 to 0.6 when 30^o of difference between wind and wave orientations is observed. Note that the small isotropies encountered correspond also with the highest SWHs.

Furthermore, we observe in this figure that the minimum of the isotropy does not occur at $\Delta\alpha = 0$ as expected but at around 15^o. This bias could be related to the bias between slope PDF azimuth and true wind direction, since $\Delta\alpha$ is not the exact angle difference between wind and waves but the difference between SPA and waves.

Departure from Gaussianity

The analysis of parameter b''_o clearly shows that, in this high wind speed regime, it is higher than the value 0.04 mentioned by Cox and Munk. The importance of this value for their analysis comes from the necessity to account for the missing data ($a'_o s^2 \geq 4$) to evaluate the total slope variance. Cox and Munk extrapolate their fit results out to $a'_o s^2 \leq 8$ to estimate for what they called the *incomplete* slope variances. This limit can be judged quite arbitrary, and is in fact strongly depending upon the ratio a''_o/a'^2_o [Chapron *et al.*2000]. When this value is less or equal to the chosen constant 0.04, the extrapolation procedure can be tested and a

posteriori justified. But, it is not the case for higher values (in fact obtained for wind speeds higher than 6 m/s).

As observed in figure 8.21(a), the fourth order moment a_o'' of the slope distribution is a decreasing function of the wind in the range 9 - 13 m/s. The regression line computed regardless of the outlier gives:

$$a_o'' = 18.1942 - 0.7316 U_{10}. \tag{8.40}$$

The parameter b_o'' (see figure 8.21(b)) spans between 0.05 and 0.07 and presents slow increasing variations with wind speed, according to the regression line:

$$b_o'' = \frac{a_o''}{a_o'^2} = 0.0569 + 2 \times 10^{-4} U_{10}. \tag{8.41}$$

Note that some of the Cox and Munk's data fall into the obtained ranges of values.

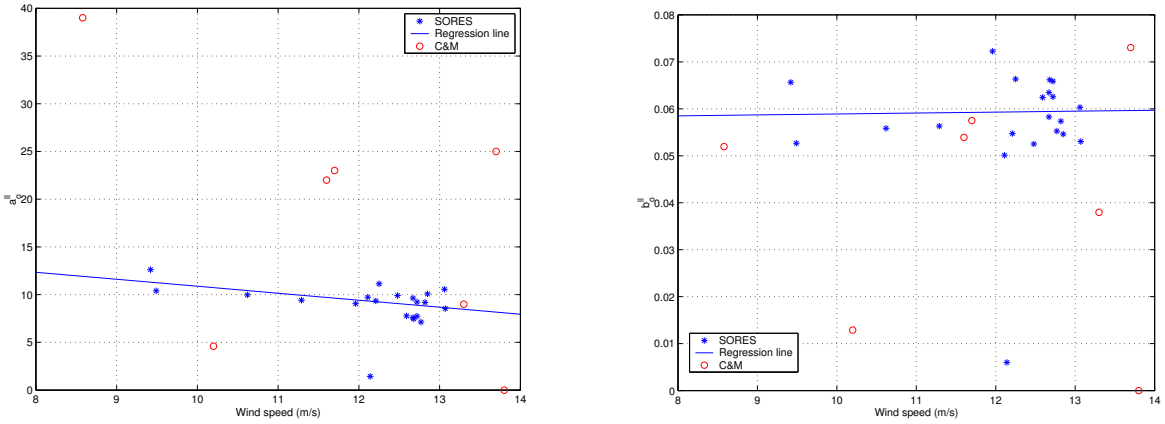

(a) a_o'' (b) b_o''

Figure 8.21: Parameters a_o'' (a) and b_o'' (b) versus wind speed. Cox and Munk's data are also plotted (red circles).

The blanket adjustment factor used by Cox and Munk, along with its implicit relation to the PDF 4^{rth} order correction, is potentially highly variable (sea-state, stability, current, slick, ...). The strong sea-state observed during the present experiment may explain the quite high departure of the slope PDF from Gaussianity, depicted by b_o''=0.057, compared to the mean value of 0.04 computed by Cox and Munk for a wider range of wind speeds (from 0.5 to 14 m/s). In addition, Cox and Munk clearly observed values lower than 0.04 for wind speeds lower than 5 m/s and a SWH not exceeding 1 m. Therefore, the parameter b_o'' certainly depends more on the sea-state than on the sea-surface roughness.

As understood, this value impacts the variance estimation and the predicted occurrence of the infrequent but very large ocean slope components. This factor does strongly impact the shape of the PDF, and thus the corresponding optical and radar cross sections in quasi-specular reflections.

8.5 Conclusions

We have presented in this Chapter a re-do of the Cox and Munk experiment which aimed at DMSS retrieval through inversion of Tilt-Azimuth Map of Sun glitter optical photographs. A set of 25 photographs has been analyzed by the SORES processor along a path aligned with Jason's track, close to the Catalan coast. We have retrieved the DMSS profile along the track with a very good agreement compared to the altimeter data.

Estimated sea-surface mean square slopes range between 0.04 and 0.08 and are linearly proportional to the wind speed. Slope PDF Isotropies present quite strong variations from 0.8 to 0.5. The wind direction agrees very well with the ground truth given by ECMWF model and numerical models from INM.

A spectral analysis has been carried out to extract further parameters of the sea surface, such as wave direction, wavelength and long wave slope variance. These parameters have been estimated along the track, showing very consistent results. These additional parameters allowed us to improve the understanding of the long wave impact on the DMSS, which has been enhanced through simulations.

In particular, we have seen that a SWH of 2 meters could increase the slope variance of about 20%. The explanation comes from the tilting effect of the long waves on the small scale roughness. It has been shown that the direction of the wind-generated waves with respect to the wind direction significantly impacts the isotropy of the PDF. This effect has been clearly observed experimentally. The discrepancy between wind and waves orientations clearly lowers the anisotropy of the slope PDF, i.e., increases the SPI. In addition, we have shown that swell and wind misalignment can lead to estimation biases in the wind direction up to 15^o.

A comparison has been undertaken with Cox and Munk's results. The main difference in the processing of the data comes from the fact that they limitated the fit of the sea-surface slope PDF to maximum slopes of about 20-25^o, while we have here considered the whole image with detectable slopes up to 40^o. The motivation of this approach was to develop a background model, whose parameters are minimized during the inversion procedure. Therefore, we don't need any correction or so-called "blanket" factor—as introduced by Cox and Munk—to estimate the sea-surface slope variance. However, the slope variances are 20% higher than the ones estimated by Cox and Munk for high wind speeds. This is consistent with the fact that we observed wave heights two times bigger than the ones observed by Cox and Munk for the same wind conditions.

The non negligible contribution of the long wave slope variance in the overall mean square slope confirms that the sea-state affects considerably the estimation of the wind-related DMSS.

Furthermore, a strong departure of the PDF to Gaussianity has been observed during this experiment. It has been suggested that the parameter b_o'' is strongly dependent to SWH. Further experimental data taken for different wind speed and SWH conditions are needed to confirm this statement.

Chapter 9

Scatterometry with GNSS-R

This Chapter presents estimation of DMSS during the Eddy Experiment Flight by inversion of the bi-dimensional Delay-Doppler Maps. The method uses a Least-Square approach and permits to retrieve simultaneously at L-band the Total MSS, Slope PDF Isotropy and Slope PDF Azimuth. This work has been carried out in the frame of the OPPSCAT II ESA project (see [Germain *et al.*2003]).

The data set is first described with the specific delay and Doppler resolutions. Section (9.2) reports then the retracking and inversion procedures that have been carried out on the scatterometric data products. Furthermore, the estimated DMSS are analyzed in section (9.3) through their confidence interval length. Finally, the results are compared to SORES inversion and ground truth.

9.1 The data set

As it would have been too computationally extensive to analyze the full track, the latter was divided into 46 10-second long arcs, sampled every 50 seconds. The first arc starts at SOW=468008.63. Given the speed of the aircraft, one arc spans roughly 500 meters. Figure 9.1 shows a plot of those arcs while aircraft kinematic parameters are presented on figure 9.2.

The first processing step consists in performing a delay-Doppler PRN code despreading to coherently detect the direct signal (from GPS emitter) and the reflected signal (scattered by the sea-surface). We used the Starlab in-house software (Starlight) to produce three DDMs time-series (one per PRN), sampled into 46 arcs of 10 seconds each. The general strategy of the processing is to track the delay-Doppler of direct signal and then compute DDMs for both direct and reflected signals. As described in section (4.1) of Chapter 4, those DDMs actually represent the complex amplitude of incoming signals when processed with a delay-Doppler value slightly different from the estimated delay-Doppler center. The coherent integration time was set to 20 ms to ensure a Doppler resolution of 50 Hz. The delta-delay spans -40 to 40 correlation lags (i.e., +/- 1.95 μs) with a lag step (48.9 ns) and the delta-Doppler spans -200 Hz to 200 Hz with a step of 20 Hz. As a result, the Level 0 data for one PRN and one arc is a complex delay-Doppler-Time cube of size 81×21×500.

We have chosen to set the accumulation time T_a to 10 seconds so that each arc is characterized by a unique DDM, resulting from the sum of the amplitudes of 500 complex DDMs (or 500 "looks"). Thus, for each arc and each PRN, the Level 0b data is a real delay-Doppler map of size 81×21.

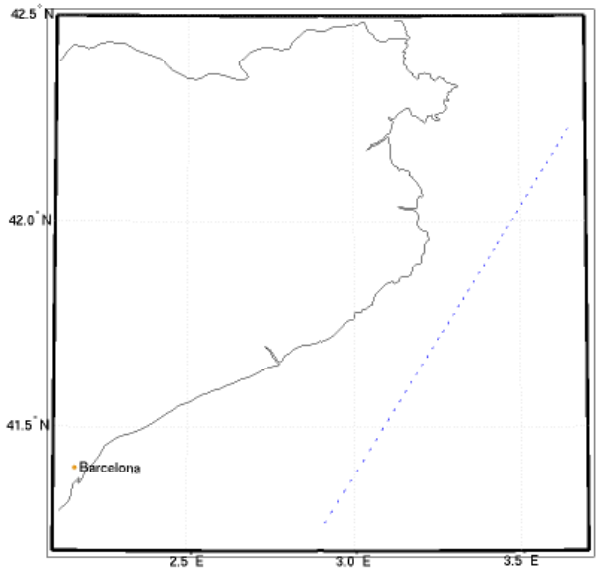

Figure 9.1: Map of the 46 10-second arcs considered along the track.

9.2 Retracking and inversion

9.2.1 The forward model

The model considers the average amplitude of the DDM. Since amplitude data are approximately Rayleigh distributed, it can be shown that the average amplitude is close to the square-root of the average power. Hence, the average amplitude of the DDM writes:

$$A(\tau, f) = \sqrt{\alpha.P(\tau, f) + g}. \tag{9.1}$$

$P(\tau, f)$ is the waveform model presented in section (3.3) of Chapter 3. As we do not claim to have a calibrated model, we also have introduced an overall scaling parameter α in the latter equation in order to fit model to data. For delays lower than one-chip, the DDM amplitude is not null but shows a constant value g (often called "grass level"). It can be shown that this value depends on the correlation length of a thermal noise corrupting the signal and the coherent integration time (see section (11.2) of Chapter 11 for further details).

To sum up, the proposed forward model features three parameters of interest and four "nuisance parameters". Those are:

- three DMSS characterizing the Gaussian slope PDF: Total MSS, isotropy (SPI) and azimuth (SPA),
- DDM delay-Doppler centers: τ_c and f_c,
- overall scaling parameter: α,
- grass level: g.

Other parameters necessary to run the forward model are recalled in Table 9.1.

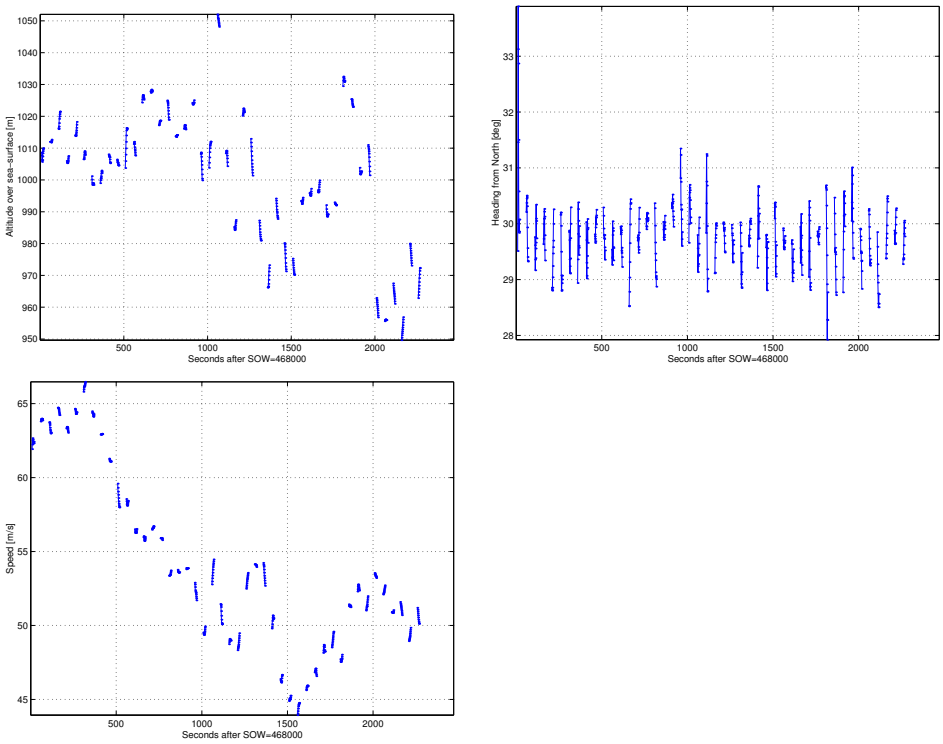

Figure 9.2: Altitude, heading (azimuth from North) and speed of the aircraft during the 46 10-second arcs.

9.2.2 Inversion scheme

As in the SORES procedure, we used a least-square approach. Let $A_d(\tau, f)$ be the data DDM and $A_\kappa(\tau, f)$ the model DDM corresponding to a κ vector of seven parameters (DMSS and nuisance parameters). The root mean square error (RMSE) between data and model is defined as the root mean square of residual:

$$\mathrm{RMSE}(\kappa) = \sqrt{\sum_{\tau,f} \left[A_d(\tau, f) - A_\kappa(\tau, f)\right]^2}, \tag{9.2}$$

Geometry	Aircraft:	Altitude, speed and heading provided at 1 Hz
	Satellite:	Elevation and azimuth provided at 1 Hz
Instrument	Antenna Pattern:	provided (see figure 9.3)
	Band:	L_1 (19 cm)
	GPS Code:	C/A
Processing	Integration Time:	20 ms
	Accumulation Time:	10 s
	Doppler span:	[-200 Hz , 200 Hz], 20 Hz step
	Delay span:	[-40 samples, 40 samples], 1 sample step

Table 9.1: Overview of the parameters necessary for running the DDM forward model.

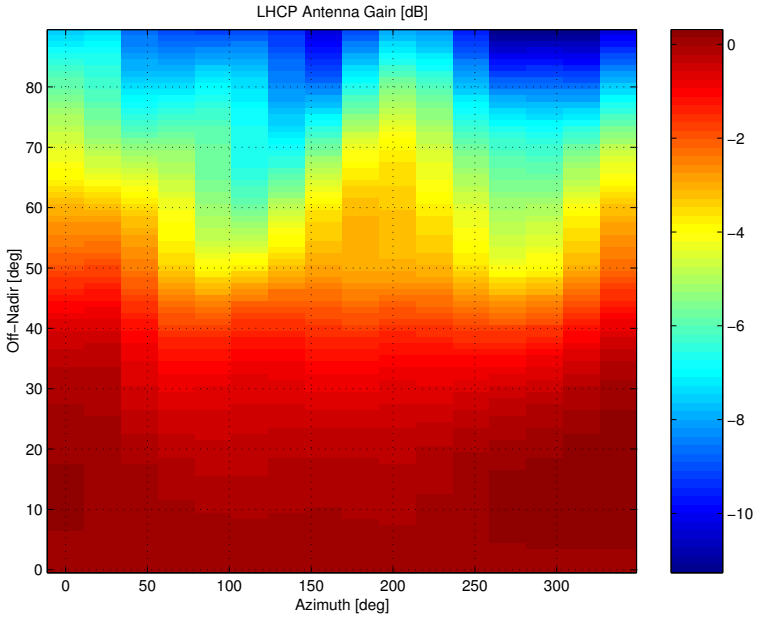

Figure 9.3: Power pattern of the LHCP antenna used to gather the GNSS-R signals (measurements provided by IEEC). It is a 3 dB antenna, having its cut-off at 55^o. It was mounted on the aircraft so that aircraft nose corresponds to azimuth 210^o.

and the estimator is the value minimizing this error:

$$\hat{\kappa} = \underset{\kappa}{\text{argmin}}\ \text{RMSE}(\kappa). \tag{9.3}$$

Theoretically, the absolute minimum of RMSE should be searched jointly over the seven parameters. In practice, this is not tractable and we have adopted the following sub-optimal strategy. First, the grass level is not optimized but *a priori* set to a value measured on data. This value is the average DDM amplitude in the domain such that delay is smaller than minus one-chip. Given the sampling, this value is estimated over $20 \times 21 \times 500 = 210,000$ samples and is therefore expected to be quite accurate. Second, the following two-step iterative algorithm was applied:

- In a first step, DMSS parameters are frozen while the three other parameters (scaling and centers) are optimized. This step is called *retracking*: given a shape for model DDM, the optimal translation is searched for in order to fit data. We recall that in GNSS-R altimetry, this operation is carried out over a waveform (a Doppler-cut in the DDM) to fine-estimating lapse between direct and reflected signals.
- In a second step, the delay-Doppler centers are frozen and the four other parameters (scaling and DMSS) are optimized. This step is called *inversion*: given a position for model DDM, the optimal shape is searched for in order to fit data.

Numerical optimization is carried out with a steepest-slope-descent algorithm based on Levenberg-Marquardt type adjustment ([Levenberg1944, Marquardt1963]). In practice, the DMSS is optimized by repeating this two-step sequence until convergence.

Two kinds of data are actually delivered by this processing. Magnitudes like delay-Doppler centers are Level 1 data that can be processed further to infer geophysical parameters. In particular, the processing of delay centers is the subject of GNSS-R altimetry

to recover sea-surface height. This can be done through the search of delay centroids (see [Aparicio *et al.*2002]) or through the retracking of the delay waveform (see [Ruffini *et al.*2003] and [Lowe *et al.*2002]). Although we will focus only on Level 2 data, namely the DMSS, we present hereafter the *scatterometric bias* which highlights how altimetric and scatterometric measurements are linked together, especially at low altitudes.

The scatterometric bias

This iterative algorithm somehow makes the implicit assumption that DDM "position" is only governed by center values while its "shape" is only DMSS dependent. If the latter statement is true, the former is only an approximation, for we know that at low altitude, DMSS also impacts the delay-Doppler DDM centers: this effect is called *scatterometric bias* in GNSS-R altimetry (see [Rius *et al.*2002]). Figure 9.4 illustrates this bias by showing two delay waveform models obtained for different MSS, such as $MSS_2 > MSS_1$. We recall that altimetry measurement consists in estimating the delay τ between the direct and reflected delay waveforms. It appears that sea-surface roughness tends to increase the delay: we have $\tau_2 > \tau_1$.

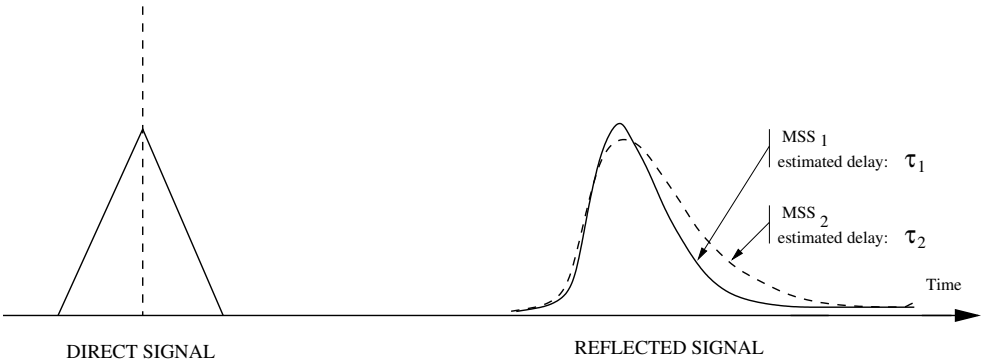

Figure 9.4: Scatterometric bias in the delay waveform.

Sensitivity analyses have been carried out to depict the *scatterometric bias* $\Delta\tau = \tau_2 - \tau_1$ with respect to SWH and the three parameters of the DMSS: MSS, SPI and SPA. We first generated an initial waveform with a given set of nominal parameters, as shown in Table 9.2. Then, we generated several model waveforms with the same set of parameters except one that spans a range of values around the nominal one. For each value of this parameter, a retracking of the initial waveform with the model waveform has been undertaken to evaluate the *scatterometric bias*.

MSS	SPA	SPI	SWH
0.025	0^o	0.55	2 m

Table 9.2: Set of nominal parameters for sensitivity analysis of parameter $\Delta\tau$.

First, sensitivity of $\Delta\tau$ to significant wave height is shown in figure 9.5 for the considered PRNs. Unlike RA, the significant wave height does not impact significantly the delay estimation. At this strong sea-state regime (SWH$\sim$2 m) the error is less than 1 cm for a discrepancy of 2 m in the SWH. This comes from the fact that the chip length in GNSS is much longer than the one used in RA. Therefore, the SWH parameter is not taken into account in the inversion.

However, figures number 9.6, 9.7 and 9.8 show the drastic impact of sea-surface roughness (respectively the wind strength related to MSS, SPI and SPA) on $\Delta\tau$. For instance, a bias of 1 meter in delay is reached when:

- the wind speed differs by 2 m/s,
- SPI is 0.25 lower than nominal,
- or SPA differs by 25^o.

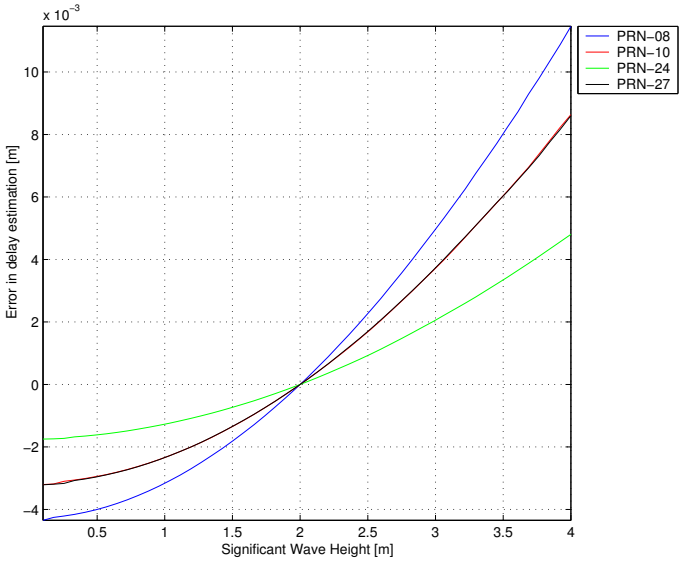

Figure 9.5: Sensitivity analysis of delay center to SWH. The nominal value is 2 m.

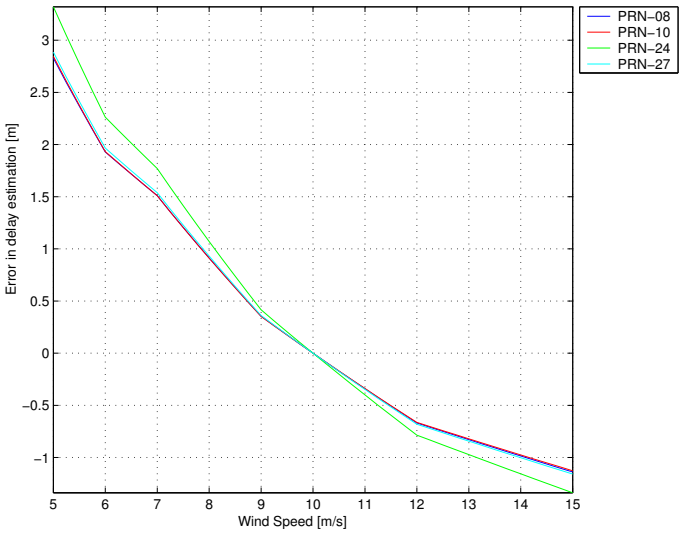

Figure 9.6: Sensitivity analysis of delay center to wind speed. The nominal value is 10 m/s (i.e., MSS = 0.025).

This sensitivity to DMSS comes from the relative size of the glistening zone (related to MSS) within the scattering area. The latter is defined as the support of the integral of the

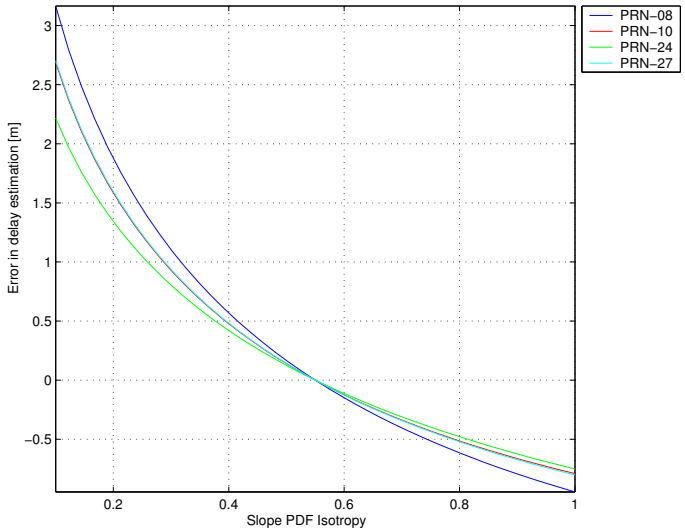

Figure 9.7: Sensitivity analysis of delay center to sea-surface slope PDF Isotropy (SPI). The nominal value is 0.55.

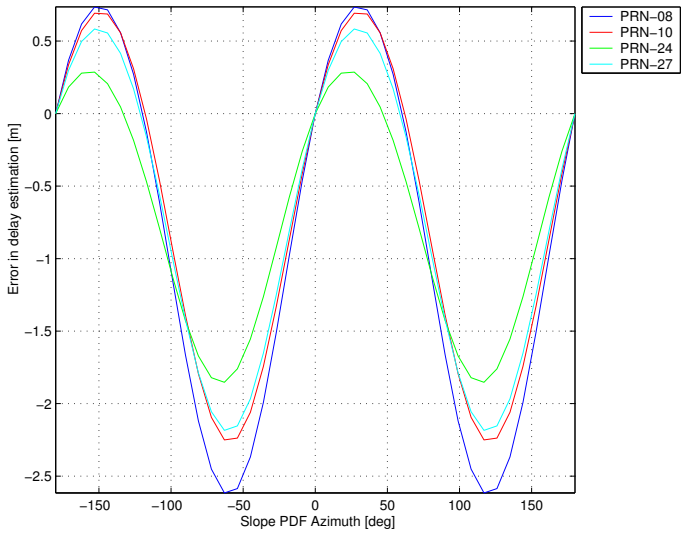

Figure 9.8: Sensitivity analysis of delay center to sea-surface slope PDF Azimuth (SPA). The nominal value is 0^o from North.

DDM waveform, which includes in addition to the glistening zone, the Woodward Ambiguity Function and antenna pattern. In the case of a low altitude receiver, the glistening zone corresponds to the smallest support and thus modulates strongly the return waveform. Note that these effects will significantly reduce at high altitude, since the glistening area is larger than the first chip zone. In a spaceborne scenario, the bias becomes constant.

We can anticipate that GNSS-R scatterometry from space will be quite challenging. The main issue addresses the spatial resolution, for the sensitivity of the DDM to DMSS appears at higher delays and Doppler frequencies than those limited by the first chip zone. Therefore, the corresponding spatial scales of the sea surface are too large compared to sea-surface roughness variations. As part of the OPPSCAT II ESA project, Starlab developed a multi-look technique which aims at producing high-resolution profiles of absolute mean square slope [Germain and Ruffini2002].

9.2.3 Empirical adjustments

The first guesses provided to the algorithm were:

- DMSS are initialized to values consistent with expected sea-state: MSS=0.025, SPA=0^o, SPI=0.65.
- Delay-Doppler centers are set to zero.
- Scaling is set to 1 and both data and model DDMs are normalized to have their maxima to 1.

The fit was not performed over the total delay-Doppler domain. As a matter of fact, we know that all useful signal is comprised in the delay range [-1 chip,+1 chip]. Therefore, only this domain was used.

9.3 Analysis of the results

In this section, we present the results obtained after inversion. Note that comparison with ground truth as well as geophysical interpretations are beyond the scope of this section and will be addressed below in section (9.4).

9.3.1 Estimated DMSS

Figure 9.9 shows the estimated DMSS together with their formal confidence interval length (CIL). The Total MSS increases along the track of the plane. PRNs 08 and 24 are pretty similar, whereas PRN 10 seems to be biased by a positive constant. As shown by the CIL, Total MSS is better estimated with PRNs of high elevation, whereas azimuth is better captured with grazing (and therefore more direction-sensitive) PRNs. Furthermore, there is a very good inter-PRN agreement in estimation of isotropy: the three PRNs do have the same trend for SPI.

Note that the estimation of SPA is degenerate in two particular cases: when the transmitter is at zenith or when the receiver moves towards the transmitter [Cardellach and Ruffini2000]. In these two cases, the delay-Doppler lines that map the glistening zone are symmetric around the receiver direction. Hence, one cannot distinguish between a slope PDF and its mirror image about the receiver direction. Here, PRN 08 has its elevation comprised between 74 and 83 degrees. It is then very likely that the SPA estimated for this PRN is degenerate. For this reason, we have added on the plot of figure 9.12 the mirror image of the SPA about the receiver direction (30^o from North). We also note that the azimuth of PRN 10 decreases down to 230^o at the end of the track, quite close from 210^o (aligned with the receiver's direction).

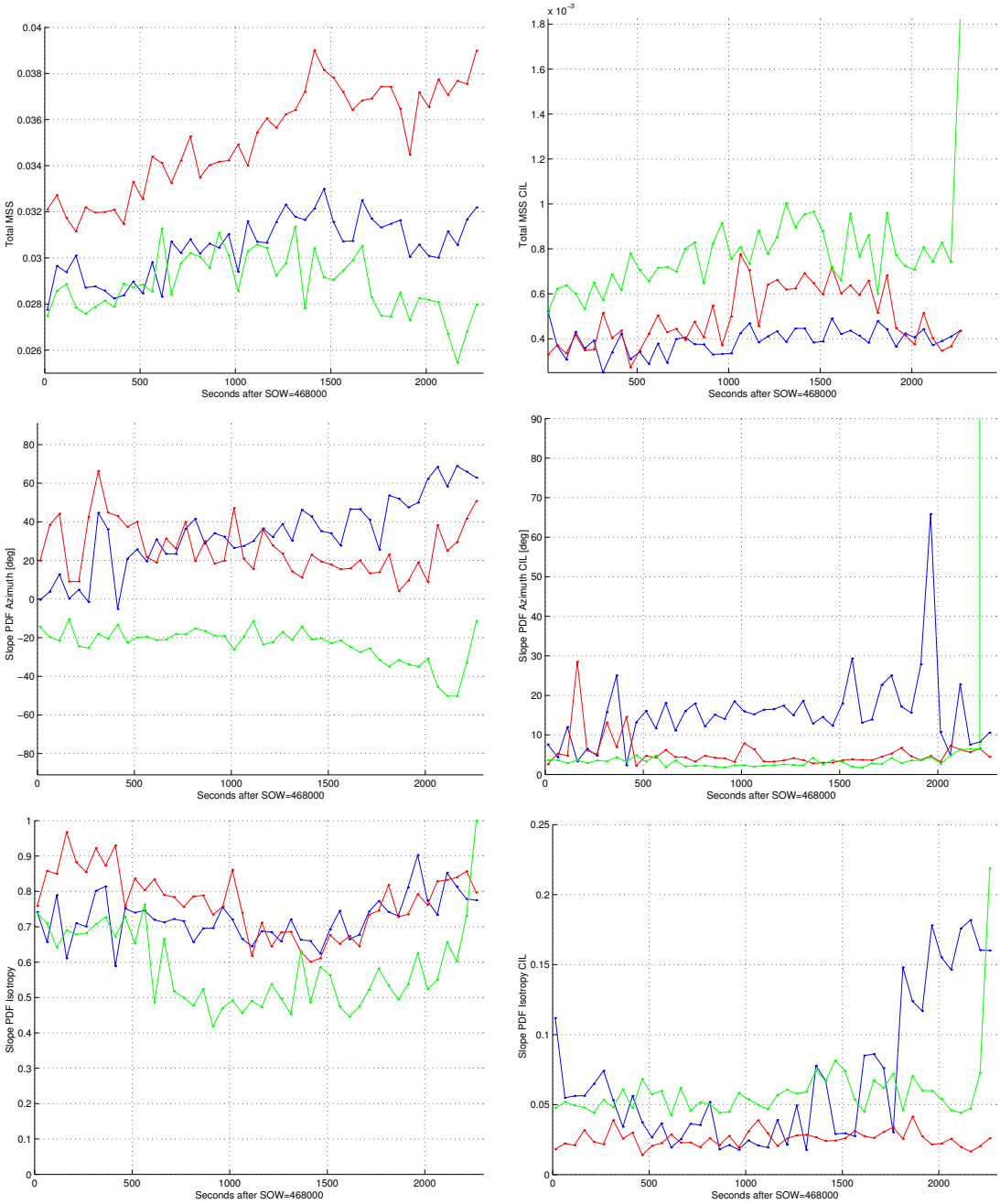

Figure 9.9: Estimated DMSS along the 46 10-second arcs for PRNs 08 (blue), 10 (red) and 24 (green). **First column**: estimated values. **Second column**: formal confidence interval length (CIL) of estimated values. **First row**: Total MSS. **Second row**: Slope PDF Azimuth. **Third row**: Slope PDF Isotropy.

PRN	**Total MSS** ($\times 10^{-3}$)		**SPA** (deg)		**SPI**	
	Trend	CIL	Trend	CIL	Trend	CIL
08	28 to 32	0.5 <	0 to 65	70 <	0.75 to 0.65 to 0.8	0.2 <
10	32 to 39	0.8 <	20 to 35	30 <	0.9 to 0.6 to 0.8	0.04 <
24	28 to 28	1 <	-20 to -20	5 <	0.75 to 0.5 to 1	0.07 <

Table 9.3: Analysis of estimated DMSS of figure 9.9.

9.3.2 Convergence and residual

Figure 9.10 illustrates the fast convergence of the optimization. After ten steps of retracking-inversion, a RMSE minimum is obtained and estimated values are stable. The graphs clearly show the monotonic variations of the three parameters of DMSS as well as delay and Doppler centers.

Figure 9.11 gives an example of DDMs aspects as well as the residual structure. High error zones generally correspond to higher delays or intermediate Doppler frequencies. Let us emphasize that the final RMSE never exceeds 2.5%. Note that these graphs resemble the graphs of figure 8.6, illustrating the complete analogy between the TAM and DDM sea-surface mappings.

9.4 Comparison of optical and L-band derived DMSS

Figure 9.12 presents Total MSS, Slope PDF Azimuth and Slope PDF Isotropy along the aircraft track between latitudes 41.2^o and 42.2^o. Black diamonds stand for SORES estimations and the blue, red and green curves for GNSS-R ones (PRNs 08, 10 and 24, respectively). Additional information when available in Jason's GDR data has been added, such as MSS in Ku- and C-bands and wind direction from ECMWF. Swell direction from the SORES spectral analysis has also been considered.

Total MSS

Total MSS has been plotted in log-scale in order to compare different frequency measurements more easily. The common trend for all bands is that slope variance increases with latitude until reaching a relative plateau. Measurements of PRNs 08 and 24 show good agreement while PRN 10 seems to be somewhat up-shifted. As expected, we observe that the level and dynamic of MSS decrease with longer wavelength: optical, Ku-, C- and L-band, in this order. Nevertheless, the level and dynamic of GNSS-R plots (especially PRN 10) seem a bit large for L-band measurements, when compared to C-band. We recall however that Jason's MSS have been obtained through the relationship MSS=κ/σ^o, κ being an empirical parameter accounting for calibration offsets. Here, we have set κ=0.45 for C-band and 0.95 for Ku-band but an uncertainty certainly remains on this parameter, making the overall levels of Jason's plots unsure.

Slope PDF Azimuth

The Slope PDF Azimuth estimation shows very consistent results in both L-band and optical regimes when comparing to the wind direction provided by the ECMWF model. Following wind propagation, the ground truth states that wind direction is around -20^o from North at high latitudes of the track and increases progressively when going South to reach a value of about 30^o at latitude 41.2^o.

Figure 9.10: Evolution of DMSS, delay center, Doppler center and RMSE values through the convergence process (here for PRN 10). Iterations number 0, 2, 4, 6, 8, 10 are respectively plotted in blue, red, green, black, clear blue and magenta. **First column**: DMSS values with, from top to bottom, the Total MSS, SPA and SPI. **Second column**: From top to bottom, delay center, Doppler center and RMSE.

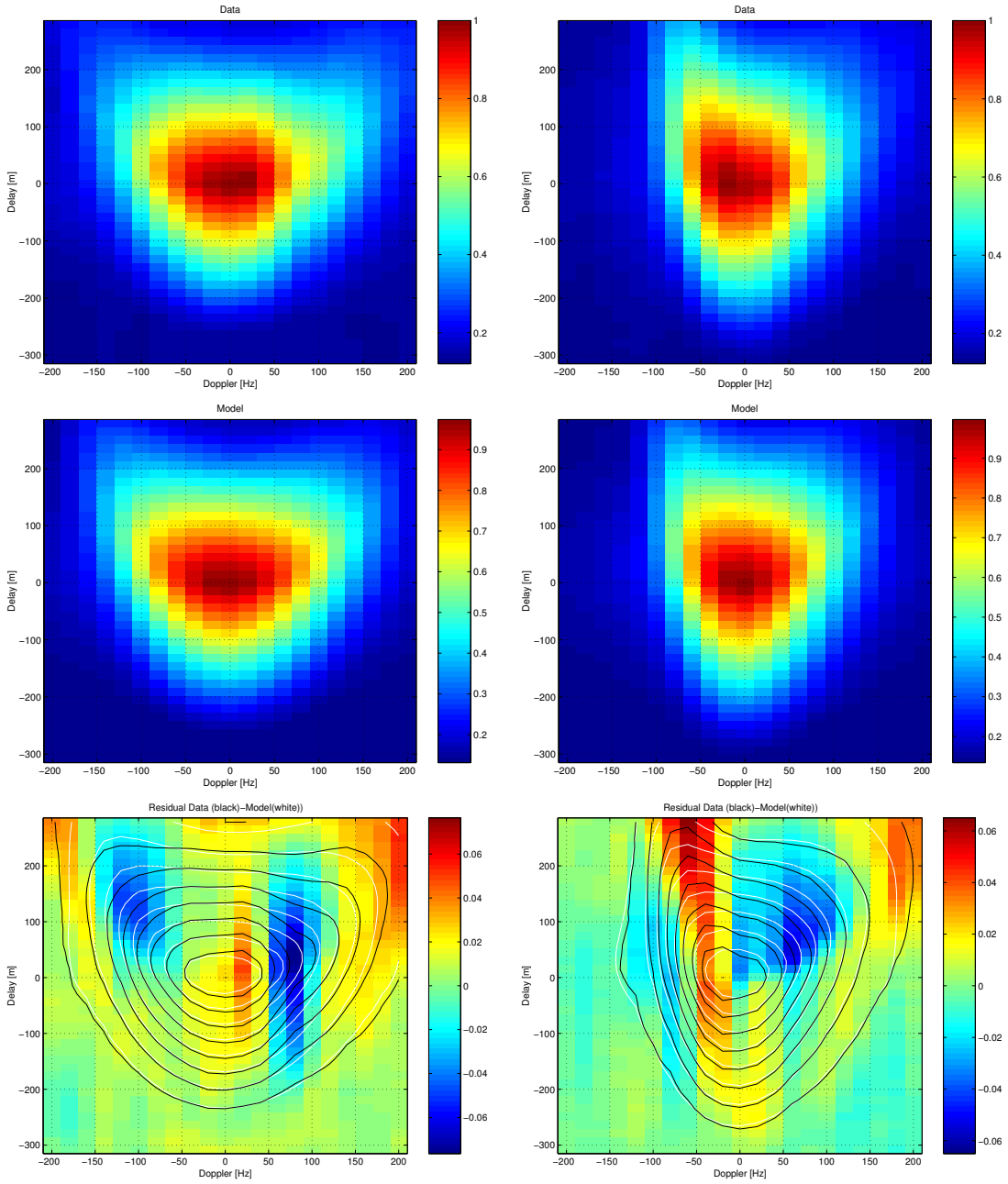

Figure 9.11: Examples of data and best-fit model DDMs. Those correspond to Arc01. **First column**: PRN 08. **Second column**: PRN 24. **First row**: Data DDMs. **Second row**: Best-fit Model DDMs. **Third row**: Data-model residual.

According to ECMWF data and SORES spectral analysis, wind and swell were slightly misaligned. PRN 08 (or its mirror image) matches very well the swell direction. So does PRN 10 along most of the track. This result underlines the fact that GNSS-R is not sensitive to wind only and that swell has a strong impact too. PRN 24 has a different behavior, in line with SORES. Those two measurements agree relatively better with wind direction, although a discrepancy of 30^o is observed at the beginning of the track.

Slope PDF Isotropy

It is worthy reminding that Elfouhaily's spectrum predicts a SPI value of 0.65, hardly sensitive to wind speed. Here, we note that SPI varies quite significantly along the track for both GNSS-R and SORES. The important departure observed from the 0.65 nominal value is probably a signature of an immature sea and presence of strong swell. Note that further research should be undertaken in order to better understand the potential information contained in this product.

9.4.1 Link to wind speed

On figure 9.13, we have plotted the estimated total MSS versus Jason's wind speed together with two theoretical links:

- Elfouhaily's sea-height spectrum, integrated for different cut-off wavelengths,
- An empirical model proposed by Katzberg for L-band, based on a modification of Cox and Munk's relationship: MSS=$0.9.10^{-3}\sqrt{9.48U_{10} + 6.07U_{10}^2}$.

We see that both SORES and GNSS-R estimations follow the Elfouhaily's model trend (integrated at 3 wavelengths) but give higher values of MSS (from to 20 to 40% up-shifted). Actually, estimations of PRNs 08 and 24 are very well fitted by Elfouhaily's spectrum integrated down to one wavelength only. The 20% discrepancy can be explained by a strong sea-state with a SWH twice as high as the one observed during the Cox and Munk's experiment (2 m compared to 1 m) for the same wind conditions. At any rate, those results tend to show that the wind to MSS link is not straightforward and that the MSS should probably be considered as a self-standing product for oceanographic users.

9.5 Conclusions

We have reported the first inversion of GNSS-R full Delay-Doppler Map for the retrieval of the sea-surface directional mean square slope. In addition, we compared the estimated DMSS with those obtained by the SORES data inversion.

Our results show that both optical and L-band total MSS are 20% higher than what predicted by Elfouhaily's model for the observed wind speed (9 to 13 m/s). The SPA estimated by GNSS-R matches the swell direction with good accuracy for at least 2 out of 3 PRNs. A geophysical product has been put forward: the slope PDF isotropy which can be related to wind/wave misalignement as well as sea degree of development. The analysis highlighted the important impact of sea-state (SWH) in addition to wind stress over DMSS. Speculometry being sensitive to slope processes over a wide range of scales, the link between DMSS and wind is not straightforward: total MSS and SPA are definitely impacted by swell. Quantitatively, the 20% bias observed in SORES results can be explained by SWH. Other geophysical parameters could affect the sea-surface roughness. For instance, it was found by [Huang *et al.*1973] that MSS is extremely sensitive to the change of current conditions. They even suggested to use the

sea-surface roughness parameter as a measure of local current changes. Consequently, DMSS can and should be studied as an independent parameter, of intrinsic independent geophysical value.

Let us finally emphasize that the flight was not optimized for speculometry (1000 m altitude, 50 m/s speed) and that higher/faster flights are needed in the future in order to consolidate the concept of DDM inversion for DMSS estimation.

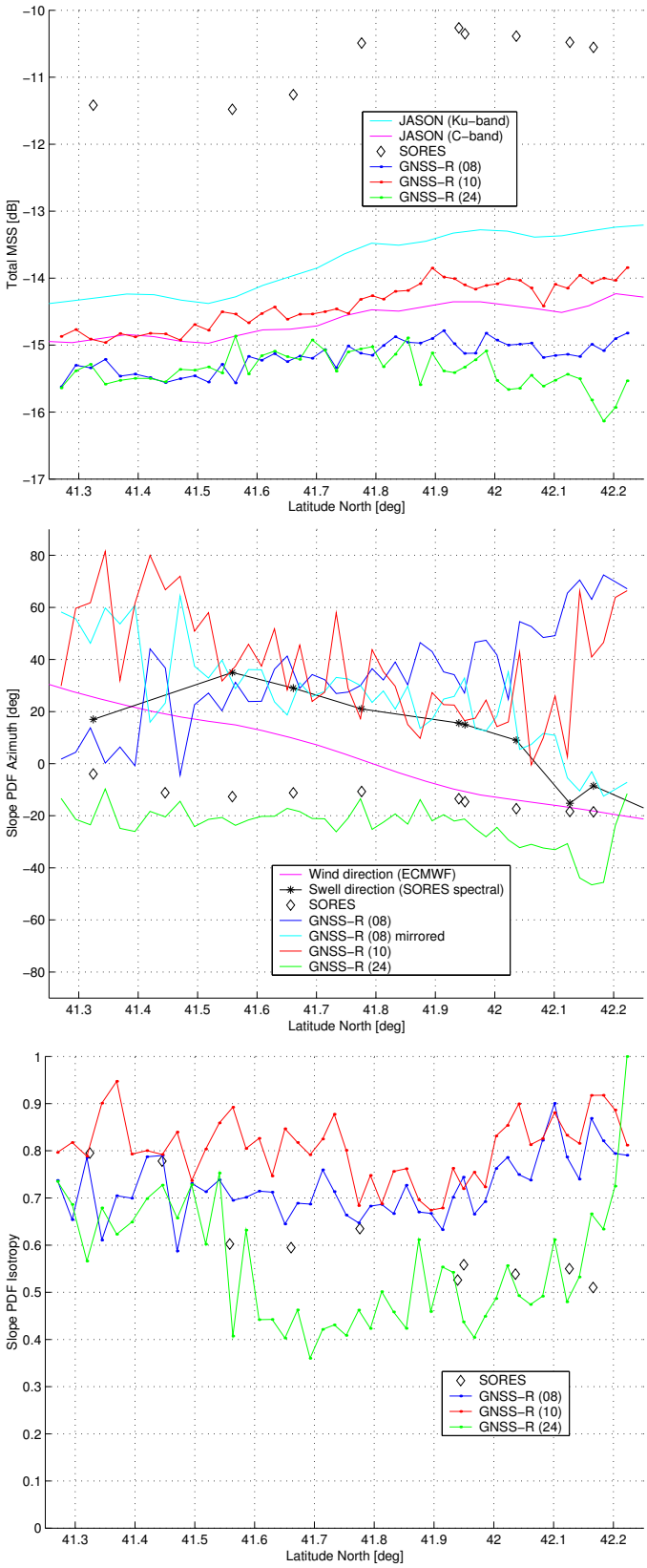

Figure 9.12: DMSS estimated along the aircraft track. **First row**: Total MSS (in dB). **Second row**: Slope PDF Azimuth. **Third row**: Slope PDF Isotropy.

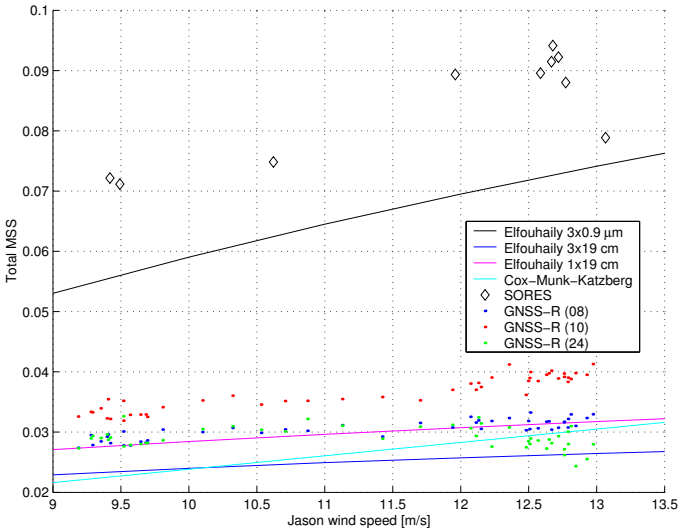

Figure 9.13: Total MSS versus Jason's wind speed.

Part IV

Other GNSS-R Applications

Chapter 10

Sensitivity to Salinity

The goal of this Chapter is to analyze the sensitivity of GNSS reflections to salinity through a simple ground experiment. The Salpex Experiment (a Starlab/Ifremer Contract) focused on dielectric mapping sensitivity and methods at L-band (see [Soulat and Ruffini2003]). The goal is to extract absolute reflectance measurements from a salty surface by measuring the power interference pattern at different incidence angles. The main strategy is to exploit the long time scales available to extract measurements, which allows, in principle, to average out other effects.

This report is divided into three main sections. The first section presents the Salpex experimental campaign, where we studied reflections from a flat surface, over a swimming pool, with different salinities. Section (10.2) addresses the theoretical analysis of water dielectric constant detection. For this purpose the received power is modeled. Section (10.3) is dedicated to the data analysis.

10.1 Experimental campaign

The campaign gathered reflected GNSS signals over a small swimming pool along with direct signals with one Right Hand Circularly Polarized (RHCP) antenna. Note that a similar experiment was carried out by [Kavak *et al.*1996].

10.1.1 Description

As shown in figure 10.1, the antenna is deployed to gather interferences between direct and reflected GNSS signals. The antenna is at h=56 cm above the surface (d=15 cm). The output of the antenna is then gathered by a GPS receiver. It is expected, as presented in the following section, to get an interference pattern in power with the variations of the elevation of the satellite.

Two kinds of data sets have been recorded with the same experimental set-up:

- **Salted water**: the first recordings took place the 25^{th} and 26^{th} of November 2002, with a water conductivity ranging between 42 and 43 mS (29 to 30 psu). The water surface temperature ranged between 9 and 11.3 degrees Celsius.
- **Pure water**: the second set of recordings took place the 28^{th} and 29^{th} of November 2002, with a water conductivity ranging between 1.1 and 1.2 mS (1 psu). The water surface temperature ranged between 10 and 14 degrees Celsius.

These experimental campaigns have been carried out for the same configuration of the satellites in view (the GPS constellation has a period of one sideral day, which corresponds to 24

hours minus 4 minutes). The two recordings made for each scenario is an attempt to check the repeatability of the interference pattern and get an estimation of the noise.

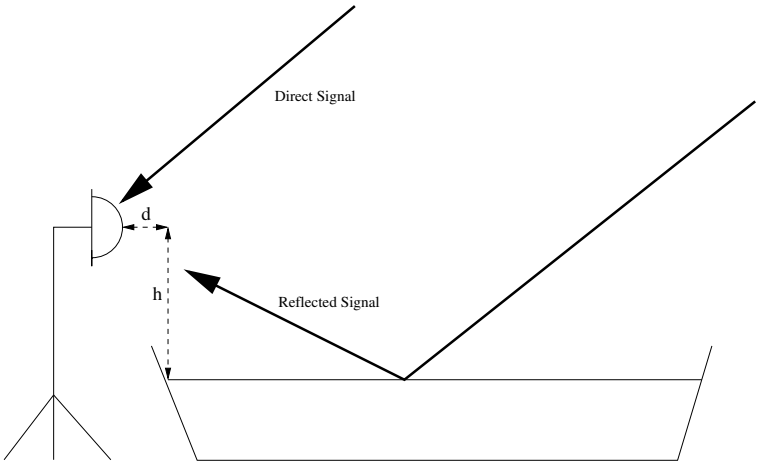

Figure 10.1: Geometry of the Salpex Experiment.

10.1.2 Instrumentation

The material used for this campaign (see figure 10.2) is:

- a small swimming pool, containing approximately 1 m^3 of salted/pure water (we thank Pablo Sedo for lending us his swimming pool),
- a tripod where the antenna is fixed,
- one RHCP antenna, Allan Osborne Associates (ESTEC/ESA),
- one TurboRogue receiver (ESTEC/ESA), delivering the GNSS observables,
- one portable computer (Starlab).

10.1.3 Satellites in view

Two satellites have been used to analyze the data sets. PRNs 15 and 17 seemed to be the appropriate candidates according to the available space window plotted in green in figure 10.3. This green mask represents the area where the GPS signal reflections are supposed to be free of shadowing phenomena due to the environment of the swimming pool, and therefore only the satellite within this mask can be taken into consideration for further analysis. Each colored arc represents the position of a GPS satellite during the experiment. The PRN number is closed to the beginning of the data. The clockwise angles stand for satellite azimuths and the center point of the graph corresponds to 90^o elevation angle.

10.2 Theoretical analysis

In this experiment the reflected signal writes, under the Fresnel assumption, simply as the polarization matrix times the incident signal:

$$\begin{bmatrix} E_R^s \\ E_L^s \end{bmatrix} = \begin{bmatrix} U_{RR} & U_{LR} \\ U_{RL} & U_{LL} \end{bmatrix} \begin{bmatrix} E_R^i \\ E_L^i \end{bmatrix}. \tag{10.1}$$

Figure 10.2: Salpex experimental campaign.

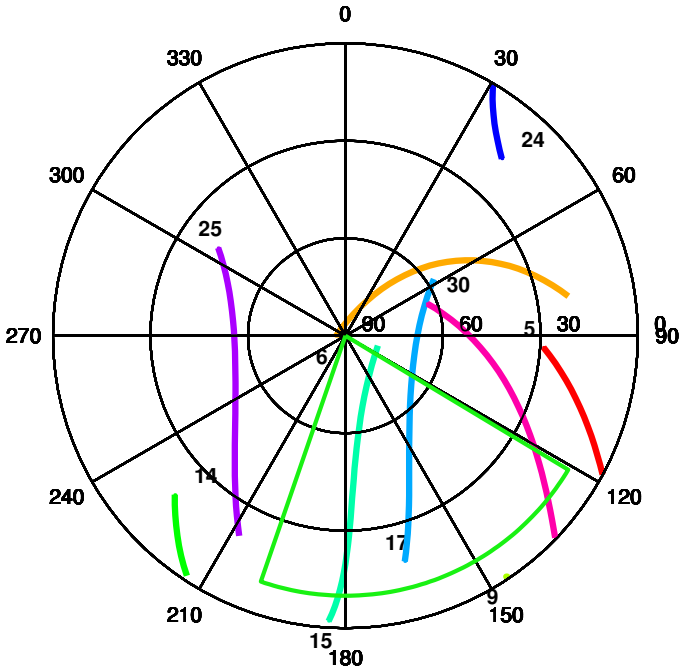

Figure 10.3: Satellites in view during Salpex experiment. Each colored arc represents the position of a GPS satellite during the experiment. The PRN number is closed to the beginning of the data. The green mask represents the area where the GPS signal reflections are supposed to be free of shadowing phenomena due to the environment of the swimming pool, and therefore only the satellite within this mask can be taken into consideration for further analysis.

The polarization matrix, expressed in the circular basis, reduces to:

$$\begin{bmatrix} U_{RR} & U_{LR} \\ U_{RL} & U_{LL} \end{bmatrix} = \frac{1}{2}\begin{bmatrix} \mathcal{R}_\perp + \mathcal{R}_{||} & \mathcal{R}_\perp - \mathcal{R}_{||} \\ \mathcal{R}_\perp - \mathcal{R}_{||} & \mathcal{R}_\perp + \mathcal{R}_{||} \end{bmatrix}, \tag{10.2}$$

where the local Fresnel coefficients are given by:

$$\begin{aligned} \mathcal{R}_\perp &= \frac{\sin\gamma - \sqrt{\epsilon - \cos^2\gamma}}{\sin\gamma + \sqrt{\epsilon - \cos^2\gamma}} \\ \mathcal{R}_{||} &= \frac{\epsilon\sin\gamma - \sqrt{\epsilon - \cos^2\gamma}}{\epsilon\sin\gamma + \sqrt{\epsilon - \cos^2\gamma}}. \end{aligned} \tag{10.3}$$

The parameter ϵ is the complex dielectric constant of sea water and γ is the elevation angle. The latter is defined as the angle between the incident field direction and the water surface plane: γ=90^o for a satellite at zenith.

In this case, **the de-polarization only comes from the dielectric nature of sea water**. Assuming that the surface of the water in the swimming pool is flat, we conclude that the received power P is proportional to the squared Fresnel coefficients.

10.2.1 Received power versus elevation angle

The total field received by the antenna is the sum of direct signal and specularly reflected signal. The reflected signal arrives with a phase shift that can be written $\phi = 4\pi h/\lambda\sin\gamma$, with λ the wavelength (we recall here λ=0.19 m). The interference between the incident and scattered field writes:

$$\begin{bmatrix} E_R^i \\ E_L^i \end{bmatrix} + \begin{bmatrix} E_R^s \\ E_L^s \end{bmatrix} e^{i\phi}, \tag{10.4}$$

where E_R^i (E_L^i) is the right (left) component of the incident complex field, E_R^s (E_L^s) is the right (left) component of the scattered complex field.
Introducing the polarization matrix, we get:

$$\begin{bmatrix} E_R^i \\ E_L^i \end{bmatrix} + \begin{bmatrix} U_{RR} & U_{LR} \\ U_{RL} & U_{LL} \end{bmatrix}\begin{bmatrix} E_R^i \\ E_L^i \end{bmatrix} e^{i\phi} = \begin{bmatrix} E_R^i + (U_{RR}E_R^i + U_{LR}E_L^i)e^{i\phi} \\ E_L^i + (U_{RL}E_R^i + U_{LL}E_L^i)e^{i\phi} \end{bmatrix}. \tag{10.5}$$

The emitted GPS signal is assumed purely Right Hand Circular Polarized and the reflection off the sea-surface makes it mostly Left Hand Circular Polarized at reception. With E_L^i=0, the interference field becomes:

$$E_R^i \begin{bmatrix} 1 + U_{RR}e^{i\phi} \\ U_{RL}e^{i\phi} \end{bmatrix}. \tag{10.6}$$

The received power is modulated by the gain pattern of the RHCP antenna in both right polarization (G^R) and left polarization (G^L). We finally obtain:

$$P \propto \left| G^R(1 + U_{RR}e^{i\phi}) + G^L U_{RL}e^{i\phi} \right|^2. \tag{10.7}$$

We recall that:

- ϕ is related to γ and h by the relation $\phi = 4\pi h/\lambda\sin\gamma$,
- the polarization coefficients U_{RR} and U_{RL} are functions of γ and the water dielectric constant ϵ (which is function of salinity S and surface temperature T),

- the antenna gains G^R and G^L are function of the elevation γ and the azimuth of the satellite.

During our experimental campaigns, h is known and fixed, S and T measured. The received power becomes a function of γ only. Defining the polarization parameters $U_{RR} = |U_{RR}|\, e^{i\phi_{RR}}$ and $U_{RL} = |U_{RL}|\, e^{i\phi_{RL}}$, equation 10.7 rewrites:

$$\begin{aligned} P \propto {G^R}^2 + {G^R}^2 |U_{RR}|^2 + {G^L}^2 |U_{RL}|^2 \\ +2{G^R}^2 |U_{RR}| \cos(\phi + \phi_{RR}) + 2G^R G^L |U_{RL}| \cos(\phi + \phi_{RL}) \\ +2G^R G^L |U_{RR}|\, |U_{RL}| \cos(\phi_{RL} - \phi_{RR}). \end{aligned} \tag{10.8}$$

10.2.2 Dielectric constant model

A more detailed discussion about the properties of the dielectric constant ϵ can be found in Ulaby et al. [Ulaby *et al.*1986], (vol III, p2019). In general, ϵ is complex, consisting of a real part, ϵ', and an imaginary part, ϵ'':

$$\epsilon = \epsilon' - j\epsilon''. \tag{10.9}$$

Usually, ϵ' is referred as the *permittivity* of the material, whereas ϵ'' is occasionally referred to as the *dielectric loss factor* of the material.

In the microwave range, the permittivity of ocean water is a complex function of the temperature T, salinity S, and also of microwave frequency f. Usually, the Debye or more adequate Cole-Cole relaxation models are used for microwave remote sensing applications. The basic idea is to consider that the permittivity of sea water will be a slight deviation from that of pure water due to addition of ionic constituents. At low microwave frequencies ($f <$ 20 GHz), the dielectric constant of sea water can thus be modeled by a Debye relaxation plus a conductivity term of the form:

$$\epsilon_{sw}(T, S, f) = \epsilon_{sw}^{\infty}(T, S) + \frac{\epsilon_{sw}^{o}(T, S) - \epsilon_{sw}^{\infty}(T, S)}{1 - 2\pi f \tau_{sw}(T, S)} + j\frac{\sigma_i(T, S)}{2\pi\epsilon_o f}, \tag{10.10}$$

where

- $\epsilon_{sw}^{\infty}(T, S)$ is the high-frequency (or optical) limiting value of the dielectric constant of saline water,
- $\epsilon_{sw}^{o}(T, S)$ is the static value of the dielectric constant of saline water,
- $\tau_{sw}(T, S)$ is the relaxation time in seconds,
- ϵ_o is the permittivity of free space ($\epsilon_o = 8.854 \times 10^{-12}$ F·m^{-1}),
- $\sigma_i(T, S)$ is the ionic conductivity of the aqueous saline solution in S·m^{-1}.

These Debye parameters depend upon the temperature T and the concentration of the ionic salt. We choose to represent the concentration in terms of S, but it can be represented in term of chlorinity or normality. Previous works which describe models of permittivity of sea water and aqueous saline solutions are those of Stogryn, [Klein and Swift1977] and Swift, Aggarwal and Johnston, Singh et al., and [Ellison *et al.*1998]. A complete and critical discussion of the literature survey concerning the dielectric properties of sea water and aqueous ionic solutions can be found in [Ellison *et al.*1996].

Briefly, the basic assumption behind all the proposed interpolation models is that for a fixed temperature, and in the frequency range 0-100 GHz, the permittivity of pure water and

that of an aqueous saline solution (sea water or a more simple substance) is described by a simple Debye function. The second assumption is that for a given electrolyte, the Debye parameters are related to the Debye parameters of pure water by a linear function of the concentration.

In the present work, we will only consider the model developed by Klein and Swift (based on Stogryn's model). Aqueous solution of NaCl have been used to estimate the permittivity data. Stogryn reasoned that since NaCl is the principal ionic constituent of sea water, the dielectric behavior of sea water will not be significantly different of that of an aqueous NaCl solution of the same salinity. Moreover, Stogryn points out that there is no evidence to indicate that ϵ_{sw}^{∞} depends on salinity and consider the variation of this Debye parameter with temperature to be very low so that it is considered constant. Klein and Swift used exactly the same analytical expressions than Stogryn for the Debye parameters but modified them numerically by taking into account the measured data of Ho and Hall which were performed at 1.43 GHz for an NaCl solution.

The following graphs show ϵ' and ϵ'' as a function of temperature for a few representative salinities (figure 10.4) and as function of salinity for a few representative temperatures (figure 10.5), for Klein and Swift's model at 1.575 GHz.

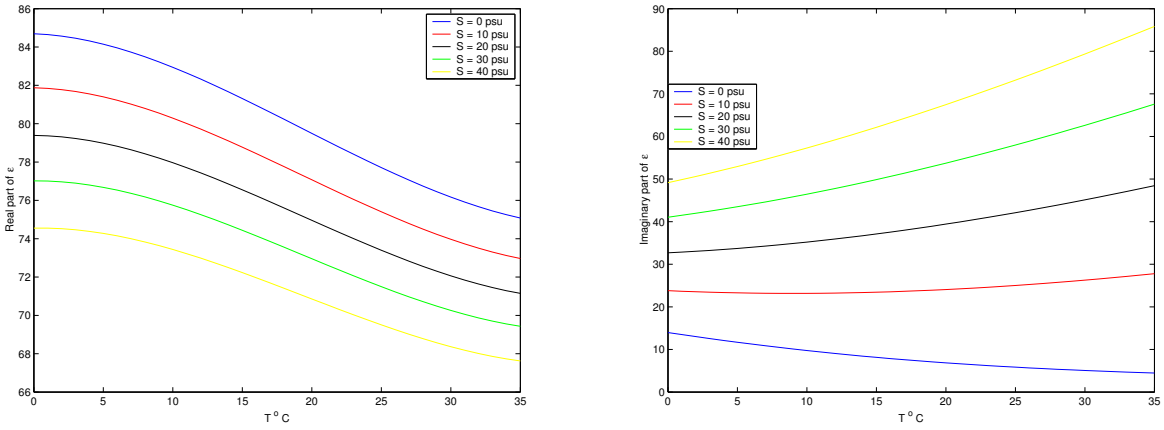

(a) Permittivity

(b) Dielectric loss factor

Figure 10.4: Dependence of the real and imaginary parts of the dielectric constant as function of temperature T for different salinities (in psu). Klein and Swift's models at 1.575 GHz.

The sensitivity to salinity changes as a function of temperature is clearly visible. As found by Razer et al. in the decimeter band, the real part of the complex permittivity of ocean water depends weakly on salinity: a decrease in ϵ' by no more than about 10 units results from a change in salinity from 0 to 40 psu. On the other hand, the imaginary part of the dielectric constant is much more sensitive to salinity than its real part because of ionic conductivity. Thus, when the salinity is changed from 0 to 40 psu at 1.575 GHz, the value of ϵ'' increases by about 40 to 90 units depending on temperature: the sensitivity to salinity changes of the dielectric loss factor is much higher (more than twice) at warm sea temperatures than at cold temperatures.

Note that the reflectivity, defined as the square of the absolute value of the Fresnel coefficient, is not very sensitive to salinity, as shown in figure 10.6 in parallel polarization.

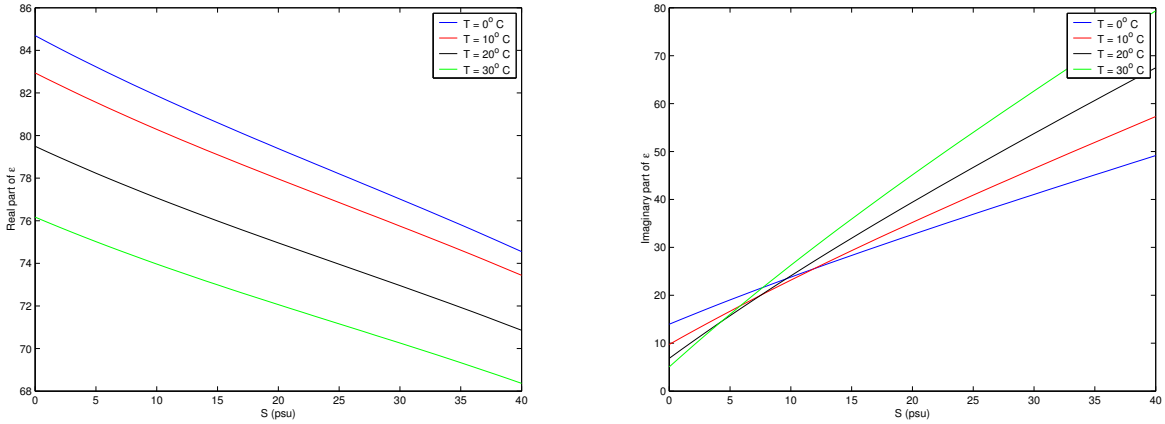

(a) Permittivity

(b) Dielectric loss factor

Figure 10.5: Dependence of the real and imaginary parts of the dielectric constant as function of salinity S for different temperatures. Klein and Swift's model at 1.575 GHz.

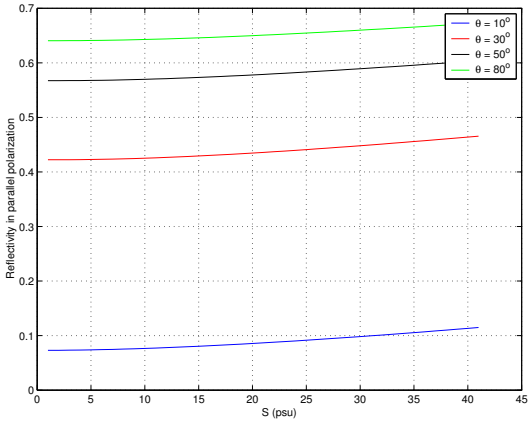

Figure 10.6: Dependence of the reflectivity in parallel polarization as a function of salinity S for different elevation angles.

Penetration depth

For a plane wave propagating in a lossy medium in the z direction, the electric-field intensity at a point z is given by:

$$E(z) = E_o \exp(-Cz), \tag{10.11}$$

where E_o is the field intensity at z=0, and:

$$C = A + jB, \tag{10.12}$$

where C, A and B are the propagation, absorption and phase constants of the medium. They are related to ϵ by:

$$\begin{aligned} A &= k_o |Im(\sqrt{\epsilon})|, \\ B &= k_o Re(\sqrt{\epsilon}). \end{aligned} \tag{10.13}$$

where $k_o = 2\pi/\lambda_o$ is the wave number in free space, and λ_o is the free-space wavelength in meters. Ignoring scattering losses in the medium, the power density $S(z)$ at a point is given by:

$$S(z) = S_o \exp(-\kappa_a z), \tag{10.14}$$

where κ_a is the power absorption coefficient and is related to A by:

$$\kappa_a = 2A. \tag{10.15}$$

Often, κ_a and A are each expressed in dF·m^{-1} through the relation:

$$\kappa_a(\mathrm{dB} \cdot \mathrm{m}^{-1}) = 4.34\kappa_a(\mathrm{Np} \cdot \mathrm{m}^{-1}). \tag{10.16}$$

A related quantity of interest in remote sensing is the penetration depth δ_p. For a free scatterer medium:

$$\delta_p = 1/\kappa_a = \frac{\lambda_o}{4\pi Im(\sqrt{\epsilon})}. \tag{10.17}$$

The depth of the skin-layer δ_p (depth of the electromagnetic wave's penetration) at frequency

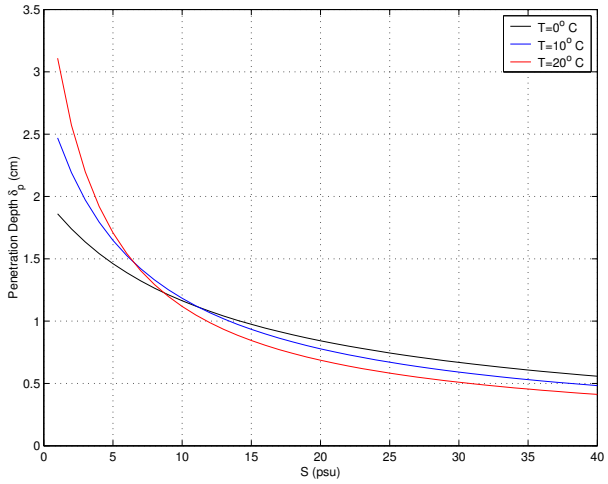

Figure 10.7: Penetration depth in cm versus salinity for different temperatures. Klein's model at 1.575 GHz.

f changes in relation to the water parameter S and T, since ϵ is dependent on this parameters. It can be calculated by the formula 10.17.

The calculations show that the depth of penetration of millimeter and centimeter microwaves in the ocean water is equal to $\delta_p \sim (0.01 - 0.1)\lambda_o$. In this wavelength range, the value of δ_p weakly depends on salinity and temperature of the water. But in the decimeter range, the depth of the skin-layer depends essentially on salinity and temperature, and can be equal to several centimeters (see figure 10.7).

One can see from these curves that understanding the physics of the skin-layer, and particularly the vertical distributions of salinity and temperature in this layer is crucial for remote sensing of salinity using L-band GNSS signals.

10.2.3 How do the polarization coefficients depend on salinity?

Using the dielectric constant model presented above, we analyze the polarization coefficients U_{RR} and U_{RL} in amplitude and phase. Figure 10.8 and figure 10.9 present the amplitude and phase of U_{RR} and U_{RL}, respectively, versus the sine of the satellite's elevation for different salinities and temperatures.

The temperature does not affect significantly the magnitude of the polarization coefficients. However, it shifts the phase by a few degrees.

The coefficient $|U_{RR}|$ decreases with the elevation angle, so that at nadir the right component of the incident field is totally converted into the left component. The phase of U_{RR} tends to stabilize as the elevation increases, and there is a difference of about 10^o at nadir between pure and salted water. On the contrary, $|U_{RL}|$ increases with elevation angle and slightly increases with salinity. The phase term behaves differently from the case S=1 psu to S=30 psu at low elevation angles (we observe higher sensitivity for the salted water), and stabilizes at higher elevation. The difference in ϕ_{RL} between the pure and salted case at nadir is about 2^o. This represents a very small phase shift of about one millimeter.

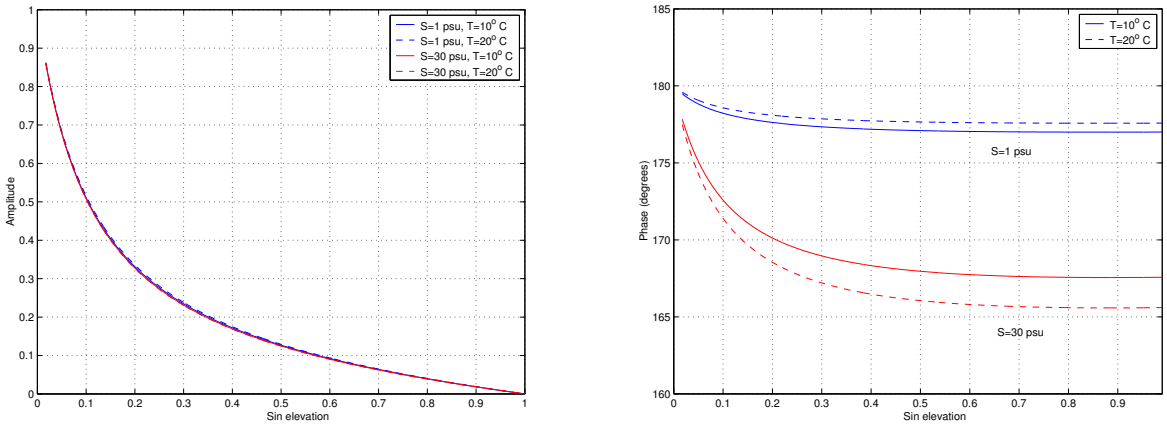

(a) Amplitude

(b) Phase

Figure 10.8: Amplitude and phase of U_{RR} versus $\sin\gamma$. Both pure water case (blue curve) and salted water case (red curve) are plotted for T=10^o C (full line) and T=20^o C (dashed line).

It is expected for a perfect conductor (and still assuming the total in-plane scattering) that we get U_{RR}=0 and U_{RL}=-1. This means that the phase of U_{RL} should tend to -180^o as the imaginary part of ϵ tends to infinity. On the contrary, we observe in figure 10.9(b) a clear departure of ϕ_{RL} with the value -180^o for a higher salinity. This behavior is due to the fact that in the range S=0 to 40 psu, the permittivity and dielectric loss factor are of the same order of magnitude. The graph on figure 10.10(a) illustrates the behavior of ϕ_{RL} at nadir as function of the real part of ϵ for different values of the imaginary part. Similarly, the behavior of ϕ_{RL} at nadir as function of the imaginary part of ϵ for different values of the real part is presented in figure 10.10(b). These two graphs highlight the impact of the relative magnitudes between the permittivity and the dielectric loss factor.

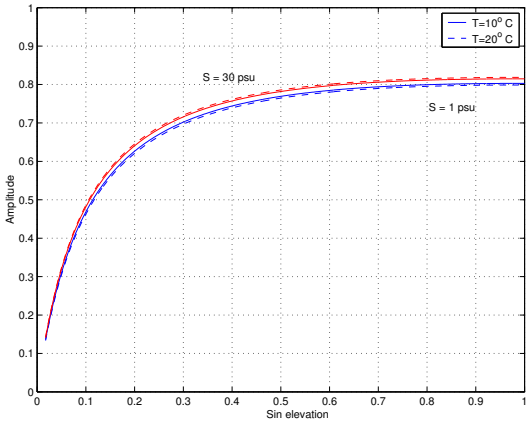

(a) Amplitude

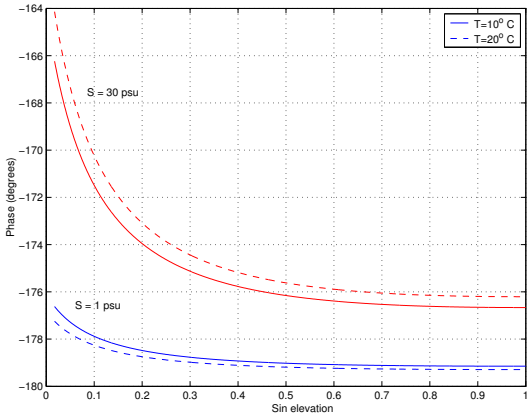

(b) Phase

Figure 10.9: Amplitude and phase of U_{RL} versus $\sin\gamma$. Both pure water case (blue curve) and salted water case (red curve) are plotted for T=10^o C (full line) and T=20^o C (dashed line).

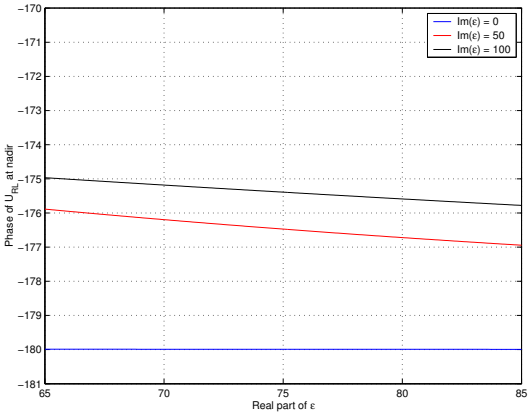

(a)

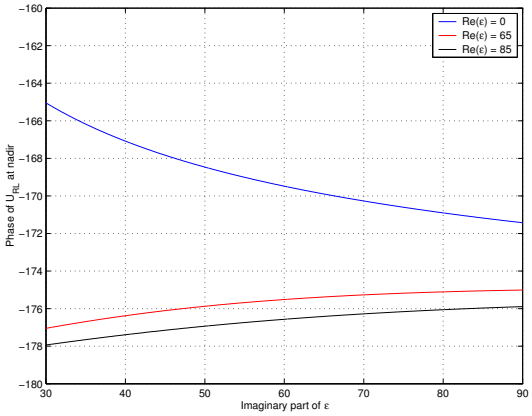

(b)

Figure 10.10: (a) Phase of U_{RL} at nadir versus permittivity. Dielectric loss factor is 0, 50 and 100. (b) Phase of U_{RL} at nadir versus dielectric loss factor. Permittivity is 0, 65 and 85.

To conclude, all the information needed to derive sea-surface dielectric constant is contained in the polarization coefficients. They present a slight dependency to salinity both in amplitude and phase. The analysis of these coefficients showed two regimes in the phase. A transition regime occurs for low elevation angles, where the phase variation is quite sensitive to the salinity. For higher elevation angles, the phase stabilizes and a phase shift of about 0.2 cm should be detected in the cross polarization coefficient U_{RL}, in order to detect a variation in salinity of ΔS=30 psu.

10.2.4 Power model

The effects of the water surface salinity on the received power are shown in figure 10.11. The modeled power presented in equation 10.7 is plotted as a function of the satellite elevation angle. The plots are done for S=1 psu (blue curve) and 30 psu (red curve), T=11^o Celsius, and h=0.56 m, which corresponds approximately to the experimental conditions. It corresponds, according to the used model, to $\epsilon = 82.3579 + i10.8664$ for S=1 psu and $\epsilon = 75.5106 + i47.1052$ for S=30 psu.

The antenna gain is taken into account considering elevation and azimuth variations of PRN 17. We have checked that water surface temperature, with ranges observed during our experiment, does not impact significantly the power interference pattern. As observed, we expect the effects of salinity on the received power to be very small.

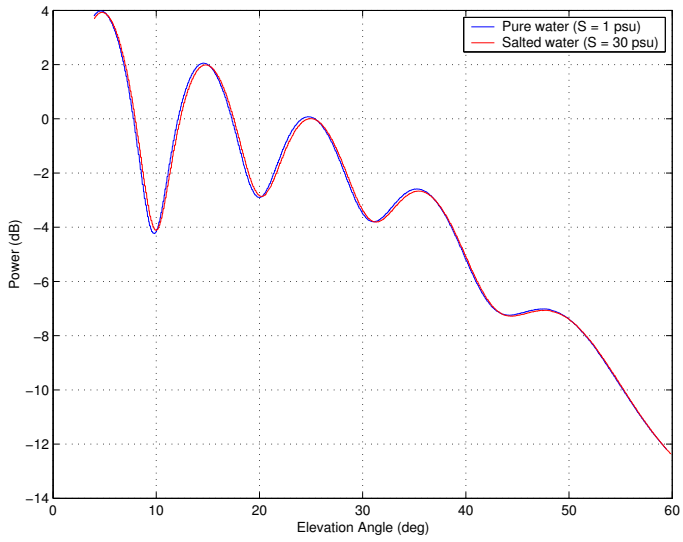

Figure 10.11: Power model versus elevation angle for two different values of salinity (S=1 psu and S=30 psu). The experimental conditions are similar to the Salpex ones. T=11^{o}C. PRN 17.

10.3 Data analysis

We present in this section the results of the measured power as a function of the satellite's elevation. The power is derived from the SNR (in amplitude) provided by the TurboRogue receiver for each selected satellite. The interference pattern is shown for pure water (1psu) and salted water (30 psu) with PRN 15 (cf figure 10.12(a)) and PRN 17 (cf figure 10.12(b)).

Several observations can be made:

- The data repeat quite well. The repeatability is better for salted water, as shown in figure 10.13, where the difference between the two measurements (with same experimental conditions) are plotted both for pure and salted water. This is consistent with the fact that a higher conductivity of the surface produces less noisy data.
- The drops observed with a salted water appear to be deeper than the ones observed for a pure water. This is also consistent with the fact that a high conductive medium produces deeper fades in the interference pattern.
- For a given salinity, the patterns differ from one PRN to the other. The azimuth of the satellite seems to corrupt strongly the interference pattern.
- The position of some drops seems to correspond with the ones predicted by the model. However, there are drops that are not predicted by the model, especially for high elevation angles.
- The main trend of the interference pattern with elevation angle seems different from the model. Indeed, the modeled power decreases of about 12 dB in the range 0 to 60^o, as shown in figure 10.11. Moreover, this trend changes with the PRN; it is thus sensitive to its azimuth.

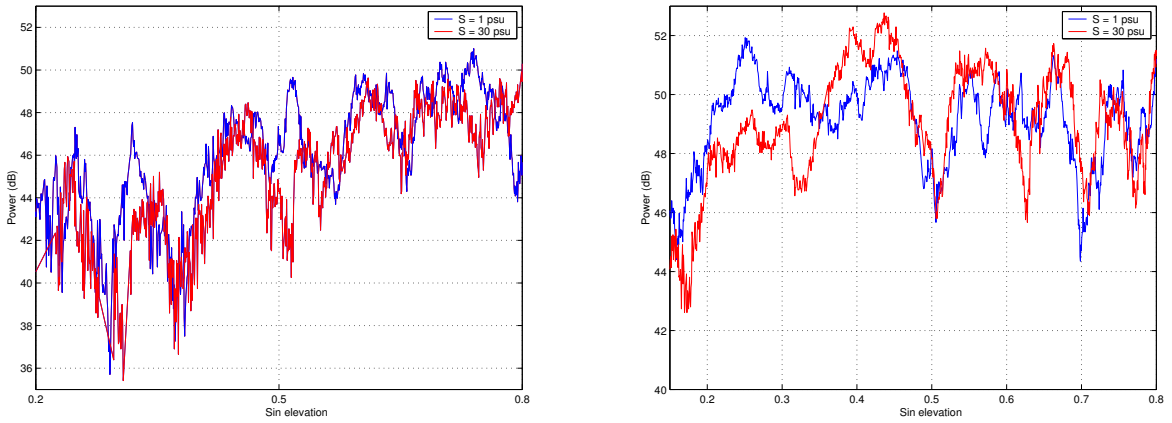

(a) PRN 15

(b) PRN 17

Figure 10.12: Interference pattern as a function of the sine of the elevation for pure water (blue curve) and salted water (red curve).

It is obvious that the model presented in figure 10.11 doesn't fit the observed data. The drops position and shape do not correspond to the ones in the modeled interference pattern. The presence of additional drops—i.e., higher frequency in the signal—provides the proof of the presence of reflections with the ground. The model has been then modified by taking into account these reflections:

$$P' \propto \left| G^R(1 + U_{RR_w} e^{i\phi_w} + U_{RR_g} e^{i\phi_g}) + G^L(U_{RL_w} e^{i\phi_w} + U_{RL_g} e^{i\phi_g}) \right|^2, \qquad (10.18)$$

where subscript w stands for water contribution and g stands for ground contribution. A first attempt to fit the experimental data has been done using a ground dielectric constant at

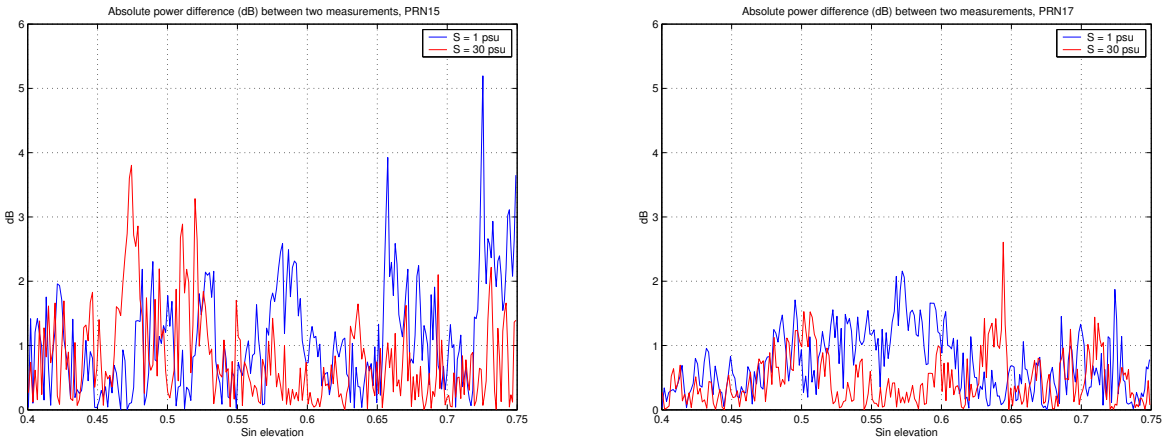

(a) PRN 15 (b) PRN 17

Figure 10.13: Repeatability of the data. Plot of the power difference between two measurements with same experimental conditions, for both pure water (blue curve) and salted water (red curve).

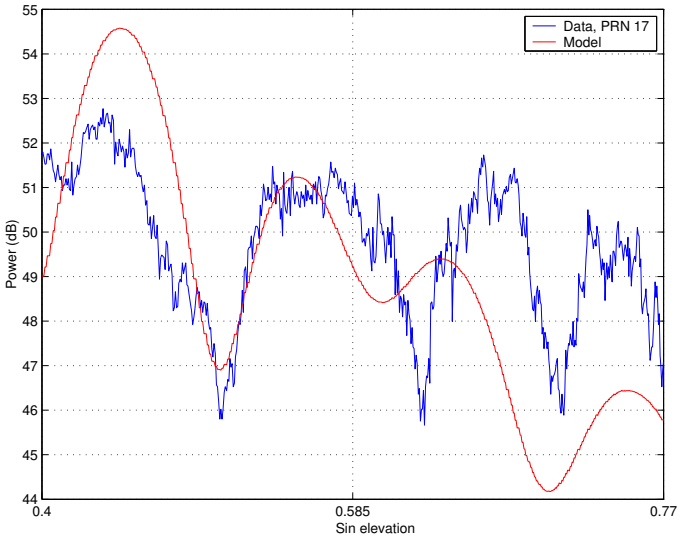

Figure 10.14: Fit of the Salpex experimental data using model presented in equation 10.18, when the ground contribution is taken into account. The data correspond to a salted water (30 psu). PRN 17.

L-band of about $\epsilon_g = 3 + i0.02$ (from http://home.earthlink.net/~jimlux/radio/soildiel.htm). Figure 10.14 presents the fit of the data taking into account the ground contribution included in the formula 10.18. The fit spans for elevation angles γ ranging from 24^o to 50^o.

It is clear that we have detected a non negligible contribution of the ground. The water surface area (delimited by the swimming pool) is not large enough to contain the whole footprint of the reflection, although the antenna has been positioned close to the surface on this purpose. This contribution shall explain mostly the observed sensitivity of the trend of the interference pattern with the azimuth of the satellite in view. As a matter of fact, it is quite difficult to model the ground reflections, according to the complexity of the clutter and obstacles around the swimming pool (trees, grass, bench, ...).

10.4 Discussion on salinity estimation

In radiometry, salinity is measured through the brightness temperature of the sea surface. A simple model for brightness temperature T_B introduces the sea-surface emissivity e:

$$T_B = e \cdot T. \tag{10.19}$$

At a fixed temperature in a smoothed ocean surface (i.e., assuming the effects of wind-induced surface roughness, wind generated foam and whitecaps negligible) increasing salinity is associated with decreasing emissivity and the lower the incidence angle, the higher the sensitivity of brightness temperature to salinity. It can be shown that for a 20^o surface temperature a 1% change in brightness temperature corresponds to a variation in salinity of 2 psu.

In bistatic remote sensing, salinity is measured through the magnitude squared of the Fresnel reflection coefficient, which is related to emissivity:

$$|\mathcal{R}|^2 = 1 - e. \tag{10.20}$$

We define the percent change in power τ between S=40 psu and S=20 psu at T=20^{o}C as:

$$\tau = 100 \cdot \frac{|U_{RL}(S = 40\text{psu}, T = 20^o\text{C}, \gamma)|^2 - |U_{RL}(S = 20\text{psu}, T = 20^o\text{C}, \gamma)|^2}{|U_{RL}(S = 30\text{psu}, T = 20^o\text{C}, 90^o)|^2}. \tag{10.21}$$

Figure (10.4) shows this percent change in power as a function of the sine of elevation. As expected, the sensitivity is higher around the Brewster angle and reaches 5% of change in measured power to get a variation in salinity of 20 psu. In other words, a 1% change in power corresponds to a variation in salinity of 4 psu. This is twice what we obtain with current radiometers, i.e, half the sensitivity.

This sensitivity may still hold to get valuable information on sea-surface salinity. An experiment consisting in a fixed ground GNSS antenna recording long time power series would be interesting to confirm this figure and also understand how sea-surface roughness corrupts the salinity estimation.

10.5 Conclusions on salinity retrieval with GNSS-R

The Salpex Experiment has been a first attempt to determine whether it is possible to determine water surface dielectric constant through the use of GNSS reflections. We have analyzed the power coming from a RHCP antenna that gathers interferences between direct GNSS signal along with reflected signals over a calm water surface.

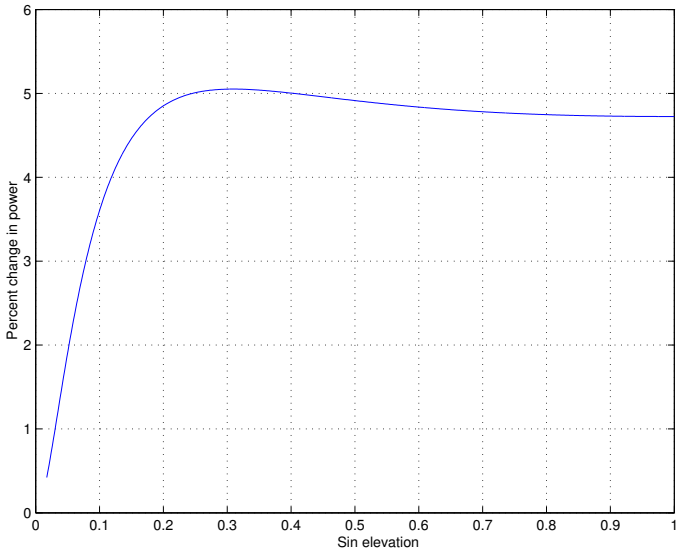

Figure 10.15: Percent change in power between S=40 psu and S=20 psu as a function of sine of elevation angle (see equation 10.21).

This was a simple approach, and more complex set-ups can certainly be devised. However, our first goal was to perform a simple analysis of the impact of salinity on the signals, and develop the models.

The derived model uses the Klein and Swift's model for the dielectric constant, and states that the salinity impact on the return power is very poor. All the information needed to derive sea-surface dielectric constant is contained in the polarization coefficients. The analysis of these coefficients showed two regimes in the phase. A transition regime occurs for low elevation angles, where the phase variation is quite sensitive to the salinity. For higher elevation angles, the phase stabilizes and a phase shift of about 0.2 cm should be detected in the cross polarization coefficient U_{RL} in order to detect a variation in salinity of ΔS=30 psu.

Thus, differential phase analysis of the return power could in principle provide another mean for salinity determination, given the fact that the instrument is accurate enough to detect small changes in the phase. However, a target of <1 mm in altimetry is a hard one, even from a fixed platform and after 1 month averaging (recall that salinity is in principle slowly varying). This means that using an altimetric approach for salinity monitoring will be challenging.

In turn, we can also conclude from this analytical study that salinity will not impact single frequency L-band altimetric measurements beyond the level of a few mm.

Another approach is to focus on the reflected power. We have seen that in order to be sensitive to salinity we should aim at a 1% relative power precision after 1 month averaging. The term "relative" is important. In principle, the best approach, exploiting the technique's strengths, is to focus on the reflected over direct power, a ratio more immune to equipment variability.

The analysis of the data shows a noisy interference pattern giving clear fade events with a very good repeatability. The noise, which is much larger than the predicted salinity impact, has been partially understood by the presence of reflections coming from the ground and

other multipaths. A better fit of the data has been done by taking into account the ground contribution, which corrupts quite significantly the interference pattern.

Neither the apparatus nor the experimental conditions were appropriate to judge whether we can reach a 1% relative power precision after 1 month averaging. A second Salpex experiment using more precise equipment near the open sea or a larger swimming pool would improve strongly the quality of the data.

Chapter 11

Emissivity Retrieval

This Chapter addresses the analysis of reflected GNSS signals gathered during the experimental campaign carried out in the frame of the L-band Radiometry Experiment, an Ifremer Contract (see [Soulat and Ruffini2002]). The purpose of this analysis is to provide some preliminary conclusions on the capability of a GNSS processor as a radiometer. In the following section, we provide the description of the experiment. A power model is then proposed in section (11.2), and estimations of the parameters of interest are derived. For radiometric purposes, we introduce the parameter K which represents the ratio of direct and reflected noise variances. A simulation has been carried out to check the validity of the estimators, in section (11.3). The experimental data are then analyzed in section (11.4).

11.1 Experimental campaign

The experiment took place at the Barcelona harbor the 4^{rth} of September 2002. We thank Jordi Vilà from the Barcelona Port Authority. Two antennas were deployed, as shown in figure 11.1, over a 30 meter high building located on a pier. The material was similar to the one used during the Eddy Experiment Flight (see Chapter 7) and the Salpex Experiment (see Chapter 10). For the purpose of sea-surface emissivity characterization, the experiment consisted in gathering GNSS-R over a calm sea, for two different antenna configurations:

- Part A: both RHCP and LHCP antennas are zenith pointing.
- Part B: RHCP antenna is zenith pointing and LHCP antenna is nadir pointing.

The underlying idea is that the signature of sea-surface emissivity should be observed by comparing the statistics of the LHCP antenna output signal between Part A and Part B. The wind speed at ten meters was around 4 m/s, so that sea-surface roughness variability effects were reduced.

Thirty seconds of data have been analyzed for each part of the experiment. An integration time of 10 ms has been used in Starlab's GNSS processor. PRN 01 was the only good candidate to make the correlations, since reflections were free of shadowing given its elevation and azimuth. Figure 11.2 shows the time serie of the peak power (in dB) using PRN 01, during Part A and Part B, respectively. The corresponding satellite elevation is 21^o (its azimuth is 61^o) during Part A, and 20^o (azimuth 62^o) during Part B. Several main observations can be made:

- The peak power from RHCP antenna is quite steady in both Part A and Part B, as expected.

- In Part A, we observe many fadings in the power gathered by the LHCP antenna. However, some good correlation peaks appear from time to time.
- In Part B, the correlation peaks of the LHCP antenna are much higher. The down-looking antenna has gathered reflected signals.

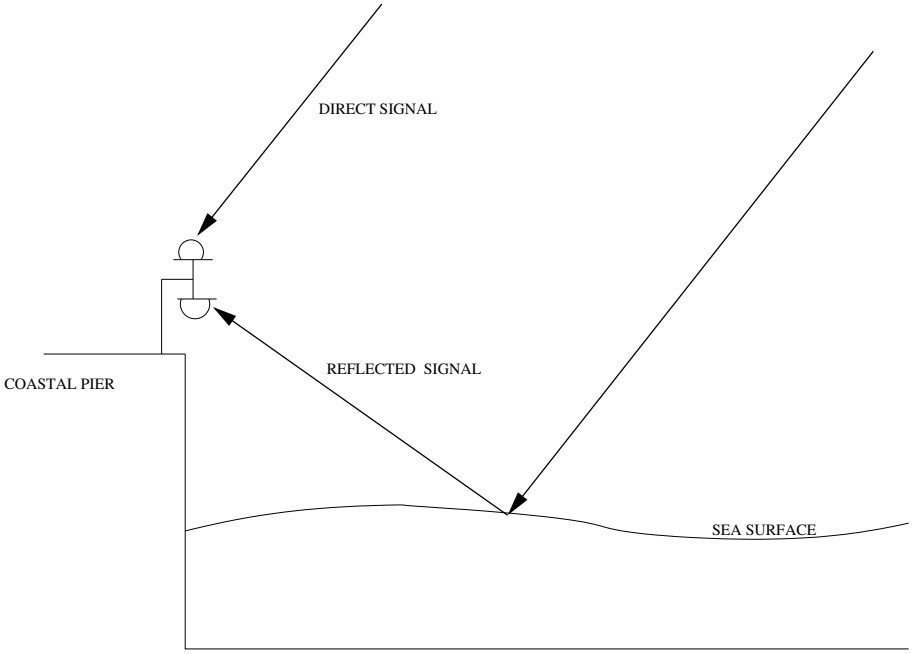

Figure 11.1: Geometry of the experiment during Part B.

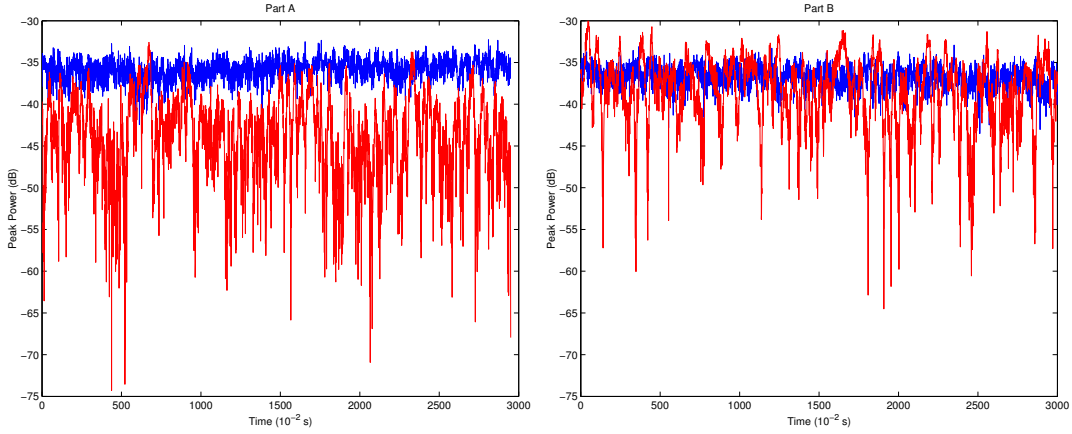

Figure 11.2: Time series of the peak power (in dB), using PRN 01, of RHCP antenna (blue curve) and LHCP antenna (red curve). *Left*: Part A, the corresponding satellite elevation is 21^o (its azimuth is 61^o). *Right*: Part B, the elevation is 20^o (azimuth 62^o).

11.2 Power model

This section presents a statistical analysis of the direct and reflected squared waveforms, based on a simple power model introducing a speckle noise model. We derive analytic expressions

of the 1-D mean power waveform and its normalized variance. Similarly, the statistics of the ratio of the two signals is presented.

First, we recall that the waveform is generated through a correlation process defined by:

$$C_{a,b}(\tau) = \frac{1}{T_i}\int_0^{T_i} a(t)b^*(t-\tau)dt, \tag{11.1}$$

where T_i is the coherent integration time.

Second, the direct return power in delay is computed from the squared complex correlation coefficients (in two channels I and Q) of the replica R with the incoming signal $S+N_{dI}+jN_{dQ}$. We assume N_{dI} and N_{dQ} to be two white Gaussian noises with mean zero and variance σ_d^2. The direct squared correlation coefficient thus writes:

$$\tilde{P}_d(\tau) = \left(\frac{C_{S+N_{dI},R}(\tau)}{\sqrt{C_{S+N_d,S+N_d}(\tau)C_{R,R}(\tau)}}\right)^2 + \left(\frac{C_{N_{dQ},R}(\tau)}{\sqrt{C_{S+N_d,S+N_d}(\tau)C_{R,R}(\tau)}}\right)^2. \tag{11.2}$$

Applying the large noise assumption that characterizes GNSS signals (σ_d is greater than the signal strength) to equation 11.2, we obtain:

$$\tilde{P}_d(\tau) = \frac{\left[C_{S,R}(\tau) + C_{N_{dI},R}(\tau)\right]^2}{\sigma_d^2} + \frac{C_{N_{dQ},R}^2(\tau)}{\sigma_d^2}. \tag{11.3}$$

$C_{S,R}(\tau)$ is here a deterministic triangle function, depending on the integration time T_i, the chip length, the antenna gain and the geometry (emitter elevation, receiver position, ...). A simple expression is: $C_{S,R}(\tau) = A_d\Lambda(\tau)$, with A_d the maximum amplitude of the waveform.

We recall that GNSS reflections come essentially from the contribution of scattering points on the sea surface. The averaged contribution of these different scatterers introduces fading phenomena, which can be described by a speckle noise. We can then define the reflected power as:

$$\tilde{P}_r(\tau) = \frac{\left[C_{\sqrt{n}S,R}(\tau) + C_{N_{rI},R}(\tau)\right]^2}{\sigma_r^2} + \frac{C_{N_{rQ},R}^2(\tau)}{\sigma_r^2}, \tag{11.4}$$

where, similarly, N_{rI} and N_{rQ} are two white Gaussian noises with mean zero and variance σ_r^2. We assume n to be a speckle noise following a Gamma Law with mean μ=1 and order L, such as:

$$\mathcal{P}(n) = \frac{L^L}{\mu\Gamma(L)}\left(\frac{n}{\mu}\right)^{L-1} e^{-L\frac{n}{\mu}}. \tag{11.5}$$

The parameter L is defined as the shape parameter of the distribution. It is linked to the degree of development of the sea surface: for a fully developed speckle, L equals 1. We have:

$$\begin{aligned} \langle n\rangle &= \mu = 1 \\ \langle n^2\rangle &= \frac{1}{L} + 1. \end{aligned} \tag{11.6}$$

Considering the ensemble average over successive waveforms, we get respectively for the direct and reflected powers:

$$\langle\tilde{P}_d\rangle = \frac{A_d^2\Lambda^2}{\sigma_d^2} + \sqrt{2\pi}\frac{\tau_n}{T_i}, \tag{11.7}$$

$$\langle\tilde{P}_r\rangle = \frac{A_r^2\Lambda^2}{\sigma_r^2} + \sqrt{2\pi}\frac{\tau_n}{T_i}, \tag{11.8}$$

where τ_n is the correlation length of the noise.

Since the GNSS-R system is at low altitude in this experiment, the Delay-Doppler Mapping over the sea surface is much wider than the portion of the surface contributing to the reflection process (the glistening zone). The correlation waveform of the reflected signal can thus be approximated by a triangle function, like the direct one. Note, that the noise power is inversely proportional to the number of *independent samples*, defined by the ratio of the coherent integration time and the noise correlation time.

We now consider the normalized variance defined as:

$$NV(\tau) = \frac{\langle \tilde{P}^2 \rangle - \langle \tilde{P} \rangle^2}{\langle \tilde{P} \rangle^2}, \tag{11.9}$$

and we obtain for the direct and reflected waveforms, respectively:

$$NV_d(\tau) = \frac{\sqrt{8\pi}\frac{A_d^2\Lambda^2}{\sigma_d^2}\frac{\tau_n}{T_i} + 2\pi\left(\frac{\tau_n}{T_i}\right)^2}{\frac{A_d^4\Lambda^4}{\sigma_d^4} + \sqrt{8\pi}\frac{A_d^2\Lambda^2}{\sigma_d^2}\frac{\tau_n}{T_i} + 2\pi\left(\frac{\tau_n}{T_i}\right)^2}, \tag{11.10}$$

$$NV_r(\tau) = \frac{\frac{1}{L}\frac{A_r^4\Lambda^4}{\sigma_r^4} + \sqrt{8\pi}\frac{A_r^2\Lambda^2}{\sigma_r^2}\frac{\tau_n}{T_i} + 2\pi\left(\frac{\tau_n}{T_i}\right)^2}{\frac{A_r^4\Lambda^4}{\sigma_r^4} + \sqrt{8\pi}\frac{A_r^2\Lambda^2}{\sigma_r^2}\frac{\tau_n}{T_i} + 2\pi\left(\frac{\tau_n}{T_i}\right)^2}. \tag{11.11}$$

We introduced, in the above expressions, the ratios $A_d^2\Lambda^2/\sigma_d^2$ and $A_r^2\Lambda^2/\sigma_r^2$, which can be seen as a Signal to Noise Ratio. In the grass (i.e., low SNR), we have for both direct and reflected signals:

$$NV(\tau) \approx 1. \tag{11.12}$$

For time lags around lag zero (i.e., high SNR), we have:

$$NV_d(\tau) \approx \sqrt{8\pi}\frac{\sigma_d^2}{A_d^2\Lambda(\tau)^2}\frac{\tau_n}{T_i}, \tag{11.13}$$

$$NV_r(\tau) \approx \frac{1}{L}. \tag{11.14}$$

As expected, equation 11.13 states that the normalized variance gets higher values for high noise power. In the scope of this study, the parameter of interest is σ_r^2. It is not possible to infer this parameter from equation 11.14. Note that the normalized variance is 1 when the speckle is fully developed (L=1).

We have seen, in this first analysis, that the normalized variances are function of the ratio $A^2\Lambda^2/\sigma^2$. Due to a lack of knowlegde on A, the study of the ratio of the two signals (direct and reflected) seems more appropriate. It introduces, as shown, the ratio of the two noise variances.

11.2.1 Reflected to direct signal ratio analysis

We focus now on the statistical description of the ratio of the two waveforms:

$$\tilde{P}_{ratio}(\tau) = \frac{\tilde{P}_r(\tau)}{\tilde{P}_d(\tau)}. \tag{11.15}$$

This analysis was motivated by the fact that, as mentioned above, the reflected power has no (or almost no) trailing edge for a low receiver platform. However, the intensity has dropped down with a factor α, due to the reflection process:

$$A_r = \sqrt{\alpha} A_d. \tag{11.16}$$

The parameter α is essentially a function of the sea-state and the Fresnel coefficients.
At lag zero, we have:

$$\langle \tilde{P}_{ratio}(0) \rangle \approx \frac{\alpha}{K}. \tag{11.17}$$

We have introduced here the parameter $K = \sigma_r^2/\sigma_d^2$. Equation 11.17 is the basis of emissivity retrieval, through the estimation of K. It is however corrupted by the α parameter which is sea-state dependent.

11.2.2 Summary

We presented a power model for GNSS-R data collected at low altitude. The proposed parameters are:

- σ_d^2 and σ_r^2: the noise variances of the direct and reflected signals, respectively. These parameters are the ones to be estimated in the scope of this study. Their ratio $K = \sigma_r^2/\sigma_d^2$ is the appropriate parameter to be investigated.
- L: shape parameter of the Gamma Law. It provides the degree of development of the speckle noise. It is sea-state dependent.
- α: attenuation factor due to the reflection process. It is also sea-state dependent.

11.3 Simulations

Simulations have been carried out to check the validity of the previous equations, and verify that there is no undesired effect due to the one-bit sampling. We focus especially on equations number 11.8, 11.13 and 11.17.

We consider, as an input of the correlator, the following signal:

$$S(t) = CA(t)e^{j\omega t} + N_I(t) + jN_Q(t), \tag{11.18}$$

where CA is the C/A code of PRN 01, N_I and N_Q two random variables with mean zero and variance σ^2. The carrier frequency we consider here is the IF frequency: 308 kHz. This signal is one-bit sampled with a sampling frequency of 20.456 MHz. These frequencies are in line with the ESA equipment specifications. Before making the correlation between the signal and the replica, we remove the carrier and consider the signal $S' = S(t)e^{-i\omega t}$.

The result of the mean squared correlation over 1000 realizations is shown in figure 11.3, for different noise variances σ^2. The choice of these variances is related to the observed peak value in the data. The width of the waveform is approximately 40 samples since the C/A code chip length is about 1 microsecond (we recall that there are 1023 chips in one C/A code period, one chip lasts 1/1023 ms).

As observed, the mean power drops down when the C/A code is corrupted by a random noise. This in agreement with equation 11.7 (or 11.8). Furthermore, the signal is constant in the grass whatever the value of σ, as shown in the right hand side graph of figure 11.3. This is also consistent with equation 11.7. However, we note that the noise variance can be

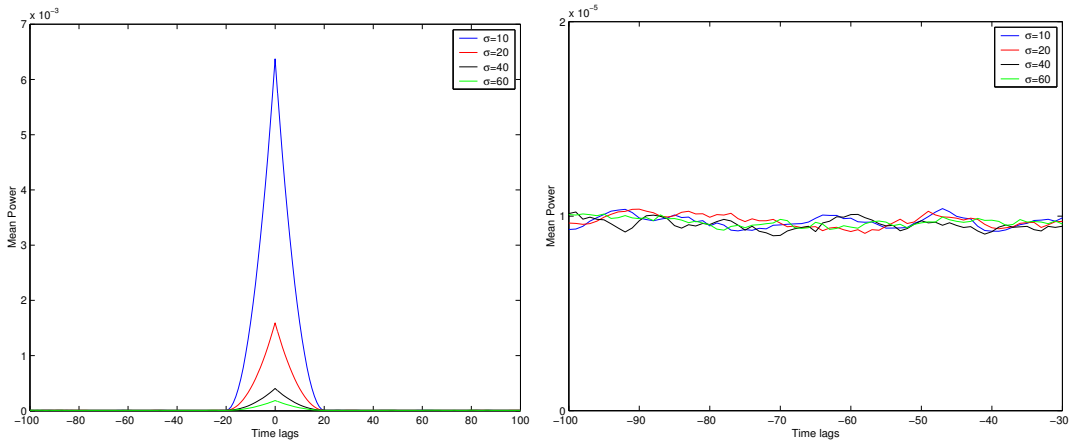

Figure 11.3: *Left*: Mean power $\langle \tilde{P}(\tau) \rangle$ for different noise levels (σ=10, 20, 40 and 60). The choice of these variances is related to the observed peak value in the data. The peak of correlation is one for a clean signal. *Right*: Zoom of the squared correlation in the grass, before lag zero (peak position). 1000 realizations, PRN 01, T_i=10 ms.

estimated through the correlation process itself (without any normalization) if the data are sampled at 2 bits (or more).

Figure 11.4 shows the variations of the mean peak power versus the inverse noise variance $1/\sigma^2$. As expected, it follows the relation:

$$\langle \tilde{P}(\tau = 0) \rangle \propto \frac{1}{\sigma^2}. \tag{11.19}$$

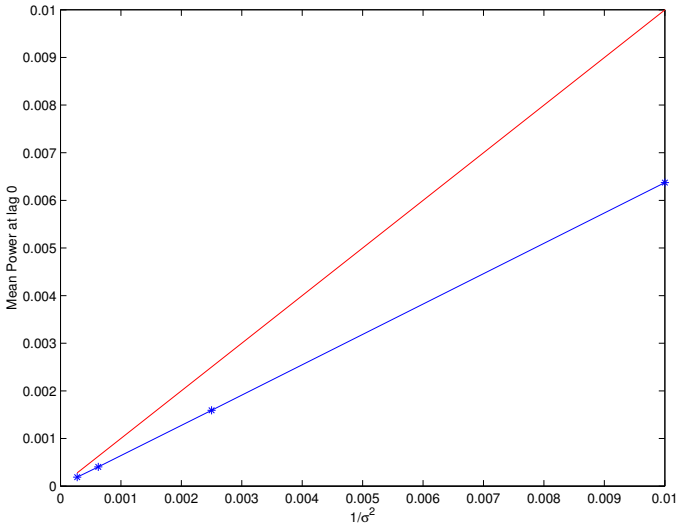

Figure 11.4: Simulated mean peak power at lag zero versus inverse noise variance $1/\sigma^2$. A line with slope 1 is also plotted. 1000 realizations, PRN 01, T_i=10 ms.

The normalized variance of the power is presented in figure 11.5. As expected, for time lags corresponding to the grass, the normalized variance of the power is equal to 1 (cf equation 11.12). It is easy to check that, for lags around the lag τ=0, the normalized variance behaves

as $1/\Lambda(\tau)^2$ (cf equation 11.13). The normalized variance at lag zero is plotted versus σ^2 on the right hand side of figure 11.5, which shows that equation 11.13 is valid.

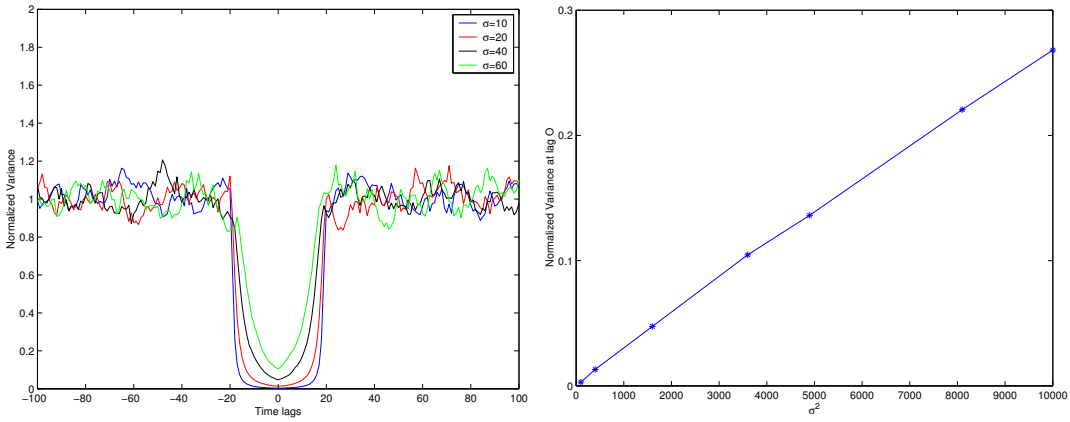

Figure 11.5: *Left*: Normalized variance of the power for different noise levels (σ=10, 20, 40 and 60). *Right*: Normalized variance at lag zero versus σ^2. 1000 realizations, PRN 01, T_i=10 ms.

11.3.1 Reflected to direct signal ratio analysis

We consider now in our simulations the power ratio of two GNSS signals:

- the direct signal with variance σ_d^2,
- reflected signals with different variances σ_r^2 ranging from σ_d^2 to $5\sigma_d^2$.

As observed in figure 11.6, we easily check that the variations of the mean peak power are proportional to K^{-1}, which validates equation 11.17. Hence, looking at the ratio of the two signals seems powerful if the attenuation factor is known. A model for α is therefore needed.

11.4 Data analysis

Figures number 11.7 and 11.8 present the mean power gathered by the RHCP antenna (thick curve) and the LHCP antenna (dashed curve) during Part A and Part B, respectively. As expected, the peak power received by the LHCP antenna is quite low during Part A. It is much higher during Part B, since the GNSS signal becomes mostly LHCP at the reflection. As far as the noise is concerned, we first observe, in both configurations, that noise levels are slightly different from one antenna to another. We also note that the noise level of the direct signal changes a bit from Part A to Part B.

Figure 11.9 shows the normalized variance of the squared correlation for the RHCP antenna (thick curve) and the LHCP antenna (dashed curve). The curves are consistent with the model and simulations in term of shape and relative magnitudes. We particularly notice that the normalized variance of the LHCP antenna in Part A is one all along the waveform. The SNR is indeed not high enough. During Part B, however, the normalized variance behaves like $1/\Lambda(\tau)^2$ and is above the RHCP curve.

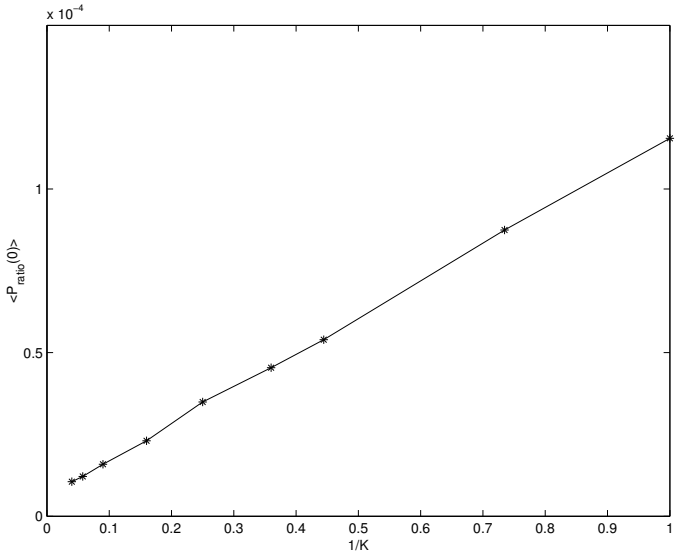

Figure 11.6: Mean of the ratio of two power waveforms (with noise σ_d^2 and σ_r^2) at lag zero versus K^{-1}, with $K = \sigma_r^2/\sigma_d^2$. $\sigma_d = 60$, and σ_r ranges between 60 and 300.

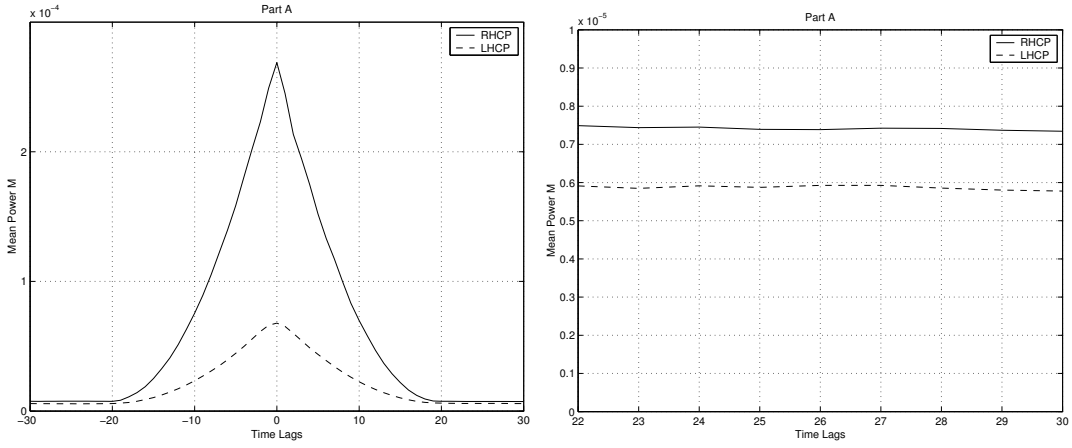

Figure 11.7: *Left*: Mean power of RHCP antenna (thick curve) and LHCP antenna (dashed curve), PRN 01, Part A. *Right*: Zoom of the squared correlation in the grass, after lag zero.

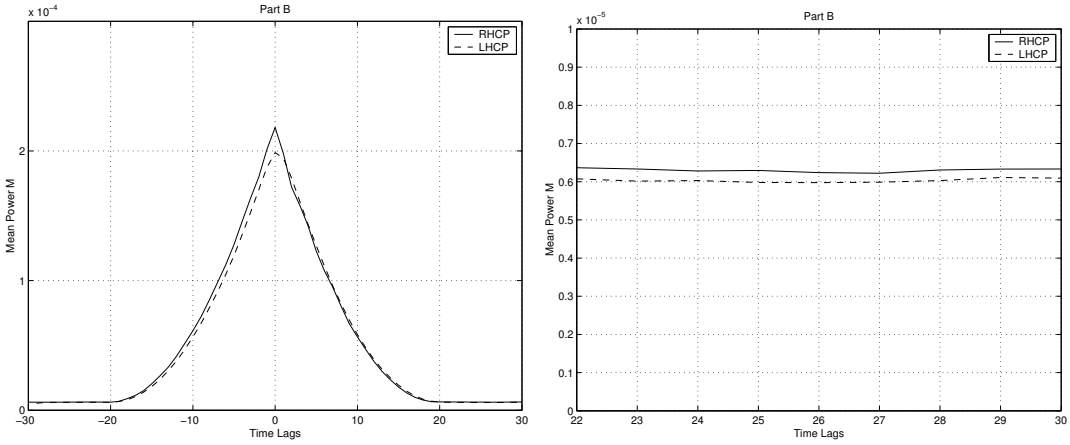

Figure 11.8: *Left*: Mean power of RHCP antenna (thick curve) and LHCP antenna (dashed curve), PRN 01, Part B. *Right*: Zoom of the squared correlation in the grass, after lag zero.

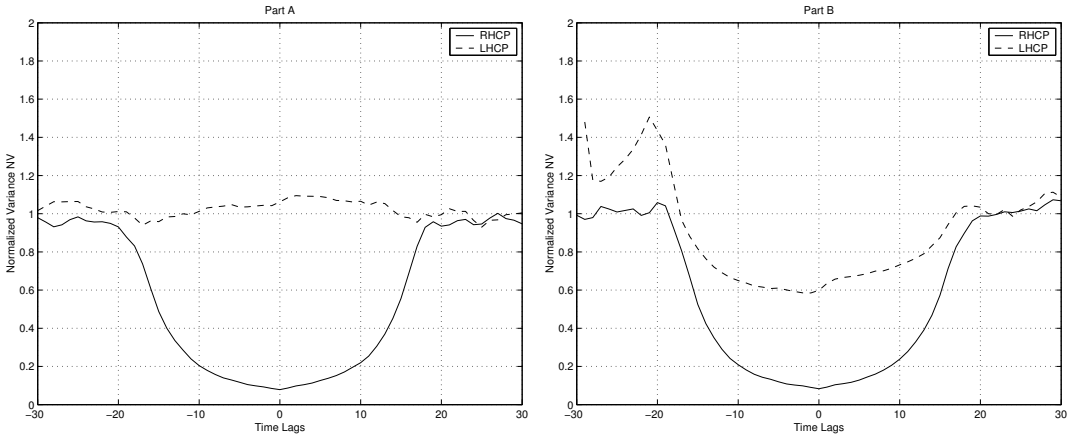

Figure 11.9: Normalized variance of the squared correlation for the RHCP antenna (thick curve) and the LHCP antenna (dashed curve), PRN 01. *Left*: Part A. *Right*: Part B.

11.5 Conclusions on radiometry with GNSS-R

A simple GNSS-R ground experiment has been carried out to characterize the signal power and relate its statistics to emissivity. For this purpose, a GNSS-R power model has been presented with theoretical estimation of the parameters of interest such as the ratio K of the direct and reflected signal noise variances. The model has been validated through simulations, specifically to verify that it is valid in the case of one-bit sampled data, as those gathered by the ESA equipment. Experimental data have been then analyzed demonstrating that the investigation of the statistics between successive waveforms could be effective for sea-surface emissivity measurement.

The radiometric solution using GNSS-R could be improved by considering the following points:

- As observed in the derived equations, sea-state dependent parameters are corrupting the estimation of the emissivity noise. Models for parameters α and L are nedeed to improve this estimation.
- The use of another recording device, which would sample the data at two bits, say, would definitely improve the thermal noise estimation, by a close analysis of the grass of the correlation.

Conclusions and Perspectives

This study investigated the GNSS-R remote-sensing capabilities for oceanographic applications. We depicted GNSS-R sensitivity to sea-surface geophysical parameters, such as directional mean square slope, salinity and emissivity, through theoretical and experimental analyses. Particular emphasis was put on the speculometric application, through the first inversion of GNSS-R full Delay-Doppler Maps. Solar bistatic reflections was also analyzed through a similar sea-surface mapping (Tilt-Azimuth Map) in order to enhance the understanding of specular scattering.

The first part of this dissertation depicted the mechanisms involved in the bistatic scattering process at L-band. It included the knowledge of GNSS signal characteristics, electromagnetic scattering model, random sea-surface features and basics of processing of direct and reflected signals. From a theoretical point of view, we particularly focused on the validation at L-band of the GO approximation of the Kirchhoff scattering theory, through simulations. A new model of the scatterometric 2-D waveform model (DDM) was then proposed. The DDM data product is the basis of sea-surface roughness parameter inversion.

In the second part, a simulator of GNSS-R signals was developed from the knowledge acquired in Part I. This simulator is composed of two possible models (GRADAS and IS) based on the Kirchhoff theory and GO model. An application of this simulator was reported for the study of SWH retrieval from a coastal platform. It was shown that the behavior of the reflected field is sensitive to sea-surface height dynamics. In particular, the simulations with wind-driven ocean spectrum showed that the RMS of the amplitude of the derivative of the complex field increases linearly with SWH. This is a promising future line of research.

The third part of the study provided experimental results on scatterometric GNSS-R airborne capabilities, based on a flight experiment carried out in the scope of the ESA PARIS-γ project. First, we reported a repetition of the Cox and Munk experiment, through the inversion of optical high-resolution images which have been simultaneously gathered during the experiment (SORES data). The derived MSS enhanced the understanding of GNSS-R scatterometric measurements. In particular, the analysis highlighted the important impact of sea-state (SWH) in addition to wind stress over DMSS, and a non-negligeable departure from Gaussianity of the sea-surface slope PDF. We observed that estimated optical MSS can be larger by up to 20% than MSS predicted by a wind-driven spectrum. The SORES technology also permitted to measure the swell direction and associated long wave variance through spectral analysis of the photographs.

An inversion procedure for DDM has then been presented and DMSS revealed to be very consistent with models and ground truth, meaning that the developed inversion method was effective. Our results showed that both optical and L-band total MSS are 20% higher than what predicted by Elfouhaily's model for the observed wind speed (9 to 13 m/s). The SPA estimated by GNSS-R matched the swell direction with good accuracy for most cases. A new geophysical product has been put forward: the slope PDF isotropy which can be related to wind/wave misalignment as well as sea degree of development.

We emphasized that these two forward scattering instruments (GNSS-R and SORES) are sensitive to DMSS, the directional probability distribution of specular scatterers, and only indirectly to wind speed and direction: the relationship is modulated by other physical phenomena affecting DMSS, such as swell magnitude and direction. This scatterometric analysis showed that the sea-surface roughness is a self-standing product, which can not be directly associated to the wind. The roughness of the ocean surface can be seen as a combination of several physical processes. Therefore, roughness variations observed on the surface do not come systematically from the wind stress.

Finally, specific studies on other possible GNSS-R applications have been reported in a fourth part. They provided some preliminary conclusions on the possible salinity and emissivity retrievals, through simple ground experiments.

The goal of the Salpex Experiment was to perform a simple analysis of the impact of salinity on the signals, and develop the models to compare it to. On this purpose, we have analyzed the power coming from an RHCP antenna that gathers interferences between direct GNSS signals along with reflected signals over a calm water surface. The analysis of the data showed a noisy interference pattern giving clear fading events with a very good repetivity. The main observation was that the noise is much larger than the predicted salinity impact, which is theoretically very tiny. A phase approach could in principle provide the means for salinity determination, given the fact that the instrument is accurate enough to detect small changes in the phase. However, the needed target of <1 mm in altimetry is a very challenging one, even from a fixed platform and after 1 month averaging. Another approach was to focus on the reflected power. We have seen that in order to be sensitive to salinity we should aim at a 1% relative power precision after 1 month averaging. In principle, the best approach is to focus on the reflected over direct power, a ratio more immune to equipment variability.

The purpose of the L-band Radiometry Experiment was to provide some preliminary conclusions on the capability of the GNSS processor as a radiometer. We provided a power model and algorithms to estimate the parameters of interest (emissivity noise variance). The model has been checked and validated through simulations. The ratio of direct and reflected signals appears to be the more appropriate way to infer emissivity, by estimating the ratio of the noise variances. However, its estimation relies on an a priori knowledge of the sea-state.

From the experience of this study, scatterometry with GNSS-R requires more flight experiments, in order to consolidate the concept of GNSS-R sea-roughness retrieval. Let us emphasize that the Eddy Experiment Flight was not optimized for speculometry (1000 m altitude, 50 m/s speed) and that higher/faster flights are needed. The strength of this technique would re-enforce significantly the remote-sensing community. It appears clearly, for instance, that future radiometers such as the Soil Moisture and Ocean Salinity ESA mission (SMOS)—working also at L-band—will require a good knowledge of DMSS for calibration.

As far as the emissivity and salinity retrievals are concerned, more experimental campaigns are needed over a real sea surface.

Regardless of the application, altimetry, speculometry or radiometry, the important thing to keep in mind is that GNSS-R is a differencing approach (reflected-direct signals). Engineering efforts should focus on stability of the system and maximal exploitation of the differencing scheme.

Part V

Appendix

Appendix A

Relevant Symbols

Symbol	Units	Name
α	rad, degrees	Sea-surface slope azimuth
β	rad, degrees	Sea-surface slope tilt
γ	rad, degrees	Satellite elevation
θ	rad, degrees	Incidence angle with respect to the normal to the surface
ζ	meters	Sea-surface height
λ	meters	Emitted wavelength (~ 20 cm at GNSS frequencies)
ϵ		Sea-water dielectric constant
ϕ	rad, degrees	Sun elevation
τ	seconds	Time delay between direct and reflected GNSS signals
τ_P	seconds	P code chip length (~ 30 m)
$\tau_{C/A}$	seconds	C/A code chip length (~ 300 m)
σ^o		Scattering coefficient
σ_ζ	meters	Sea-surface RMS height
σ_s^2 or MSS		Sea-surface slope variance
σ_c^2		Sea-surface slope variance in the *crosswind* direction
σ_u^2		Sea-surface slope variance in the *upwind* direction
$A(\vec{\rho})$		Sea-surface height autocorrelation function
l	meters	Sea-surface correlation length
$\mathcal{P}_\zeta$		Sea-surface height PDF
$\mathcal{P}_s$		Sea-surface slope PDF
$\vec{q} = (\vec{q}_\perp, q_z)$	rad.m^{-1}	Scattering vector
$\mathcal{R}$		Fresnel coefficient
r_c	meters	Mean radius of curvature of surface
s_x		Sea-surface slope along x-axis
s_y		Sea-surface slope along y-axis
S	psu	Sea-surface salinity
T	degrees Celsus	Sea-surface temperature
T_a	seconds	Incoherent integration time
T_i	seconds	Coherent integration time
U_{height}	m/s	Wind speed measured at *height* m above sea level

Appendix B

Acronyms

AD	Artificial Data
ARNS	Aeronautical Radio Navigation Service
CEOS	Committee on Earth Observation Satellites
CIL	Confidence Interval Length
DDM	Delay-Doppler Map
DMSS	Directional Mean Square Slope
ECMWF	European Centre for Medium-Range Weather Forecasts
ESA	European Space Agency
ESTEC	European Space Research and Technology Centre
FCZ	First Chip Zone
FFT	Fast Fourier Transform
GDR	Geophysical Data Records
GNSS	Global Navigation Satellite System
GNSS-R	GNSS Reflections
GO	Geometric Optics
GPS	Global Positioning System
GRADAS	GNSS Reflections Artificial Data Synthesiser
ICC	Catalan Cartographic Institute
IEEC	Catalan Space Research Institute
INM	(Spanish) National Meteorological Institute
INS	Inertial Navigation System
IS	Intermittent Screamers
LEO	Low Earth Orbit
LHCP	Left Hand Circularly Polarized
MSL	Mean Sea Level
MSS	Mean Square Slope
MTF	Modulation Transfer Function
NWP	Numerical Weather Prediction model
NRCS	Normalized Radar Cross Section
PARIS	PAssive Reflectometry and Interferometry System
PDF	Probability Density Function
PO	Physical Optics
PRN	Pseudo Random Noise

RA	Radar Altimeter
RHCP	Right Hand Circularly Polarized
RMS	Root Mean Square
RMSE	Root Mean Square Error
RNSS	Radio Navigation Satellite Service
SAR	Synthetic Aperture Radar
SMOS	the Soil Moisture and Ocean Salinity mission
SNR	Signal to Noise Ratio
SORES	SOlar REflectance Speculometer
SOW	Second Of the Week
SP	Specular Point
SPA	Slope PDF Azimuth
SPA	Stationary Phase Approximation
SPI	Slope PDF Isotropy
SPM	Small Perturbation Method
SSH	Sea Surface Height
SWH	Significant Wave Height
TAM	Tilt-Azimuth Mapping
T/P	Topex/Poseidon
UTC	Coordinated Universal Time
WAF	Woodward Ambiguity Function

List of Figures

1 Structure of Part I. 15

1.1 Present GPS signals. 20
1.2 L_1 signal structure. 21
1.3 Structure of a GPS receiver. 23
1.4 Present and future civil GPS frequencies (from [MacDonald2002]'s paper). 23
1.5 Geometry of multistatic GNSS radar system (from V. U. Zavorotny, Bistatic GPS Signal Scattering from an Ocean Surface: Theoretical Modeling and Wind Speed Retrieval from Aircraft Measurements, 1999). 25
1.6 Galileo frequency plan (as of 2003) together with GPS and GLONASS systems. ARNS is the acronym for Aeronautical Ratio Navigation Service. This band is dedicated to safety-of-life services (i.e., civil aviation). RNSS is the acronym for Radio Navigation Satellite Service. 27

2.1 Correlation function for different wind speeds (U_{10}=1, 3, 5, ..., 17 m/s), with Gaussian spectrum from [Elfouhaily *et al.*1997]. 33
2.2 Sketch of sea-surface slope PDF and related frames. 35
2.3 Variation of sea-surface slope variance at L-band with current speed, with wind speed as a parameter (see equation 2.17). 36

3.1 Definition of the scattering vector $\vec{q} = k(\vec{s} - \vec{i})$. 40
3.2 Vector geometry for scattering. 42
3.3 Associated parabola for specular point determination. 46
3.4 Fresnel field magnitude relative to surface resolution for two different radii of curvature: (a) r_x=r_y=5 m, (b) r_x=r_y=10 m. The receiver is at 500 meters over a 10×10 m^2 parabolic surface. 47
3.5 Fresnel field magnitude relative to the tabulation size of the surface for two different radii of curvature: (a) r_x=r_y=5 m and (b) r_x=r_y=10 m. The resolution is 3 cm and the receiver is at 500 meters transmitting in L-band. 47
3.6 Effect of small ripples added on a very smooth parabolic wave. Under the curve, there is a difference of ±10% between Fresnel magnitude and the magnitude computed on a perfect parabolic surface in L-band. 48
3.7 Specular points number relative to wind speed for backscattering (25x25 meter surface with 5 cm resolution). 49
3.8 Specular points position for (a) U_{10}=5 m/s and (b) U_{10}=15 m/s. 50
3.9 Correlation between the reflected power and specular point number on a Gaussian ocean model in L-band (L_1=19 cm) within 2 seconds: 5×5 m^2, 5 cm resolution, U_{10}=15 m/s, receiver at nadir incidence at 50 meters. 50
3.10 Correlation between the specular points number and the reflected power computed with the Fresnel integral, for an incident wavelength L_1=1 cm or L_2=20 cm. 51

4.1 Data product levels in GNSS-R processing. 61
4.2 The top high level flowchart of the GNSS-R processor for PRN i. 62
4.3 Initialization module of the GNSS-R processor. 63
4.4 An example of correlation peak in arbitrary units, for 5 ms of coherent integration time, using the PRN code number 9. 64
4.5 Effect of the navigation bit transition on the correlation process. 65
4.6 Example of the search for the navigation bit synchronism. As the 20 ms long code replica slides on the signal (a, b, c, d, e, f), the value of its product (green curve at the bottom) with the signal (first row) depends on the position of the navigation bit (red) transition within the code replica. 66
4.7 Tracking module of the GNSS-R processor. 67
4.8 DDM of direct (a) and reflected (b) signals from the Eddy Experiment Flight (PARIS$-\gamma$ ESA Contract). The DDMs are plotted in amplitude times 10^3. . . 68

5.1 Schematic drawing of the *minimum representative patch*. 75
5.2 Spectrum estimation of the true temporal spectrum of the reflected field over a 200×200 m^2 surface (thick line) with 2 sub-patches only: 12.8 m side (dotted line), 25.6 m side (dashed line), 51.2 m side (dashed dot dot line). 76
5.3 Inputs and outputs of the GRADAS simulator. 78
5.4 LEO geometry for the GRADAS simulator. 78
5.5 GRADAS algorithm. 80
5.6 First chip zone: the 20.456 MHz sampling rate of the C/A code corresponds approximatively to 20 samples each chip. The first chip zone is divided into 20 rings. We can see an example of a patch (25×25 m^2) located in zone 4. 81
5.7 From left to right are plotted the phase, the amplitude and the power spectrum of the reflected field from 240 patches (6×400 m^2) democratically located in the 200Hz Doppler zone of the first chip zone. The receiver moves at 7 km/s along the x-axis, its altitude is 500 km. The sampling rate is 10 kHz, 0.5 second evolution, U_{10}=10 m/s. 82
5.8 The lower line in the left-hand figure, represents the phase of the electromagnetic field generated with the democratic patching of the ocean surface, before C/A code modulation. In this example, 240 patches located in the 200Hz Doppler zone are considered, the receiver is moving at 7 km/s, the wind speed is U_{10}=10 m/s. The red curve is the phase retrieved with the GPS open loop processor. On the right-hand side, the retrieved amplitude is shown with the difference in phase (crosses) between the unwrapped phase. The relation between fadings and the lose of the phase is clearly observed. 83
5.9 Flowchart of the code implementing the IS-model. 85
5.10 The waveform (blue curve) resulting from the correlation between the simulated ocean-reflected GPS data and a clear replica of the corresponding C/A code. In red, for purpose of comparison, the autocorrelation of the same code. The asymmetry of the waveform reflect the extension, in chips units, of the sea surface taken into consideration in the signal generation process. The number of chips is the time-delay unit on the x-axis. On the y-axis, arbitrary units. . . 86
5.11 The phases as retrieved by the open-loop GPS processor (in black) and the one from the simulated physical field (in red), after the spatial filtering with the *triangular function*. A cycle slip in the tracker can be observed. 87

5.12 The blue curve represents the difference between the retrieved phase and the one of the electromagnetic field. The green curve represents the field amplitude, in dB_v. Clearly, when a fading occurs, the tracking of the phase can fail. In normal conditions the phase is well reconstructed. 88

6.1 The dynamic L-band electromagnetic field in a complex phasor representation produced by a wind-driven ocean model. 90
6.2 Standard deviation of the derivative of the reflected phase ($\sigma_{\delta\theta}$) as a function of sea elevation RMS σ_ζ. L_5, 1 minute simulation. 91
6.3 Standard deviation of the reflected amplitude (σ_r) as a function of sea elevation RMS σ_ζ. L_5, 1 minute simulation. 91
6.4 Standard deviation of the derivative of the amplitude of the reflected field ($\sigma_{\delta r}$) as a function of sea elevation RMS σ_ζ. L_5, 1 minute simulation, with 4σ error bars. 92
6.5 *Left*: Standard deviation $\sigma_{|\delta F|}$ of the amplitude of derivative of the reflected field as a function of sea elevation RMS σ_ζ. L_5, 1 minute simulation. *Right*: Same plot with 10 s $\sigma_{|\delta F|}$ estimation (squares). 93

7.1 Map of the flight trajectory. The blue line shows the Jason's track. The points P1 and P2 mark the experiment boundaries, while the green points indicate the positions of scheduled GPS buoy measurements. 98
7.2 Views of the sea surface during the experiment from the air and sea. 98
7.3 Aircraft set-up configuration. 99
7.4 ESA equipment used during the Eddy Experiment Flight. 100
7.5 Elevation and azimuth of three GPS satellites in view during the experiment. . 101
7.6 Map of the one-chip iso-delays and iso-Dopplers (-100 Hz, 0 and +100 Hz) for PRNs 08 (blue), 10 (red) and 24 (green) at the beginning (*left*) and end (*right*) of the track. The -3dB antenna pattern is also represented in black. 101
7.7 Wind field and SWH at 12 UTC in the observation area (data from INM). . . . 102
7.8 (a) Mean square slope from Jason along the track in both Ku-band (blue curve) and C-band (red curve). (b) Wind speed from Jason along the track. 103
7.9 The SWH from RA Jason in Ku-band (blue curve) and C-band (red curve). . . 103

8.1 High resolution camera and GPS LHCP antenna located at the bottom of the plane. 106
8.2 Localization of the snapshots along the track of the plane. Each photograph is labeled by a number ranging from 35 to 63. 106
8.3 **Top**: Example of SORES raw data (photograph 47). **Bottom**: Example of breaking event observed during the experiment. 108
8.4 Geometry of SORES sensing during the Eddy Experiment Flight. 110
8.5 (a) Photograph 41 with the TAM. (b) Data intensity I_d. 113
8.6 Examples of data and best-fit model TAMs. **Top**: Data TAMs. **Middle**: Best-fit model TAMs. **Bottom**: Data-model residual. 114
8.7 Up-wind mean square slope and slope PDF isotropy along the track. 116
8.8 Slope PDF azimuth and b_o'' along the track. 116
8.9 (a) Centered intensity I_c in optimal region of photograph 47. (b) 2-D Fourier transform of I_c. 118
8.10 (a) Sea elevation estimated spectrum $S(k)$. (b) Passband filtered $S(k)$. 119
8.11 Integrated spectrum versus tilt β. 120
8.12 Swell direction α_s along the track from a spectral analysis of the images. 120

8.13 (a) Total MSS, mss_w and mss_l versus latitude. (b) Long wave variance contribution in percent to the overall slope variance. 121
8.14 Simulated photographs with the Eddy Experiment Flight camera specifications. The up-wind MSS is 0.031. **Top**: without swell. **Bottom**: with swell (H=1 m). 122
8.15 Impact of wave height H on σ_u^2 and SPI. $\Delta\alpha = 45^o$. 123
8.16 Impact of H on wind direction estimation. $\Delta\alpha = 45^o$. 124
8.17 Impact of $\Delta\alpha$ on σ_u^2 (a) and SPI (b). H is 0.7 (blue curve) and 1 meter (red curve). The black line corresponds to the nominal value of the analyzed parameter. 124
8.18 Impact of $\Delta\alpha$ on wind direction estimation. H is 0.7 (blue curve) and 1 meter (red curve). 125
8.19 (a) Total MSS versus wind speed. Cox and Munk slope variances are also plotted (red circles). (b) Angle difference between slope PDF azimuth and swell direction ($\Delta\alpha = \alpha_s - \alpha_o$) versus wind speed. 126
8.20 (a) Slope PDF isotropy versus wind speed. (b) Slope PDF isotropy versus $\Delta\alpha$. 127
8.21 Parameters a_o'' (a) and b_o'' (b) versus wind speed. Cox and Munk's data are also plotted (red circles). 128

9.1 Map of the 46 10-second arcs considered along the track. 132
9.2 Altitude, heading (azimuth from North) and speed of the aircraft during the 46 10-second arcs. 133
9.3 Power pattern of the LHCP antenna used to gather the GNSS-R signals (measurements provided by IEEC). It is a 3 dB antenna, having its cut-off at 55^o. It was mounted on the aircraft so that aircraft nose corresponds to azimuth 210^o. 134
9.4 Scatterometric bias in the delay waveform. 135
9.5 Sensitivity analysis of delay center to SWH. The nominal value is 2 m. 136
9.6 Sensitivity analysis of delay center to wind speed. The nominal value is 10 m/s (i.e., MSS = 0.025). 136
9.7 Sensitivity analysis of delay center to sea-surface slope PDF Isotropy (SPI). The nominal value is 0.55. 137
9.8 Sensitivity analysis of delay center to sea-surface slope PDF Azimuth (SPA). The nominal value is 0^o from North. 137
9.9 Estimated DMSS along the 46 10-second arcs for PRNs 08 (blue), 10 (red) and 24 (green). **First column**: estimated values. **Second column**: formal confidence interval length (CIL) of estimated values. **First row**: Total MSS. **Second row**: Slope PDF Azimuth. **Third row**: Slope PDF Isotropy. 139
9.10 Evolution of DMSS, delay center, Doppler center and RMSE values through the convergence process (here for PRN 10). Iterations number 0, 2, 4, 6, 8, 10 are respectively plotted in blue, red, green, black, clear blue and magenta. **First column**: DMSS values with, from top to bottom, the Total MSS, SPA and SPI. **Second column**: From top to bottom, delay center, Doppler center and RMSE. 141
9.11 Examples of data and best-fit model DDMs. Those correspond to Arc01. **First column**: PRN 08. **Second column**: PRN 24. **First row**: Data DDMs. **Second row**: Best-fit Model DDMs. **Third row**: Data-model residual. . . . 142
9.12 DMSS estimated along the aircraft track. **First row**: Total MSS (in dB). **Second row**: Slope PDF Azimuth. **Third row**: Slope PDF Isotropy. 145
9.13 Total MSS versus Jason's wind speed. 146

10.1 Geometry of the Salpex Experiment. 150

10.2 Salpex experimental campaign. 151
10.3 Satellites in view during Salpex experiment. Each colored arc represents the position of a GPS satellite during the experiment. The PRN number is closed to the beginning of the data. The green mask represents the area where the GPS signal reflections are supposed to be free of shadowing phenomena due to the environment of the swimming pool, and therefore only the satellite within this mask can be taken into consideration for further analysis. 151
10.4 Dependence of the real and imaginary parts of the dielectric constant as function of temperature T for different salinities (in psu). Klein and Swift's models at 1.575 GHz. 154
10.5 Dependence of the real and imaginary parts of the dielectric constant as function of salinity S for different temperatures. Klein and Swift's model at 1.575 GHz. 155
10.6 Dependence of the reflectivity in parallel polarization as a function of salinity S for different elevation angles. 155
10.7 Penetration depth in cm versus salinity for different temperatures. Klein's model at 1.575 GHz. 156
10.8 Amplitude and phase of U_{RR} versus $\sin\gamma$. Both pure water case (blue curve) and salted water case (red curve) are plotted for T=10^o C (full line) and T=20^o C (dashed line). 157
10.9 Amplitude and phase of U_{RL} versus $\sin\gamma$. Both pure water case (blue curve) and salted water case (red curve) are plotted for T=10^o C (full line) and T=20^o C (dashed line). 158
10.10(a) Phase of U_{RL} at nadir versus permittivity. Dielectric loss factor is 0, 50 and 100. (b) Phase of U_{RL} at nadir versus dielectric loss factor. Permittivity is 0, 65 and 85. 158
10.11Power model versus elevation angle for two different values of salinity (S=1 psu and S=30 psu). The experimental conditions are similar to the Salpex ones. T=11^{o}C. PRN 17. 159
10.12Interference pattern as a function of the sine of the elevation for pure water (blue curve) and salted water (red curve). 160
10.13Repeatability of the data. Plot of the power difference between two measurements with same experimental conditions, for both pure water (blue curve) and salted water (red curve). 161
10.14Fit of the Salpex experimental data using model presented in equation 10.18, when the ground contribution is taken into account. The data correspond to a salted water (30 psu). PRN 17. 161
10.15Percent change in power between S=40 psu and S=20 psu as a function of sine of elevation angle (see equation 10.21). 163

11.1 Geometry of the experiment during Part B. 166
11.2 Time series of the peak power (in dB), using PRN 01, of RHCP antenna (blue curve) and LHCP antenna (red curve). *Left*: Part A, the corresponding satellite elevation is 21^o (its azimuth is 61^o). *Right*: Part B, the elevation is 20^o (azimuth 62^o). 166
11.3 *Left*: Mean power $\langle\tilde{P}(\tau)\rangle$ for different noise levels (σ=10, 20, 40 and 60). The choice of these variances is related to the observed peak value in the data. The peak of correlation is one for a clean signal. *Right*: Zoom of the squared correlation in the grass, before lag zero (peak position). 1000 realizations, PRN 01, T_i=10 ms. 170

11.4 Simulated mean peak power at lag zero versus inverse noise variance $1/\sigma^2$. A line with slope 1 is also plotted. 1000 realizations, PRN 01, T_i=10 ms. 170
11.5 *Left*: Normalized variance of the power for different noise levels (σ=10, 20, 40 and 60). *Right*: Normalized variance at lag zero versus σ^2. 1000 realizations, PRN 01, T_i=10 ms. 171
11.6 Mean of the ratio of two power waveforms (with noise σ_d^2 and σ_r^2) at lag zero versus K^{-1}, with $K = \sigma_r^2/\sigma_d^2$. $\sigma_d = 60$, and σ_r ranges between 60 and 300. . . . 172
11.7 *Left*: Mean power of RHCP antenna (thick curve) and LHCP antenna (dashed curve), PRN 01, Part A. *Right*: Zoom of the squared correlation in the grass, after lag zero. 172
11.8 *Left*: Mean power of RHCP antenna (thick curve) and LHCP antenna (dashed curve), PRN 01, Part B. *Right*: Zoom of the squared correlation in the grass, after lag zero. 173
11.9 Normalized variance of the squared correlation for the RHCP antenna (thick curve) and the LHCP antenna (dashed curve), PRN 01. *Left*: Part A. *Right*: Part B. 173

List of Tables

1 Related experiments carried out during the thesis. 13

8.1 Parameter estimation in chronological order. 115

9.1 Overview of the parameters necessary for running the DDM forward model. . 133
9.2 Set of nominal parameters for sensitivity analysis of parameter $\Delta\tau$. 135
9.3 Analysis of estimated DMSS of figure 9.9. 138

Bibliography

[Anderson1999] Anderson. Study of the impact of sea state on nadir looking and side looking microwave backscatter. Technical report, Inventory of Models, ESA Contract No. 12934/98/NL/GD, 1999.

[Aparicio *et al.*2000] J.M. Aparicio, G. Ruffini, E. Cardellach, and A. Rius. Constellation performance for GNSS scatterometry. Technical report, OPPSCAT-I WP3100 - ESA ESTEC Contract No. 13461/99/NL/GD, 2000.

[Aparicio *et al.*2002] J.M. Aparicio, E. Cardellach, and A. Rius. Paris Alpha: experiment analysis. Technical report, PARIS Alpha CCN3 - ESA ESTEC Contract No. 13461/99/NL/GD, 2002.

[Apel1994] J.R. Apel. An improved model of the ocean surface wave vector spectrum and its effects on radar backscatter. *Journal of Geophysical Research*, 99, 1994.

[Apel1995] J.R. Apel. Principles of ocean physics. *International Geophysics Series*, 38, 1995.

[Barrick1968] D. Barrick. Rough surface scattering based on the specular point theory. *IEEE Trans. Antennas and Propagation*, AP-16(4):449–454, 1968.

[Beckmann and Spizzichino1963] P. Beckmann and A. Spizzichino. *The scattering of electromagnetic waves from rough surfaces.* 1963.

[Bjerkaas and Riedel1979] A.W. Bjerkaas and F.W. Riedel. Proposed model for the elevation spectrum of a wind-roughened sea surface. Technical report, Appl. Phys. Lab., Johns Hopkins Univ., Laurel, Md., APL-TG-1328-I-31, 1979.

[Born and Wolf1993] M. Born and E. Wolf. *Principles of Optics.* 1993.

[Cardellach and Ruffini2000] E. Cardellach and G. Ruffini. End to end performance. Technical report, 2000. WP3400 of OPPSCAT 1 Project - ESA Contract 13461/99/NL/GD.

[Cardellach *et al.*2003] E. Cardellach, G. Ruffini, D. Pino, A. Rius, A. Komjathy, and J. Garrison. Mediterranean balloon experiment: GPS reflection for wind speed retrieval from the stratosphere. *To appear in Remote Sensing of Environment*, 2003.

[Cardellach2002] E. Cardellach. Sea surface determination using GNSS reflected signals. *Thesis Dissertation*, Universitat Politècnica de Catalunya, 2002.

[Chapron *et al.*2000] B. Chapron, V. Kerbaol, D. Vandemark, and T. Elfouhaily. Importance of peakedness in sea surface slope measurements and application. *Journal of Geophysical Research*, 105:17195–17202, 2000.

[Chen and Fung1988] M.F. Chen and A.K. Fung. A numerical study of the regions of validity of the Kirchhoff and small-perturbation rough surface scattering models. *Radio Science*, 23:163–170, 1988.

[Courant and Hilbert1989] R. Courant and D. Hilbert. *Methods of Mathematical Physics*, volume 1. 1989.

[Cox and Munk1954] C. Cox and W. Munk. Measurement of the roughness of the sea surface from photographs of the sun's glitter. *Journal of the Optical Society of America*, 44:838–850, 1954.

[Cox and Munk1956] C. Cox and W. Munk. Slopes of the sea surface deduced from photographs of sun glitter. *Bull. Scripps Inst. Ocean.*, 6:401–488, 1956.

[Dierendonck2000] Dierendonck. The new L5 civil GPS signal. *GPS World 2000, http://www.gpsworld.com/1000/1000inov.html*, 2000.

[Donelan and Pierson1987] M.A. Donelan and W.J.P. Pierson. Radar scattering and equilibrium ranges in wind-generated waves. *Philos. Trans. R. Soc. London, Ser A*, pages 509–562, 1987.

[Duncan *et al.*1974] J.R. Duncan, W.C. Keller, and J.W. Wright. Fetch and wind speed dependence of Doppler spectra. *Radio Science*, 9(10):809–819, 1974.

[Durden and Vesecky1990] S.L. Durden and J.F. Vesecky. A numerical study of the separation wavenumber in the two-scale scattering approximation. *IEEE Trans. Geosc. Remote Sens.*, 28(2):271–272, 1990.

[Elfouhaily *et al.*1997] T. Elfouhaily, B. Chapron, K. Katsaros, and D. Vandemark. A unified directional spectrum for long and short wind-driven waves. *Journal of Geophysical Research*, 102(15):781–796, 1997.

[Elfouhaily *et al.*1999a] T. Elfouhaily, D.Thompson, D. Vandemark, and B. Chapron. Weakly nonlinear theory and sea state bias estimation. *Journal of Geophysical Research*, 104(C4):7641–7647, April 1999.

[Elfouhaily *et al.*1999b] T. Elfouhaily, D. Thompson, D. Vandemark, and B. Chapron. A new bistatic model for electromagnetic scattering from perfectly conducting rough surfaces. *Waves Random Media*, 9:281–294, 1999.

[Elfouhaily *et al.*2002] T. Elfouhaily, D.Thompson, and L. Linstrom. Delay-Doppler analysis of bistatically reflected signals from the ocean surface: Theory and application. *IEEE Transactions on Geoscience and Remote Sensing*, 40(3), 2002.

[Ellison *et al.*1996] W. Ellison, A. Balana, G. Delbos, K. Lamkaouchi, L. Eymard, C. Guillou, and C. Prigent. Study and measurements of the dielectric properties of sea water. Technical Report 11197/94/NL/CN, European Space Agency, 1996.

[Ellison *et al.*1998] W. Ellison, A. Balana, G. Delbos, K. Lamkaouchi, L. Eymard, C. Guillou, and C. Prigent. New permittivity measurements of sea water. *Radio Sci.*, 33(C3):639–648, 1998.

[Fontana *et al.*2001] R.D. Fontana, W. Cheung, and T. Stansell. The modernized L2 civil signal. *GPS World*, 2001.

[Fung and Lee1982] A. Fung and K.K. Lee. A semi-empirical sea-spectrum model for scattering coefficient estimation. *IEEE J. Oceanic Eng.*, 7(4):166–176, 1982.

[Fung1994] A. K. Fung. *Microwave Scattering and Emission Models and their Applications*. Norwood, MA: Artech House, 1994.

[Gardashov2000] R.G. Gardashov. The probability density of the total curvature of a uniform random gaussian sea surface in the specular points. *International Journal of Remote Sensing*, 21(15):2917–2926, 2000.

[Garrison2002] J.L. Garrison. Wind speed measurement using forward scattered GPS signals. *IEEE Trans. Geoscience and Remote Sensing*, 40:50–65, 2002.

[Garrison2003] J.L. Garrison. Anisotropy in reflected GPS measurements of ocean winds. In *Proc. IEEE IGARSS, Toulouse, France*, 2003.

[Germain and Ruffini2002] O. Germain and G. Ruffini. Multi-look techniques: SHArp Reflectometry Profiling. Technical report, Starlab, 2002. WP400 of OPPSCAT II Project - ESA Contract RFQ/3-10120/01/NL/SF.

[Germain *et al.*2003] O. Germain, G. Ruffini, F. Soulat, M. Caparrini, B. Chapron, and P. Silvestrin. The GNSS-R Eddy Experiment II: L-band and optical speculometry for directional sea-roughness retrieval from low altitude aircraft. In *Proceedings of the 2003 Workshop on Oceanography with GNSS-R*. Starlab, July 2003.

[Gourrion *et al.*2002a] J. Gourrion, D. Vandemark, S. Bailey, and B. Chapron. Investigation of C-band altimeter cross section dependence on wind speed and sea state. *Accepted for publication in Canadian Journal of Remote Sensing*, 2002.

[Gourrion *et al.*2002b] J. Gourrion, D. Vandemark, S. Bailey, B. Chapron, C. Gommenginger, P.G. Challenor, and M.A. Srokosz. A two parameter wind speed algorithm for Ku-band altimeters. *J. Atmos. Oceanic Tech.*, 19:2030–2048, 2002.

[Hara *et al.*1994] T. Hara, E.J. Bock, and D. Lyzenga. In situ measurements of capillary-gravity wave spectra using a scanning laser slope gauge and microwave radars. *Journal of Geophysical Research*, 99(12):593–602, 1994.

[Hasselmann1973] K. Hasselmann. Measurements of wind-wave growth and swell during JONSWAP 1973. *Dtsch. Hydrogr. Z.*, page 95, 1973.

[Hein *et al.*2002] G.W. Hein, J. Godet, J.L Issler, J.C Martin, P. Erhard, R. Lucas-Rodriguez, and T. Pratt. Status of Galileo frequency and signal design. Technical report, Galileo Signal Task Force of the European Commission, 2002.

[Hofmann-Wellenhof *et al.*1997] B. Hofmann-Wellenhof, H. Lichtenengger, and J. Collins. *GPS, Theory and Practice*. 1997.

[Holliday1987] D. Holliday. Resolution of a controversy surrounding the Kirchhoff approach and the small perturbation method in rough surface scattering theory. *IEEE Trans. Antennas Propag.*, 35:120–122, 1987.

[Huang *et al.*1973] N.E. Huang, D.T. Chen, C. Tung, and J.R. Smith. Interactions between steady non-uniform currents and gravity waves with applications for currents measurements. *Journal of Physical Oceanography*, pages 420–431, 1973.

[ICD-GPS-7052002] ICD-GPS-705. Navstar GPS space segment / user segment L5 interfaces. Technical report, GPS NAVSTAR JPO, Second Draft Version, 29 March, 2002.

[Jähne and Riemer1990] B. Jähne and K.S. Riemer. Two-dimensional wavenumber spectra of small-scale water surface waves. *Journal of Geophysical Research*, 95(11):531–546, 1990.

[Kavak *et al.*1996] A. Kavak, G. Xu, and W.J. Vogel. GPS multipath fade measurements to determine L-band ground reflectivity properties. *Proc. NAPEX XX JPL*, 1996.

[Klein and Swift1977] L. Klein and C. Swift. An improved model for the dielectric constant of sea water at microwave frequencies. *IEEE Trans. Antennas and Propagation*, AP-25:104–111, 1977.

[Kodis1966] R. Kodis. A note on the theory of scattering from an irregular surface. *IEEE Trans. Antennas and Propagation*, AP-14(1):77–82, 1966.

[Komjathy *et al.*2000a] A. Komjathy, J.A. Maslanik, V.U. Zavorotny, P. Axelrad, and S.J. Katzberg. Sea ice remote sensing using surface reflected GPS signals. In *Proceedings of the IEEE International Geoscience and Remote Sensing Symposium, Honolulu, Hawaii*, July 2000.

[Komjathy *et al.*2000b] A. Komjathy, V.U. Zavorotny, P. Axelrad, G.H Born, and J.L. Garrison. GPS signal scattering from sea surface: Wind speed retrieval using experimental data and theoretical model. *Remote Sensing of Environment*, 73:162–174, 2000.

[Kudryavtsev *et al.*1999] V. Kudryavtsev, V. Makin, and B. Chapron. Coupled sea surface atmosphere model. part 2. spectrum of short wind waves. *Journal of Geophysical Research*, 104(C4):7625–7639, 1999.

[Levenberg1944] K. Levenberg. A method for the solution of certain nonlinear problems in least squares. *Quart. Appl. Math.*, 2:164–168, 1944.

[Longuet-Higgins1958] M.S. Longuet-Higgins. The statistical distribution of the curvature of a random gaussian surface. In *Proceedings of the Cambridge Philosophical Society*, 1958.

[Lowe *et al.*2002] S. Lowe, C. Zuffada, Y. Chao, P. Kroger, J.L LaBreque, and L.E. Young. 5-cm precision aircraft ocean altimetry using GPS reflections. *Geophysical Research Letters*, (29):4359–4362, 2002.

[Lowe1999] S.T. Lowe. Voltage signal-to-noise ratio (SNR) nonlinearity resulting from incoherent summation. Technical report, NASA-JPL, 1999.

[MacDonald2002] K. D. MacDonald. The modernization of GPS: Plans, new capabilities and the future relationship to Galileo. *The Journal of Global Positioning Systems*, 1:1–17, 2002.

[Marchand and Brown1998] R.T. Marchand and G.S. Brown. Inferring rough surface parameters from average scattering data using approximate scattering models 2. Pierson-Moskowitz spectrum. *Radio Science*, 33(4):835–843, 1998.

[Marquardt1963] D.W. Marquardt. An algorithm for least-squares estimation of nonlinear parameters. *Journal of the Society for Industrial and Applied Mathematics*, 11:431–441, 1963.

[Martìn-Neira1993] M. Martìn-Neira. A PAssive Reflectometry and Interferometry System (PARIS): application to ocean altimetry. *ESA Journal*, 17:331–355, 1993.

[Masters *et al.*2002] D. Masters, V. Zavorotny, S. Katzberg, and W. Emery. GPS signal scattering from land for moisture content determination. In *IGARSS 2002 Proceedings*, 2002.

[Masters *et al.*2003] D. Masters, S. Katzberg, and P. Axelrad. Airborne GPS bistatic radar soil moisture measurements during smex02. In *Proceedings of the 2003 Workshop on Oceanography with GNSS-R*, July 2003.

[PARIS Gamma2003] PARIS Gamma. PARIS technology concept definition. Technical Report ASTRIUM-Starlab Contract 12050061SUB, 2003.

[Parkinson and Spilker1996] B.W. Parkinson and J.J. Spilker, editors. *Global Positioning System: Theory and Applications*, volume 1. AIAA, 1996.

[Phillips1966] O.M. Phillips, editor. *The dynamics of the upper ocean.* Cambridge University Press, 1966.

[Picardi *et al.*1998] G. Picardi, R. Seu, S. G. Sorge, and M. Martìn-Neira. Bistatic model of ocean scattering. *IEEE Trans. Antennas and Propagation*, 46(10):1531–1541, 1998.

[Pierson and Moskowitz1964] W.J. Pierson and L. Moskowitz. A proposed spectral form for fully developed wind sea based on the similarity theory of S.A. Kitaigorodskii. *Journal of Geophysical Research*, 69:5181–5190, 1964.

[PIPAER2000] PIPAER. Paris Interferometric Processor Analysis and Experiment Results. Technical report, IEEC and GMV - ESA Contract 14071/99/NL/MM, 2000.

[Rice1951] S. Rice. Reflection of electromagnetic waves from slightly rough surfaces. *Commun. Pure Appl. Math.*, 4:251, 1951.

[Rius *et al.*2002] A. Rius, J.M. Aparicio, E. Cardellach, M. Martìn-Neira, and B. Chapron. Sea surface state measured using GPS reflected signals. *Geophysical Research Letters*, 29(23):2122, 2002.

[Rodriguez and Kim1992] E. Rodriguez and Y. Kim. A unified perturbation expansion for surface scattering. *Radio Science*, 27:79–93, 1992.

[Ruffini and Soulat2000a] G. Ruffini and F. Soulat. Monte-Carlo simulations for L-band electromagnetic reflections. Technical report, OPPSCAT I WP3230 - ESA ESTEC Contract No. 13461/99/NL/GD, 2000.

[Ruffini and Soulat2000b] G. Ruffini and F. Soulat. PARIS interferometric processor analysis and experiment results, http://arxiv.org/physics/0011027. Technical report, IEEC and GMV - ESA Contract 14071/99/NL/MM, 2000.

[Ruffini *et al.*1999] G. Ruffini, E.Cardellach, A.Rius, and J.M.Aparicio. Remote sensing of the ocean by bistatic observations: a review. Technical report, OPPSCAT WP1000 - ESA ESTEC Contract 13461/99/NL/GD, 1999. Available online at http://starlab.es.

[Ruffini *et al.*2000] G. Ruffini, J.L. Garrison, E. Cardellach, A. Rius, M. Armatys, and D. Masters. Inversion of GPS-R delay-Doppler mapping waveforms for wind retrieval. In *Proc. IEEE IGARSS, Honolulu, HA*, 2000.

[Ruffini *et al.*2001a] G. Ruffini, M. Caparrini, O. Germain, F. Soulat, and J. Lutsko. Remote sensing of the ocean by bistatic radar observations: a review. Technical report, PARIS Beta WP1000 - ESA ESTEC Contract No. 15083/01/NL/MM, 2001. Available online at http://starlab.es.

[Ruffini *et al.*2001b] G. Ruffini, O. Germain, F. Soulat, M. Caparrini, J. Lutsko, and B. Chapron. Modelling of the received signal characteristic. Technical report, PARIS Alpha WP2000 - ESA Contract 14285/85/NL/PB, 2001.

[Ruffini *et al.*2003] G. Ruffini, F. Soulat, M. Caparrini, and O. Germain. The GNSS-R Eddy Experiment I: altimetry from low altitude aircraft. In *Proceedings of the 2003 Workshop on Oceanography with GNSS-R*. Starlab, July 2003.

[Schooley1962] A. H. Schooley. Upwind-downwind ratio of radar return calculated from facet size statistics of a wind-distributed water surface. *Proc. IRE*, 50:456–461, 1962.

[Shaw2000] Shaw. Modernization of the Global Positioning System. *GPS World 2000, http://www.gpsworld.com/1000/1000shaw.html*, 2000.

[Soulat and Ruffini2002] F. Soulat and G. Ruffini. L-band radiometry with GNSS-R. Technical report, IFREMER Contract, 2002.

[Soulat and Ruffini2003] F. Soulat and G. Ruffini. Salpex 1: Salinity experiment with GNSS-R. Technical report, IFREMER Contract, 2003.

[Soulat *et al.*2002a] F. Soulat, M. Caparrini, G. Ruffini, O. Germain, and K. Sharman. GRADAS: a tool for GNSS-R scattering simulations. Technical report, PARIS-BETA WP3100 - ESA ESTEC Contract No. 15083/01/NL/MM, 2002.

[Soulat *et al.*2002b] F. Soulat, B. Chapron, G. Ruffini, J. Gourrion, and O. Germain. Sea surface slope / wind coupling. Technical report, OPPSCAT II/WP600 - Speculometry with GNSS-R. ESA ESTEC Contract No. RFQ/3-10120/01/NL/SF, 2002.

[Soulat *et al.*2003] F. Soulat, B. Chapron, and G. Ruffini. SORES data inversion. Technical report, OPPSCAT II/CCN2 WP140 - Speculometry with GNSS-R. ESA ESTEC Contract No. RFQ/3-10120/01/NL/SF, 2003.

[Stegelmann and Garvey1973] E. Stegelmann and J. Garvey. Ocean sunglitter background in the infrared. *IRIS*, 18, 1973.

[Tatarskii1993] V. I. Tatarskii. The expansion of the solution of the rough-surface scattering problem in powers of quasi-slopes. *Waves Randiom Media*, 3:127–146, 1993.

[Ulaby *et al.*1986] F.T. Ulaby, R.K. Moore, and A.K. Fung. *Microwave Remote Sensing, Active and Passive*. Artech House, 1986.

[Valenzuela1978] G. Valenzuela. Theories for the interaction of elctromagnetic and oceanic waves. *Bound. Layer Met.*, 13:61–85, 1978.

[Vandemark *et al.*2003] D. Vandemark, B. Chapron, J. Sun, and G. Crescenti. Examination of ocean altimeter backscatter variability using aircraft-derived wind, sea slope and Ka-band radar measurements. *In review*, 2003.

[Voronovich1994] A.G. Voronovich. Small-slope approximation for electromagnetic wave scattering at a rough interface of two dielectric half spaces. *Waves Random Media*, 4:337–367, 1994.

[Zavorotny and Voronovich2000] V. Zavorotny and A. Voronovich. Scattering of GPS signals from the ocean with wind remote sensing application. *IEEE Trans. Geoscience and Remote Sensing*, 38(2):951–964, 2000.

[Zuffada and Elfouhaily2000] C. Zuffada and T. Elfouhaily. Determining wind speed and direction with ocean reflected GPS signals. In *Proceedings of Sixth Int. Conf. on Remote Sensing for Marine and Coastal Environments, Charleston*, 2000.